In compliance with the
Canadian Privacy Legislation
some supporting forms
may have been removed from
this dissertation.

While these forms may be included
in the document page count,
their removal does not represent
any loss of content from the dissertation.

University of Alberta

Frequency Code Multiple Access, a New Physical Layer for Optical Metropolitan Area Networks

by

Craig Wesley Unick ©

A thesis submitted to the Faculty of Graduate Studies and Research in partial fulfilment of the requirements for the degree of Doctor of Philosophy.

Department of Electrical and Computer Engineering

Edmonton, Alberta

Fall, 2003

National Library of Canada
Acquisitions and Bibliographic Services
395 Wellington Street
Ottawa ON K1A 0N4
Canada

Bibliothèque nationale du Canada
Acquisisitons et services bibliographiques
395, rue Wellington
Ottawa ON K1A 0N4
Canada

Your file Votre référence
ISBN: 0-612-88060-5
Our file Notre référence
ISBN: 0-612-88060-5

The author has granted a non-exclusive licence allowing the National Library of Canada to reproduce, loan, distribute or sell copies of this thesis in microform, paper or electronic formats.

L'auteur a accordé une licence non exclusive permettant à la Bibliothèque nationale du Canada de reproduire, prêter, distribuer ou vendre des copies de cette thèse sous la forme de microfiche/film, de reproduction sur papier ou sur format électronique.

The author retains ownership of the copyright in this thesis. Neither the thesis nor substantial extracts from it may be printed or otherwise reproduced without the author's permission.

L'auteur conserve la propriété du droit d'auteur qui protège cette thèse. Ni la thèse ni des extraits substantiels de celle-ci ne doivent être imprimés ou aturement reproduits sans son autorisation.

Canada

University of Alberta

Library Release Form

Name of Author: Craig Wesley Unick

Title of Thesis: Frequency Code Multiple Access, a New Physical Layer for Optical Metropolitan Area Networks

Degree: Doctor of Philosophy

Year this Degree Granted: 2003

Permission is hereby granted to the University of Alberta Library to reproduce single copies of this thesis and to lend or sell such copies for private, scholarly, or scientific research purposes only.

The Author reserves all other publication and other rights in association with the copyright in this thesis, and except as hereinbefore provided, neither the thesis nor any substantial portion thereof may be printed or otherwise reproduced in any form whatever without the author's prior written permission.

2

Date: Sept 10/2003

University of Alberta

Faculty of Graduate Studies and Research

The undersigned certify that they have read, and recommend to the Faculty of Graduate Studies and Research for acceptance, a thesis entitled **Frequency Code Multiple Access, a New Physical Layer for Optical Metropolitan Area Networks** submitted by Craig Wesley Unick in partial fulfilment of the requirements for the degree of Doctor of Philosophy.

Dr. Jim McMullin, Supervisor

Dr. Ray Decorby

Dr. Chris Haugen

Dr. Ying Tsui

Dr. Richard Marchand

Dr. Paul Jessop, External Examiner

Date: Sept. 9, 2003.

“Learning is the process of becoming unconfused.”

Roy Ludwig

Dedication

Dedicated to the memory of my parents:

Marjorie (1941 - 1999)

and

Ernest (1936 - 2003)

Abstract

The optical physical layer design of optical communication networks is most commonly based on intensity modulation and direct detection. This thesis proposes a multilevel frequency shift keyed optical system as an alternative. The features of this optical link design enable a multiple access scheme to be employed on a subwavelength granularity, the scheme is denoted Frequency Code Multiple Access (FCMA). Each channel of the multiplexed signal is separated out at the receiver using a parallel architecture of harmonically related Mach-Zehnder optical filters. The demultiplexing is effected passively in the optical domain.

Some network architectures are suggested in this work where the unique features of FCMA can be exploited. The majority of this dissertation concentrates on the construction of the enabling network components and the performance of a prototype single wavelength FCMA system.

The performance matrix suggests that FCMA is limited to applications with transmitted symbol rates ranging from 622 Mega-symbols per second to 2488 Mega-symbols per second (two common SONET line rates). Transmission is limited to distances ranging from tens of kilometers to a couple hundred kilometers which suggests a metropolitan area network application. The number of channels that can be multiplexed is limited by the linewidth of the transmission light source.

Acknowledgement

I'd like to thank TRLabs for providing the support and facilities without which this work would not have been possible. Thanks also to Drs. Ian MacDonald, Jim McMullin and Jan Conradi for help and guidance along the way.

I'd also like to thank the many students with whom I studied with at the U. of A. An extra special thank you to my good friends Dr. David Boertjes, Dr. Raj Nagarajan, Deepak Sarda, Robert Hang and Peng Mok. A thank you to David Clegg, lab manager at TRLabs, for advice and help in the lab and good conversations over lunch.

A thank you also goes to my comrades at Nortel Networks; my former manager Dr. Gen Ribakovs and former director Dr. Robert Keys, as well as Francois Boudreault and Sam Zaid my peers, also Dr. Marc Veilleux and Mike Moyer. Many battles long fought and hard won together.

Table of Contents

Chapter 1. Introduction. 1

1.1 Metropolitan Area Networks. 1

1.1.1 Established MAN Technologies. 3

1.1.2 A New Format - Gigabit Ethernet. 4

1.1.3 Comments on Deploying a Broadband Network. 4

1.1.4 The Physical Layer of a Fiber Optic Communication Link. 4

1.1.5 Increasing Utility Through Multiplexing and Multiple Access. 6

1.1.6 Summary of Metropolitan Area Networks. 8

1.2 A Potpourri of Design Requirements. 8

1.2.1 Physical Layer Design Requirements. 8

1.2.2 Network Design Requirements. 10

1.3 An Introduction to FCMA. 11

1.3.1 FCMA, A Coherent Optical Physical Layer Solution. 11

1.4 FCMA Transmitted Signal Format. 12

1.4.1 Multilevel FSK in the Optical Frequency Domain. 14

1.4.2 Constructing a 16 Level Signal from Four Binary Channels. 16

1.5 Harmonic Decoding. 17

1.6 Intermediate Signal Space Diagrams for FCMA. 21

1.6.1 $\log_2 M$ Binary e-ASK Channels to one M-ary e-ASK Channel. 21

1.6.2 M-ary e-ASK to M-ary o-ISK. 22

1.6.3 M-ary o-ISK to M-ary o-FSK. 23

1.6.4 One M-ary o-FSK to $\log_2 M$ Differential Binary o-ISK Channels. 23

1.6.5 Differential Binary o-ISK to Binary e-ASK. 26

1.7 Comments on Signal Conversion Linearities. 28

1.8 Design Limitations of the First Generation FCMA System. 29

1.8.1 Chromatic Dispersion Limitations. 30

1.8.2 Optical Power Budgeting, the Link Budget. 32

1.8.3 Summary of Design Limitations. 34

1.9 Hardware Implementation Options. 34

1.9.1 Transmitter Options. 34

1.9.2 Harmonic Decoder Options. 35

1.9.3 Receiver Options. 35

1.9.4 Implementation Option Summary. 36

1.10 Goals of the First Generation FCMA System. 36

1.11 FCMA Metropolitan Area Networks. 37

1.11.1 A Single FCMA Link. 37

1.11.2 An Electrical Cross-Connect Network Node. 38

1.11.3 Head-End Switching. 40

1.11.4 FCMA with WDM. 43

1.11.5 Bi-directional Bus Architecture. 44

1.11.6 Network Summary. 46

1.12 Summary of Chapter 1 and Chapter by Chapter Overview. 46

Chapter 2. Semiconductor Laser Theory for Frequency Shift Keying. 48

2.1 The Mathematical Description of Laser Frequency Response. 49

2.2 Semiconductor Laser Rate Equations. 50
2.3 Laser Parameter Values and Subsidiary Equations. 53
  2.3.1 General Subsidiary Equations. 54
  2.3.2 Laser Oscillation Frequency. 56
  2.3.3 Gain Compression. 57
  2.3.4 Optical Powers Inside and Outside of the Laser. 59
  2.3.5 Section 2.3 Summary. 59
2.4 Semiconductor Laser Modelling using the Runge Kutta Method. 60
2.5 Free-Running Single-Mode Semiconductor Lasers. 60
  2.5.1 Continuous Wave Operation. 62
  2.5.2 Electrically Modulated Semiconductor Lasers. 66
  2.5.3 A Note on External Modulation of Semiconductor Lasers. 71
2.6 Semiconductor Lasers that are not Single-Moded. 72
2.7 Optical Injection in Semiconductor Lasers. 73
2.8 Optical Injection in DFB Semiconductor Lasers. 75
  2.8.1 Continuous Wave Optical Injection in DFB Lasers. 76
  2.8.2 Modulation of DFB Lasers by Optical Injection. 90
2.9 Optical Injection in FP Semiconductor Lasers. 93
  2.9.1 Incoherent Optical Injection in FP Lasers. 95
  2.9.2 Simultaneous Coherent and Incoherent Optical Injection in FP Lasers. 96
  2.9.3 Modulation of FP Lasers by Optical Injection. 101
2.10 Comparison of DFB to FP Lasers with Optical Injection. 103
2.11 Comparison of Electrically versus Optically Modulated Lasers. 107
2.12 Generation of Multilevel FCM Signal with DFB Lasers. 107
2.13 Data Throughput Limits using Optical Injection in DFB Lasers. 115
2.14 Summary of Chapter 2. 117
Chapter 3. Optical Injection Laser Transmitters. 118
3.1 Experimental Considerations for Laser Injection. 118
3.2 Optical Injection Fabry Perot FSK Transmitter. 120
  3.2.1 Free-Running Fabry-Perot Laser Mode Spectrum. 121
  3.2.2 Mode Partition Noise in Semiconductor FP Lasers. 124
  3.2.3 Spontaneous Emission Injection and Mode Stabilization. 125
  3.2.4 Injection of Laser Light. 131
  3.2.5 Co-injection of Spontaneous Emission and Laser Light. 133
  3.2.6 Frequency Modulation of the Slave Laser. 139
  3.2.7 Summary of Injection in FP Lasers. 141
3.3 Optical Injection Distributed Feedback FSK Transmitter. 141
  3.3.1 Injection of Laser Light into Residual FP Modes of DFB Lasers. 143
3.4 Summary of Optical Injection Experiments. 148
Chapter 4. Mach-Zehnder Interferometer Harmonic Decoders. 150
4.1 Interference for a Mach-Zehnder Interferometer. 152
  4.1.1 Equal Incident Amplitudes and Constant Optical Frequency. 153
  4.1.2 MZ Interferometer Response to an Arbitrary Signal. 156
4.2 Design of the Free Space Mach-Zehnder Interferometer. 157
  4.2.1 Optical Component Layout. 158
  4.2.2 Optical Component Specifications. 159

4.2.3 Operation of the Free-Space Mach-Zehnder Interferometer. 160
4.2.4 The Signal Power Budget. 162
4.2.5 Experimental Values for Beam Splitter Equation Coefficients. 165
4.3 Design of the Integrated Mach-Zehnder Interferometers. 166
4.3.1 Device Layout. 167
4.3.2 Waveguide Parameters. 168
4.3.3 Multi-mode Interference Devices. 170
4.3.4 Novel Bending Architecture. 173
4.3.5 Waveguide Bend Loss Calculations. 174
4.3.6 Thermal Control. 181
4.3.7 Recombination Phase Errors. 181
4.3.8 Integrated Mach-Zehnder Decoder Fabrication. 182
4.3.9 Tests of the Integrated Mach-Zehnders. 183
4.3.10 Coupling and Propagation Loss Estimates for PLC MZs. 184
4.4 Simulated Response of the MZ to the FCM Signal. 186
4.4.1 Ideal MZ Decoder Response to the FCM Signal. 187
4.4.2 Free-Space MZ Response to the FCM Signal. 190
4.5 Phase Noise Impact on Signal to Noise Ratio. 195
4.5.1 Error Probabilities with Ideal Signal Levels. 198
4.5.2 Sensitivity of the BER to Linewidth and Signal Frequency Errors. ... 201
4.6 Mach-Zehnder Harmonic Decoder Design Summary. 205
Chapter 5. Dual Differential Optical Receivers. 207
5.1 Receiving Digital Data with Dual Differential Receivers. 208
5.2 Dual Differential Receiver Design. 209
5.3 PIN Photodiodes and Transimpedance Amplifiers. 213
5.4 Proposed Receiver Circuit. 214
5.4.1 PIN Diode Equivalent Circuit. 217
5.4.2 Equivalent Circuit for Simulation. 218
5.4.3 Optical Receiver Simulation Results. 220
5.5 Receiver RF Substrate Layout. 221
5.6 Measured Response of the Optical Receiver. 223
5.6.1 Comparison of Receiver Simulations and Measurements. 227
5.7 Received Signal Eye Diagrams for Back-to-Back FCMA Links. 229
5.8 Theoretical BER Performance of Back-to-Back FCMA Links. 231
5.9 Summary of Dual Differential Receiver. 235
Chapter 6. FCMA MAN Design - A Discussion and Review. 236
6.1 FCMA Link Power Budget Revisited. 237
6.1.1 BER and the per Channel Optical Power Splitting of the Decoder. ... 238
6.1.2 Achievable FCMA Link Length. 241
6.2 Transmission Fiber Dispersion and FCM Signals. 242
6.2.1 Chromatic Dispersion and 16 Level FCM Signal Distortion. 242
6.2.2 Chromatic Dispersion and 4 Level FCM Signal Distortion. 246
6.3 Optically Amplified FCMA System Concepts. 249
6.4 WDMA and Optically Amplified FCMA System Concepts. 250
6.5 FCMA - A Review. 252

Chapter 7. Conclusions and Future Work. 260
- **7.1** Chapter 2 Conclusions and Future Work. 260
- **7.2** Chapter 3 Conclusions and Future Work. 262
- **7.3** Chapter 4 Conclusions and Future Work. 263
- **7.4** Chapter 5 Conclusions and Future Work. 265
- **7.5** Chapter 6 Conclusions and Future Work. 266
- **7.6** General Conclusions and Future Work. 267

Appendix A. Mach-Zehnder Delay Lengths. 282

Appendix B. PIN Diode Characterization and Simulation. 285
- **B.1** Network Analyser Measurement of PIN Diode S_{11}. 286
- **B.2** From Measured Data to Equivalent Circuit Model. 288
- **B.3** Discussion of the PIN Diode Model. 288

Appendix C. Receiver Transfer Function Measurement. 290
- **C.1** Measurement of the Lucent Mach-Zehnder Modulator Transfer Function. 291
- **C.2** Separation of the Mach-Zehnder and Receiver Responses. 293
  - **C.2.1** Measured Optical Receiver Transfer Function. 294

Appendix D. Receiver Sensitivity from Noise Calculations. 295
- **D.1** Calculation of Personicks Integrals for a Known Transfer Function. 296
- **D.2** Justification of Relevant Noise Terms. 297
- **D.3** Evaluation of Personick's Integrals. 298
- **D.4** Signal and Noise Amplitudes as Functions of the Received Power. 299
- **D.5** Bit Error Ratios for a Differential Receiver. 301

List of Figures

Figure 1-1: Schematic depiction of generic fiber optic communication link. 5

Figure 1-2: Schematic demonstration of multiple access using WDM over a common optical fiber. $Tx_{\lambda 1}$ and $Tx_{\lambda 2}$ represent the transmitters for transmitted information at optical wavelength λ_1 and λ_2. $Rx_{\lambda 1}$ and $Rx_{\lambda 2}$ represent the receivers for received information at optical wavelength λ_1 and λ_2. 7

Figure 1-3: A block diagram depicting successive signal conversions for a two channel FCMA link, including the transmitter and receiver. 13

Figure 1-4: Representation of the optical frequency of an ideal four level FCMA signal for an eight symbol duration. 14

Figure 1-5: A pictorial representation of the FCMA signal codes and the frequencies that correspond to those codes for a 16 level (4 channel) FCMA system. For example, signal code 10 corresponds to an optical frequency of $\nu_0 + 10\Delta\nu$. 15

Figure 1-6: Circuit schematic for combining four channels of binary ASK data of equal pulse amplitude to create a 16 level voltage signal (16-ary ASK). 17

Figure 1-7: A representative schematic of a passive optical demultiplexor based on imbalanced Mach-Zehnder interferometers used for demultiplexing and decoding the four channels of a 16 level FCM signal. The imbalance (or delay) lengths are represented by ΔL_1, ΔL_2, ΔL_3 and ΔL_4. 18

Figure 1-8: Signal space diagram of an electrical ASK signal and corresponding voltage levels. V_0 and V_1 represent the voltage levels of a binary 0's and 1's, respectively. 21

Figure 1-9: An equally spaced 16-level amplitude shift keyed voltage signal. 22

Figure 1-10: An equally spaced 16-level intensity shift keyed optical power signal. 22

Figure 1-11: An equally spaced 16-level frequency shift keyed optical power signal. 23

Figure 1-12: An equally spaced 16-level frequency shift keyed optical power signal after being split at the receiving end of the link and passing through the Mach-Zehnder filter for channel four. Optical power is plotted on the horizontal axis and optical frequency is on the vertical axis where the symbols are represented by the numeric subscripts. 24

Figure 1-13: Optical frequency versus optical power of all transmitted FCMA symbols as they appear at the output of the Mach-Zehnder demultiplexor for a four channel system (the P_{MZ+} output only). **a)** channel 1. **b)** channel 2. **c)** channel 3. **d)** channel 4. 25

Figure 1-14: Electrical signal voltages of all transmitted FCMA symbols as they appear at the output of the dual differential receivers for a four channel system (V_{MZ} from Equation (3)). **a)** channel 1. **b)** channel 2. **c)** channel 3. **d)** channel 4. 26

Figure 1-15: The diagram depicts the most basic functional representation of a single four-channel FCMA link. There are four electrical channels that are multiplexed at the transmitter (Tx), transmitted over a fiber optic link on a single wavelength (λ) and demultiplexed into four output electrical channels at the receiver (Rx). 38

Figure 1-16: A diagram depicting the electrical and optical connections that cross connect two pairs of FCMA links. Transmitters and receivers are labelled Tx and Rx respectively, with subscripts to denote the manner in which they are connected. 39

Figure 1-17: A diagram representation of an electrical cross connect network node that provides local access. 40

Figure 1-18: An example of a more complex network connectivity that shows the internal electrical multiplexing elements of one of the transmitters, Tx_d. Figure 1-19 will show the details of what is happening inside of Tx_d. 41

Figure 1-19: A diagrammatical representation of what is necessary for Tx_d to perform switching of 1/4 of its aggregate data from Tx_f to Tx_g as depicted in Figure 1-18 without decoding the addressing information of the constituent channels. **a)** represents the initial gain configuration and **b)** represents the gain configuration after switching. 42

Figure 1-20: A two optical channel example of co-directional wavelength division multiplexing of FCM signals on different wavelengths. 43

Figure 1-21: A two optical channel example of bi-directional wavelength division multiplexing of FCM signals on different wavelengths. Concatenation of network nodes and links of this type creates a bidirectional bus network. ... 45

Figure 2.1: Optical power output from one facet of a DC biased laser, biased at twice threshold, as a function of time. 61

Figure 2.2: Optical frequency offset from the threshold oscillation frequency of a DC biased laser, biased at twice threshold, as a function of time. 61

Figure 2.3: Output optical power versus normalized bias current (bias current divided by the threshold current) for gain compressions of 3 and 6 W^{-1}. 63

Figure 2.4: Output optical frequency offset from the threshold frequency versus normalized bias current (bias current divided by the threshold current) for gain compressions of 3 and 6 W^{-1}. 64

Figure 2.5: Optical frequency offset to output optical power ratio versus laser bias current for gain compressions of 3 and 6 W^{-1}. 65

Figure 2.6: An example calculation result of the output optical power for a binary signal by current modulating a semiconductor laser, with a gain compression of 6 W^{-1}. 67

Figure 2.7: An example calculation result of the output optical frequency offset from threshold for a binary signal by current modulating a semiconductor laser, with a gain compression of 6 W^{-1}. 68

Figure 2.8: An expanded view of a high to low bit transition for the optical power and optical frequency offset for the example calculation result plots of Figures 2.6 and 2.7 highlighting the relaxation oscillations. 69

Figure 2.9: An expanded view of a high to low bit transition for the optical power and optical frequency offset for an example calculation with the same bit sequence as Figures 2.6 and 2.7, but a gain compression of 3 W^{-1}, highlighting the relaxation oscillations. 70

Figure 2.10: Schematic diagram of an optical injection system that uses a master/

slave laser arrangement. 76

Figure 2.11: Instability (oscillation) of the optical power output from one facet for two modes of a DC biased DFB laser, biased at three times threshold, with DC optical injection as a function of time. 77

Figure 2.12: Instability (oscillation) of the optical frequency, offset from the threshold oscillation frequency, for the dominant mode of a DC biased DFB laser, biased at three times threshold, with DC optical injection as a function of time. 77

Figure 2.13: Self-pulsation of the optical power output from one facet for two modes of a DC biased DFB laser, biased at three times threshold, with DC optical injection as a function of time. 78

Figure 2.14: Optical frequency offset from the threshold oscillation frequency during self-pulsation for the dominant mode of a DC biased DFB laser, biased at three times threshold, with DC optical injection as a function of time. 79

Figure 2.15: Root mean square deviation of the free-running optical frequency of a DFB laser as a function of incident injected optical power for a sidemode suppression of 30 dB and five values of injected frequency detuning. 80

Figure 2.16: Root mean square deviation of the free-running optical frequency of a DFB laser as a function of incident injected optical power for a sidemode suppression of 30 dB and five values of injected frequency detuning. 80

Figure 2.17: Root mean square deviation of the free-running optical frequency of a DFB laser as a function of incident injected optical power for a sidemode suppression of 20 dB and five values of injected frequency detuning. 81

Figure 2.18: Root mean square deviation of the free-running optical frequency of a DFB laser as a function of incident injected optical power for a sidemode suppression of 20 dB and five values of injected frequency detuning. 82

Figure 2.19: Optical power output from one facet of a DC biased laser, biased at three times threshold, with 1 mW incident optical injection power and a detuning of -20 GHz as a function of time. 83

Figure 2.20: Output optical frequency offset for the free-running mode of a DC biased laser, biased at three times threshold, with 1 mW incident optical injection power and a detuning of -20 GHz as a function of time. 83

Figure 2.21: The time averaged optical power of the free-running mode of the semiconductor laser plotted as a function of incident injected optical power with a sidemode suppression of 30 dB and biased at three times threshold. Various optical frequency detunings are shown. The horizontal sections for detunings of -15, -18 and -20 GHz detunings are for unstable operation. 84

Figure 2.22: The time averaged optical frequency offset from threshold of the free-running mode of the semiconductor laser plotted as a function of incident injected optical power with a sidemode suppression of 30 dB and biased at three times threshold. Various optical frequency detunings are shown. The horizontal sections for detunings of -15, -18 and -20 GHz detunings are for unstable operation. 85

Figure 2.23: The output optical power of the free-running mode from one facet of the laser with the maximum amount of incident injection power for laser bias currents between two and four times threshold with injection detuning as a parameter. The output power of this mode without injection is included to demonstrate the effect of the injection. 86

Figure 2.24: The optical powers from Figure 2.23 are replotted as the difference between the free-running optical power without injection minus the free-running optical power at maximum injection for the same frequency detunings and normalized laser biases. 87

Figure 2.25: The maximum frequency modulation depth of the free-running mode of the laser for laser bias currents between two and four times threshold. The injection frequency detuning is a parameter. 88

Figure 2.26: The total output optical power (free-running and injected modes) from one facet of the laser with the maximum amount of incident injection power for laser bias currents between two and four times threshold with injection detuning as a parameter. The output power of the free-running mode without injection is included to demonstrate the effect of the injection. 89

Figure 2.27: The maximum incident injected optical power at the facet of the laser for bias currents between two and four times threshold with injection detuning as a parameter. 90

Figure 2.28: Schematic diagram of an optical injection system that uses a master/slave laser arrangement that uses an electro-optic modulator to modulate the injected signal. 91

Figure 2.29: An example calculation result of the output optical power for a binary signal by optical injection modulating a DFB laser. 92

Figure 2.30: An example calculation result of the output optical frequency offset from the threshold frequency for the free-running mode of a DFB laser for a binary signal by optical injection modulation. 93

Figure 2.31: Schematic diagram of an optical injection system that uses a master/slave laser arrangement with additional Amplified Spontaneous Emission (ASE) injection. 94

Figure 2.32: The sidemode suppression ratio with spontaneous emission injection is plotted against the original sidemode suppression ratio of the laser with the Relative Spontaneous Emission Spectral Density (RSESD) as a parameter. 95

Figure 2.33: Maximum frequency modulation depth of a Fabry-Perot laser with RSESD = 10 for the main mode and coherent optical injection into a sidemode with the original sidemode suppression ratio as a parameter. 97

Figure 2.34: Maximum frequency modulation depth of a Fabry-Perot laser with RSESD = 100 for the main mode and coherent optical injection into a sidemode with the original sidemode suppression ratio as a parameter. 98

Figure 2.35: Maximum frequency modulation depth of a Fabry-Perot laser with RSESD = 1000 for the main mode and coherent optical injection into a sidemode with the original sidemode suppression ratio as a parameter. 99

Figure 2.36: Maximum change of free-running mode optical power due to coherent sidemode injection with different amounts of spontaneous emission injection into the main mode. RSESD (= 10) refers to the relative spontaneous emission spectral density. 99

Figure 2.37: Maximum change of free-running mode optical power due to coherent sidemode injection with different amounts of spontaneous emission injection into the main mode. RSESD (= 100) refers to the relative spontaneous emission spectral density. 100

Figure 2.38: Maximum change of free-running mode optical power due to coherent sidemode injection with different amounts of spontaneous emission injection into the main mode. RSESD (= 1000) refers to the relative spontaneous emission spectral density. 100

Figure 2.39: Schematic diagram of an optical injection system that uses a master/slave laser arrangement that uses an electro-optic modulator to modulate the injected signal, including an ASE source to select and stabilize the dominant mode of the slave laser. 101

Figure 2.40: An example calculation result of the output optical frequency offset from the threshold frequency for the free-running mode of a FP laser for a binary signal by optical injection modulation with RSESD = 1000. 102

Figure 2.41: An example calculation result of the output optical power for a binary signal by optical injection modulating a FP laser with RSESD = 1000. 103

Figure 2.42: The linewidth of a FP laser with binary modulated optical injection in a sidemode and RSESD = 1000 for the free-running mode as a function of time. 105

Figure 2.43: The linewidth of a DFB laser with binary modulated optical injection in a sidemode and for the free-running mode as a function of time. 106

Figure 2.44: The frequency levels of a four level FCM signal referenced to the threshold value of the free-running laser mode frequency as a function of the MZ EO modulator phase offset with a modulation index of 99% as defined in Equation (52). 110

Figure 2.45: The frequency difference between successive frequency levels of a four level FCM signal as a function of the MZ EO modulator phase offset with a modulation index of 99% as defined in Equation (52). 110

Figure 2.46: The mean frequency level spacing of a four level FCM signal as a function of the MZ EO modulator phase offset Simulation results for modulation indices of 99% and 80% are shown. 111

Figure 2.47: The largest absolute deviation of all three frequency level spacings from the mean frequency level spacing versus the phase offset of the MZ EO modulator. Simulation results for modulation indices of 99% and 80% are shown. 112

Figure 2.48: The largest deviation of all three frequency level spacings from the mean frequency level spacing as a percentage of the mean frequency level spacing versus the phase offset of the MZ EO modulator. Simulation results for modulation indices of 99% and 80% are shown. 112

Figure 2.49: The mean frequency level spacing of a eight level FCM signal as a function of the MZ EO modulator phase offset Simulation results for modulation indices of 99% and 80% are shown. 113

Figure 2.50: The largest deviation of all seven frequency level spacings from the mean frequency level spacing as a percentage of the mean frequency level spacing versus the phase offset of the MZ EO modulator. Simulation results for modulation indices of 99% and 80% are shown. 114

Figure 3-1: Schematic diagram of a general optical injection system that uses a master/slave laser arrangement. 119
Figure 3-2: A depiction of the optical confinement properties of a typical Fabry-Perot semiconductor laser. 120
Figure 3-3: A functional diagram of a Fabry Perot Laser. The photons depicted internal to the laser cavity are shown to be "in phase" after one round trip in the cavity. 121
Figure 3-4: The free-running FP laser spectrum at 25 mA bias current is shown with laser temperature as a parameter. The spectra were measured with a monochromator. 122
Figure 3-5: The free-running FP laser spectrum at 35 mA bias current is shown with laser temperature as a parameter. The spectra were measured with a monochromator. 123
Figure 3-6: The free-running FP laser spectrum at 45 mA bias current is shown with laser temperature as a parameter. The spectra were measured with a monochromator. 123
Figure 3-7: A general depiction of the co-injection of a coherent signal and a narrow band spontaneous emission source into a laser diode. 125
Figure 3-8: The optical schematic of the narrow band spontaneous emission light source. 126
Figure 3-9: The optical spectrum of the spontaneous emission source (EDFA) used to produce the narrow band spontaneous emission injected into the FP laser. The spectrum with and without the feedback from the fiber Bragg grating (FBG) filter is shown. 127
Figure 3-10: The optical spectrum of the spontaneous emission source after amplification and filtering which becomes the narrow band spontaneous emission injected into the FP laser. 128
Figure 3-11: A close up view of the amplified and filtered spontaneous emission optical spectrum shown in Figure 3-10. 128
Figure 3-12: Experimental setup for ASE injection power calibration. A Hewlett Packard optical power meter was used to measure the optical power. 129
Figure 3-13: The optical spectrum of the FP laser with constant temperature, 17.5 °C, and 40 mA bias current with spontaneous emission injection power as a parameter (controlled via the pump current for the EDFA). 130
Figure 3-14: The optical spectrum of the FP laser with constant spontaneous emission injection power and 40 mA bias current with temperature as a parameter. 130
Figure 3-15: The optical spectrum of the FP laser subject to spontaneous emission injection power (EDFA pump laser biased at 150 mA) at a constant temperature, 17.5 °C, plotted with FP bias current as a parameter. Scanned with a monochromator. 131
Figure 3-16: The optical schematic of the optical circuit necessary to generate the ISK injection signal. (TBPF = tunable bandpass filter, ISO = optical isolator, PC = polarization controller) 132
Figure 3-17: The optical schematic of the ISK signal generation system including an optical amplifier to increase the strength of the injection. 133

Figure 3-18: An optical schematic showing the connections of the narrow-band spontaneous emission source (ASE Injection) and the ISK signal source to the slave laser. Also shown is the isolated output port where the FCM signal will appear. 134

Figure 3-19: The optical spectrum of the FP laser with spontaneous emission injection near 1550.8 nm and coherent (laser) injection near 1553.5 nm with a calibration wavelength at 1550.79 nm. Measured with a monochromator. 135

Figure 3-20: The optical spectrum of the FP laser as measured with a 40.4 GHz FSR tunable Fabry-Perot filter. The injected laser light is shown at approximately 14 GHz in the figure. The free-running FP laser mode shift is shown as a function of injected laser power. 135

Figure 3-21: The center frequency of the free-running FP laser mode as a function of injected optical power (in the fiber) for various values of optical frequency offset. The values in the legend were derived from linear least squares fits to the lines in the figure at 0 injected optical power. 137

Figure 3-22: The conversion efficiency of the free-running FP laser mode shift in GHz/mW of injected optical power (in the fiber) as a function of the free-running optical frequency without optical injection (offset arbitrarily). 138

Figure 3-23: The FP slave laser shown with ASE injection and ISK injection where the output light is filtered twice and isolated to allow only the free-running (FCM signal) mode to appear at the signal output. 139

Figure 3-24: The FP slave laser shown with ASE injection and ISK injection where the output light is filtered, amplified and filtered again, as well as isolated, to allow more power of the free-running (FCM signal) mode to appear at the signal output. 140

Figure 3-25: A functional diagram of a Distributed Feedback Laser showing that some feedback is due to reflections within the optical cavity with the ends of the laser (mirrors) providing the same feedback as they do in FP lasers. 142

Figure 3-26: The free-running spectrum of the DFB slave laser biased at 50 mA and at 14.9 °C. 142

Figure 3-27: The DFB slave laser shown with the ISK injection where the output light is filtered, amplified and filtered again, as well as isolated, to allow more power of the free-running (FCM signal) mode to appear at the signal output. 144

Figure 3-28: The optical spectrum of the DFB laser as measured with a 40.39 GHz FSR tunable Fabry-Perot filter. The injected laser light is shown at approximately 5.3 GHz in the figure. The free-running DFB laser mode shift is shown (on the right near 16 GHz) as a function of injected laser power. The calibration wavelength is near 4 GHz. 145

Figure 3-29: The center frequency of the free-running DFB laser mode as a function of injected optical power (in the fiber) for various values of optical frequency offset. The values in the legend were derived from linear least squares fits to the lines in the figure at 0 injected optical power. 146

Figure 3-30: The conversion efficiency of the free-running DFB laser mode shift in GHz/mW of injected optical power (in the fiber) as a function of the free-running optical frequency without optical injection (offset arbitrarily). 147

Figure 4-1: General optical layout of a free-space Mach-Zehnder interferometer with a path length difference of ΔL between Optical Path B and Optical Path A. (M1 and M2 are mirror 1 and 2, BS1 and BS2 are beam splitter 1 and 2.) 150

Figure 4-2: Schematic diagram of a 50% optical power splitter employing a partially reflective mirror. Input electric fields are $E_A(t)$ and $E_B(t)$ and the exiting light is denoted by optical powers $P_{out1}(t)$ and $P_{out2}(t)$. 153

Figure 4-3: Optical component layout of a free-space Mach-Zehnder interferometer based on an equilateral triangle geometry (shown in plan view looking from above the optical table). The arrows show the direction the light travels along the optical paths in thick lines. 158

Figure 4-4: The optical schematic for measuring the free spectral range of the free-space MZ interferometer. (TFPF = tunable Fabry-Perot filter, SM = single mode) 161

Figure 4-5: Light that is input to the free space interferometer is shown to be partially reflected by the partially reflective mirror of the beam splitter cube. . 162

Figure 4-6: Light re-enters the beam splitter cube of the free space interferometer and is forced to interfere at the by the partially reflective mirror of the beam splitter cube producing two output light beams. 163

Figure 4-7: An example device layout for the photomask. This device has four MZ interferometers that have a common input. 167

Figure 4-8: A scale drawing of the single mode waveguide sections of the harmonically related MZ interferometer devices that were fabricated. The waveguide core is 2 μm high by 2.5 μm wide with a refractive index of 1.55, and the substrate has a refractive index of 1.5. 169

Figure 4-9: Example plots of waveguide bend functions that subtend angles greater than or equal to 180° with values of α_C of 1/2, 1 and 2. Only part of the curve is used for the waveguide bend. 174

Figure 4-10: The vertical effective refractive index for vertically polarized light with a wavelength of 1550 nm in a waveguide structure with refractive indices and dimensions shown in Figure 4-8. 175

Figure 4-11: The integrated vertical electric field profile of the single mode waveguide for vertically polarized light. The core of the waveguide is centered at 0 in the figure and extends +/- 1.25 μm in either direction. 176

Figure 4-12: The insertion loss of 30 concatenated quarter circle waveguide bends for both vertical and horizontal polarized light, not including mode mismatch loss. 177

Figure 4-13: The insertion loss of 15 concatenated 90° cosine waveguide bends for both vertical and horizontal polarized light. 178

Figure 4-14: The insertion loss of 30 concatenated 45° cosine waveguide bends for both vertical and horizontal polarized light. 179

Figure 4-15: The insertion loss of 15 concatenated bends for the waveguide bends with the functional form given by Equation (88) for both vertical and horizontal polarized light. The parameter α_C takes on the value for the bends that were used in the MZ decoder. 180

Figure 4-16: An example of a damaged area on an integrated MZ harmonic decoder wafer. Three waveguides run vertically through the picture, they are

chipped off the substrate and surrounded by debris. 183
Figure 4-17: A photograph of a polished input waveguide on an integrated MZ harmonic decoder wafer. All of the layers are identified and the core of the waveguide is in the circle in the center of the photo. 184
Figure 4-18: Six eye diagrams depicting the difference between 1/2 bit overlap and 1/3 bit overlap for all three channels of an 8-ary, 622 Msps, FCM signal. The plots include the post subtraction after being received but do not include the receiver transfer function. **a)**, **b)** and **c)** are channels 1, 2 and 3 for 1/2 bit overlap and **d)**, **e)** and **f)** are channels 1, 2 and 3 for 1/3 bit overlap. 189
Figure 4-19: Six eye diagrams depicting the difference between the response of the free-space MZ without and with a neutral density filter (NDF) for all three channels of an 8-ary, 622 Msps, FCM signal. The plots include the post subtraction after being received but do not include the receiver transfer function. **a)**, **b)** and **c)** are channels 1, 2 and 3 without the NDF (denoted Real) and **d)**, **e)** and **f)** are channels 1, 2 and 3 with the NDF (denoted NDF). 192
Figure 4-20: Four eye diagrams depicting the difference between the response of an ideal MZ to the free-space MZ with a neutral density filter (NDF) for both channels of a 4-ary, 1250 Msps, FCM signal. The plots include the post subtraction after being received but do not include the receiver transfer function. **a)** and **b)** are channels 1 and 2 for the ideal MZ and **c)** and **d)** are channels 1 and 2 with the NDF (denoted NDF). 194
Figure 4-21: The response of the MZ decoder (post receiver subtraction) is shown at the top right. The bottom right plots the probability density function (pdf) for the phase of the incoming signal assuming an nominal linewidth. At the upper left is a plot of the probability density function for the optical power output from the MZ decoder. The dark lines indicate the ranges over which the pdfs must be integrated to obtain an equivalent cumulative error. 196
Figure 4-22: The BER of the $\pi/16$ symbol is shown for a symbol rate of 622 Msps as a function of signal laser linewidth, with the bit overlap as a parameter, when received on channel 4. 202
Figure 4-23: The BER is demonstrated to be a function of the frequency accuracy of the FCM symbols, specifically for the $\pi/8$ symbol of an eight or sixteen level signal received by channel 3. These calculations are for a laser linewidth of 10 MHz. 203
Figure 4-24: To achieve a BER of 10^{-9} or better at a symbol rate of 622 Msps with the $\pi/4$ symbols of the FCM signal, the linewidth of the signal laser line has to be less than the values shown for bit overlaps of 1/2 and 1/3. 204
Figure 4-25: To achieve a BER of 10^{-9} or better at a symbol rate of 1.25 Gsps with the $\pi/4$ symbols of the FCM signal, the linewidth of the signal laser line has to be less than the values shown for bit overlaps of 1/2, 1/3 and 1/4. 205
Figure 5-1: An example circuit schematic of the concatenation of PIN photodiodes in a dual differential receiver. 209
Figure 5-2: Functional diagram depicting the operation of a differential optical receiver. Optical input signals, bsig+ and bsig-, are converted to electrical signals and added to produce a single electrical output signal. 210
Figure 5-3: Circuit diagram of a transimpedance amplifier. 211

Figure 5-4: Proposed functional arrangement of the dual differential receiver. 213
Figure 5-5: The optical receiver circuit schematic (component values are listed in Table 5-1). 215
Figure 5-6: Equivalent circuit representation of a Nortel HS-PIN optical receiver diode. 217
Figure 5-7: Equivalent circuit for the optical receiver including parasitic contributions for passive components. 218
Figure 5-8: The electrical power response of the optical receiver as a function of frequency plotted as output electrical power referenced to electrical power generated by the PIN photodiode. 220
Figure 5-9: The electrical phase response of the optical receiver as a function of frequency plotted as output phase referenced to phase at the PIN photodiode with the linear phase contributions removed. 221
Figure 5-10: The top side (component side) of the receiver RF substrate. All of the circular features are via locations and all of the black areas are conductive. The circuit is not drawn to scale (see text). 222
Figure 5-11: The optical power to electrical voltage response of two optical receivers. The inverting receiver and noninverting receiver are identical and inverting, an inverting gain stage is external to the noninverting receiver. .. 224
Figure 5-12: The PIN photodiode voltage (in 50 Ω) to output voltage response of two optical receivers. The inverting receiver and noninverting receiver are identical and inverting, an inverting gain stage is external to the noninverting receiver. 225
Figure 5-13: The PIN photodiode electrical power (in 50 Ω) to electrical output power response of two optical receivers. The inverting receiver and noninverting receiver are identical and inverting, an inverting gain stage is external to the noninverting receiver. 225
Figure 5-14: The phase response of two optical receivers. The inverting receiver and noninverting receiver are identical and inverting, an inverting gain stage is external to the noninverting receiver. 226
Figure 5-15: The measured and simulated electrical power response of the optical receiver assuming the quantum efficiency is 0.75 in a 50 Ω electrical circuit. 227
Figure 5-16: The measured and simulated phase response of the optical receiver in a 50 Ω electrical circuit. 228
Figure 5-17: Four eye diagrams depicting the difference between the response of an ideal MZ to the free-space MZ with a neutral density filter (NDF) for both channels of a 4-ary, 1250 Msps, FCM signal. The plots include the post subtraction after being received and the receiver transfer function. **a)** and **b)** are channels 1 and 2 for the ideal MZ and **c)** and **d)** are channels 1 and 2 with the NDF (denoted NDF). 230
Figure 5-18: The BER for channel 1 of a 4 level FCM system evaluated for three different types harmonic decoder, ideal, real and NDF as defined in Chapter 4. The input optical power is referenced to the input of the delayed arm MZ decoder. 232
Figure 5-19: The BER for channel 2 of a 4 level FCM system evaluated for three

different types harmonic decoder, ideal, real and NDF as defined in Chapter 4. The input optical power is referenced to the input of the delayed arm MZ decoder. 233

Figure 5-20: The BER for channel 1 of a 4 level FCM system evaluated for the ideal harmonic decoder, but operated either as a dual differential receiver or a single receiver. The input optical power is referenced to the input of the delayed arm MZ decoder. 234

Figure 5-21: The BER for channel 2 of a 4 level FCM system evaluated for the ideal harmonic decoder, but operated either as a dual differential receiver or a single receiver. The input optical power is referenced to the input of the delayed arm MZ decoder. 235

Figure 6-1: A schematic diagram of the harmonic decoders of a two channel FCMA system where the insertion losses of the 1x2 splitter, IL_1 and IL_2, are labelled at the point where they would be measured with respect to the optical input. 239

Figure 6-2: Four eye diagrams of the four channels of the 16 level FCM signal transmitted at 1250 Msps. The calculation is for a back to back experiment (0 km link length). Channels 1, 2, 3 and 4 are shown in subplots **a)**, **b)**, **c)** and **d)**, respectively. 243

Figure 6-3: Four eye diagrams of the four channels of the 16 level FCM signal transmitted at 1250 Msps. The calculation is for a 40 km link length. Channels 1, 2, 3 and 4 are shown in subplots **a)**, **b)**, **c)** and **d)**, respectively. 244

Figure 6-4: Four eye diagrams of the four channels of the 16 level FCM signal transmitted at 1250 Msps. The calculation is for an 80 km link length. Channels 1, 2, 3 and 4 are shown in subplots **a)**, **b)**, **c)** and **d)**, respectively. 245

Figure 6-5: Two eye diagrams of the two channels of the 4 level FCM signal transmitted at 1250 Msps. The calculation is for an 80 km link length and an FCM signal of constant optical power. Channels 1 and 2 are shown in subplots **a)** and **b)**, respectively. 246

Figure 6-6: Two eye diagrams of the two channels of the 4 level FCM signal transmitted at 1250 Msps. The calculation is for a 320 km link length and an FCM signal of constant optical power. Channels 1 and 2 are shown in subplots **a)** and **b)**, respectively. 247

Figure 6-7: Two eye diagrams of the two channels of the 4 level FCM signal transmitted at 1250 Msps. The calculation is for an 80 km link length and a Runge Kutta generated FCM signal. Channels 1 and 2 are shown in subplots **a)** and **b)**, respectively. 247

Figure 6-8: Two eye diagrams of the two channels of the 4 level FCM signal transmitted at 1250 Msps. The calculation is for a 320 km link length and a Runge Kutta generated FCM signal. Channels 1 and 2 are shown in subplots **a)** and **b)**, respectively. 248

Figure 6-9: A diagram that illustrates the combination of a WDM multiplexor, WDM demultiplexor and an optical amplifier with multiple optical channels being transmitted over a fiber span of several km. 250

Figure 6-10: A diagram that illustrates the combination of a WDM multiplexor, WDM demultiplexor and optical amplifiers with multiple optical channels being transmitted over several fiber spans of several km each. 251

Figure 6-11: The received BER versus the optical power input to the MZ harmonic decoder, assuming ideal decoders, for channels 1 and 2 of a four level FCM transmission based on the Runge Kutta simulations of Chapter 2. The calculation includes the contribution of linewidth related noise. 257

Figure B-1: Functional electrical test schematic for measuring the (reflection) impedance of the PIN photo-diode chips. 285

Figure B-2: Circuit schematic of the equivalent circuit for the PIN diode detector. 285

Figure B-3: Smith chart plots for S_{11} reflection data from PIN diode measurements at **a)** 0 V reverse bias, **b)** 3 V reverse bias, **c)** 5 V reverse bias and **d)** 8 V reverse bias. 287

Figure B-4: Equivalent circuit model for the PIN diode. 289

Figure C-1: Electrical and optical circuits for the measurement of the Lucent Mach-Zehnder switching voltage, V_π. (ZHL 42W is the part number of a Mini-Circuits amplifier and PPL stands for Picosecond Pulse Labs.) 292

Figure C-2: Measured values of V_π for the Lucent Mach-Zehnder modulator as a function of frequency. 293

Figure C-3: Circuit Schematic for the measurement of the optical receiver transfer function. (PPL stands for Picosecond Pulse Labs.) 294

List of Tables

Table 1-1: Logic levels of four independent binary channels and the corresponding FCMA codes and transmitted optical frequencies. 16
Table 2-1: Initial parameter values for laser rate equation integration. 54
Table 2-2: Required total frequency excursions for FCM signals with different transmission formats, bit overlap times and number of frequency levels. The entries in bold are frequency ranges that are considered to be within the reach of the optical injection modulation method. The entries in italics are attainable with moderate increases in the linewidth enhancement factor and/or the gain compression coefficient. 116
Table 4-1: Numerical apertures and divergence angles for the single mode waveguides for the integrated MZ harmonic decoder. 170
Table 4-2: The effective refractive indices and modal beat lengths of the multi-mode interference (MMI) couplers. 171
Table 4-3: MMI coupler physical lengths for 1x4 and 1x2 splitters and 2x2 combiners. 172
Table 4-4: The effective refractive indices used to calculate the bend loss of the single-mode waveguide for both polarizations. 176
Table 4-5: Bit error ratios (BERs) are tabulated for the different phase values that comprise a 16-ary FCM signal. The decoder delay for the lowest FSR channel of the harmonic decoder is stated as a parameter. Any values of BER less than 10^{-21} are shown as 0. 200
Table 5-1: Component values for the circuit schematic in Figure 5-5. 216
Table 5-2: Waveguide impedances and lengths for the simulation circuit in Figure 5-7. 219
Table 6-1: A comparison for three cases of the calculated optical power necessary to achieve a BER of 10^{-9} for each channel of multilevel FCMA transmissions. 239
Table 6-2: A comparison for three cases of the insertion loss for the distribution of the FCM optical signal to different MZ decoders to achieve a BER of 10^{-9} for each channel of multilevel FCMA transmissions. 240
Table 6-3: The ratio of optical power at the receiver for equal system *Q* for FCM versus ISK transmission for FCM channels of a 16 level signal calculated for FCM symbol pairs with the same phase difference but opposite polarity. Calculated for equal peak powers and equal average powers for FCM versus ISK. 255
Table 6-4: The calculated optical power necessary to achieve a BER of 10^{-9} for both channels of a 4 level FCMA 1.25 Gsps transmission and the optimized power splitter insertion losses for the 4 level Runge Kutta generated FCM signal. 258
Table 6-5: A visual summary of the calculated results of Table 2-2 and Table 4-5 which limit the application space of the FCMA systems. The white cells in this table represent acceptable performance, grey cells are borderline performance and black cells are unacceptable performance. 259
Table D-1: Evaluated values of Personick's first and second integral for various data rates for standard transmissions and of an FCM channel 1 signal. 299

List of Abbreviations

AC	Alternating Current
AGC	Automatic Gain Control
APD	Avalanche Photodiode
ASE	Amplified Spontaneous Emission
ASK	Amplitude Shift Keyed or Keying
ATM	Asynchronous Transfer Mode
BER	Bit Error Ratio
BERT	Bit Error Ratio Testset
BS1, BS2	Beam Splitter 1 or 2
CD	Chromatic Dispersion
CDM	Code Division Multiplexed or Multiplexing
CIF	Caltech Intermediate Format
D_1, D_2, etc.	Photodiodes
DC	Direct Current
DD	Direct Detection
deMUX	(Optical) Demultiplexor
DFB	Distributed Feedback (Laser)
DQDB	Distributed Queue Dual Bus
DPSK	Differential Phase Shift Keyed or Keying
DSF	Dispersion Shifted Fiber
DWDM	Dense Wavelength Division Multiplexed or Multiplexing
e-	Electrical (signal type)
E/O	Electrical to Optical
EDFA	Erbium Doped Fiber Amplifier
EDWA	Erbium Doped Waveguide Amplifier
EO	Electro-Optic
FB_1, FB_2, FB_3	Ferrite Beads in the Optical Receiver Schematic
FBG	Fiber Bragg Grating
FCM	Frequency Code Multiplexed or Multiplexing

FCMA	Frequency Code Multiple Access
FDM	Frequency Division Multiplexed or Multiplexing
FDDI	Fiber Distributed Data Interface
FEC	Forward Error Correction
FFP	Fiber Fabry-Perot (Filter)
FP	Fabry-Perot (Laser or Filter)
FSK	Frequency Shift Keyed or Keying
FSR	Free Spectral Range
FT_1, FT_2, FT_3	Power Feed Throughs in the Optical Receiver Schematic
FWHM	Full Width at Half Maximum
FWM	Four Wave Mixing
GDSII	A photomask file format
Gbps	Gigabits per second
Gsps	Giga symbols per second
HP	Hewlett-Packard
IC (or IC_1)	Integrated Circuit
IEEE	Institute of Electrical and Electronics Engineers
IF	Intermediate Frequency
ISI	Intersymbol Interference
ISK	Intensity Shift Keyed or Keying
ISO	(Optical) Isolator
LAN	Local Area Network
LED	Light Emitting Diode
LI	Light Intensity vs. Current
LOA	Linear Optical Amplifier
LSB	Least Significant Bit
M-ary	Integer M Number of Levels
M1, M2	Mirror 1 and 2
MAN	Metropolitan Area Network
Mbps	Megabits per second
MDS	Microwave Design Simulator

MMI	Multimode Interference (Coupler)
MSB	Most Significant Bit
MUX	(Optical) Multiplexor
MZ	Mach-Zehnder
NA	Numerical Aperture
NDF	Neutral Density Filter
NDSF	Non-Dispersion-Shifted Fiber
NZDSF	Non-Zero-Dispersion-Shifted Fiber
o-	Optical (signal type)
O/E	Optical to Electrical
OC	Optical Carrier
OSI	Open Systems Interconnection
p-n	Positive-Negative
PC	Polarization Controller
pdf	Probability Density Function
PDL	Polarization Dependent Loss
PIN (diode)	Positive-Intrinsic-Negative
PLC	Planar or Photonic Lightwave Circuit
PLL	Phase-Locked Loop
PM	Polarization Maintaining (Fiber)
PMD	Polarization Mode Dispersion
PON	Passive Optical Network
PPL	Picosecond Pulse Labs
PS/C	Polarization Splitter/Combiner
PSK	Phase Shift Keyed or Keying
RC	Resistor Capacitor
RF	Radio Frequency
RHS	Right Hand Side
RLC	Resistor Inductor Capacitor
RSESD	Relative Spontaneous Emission Spectral Density
Rx	Receiver

SM	Single Mode (Fiber)
SNR	Signal to Noise Ratio
SOA	Semiconductor Optical Amplifier
SONET	Synchronous Optical Network
SPM	Self Phase Modulation
SRS	Stimulated Raman Scattering
SSB	Single-Side-Band
TBPF	Tunable Bandpass Filter
TDM	Time Division Multiplexed or Multiplexing
TFPF	Tunable Fabry-Perot Filter
Tx	Transmitter
TZ	Transimpedance
VPN	Virtual Private Network
WAN	Wide Area Network
WDM	Wavelength Division Multiplexed or Multiplexing
WDM	Wavelength Division Multiple Access
WG (or WG$_1$, etc.)	Waveguide
XPM	Cross-Phase Modulation
νI	Optical Frequency vs. Current

List of Symbols

Roman Alphabet Symbols

A_0	Electric Field Amplitude of the Light Propagating Through the Mach-Zehnder Interferometer
$A_0(t)$	Electric Field Amplitude of the Light Propagating Through the Mach-Zehnder Interferometer as a Function of Time (Slowly Varying Envelope)
b	Optical Power of the Signal Incident on the Receiver Photodiode
b_k	Laser Modulation Waveform Symbol Value in Timeslot k
b_{sig+}	Optical Signal Amplitude of the Sum Output of the Mach-Zehnder Interferometer
b_{sig-}	Optical Signal Amplitude of the Difference Output of the Mach-Zehnder Interferometer
b_{FCM}	Optical Power of the Frequency Code Multiplexed Signal in the Calculation of Q
b_{ISK}	Optical Power of the Intensity Shift Keyed Signal in the Calculation of Q
$b_{1,symbol,channel}$	Optical Power of the Signal Incident on the Receiver Photodiode from the Mach-Zehnder Output 1 for a Particular Symbol and Channel
$b_{2,symbol,channel}$	Optical Power of the Signal Incident on the Receiver Photodiode from the Mach-Zehnder Output 2 for a Particular Symbol and Channel
B	Bit-rate or Symbol-rate of an Electrical or Optical Digital Signal
BW_{eq}	Equivalent Bandwidth for Q Comparisons
c	Speed of Light in Vacuum
C_{PIN}	Reflection Capacitance of the PIN Photodiode from the Receiver
$C_1 \ldots C_9$	Receiver Capacitors Capacitances

d_l	Detuning of the Master Laser with Respect to the Free-Running Slave Laser Frequency
d_{sl}	Detuning of the Free-Running Slave Laser Frequency With Respect to the Free-Running Slave Laser Frequency at Threshold
D	Electric Displacement
E	Electric Field
E_A	Electric Field of the Light Propagating Through Path A of the Mach-Zehnder Interferometer
E_{A1}	Electric Field of the Light Propagating Through Path A of the Mach-Zehnder Interferometer Appearing at Output 1
E_{A2}	Electric Field of the Light Propagating Through Path A of the Mach-Zehnder Interferometer Appearing at Output 2
E_B	Electric Field of the Light Propagating Through Path B of the Mach-Zehnder Interferometer
E_{B1}	Electric Field of the Light Propagating Through Path B of the Mach-Zehnder Interferometer Appearing at Output 1
E_{B2}	Electric Field of the Light Propagating Through Path B of the Mach-Zehnder Interferometer Appearing at Output 2
E_l	Electric Field of Laser Mode l
f_{mod}	Modulation Frequency for the Electro-Optic Mach-Zehnder Modulator
FSR_{MZ}	Mach-Zehnder Interferometer Free-Spectral Range
$g(n,S)$	Laser Gain as a Function of Carrier Number and Photon Number
g_n	First Order Derivative of the Laser Gain with Respect to the Carrier Number in the Active Region
g_{rl}	Laser Gain Reduction Factor for Mode l
g_{th}	Threshold Value of the Laser Gain
h	Planck's Constant
$\hbar$	Planck's constant divided by 2π

$h_{out}(t)$	Optical Pulse Shape Output from the Receiver in Receiver Noise Calculations
$h_p(t)$	Optical Pulse Shape Input to the Receiver in Receiver Noise Calculations
$H_{out}(\omega)$	Fourier Transform of the Optical Pulse Shape Output from the Receiver in Receiver Noise Calculations
$H_p(\omega)$	Fourier Transform of the Optical Pulse Shape Input to the Receiver in Receiver Noise Calculations
$H_{LMZ}(f)$	Optical Mach-Zehnder Electro-Optic Modulator Transfer Function
$H_{REC}(f)$	Optical Receiver Transfer Function
$H_T(\omega)$	Optical Receiver Transfer Function for Noise Calculations
i_f	Transimpedance Amplifier Feedback Current
i_i	Transimpedance Amplifier Input Current
$\langle i^2_a \rangle$	Mean Square Amplifier Noise Current
$\langle i^2_s \rangle$	Mean Square Shot Noise Current
$\langle i^2_s(0) \rangle$	Mean Square Shot Noise Current at the Center of the Optical Signal Symbol
$I(t)$	Injection Current of a Semiconductor Laser as a Function of Time
I_b	Laser Bias Current
I_{sig}	Electrical Signal Current from the Output of the Mach-Zehnder Interferometer
$I_{sig,symbol,channel}$	Electrical Signal Current from the Output of the Mach-Zehnder Interferometer for a Particular Symbol and Channel
$\overline{I_{symbol,channel}}$	Electrical Signal Current from the Output of the Mach-Zehnder Interferometer for a Particular Symbol and Channel, Expressed as a Mean in the Receiver Noise Probability Density Function
$\overline{I_{symbol,channel}(\Delta\phi_\tau)}$	Electrical Signal Current from the Output of the Mach-

	Zehnder Interferometer for a Particular Symbol and Channel, Expressed as a Mean in the Receiver Noise Probability Density Function, also as a Function of the Mach-Zehnder Phase Delay ($\Delta\phi_\tau$)
I_{sig+}	Electrical Signal Current of the Sum Output of the Mach-Zehnder Interferometer
I_{sig-}	Electrical Signal Current of the Difference Output of the Mach-Zehnder Interferometer
$I_{sig,0}$	Signal Current for a Transmitted 0 Symbol in the Q Definition
$I_{sig,1}$	Signal Current for a Transmitted 1 Symbol in the Q Definition
I_{th}	Injection Current of a Semiconductor Laser at Threshold
I_{total}	Total Electrical Signal Current of the Output of the Mach-Zehnder Interferometer
$\overline{I_{FCM}(\Delta\phi_\tau)}$	Mean Signal Current for FCM Signal with $\Delta\phi$ as a Parameter
I_1	Personick's First Integral
I_2	Personick's Second Integral
$IL_?$	Insertion Loss for the Optical Splitter to Distribute the Signal to the Channel Mach-Zehnder Decoders, for each Channel ?
$\mathscr{I}_0$	Optical Power of a Binary or Multilevel Intensity Shift Keyed Optical Signal
$\mathscr{I}_0'$	Center Symmetric Optical Power of a Binary or Multilevel Intensity Shift Keyed Optical Signal
$\mathscr{I}_m$	Optical Power of a Binary or Multilevel Intensity Shift Keyed Optical Signal that Represents the *m*th Level of the Signal
k_B	Boltzman's Constant
l	Subscript to Enumerate Laser Modes
L	Semiconductor Laser Active Region Length (Resonator Length)
$L_{\Delta T}$	Mach-Zehnder Interferometer Delay Length as a Fraction of the Symbol or Bit Period

L_d	Distance Travelled in Fiber Under the Influence of Chromatic Dispersion
$L_{disp.\ limit}$	Chromatic Dispersion Limited Distance
L_{PIN}	Reflection Inductance of the PIN Photodiode from the Receiver
L_π	Beat Length of a Multi-Mode Interference (Waveguide) Coupler
L_1, L_2	Receiver Inductor Inductances
ΔL	Difference in Propagation Distances for Optical Paths in a Mach-Zehnder Interferometer
$\Delta L_\#$	Difference in Propagation Distances for Optical Paths in the Mach-Zehnder Interferometer that Demultiplexes the Optical Signal to Recover Channel # of a Frequency Multiplexed Optical Signal
m	An Integer Index used to Denote a General Transmitted Symbol
m_i	Laser Modulation Waveform Modulation Index
M	Number of Levels in a Multilevel Signal
n	Electrical Carrier Number in the Active Region of a Laser
n_0	Electrical Carrier Number in the Active Region of a Laser at Transparency
n_{ar}	Active Region Refractive Index for a Laser
n_{cl}	Cladding Refractive Index for a Laser
n_{effy}	Optical Slab Waveguide Effective Refractive Index in the y-Direction
n_{sp}	Spontaneous Emission Inversion Factor of a Laser
n_{th}	Electrical Carrier Number in the Active Region of a Laser at Threshold
n_{MZ}	Filter Order of the Mach-Zehnder Interferometer
$n_{MZ\#}$	Filter Order of the # Channel Mach-Zehnder Decoder
$n'_{MZ\#}$	Filter Order of the # Channel Mach-Zehnder Decoder with Respect to the Center of the Spectrum of the Input Optical Signal
NF	Receiver Amplifier Noise Figure

$p_{\Delta\phi}(\Delta\phi)$	Probability Density Function of the Phase of the Laser Line
$p_P(P_{1\text{-}2})$	Probability Density Function of the Power of the Laser Line After Passing Through A Mach-Zehnder Interferometer
P_{cm}	Common Mode Optical Power of the Two Outputs of the Mach-Zehnder Interferometer
P_{dm}	Common Mode Optical Power of the Two Outputs of the Mach-Zehnder Interferometer
P_{in}	Input Optical Power to the Electro-Optic Mach-Zehnder Modulator
P_l^{in}	Incident Optical Power Outside of the Laser Facet for and Externally Injected Optical Signal Injected into a Laser Mode with Subscript *l*
$P_l^{in}(t)$	Incident Optical Power Outside of the Laser Facet for and Externally Injected Optical Signal Injected into a Laser Mode with Subscript *l*, as a Signal Waveform
$\overline{P}_l^{in}$	Incident Optical Power Outside of the Laser Facet for and Externally Injected Optical Signal Injected into a Laser Mode with Subscript *l*, as the Mean Value in the Signal Waveform
P_l^{out}	Output Optical Power Outside of the Laser Facet for a Laser Mode with Subscript *l*
P_{out1}	Optical Power of the Light Propagating Through the Mach-Zehnder Interferometer Appearing at Output 1
P_{out2}	Optical Power of the Light Propagating Through the Mach-Zehnder Interferometer Appearing at Output 2
$P_{channel}(e)$	Probability of Error for a Particular Channel
$P_{channel}(e\|0)$	Probability of Error when a 0 is Expected for a Particular Channel
$P_{channel}(e\|1)$	Probability of Error when a 1 is Expected for a Particular Channel
$P_{symbol,channel}(e\|0)$	Probability of Error when a 0 is Expected for a Particular Symbol and Channel
$P_{symbol,channel}(e\|1)$	Probability of Error when a 1 is Expected for a Particular

$P_{1\text{-}2}$	Optical Power of the Light Propagating Through the Mach-Zehnder Interferometer Appearing at Output 1 Minus the Optical Power of the Light Propagating Through the Mach-Zehnder Interferometer Appearing at Output 2
$P_{MZ}(\nu)$	Output Optical Power of a Mach-Zehnder Interferometer as a Function of Optical Frequency where $P_{MZ}(\nu) = P_{MZ+}(\nu) - P_{MZ-}(\nu)$
$P_{MZ+}(\nu)$	Optical Signal Power at the Primary Output of an Optical Mach-Zehnder Interferometer
$P_{MZ-}(\nu)$	Optical Signal Power at the Complementary Output of an Optical Mach-Zehnder Interferometer
P_{MZmax}	Maximum Optical Signal Power at Either Output of an Optical Mach-Zehnder Interferometer
P_{OPT}	Electro-Optic Mach-Zehnder Modulator Output Optical Power
$P_{OPT}(f)$	Electro-Optic Mach-Zehnder Modulator Output Optical Power and Input Optical Power to the Optical Receiver
q	Electronic Charge
Q	Ratio of the Average Signal Amplitude to the Average Noise Amplitude
$Q_{FCM,\Delta\phi}$	Ratio of the Average Signal Amplitude to the Average Noise Amplitude for the FCM Signal, with $\Delta\phi$ as an Argument
Q_{ISK}	Ratio of the Average Signal Amplitude to the Average Noise Amplitude for the ISK Signal
r_C	Radial Coordinate of the Cardioid Waveguide Bend Cylindrical Coordinate Function
r_{25}	Reflection Coefficient of Light Entering a Beam Splitter Cube at 25° from the Normal to the Reflective Surface
r_{65}	Reflection Coefficient of Light Entering a Beam Splitter Cube at 65° from the Normal to the Reflective Surface
R_{amp}	Noise Resistance of the Receiver Amplifier

R_{eq}	Equivalent Noise Resistance of the Receiver Amplifier used to Calculate the Noise Resistance
R_f	Transimpedance Amplifier Feedback Resistance
R_m	Semiconductor Laser Mirror Reflectivities
R_{PIN}	Reflection Resistance of the PIN Photodiode from the Receiver
R_R	Relative Spontaneous Emission Spectral Density
R_s	Rate of Spontaneous Emission into the Laser Active Region
R_1	Receiver Resistor Resistance
R_{25}	Reflectivity of Light Entering a Beam Splitter Cube at 25° from the Normal to the Reflective Surface
R_{65}	Reflectivity of Light Entering a Beam Splitter Cube at 65° from the Normal to the Reflective Surface
S_l	Number of Photons in the Lasing Cavity for the Laser Mode with Subscript *l*
S_l^{in}	Number of Photons Injected into the Lasing Cavity for the Laser Mode with Subscript *l*
S_R	Receiver Sensitivity
S_{11}	Reflection Scattering Parameter
t	Time
t_{25}	Transmission Coefficient of Light Entering a Beam Splitter Cube at 25° from the Normal to the Reflective Surface
t_{65}	Transmission Coefficient of Light Entering a Beam Splitter Cube at 65° from the Normal to the Reflective Surface
t_r	Rise Time of the Modulation Waveform Symbols
T	Elapse Time of one Bit Period or Symbol Period for a Digital Optical Signal
T_K	Receiver Temperature in Kelvin
T_{25}	Transmissivity of Light Entering a Beam Splitter Cube at 25° from the Normal to the Reflective Surface
T_{65}	Transmissivity of Light Entering a Beam Splitter Cube at 65° from the Normal to the Reflective Surface
v_g	Group Velocity (Optical Group Velocity)

v_o	Transimpedance Amplifier Output Voltage
V_0	Voltage of a Binary or Multilevel Amplitude Shift Keyed Electrical Signal that Represents the Zero Level of the Signal
V_0'	Center Symmetric Voltage Reference for Binary or Multilevel Amplitude Shift Keyed Electrical Signals
V_m	Voltage of a Binary or Multilevel Amplitude Shift Keyed Electrical Signal that Represents the *m*th Level of the Signal
$V_{c\#}$	Nominal Signal Voltage of a Channel (#) of a Multi-Channel Voltage Multiplexed Multilevel Amplitude Shift Keyed Signal Prior to Passive Multiplexing.
$V_{MZ}(\nu)$	Electrical Signal that is Proportional to the Difference of the Output Optical Powers of a Mach-Zehnder Interferometer as a Function of Optical Frequency
$V_{REC}(f)$	Output Voltage from the Optical Receiver
$V_{RF}(f)$	Input Voltage to the Electro-Optic Mach-Zehnder Modulator from the Network Analyzer to Measure the Optical Receiver Transfer Function
V_{RF0-p}	Voltage Amplitude of the Electro-Optic Mach-Zehnder Modulator Drive Signal from 0 to Peak Voltage
V_π	Voltage Applied to the Electro-Optic Mach-Zehnder Modulator to Change the Input Optical Phase by π

Greek Alphabet Symbols

α	Linewidth Enhancement Factor
α_m	Optical Loss in the Active Region of a Semiconductor Laser due to Transmission through the Laser Facets
α_l	Optical Loss in the Active Region of a Semiconductor Laser due to Transmission through the Laser Facets and Scattering
α_s	Optical Scattering Loss in the Active Region of a Semiconductor Laser
α_C	Bending Parameter of the Cardioid Waveguide Bend Cylindrical Coordinate Function

φ_{os}	Mach-Zehnder Electro-Optic Modulator Phase Offset in the Modulation Waveform
ϕ_l	Phase of the Slave Laser Mode with Subscript l
ϕ_{ml}	Phase of the Master Laser Mode with Subscript l
ϕ_r	Phase Accumulated in Reflecting From a Partially Transmissive Mirror in a Mach-Zehnder Interferometer
ϕ_t	Phase Accumulated in Passing Through a Partially Transmissive Mirror in a Mach-Zehnder Interferometer
ϕ_{ttrr}	Phase Difference in a Mach-Zehnder Interferometer Accumulated Due to One Path Having Two Transmissions and the Other Path Having Two Reflections
ϕ_{trtr}	Phase Difference in a Mach-Zehnder Interferometer Accumulated Due to Each Path Having One Transmission and One Reflection
ϕ_C	Angular Coordinate of the Cardioid Waveguide Bend Cylindrical Coordinate Function
$\phi(t)$	Transmitted Signal Phase as a Function of Time
$\Delta\phi$	Argument of the Phase Probability Density Function of the Laser Light
$\Delta\phi_N(t)$	Gaussian Random Phase Noise of the Light Input to the Mach-Zehnder Interferometer
$\Delta\phi_\tau(t)$	Cumulative Phase Difference Between the Two Paths of a Mach-Zehnder Interferometer
γ_{sms}	Sidemode Suppression Factor for the Laser Gain
$\gamma_{sms,l}$	Sidemode Suppression Factor for the Laser Gain of Mode l
η	Receiver Photodiode External Quantum Efficiency
κ_c	Semiconductor Laser Optical Injection Coupling Coefficient
κ_s	Semiconductor Laser Gain Compression Coefficient Normalized to the Photon Number
κ_p	Semiconductor Laser Gain Compression Coefficient Normalized to the Optical Power
$\Delta\lambda$	Wavelength Difference
λ_1, λ_2, etc.	Optical Wavelengths of a Wavelength Division Multiple

	Access (WDMA) Transmission System
λ_l	Wavelength of Laser Mode l
Λ_g	Bragg Grating Pitch
μ_{air}	Refractive Index of Air
μ_{core}	Refractive Index of the Core of an Optical Waveguide
μ_{eMZ}	Effective Index of Refraction for an Optical Path of a Mach-Zehnder Interferometer
μ_g	Group Refractive Index
μ_{subs}	Refractive Index of the Substrate of an Optical Waveguide
$\mu(L)$	Refractive Index Encountered by Light Passing Through a Mach-Zehnder Interferometer, may be a Function of Position
$\Delta\nu$	Optical Frequency Spacing of Adjacent Symbols in the Optical Frequency Domain of the Multilevel Optical Frequency Shift Keyed Signal
$\Delta\nu_{FWHM,l}$	Optical Linewidth, Full Width at Half Maximum, of Laser Mode l
$\Delta\nu_{LW}$	Optical Linewidth, Full Width at Half Maximum
$\Delta\nu_{TOTAL}$	Optical Spectral Width of the Transmitted Signal
ν	Optical Frequency
ν_0	Optical Frequency of a Multilevel (Optical) Frequency Shift Keyed Signal for the Optical Frequency Representing a Zero
ν_0'	Center Symmetric Optical Frequency Reference for Multilevel Frequency Shift Keyed Optical Signals
ν_l	Optical Frequency of the Laser Mode l
ν_l^{in}	Optical Frequency of the Master Laser Mode l
ν_m	Optical Frequency of a Multilevel (Optical) Frequency Shift Keyed Signal for the Optical Frequency Representing the *m*th Optical Frequency Level
ν_{sl}	Optical Frequency of the Slave Laser Mode l
ν_{th}	Optical Frequency of a Laser at Threshold
ν_{thl}	Optical Frequency of a Laser at Threshold of Mode l
σ_{ILW}	Standard Deviation for the Probability Density Function of

	the Electrical Current from the Laser Light After Passing Through a Mach-Zehnder Interferometer, in a Linear Approximation
σ_P	Standard Deviation for the Probability Density Function of the Intensity of the Laser Light After Passing Through a Mach-Zehnder Interferometer, in a Linear Approximation
$\sigma_{\Delta\phi}$	Standard Deviation for the Probability Density Function of the Phase of the Laser Light
$\sigma^2_{symbol,channel}$	Total Mean Square Noise Current for the Error Calculation for a Particular Symbol and Channel
τ_d	Propagation Delay for Different Wavelengths of Light After Travelling Through Fiber with Chromatic Dispersion
τ_d'	Linear Dispersion Coefficient
τ_L	Round Trip Cavity Group Propagation Time
τ_n	Electrical Carrier Lifetime in the Active Region of a Semiconductor Laser
τ_p	Photon Lifetime in the Active Region of a Semiconductor Laser
$\tau_{\Delta L}$	Transit Time Difference Between Two Paths of a Mach-Zehnder Interferometer
$\tau_{\Delta L\#}$	Transit Time Difference Between Two Paths of a Mach-Zehnder Interferometer for Channel #
ω_l^{in}	Circular Optical Frequency of an Externally Injected Optical Signal Injected into a Laser Mode with Subscript *l*
ω_{DC}	Constant Component of the Transmitted Signal Circular Optical Frequency
ω_S	Varying (Signal Carrying) Component of the Transmitted Signal Circular Optical Frequency

Chapter 1. Introduction.

Fiber optic based systems provide communication network designers with a means to meet the demands placed on communication systems by the trend toward digital transmission of most, if not all, electronic media services; internet, phone, fax, video and data. Fiber optic communications encompasses many subsets of technology where the available data formats, signal distribution schemes and properties of guided light give designers seemingly endless alternatives for deploying systems that must meet specific requirements. The objective of this research on Frequency Code Multiple Access (FCMA) is to provide communication network designers with another alternative in the ongoing challenge to achieve optimum system deployment in a particular application area; optical Metropolitan Area Networks (MANs).

This introductory chapter begins with a brief overview of optical networks and relevant design considerations of the physical layer for present and future fiber optic networks on a scale that applies to medium and large population centers, metropolitan areas, with populations greater than about 500,000 people in Sections 1.1 and 1.2. The basic principles of a single FCMA fiber link are outlined in Sections 1.3 and 1.4. The elaboration of these principles, concerning design and implementation of a fiber optic link based on FCMA, is the subject of Sections 1.5 through 1.9. Section 1.10 outlines the goals of the first generation of FCMA link design. Section 1.11 presents a discussion of how FCMA links can be deployed in unique physical architectures that suggest architectural advantages over current network physical layer technologies. Section 1.12 summarizes Chapter 1 and outlines the topics of the remaining chapters.

1.1 Metropolitan Area Networks.

Metropolitan Area Networks (MANs) are networks with a distance scale of the size of a modern city, a few kilometers to tens of kilometers. The application of the term MAN is often used to describe the interconnectivity with respect to a number of communication services within one organization that is decentralized and may have many offices/locations spread across the defined distance scale. This type of network is called a *dedicated network*. A more general interpretation of the term applies to connecting any user or provider of communication services (such as phone, fax, data or video) to any other user or provider on the stated distance scale. This definition, called a *shared* or *public network*, can include the dedicated network as a subset of its connectivity as a virtual private network (VPN). A VPN can serve as a replacement for networks owned and operated by private organizations.

The economics of network deployment depend on a number of factors including link lengths, bandwidth capacity, bandwidth usage, density of users, and types of services provided. The cost of deployment and the projected revenues from the network, as well as quality of service considerations, determine the technology that is used to construct a network. For example, synchronous optical networks (SONET) are used for long haul transmission in wide area networks (WANs) instead of ethernet, which is used for local area networks (LANs).

Metropolitan area networks can be thought of as a bridge between LANs and WANs and have a mixture of LAN and WAN qualities. For instance, the physical density of users (or network access points) would be less than that of a LAN but greater than that for a WAN.

The MAN architectures being deployed at present are digital. Any analog signals that need to be transported, point to point or broadcast, are digitized at the source and reconstructed at the destination. These networks are also evolving to broadband networks and may employ a mixture of circuit switching and packet switching for data routing.

The remainder of this section will present a few ideas relevant to the deployment of MAN technologies as they exist today. The topics covered are neither a complete list of ideas nor a complete explanation of the ideas that are introduced. Reference materials will be suggested where it is considered necessary. The subjects covered are; established MAN technologies, gigabit Ethernet, broadband networks, physical layers and multiple access.

1.1.1 Established MAN Technologies.

Much of the discussion in reference books on the subject of MAN architectures centers on the implementation of a network that is set up for connecting one service provider to its customers (such as a cable television system) or for connecting one organization internally as a distributed but dedicated network. Prior to the popularity of home computers and the creation of graphically based internet applications, these kinds of network deployments made sense. Since the invention of the World Wide Web, email, and other digital services, the utility of deploying a private network has diminished. Integrated service networks, with the ability to provide a wide range of interconnection options, are viewed as more practical solutions for providing service. With the digital services already available, and more services appearing every day, data networks are experiencing a boom that is making old concepts (simple bus, ring, or star architectures) of MAN deployment obsolete.

Two of the options that have become standards for MAN in recent years are Fiber Distributed Data Interface (FDDI) [CON1,KE1,ST1,JAI1,AC1] and IEEE 802.6 Distributed Queue Dual Bus (DQDB) [CON1,KE1,ST1,AC1]. These technologies are network architectures whose specifications include network access, supported protocols, data rates, and topology.

FDDI is usually implemented as a ring architecture with a fixed link bit-rate of 100 Megabits per second (Mbps). It is used primarily for private data transport for interconnection of LANs or high speed workstations. The protocols implemented on FDDI are not easily switched making it difficult to use as a broadband network.

DQDB is a bidirectional bus architecture with SONET bit-rates and can be scaled up to higher bit-rates which makes it possible to evolve with new technologies. The protocol for DQDB is similar to Asynchronous Transfer Mode (ATM) that is used for long haul broadband networks in that it uses 53 byte cell units for data packets. Interfacing a DQDB network to a long haul network that uses ATM would be easier than interfacing FDDI. The efficiency of DQDB at higher bit-rates, greater than 1 Gigabit per second (Gbps), is prohibitively low, making it difficult to use as a Gigabit broadband network.

1.1.2 A New Format - Gigabit Ethernet.

Recent developments in ethernet based networks have increased the data rates for standard ethernet (10 Mbps and 100 Mbps) to include a new 1 Gbps standard. 1 Gbps ethernet is already being manufactured by a number of network equipment suppliers.

The line rate of bits on ethernet is actually 1.25 times the data rate due to a 4/5 signal encoding scheme so that what is nominally called 1 Gbps ethernet actually runs at a line rate of 1.25 Gbps. The protocol for this new standard, as far as frame structure is concerned, strongly resembles long haul WAN SONET standard frames and makes it an ideal candidate for use on an FCMA based physical layer network [DUD1,MART1].

1.1.3 Comments on Deploying a Broadband Network.

It is the requirement of deploying a Gigabit broadband network, supporting voice transmission and data transfer, that has motivated the development of new MAN architectures [DUD1,MART1]. Among the proposals for new architectures are the use of SONET as network backbone and/or the use of ATM to support broadband switching [MART1]. ATM standards, originally for WANs, are now established for LANs and it would be a matter of convenience to implement ATM and SONET on MANs [KE1].

Whether or not ATM is used as a data link protocol this research accepts the option of using SONET-like optical backbone and proposes the use of a novel multiplexing technique that may make SONET standard backbones more attractive to MAN designers. The adaptation of WAN SONET protocols to networks that are more dense could make switched networks possible on MAN distance scales. The network topologies could then evolve from rings and buses to mesh networks. This topology evolution requires a parallel evolution in physical layer design.

1.1.4 The Physical Layer of a Fiber Optic Communication Link.

The physical layer is the lowest level protocol layer in the seven layer protocol stack of the Open Systems Interconnection (OSI) model. The physical layer is responsible for establishing, maintaining and terminating connections and for transmission of digital data from a point of origin to a destination. Included in the physical layer are the specifications of the transmitted signal; the signal amplitude and/or frequency and/or phase, bit duration and logic levels (§2.3 of [ST1]).

The physical layer of a basic fiber optic communication link employs a transmitter, receiver and a connecting fiber. An electrical signal enters the link at the transmission end of the optical link and an electrical signal exits at the receiver. The electrical signal format is usually amplitude shift keying. Figure 1-1 depicts this generic definition of a fiber link.

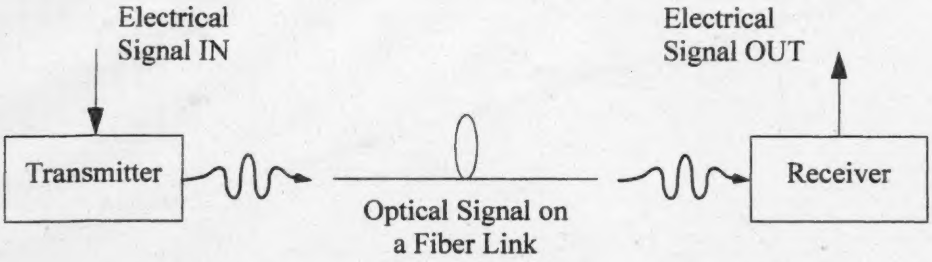

Figure 1-1: Schematic depiction of generic fiber optic communication link.

The transmitter performs an electrical to optical (E/O) conversion and the receiver performs an optical to electrical (O/E) conversion. There may also be a conversion of signal format at the transmitter and the inverse format conversion at the receiver. The particular signal format is also part of the physical layer description of the optical communication link but it is also usually amplitude shift keying.

The FDDI and DQDB based MANs are more concerned with the adjacent protocol level of the OSI model which is the data link layer. FDDI does specify the bit-rate at 100 Mbps but, because it is a ring architecture, the specifications concentrate on the efficient use of ring data link protocols for high speed fiber optic transmission and are independent of the particular type of signalling used on the transmission medium: Amplitude Shift Keying (ASK), Frequency Shift Keying (FSK), etc.(§6.1 of [ST1]). DQDB is specified at SONET rates and therefore is independent of absolute data rates but the bus nature of the physical network topology directs the focus of discussions on DQDB to optimization of bus data link protocols.

These established technologies use binary transmission, signals with two logic levels. FDDI handles network access by different parties on the network by passing a "token" around the ring; it is a token ring network. Network access for DQDB is more complicated. 53-byte slots continually pass from the start to the end of the bus through the nodes (user access points) where unused slots can be acquired by the node for transmission of data. These networks employ transmission schemes where only one transmission appears on the network during any particular time slot.

In order to increase the carrying capacity of networks based on DQDB or FDDI the bit-rate could be increased or a multiple access scheme, such as wavelength division multiple access, could be used. FCMA could provide multiple access to a DQDB network to increase the carrying capacity without a change to the bit-rate and without adding wavelengths. Changing the network design from DQDB or FDDI to a new design, like Gigabit Ethernet, is also an alternative and FCMA could be used as the supporting physical layer.

1.1.5 Increasing Utility Through Multiplexing and Multiple Access.

Multiplexing is the term used to describe the use of the same physical path in a transmission link for more than one logical path at the same time. Some common means of multiplexing are Wavelength Division Multiplexing (WDM), Frequency Division Multiplexing (FDM), Time Division Multiplexing (TDM), and Code Division Multiplexing (CDM). The reason for employing multiplexing schemes is to make more use of the physical infrastructure of a communication network without having to spend more money on physical network components. The use of one physical path by multiple users by employing a multiplexing scheme gives those users multiple access. For example, the use WDM to establish multiple access on a network is referred to as Wavelength Division Multiple Access (WDMA), which is illustrated by the graphic in Figure 1-2.

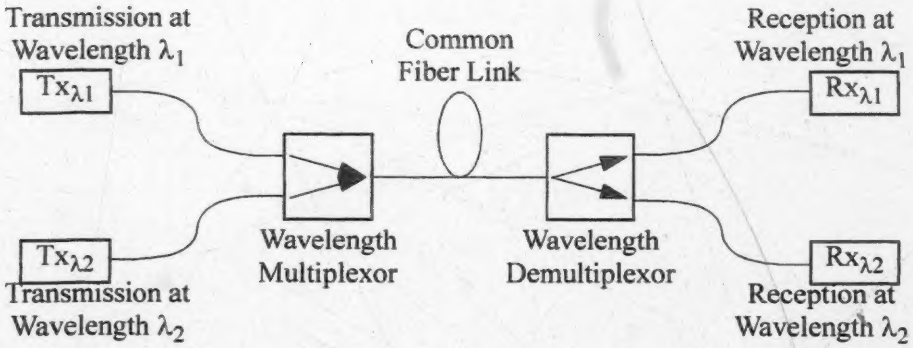
Transmission at Wavelength λ1
Tx λ1
Common Fiber Link
Reception at Wavelength λ1
Rx λ1
Tx λ2
Transmission at Wavelength λ2
Wavelength Multiplexor
Wavelength Demultiplexor
Rx λ2
Reception at Wavelength λ2

Figure 1-2: Schematic demonstration of multiple access using WDM over a common optical fiber. $Tx_{\lambda 1}$ and $Tx_{\lambda 2}$ represent the transmitters for transmitted information at optical wavelength λ_1 and λ_2. $Rx_{\lambda 1}$ and $Rx_{\lambda 2}$ represent the receivers for received information at optical wavelength λ_1 and λ_2.

The common fiber link in Figure 1-2 carries both wavelengths λ_1 and λ_2 from their respective points of transmission to their destinations which represents a two-fold increase in utility of the fiber link over the situation of single wavelength transmission on the fiber. Though the signals share the same optical path, they are distinguished by their wavelengths. The physical property of optical wavelength is used in networks like the schematic representation in Figure 1-2 to route the signals from source to destination. The wavelength demultiplexor is constructed in such a way that the signal carried by wavelength λ_1, or λ_2, reaches the correct destination.

The important point of multiple access is that each physical connection, in this example the fiber, now represents more than one logical connection, one for each wavelength λ_1 and λ_2. Two or more parties can transmit simultaneously on the same physical medium or two or more data channels can be supported on the same interconnection.

WDMA represents one option for increasing the utility of optical networks. FCMA is another option where multiple transmissions can share a common physical path and be routed simultaneously. Economic deployment of future networks will depend on the appropriate choice of physical layer and will likely include a multiple access scheme.

1.1.6 Summary of Metropolitan Area Networks.

High-speed digital networking on a distance scale of a metropolitan area will continue to be implemented with fiber optic networks. The distance scale and the connectivity of MANs are motivating the development of new technologies to optimize network deployment. Physical layer designs, including the potential for multiplexing, must reflect the larger scope of network needs.

1.2 A Potpourri of Design Requirements.

The focus of this research is on the design and implementation of a novel multiplexing scheme for the construction of MANs. The requirements can be broken down into two general categories. The first category is physical layer design requirements which cover the basics of what is necessary to transport data over a fiber optic link. This physical layer has to adhere to strict measures of performance to meet the standards of desired operating characteristics. The second category is network design requirements. The network design criteria are included here to provide clarification for discussion of the application of FCMA to optical MANs, not as a central part of the research.

1.2.1 Physical Layer Design Requirements.

The channel bit-rates chosen for this prototype system are the SONET standards of 622 Mbps (SONET OC-12) and 2.488 Gbps (SONET OC-48), as well as 1.25 Gbps (Gigabit Ethernet). The signal format and the bit-rate determine the bandwidth of the electrical components in the transmission system via the required upper and lower 3 dB points of the combined frequency response. The specifications of the optical components for the link are also determined by the bit-rate as well as the distance of the transmission.

Amplitude shift keyed OC-48 requires a high frequency 3 dB point of at least 1.244 GHz for the electrical system transfer function. Typically, the upper corner is set at approximately 0.6-0.7 times the bit-rate [EL1,TO1], which would be around 1.7 GHz. This requirement represents the minimum upper frequency of the electrical component of a transmission link to faithfully recover the highest frequency component of the ASK signal.

The lower corner of the electrical system transfer function is set to include the lowest frequency present in the transmitted signal. This lowest frequency is calculated from the number of consecutive bits of either 1 or 0 that is expected to be transmitted. A lower corner frequency that is three orders of magnitude below the upper frequency will support 1000 consecutive 1's followed by 1000 consecutive 0's. An alternate means of determining the lower corner of the system transfer function is by making it low enough that any automatic gain control (AGC) circuits employed in the system can compensate for all low frequency fluctuations.

Electrical bandwidth limiting is usually performed by the receiver and the specifics of this electrical transfer function will be discussed in Chapter 5.

The maximum acceptable accumulated optical power loss, the difference between optical power at the transmitter and receiver, is called the link loss budget. The receiver requires a minimum incident optical power on the photodetector to recover the digital signal while minimizing the reception errors. An error occurs when a 1 is received when a 0 is transmitted, or vice versa. Typical design targets for the bit error ratios (BER), the fraction of bits received erroneously, are 10^{-9} to 10^{-15}. To achieve these BER requirements, the launched optical power must be high enough to overcome the losses of the link and provide the minimum optical power at the receiver. The link budget of an FCMA link will be analyzed in Chapter 6.

The optical bandwidth of the link is determined by distortion due to the chromatic dispersion of the transport fiber. Fiber dispersion is a physical property that imposes different group velocities on light of different frequencies (wavelengths). Chromatic dispersion results in pulse spreading for any signal. The relevant factors that determine the impact of dispersion on a fiber link are the spectral width of the signal, the dispersion coefficients of the fiber at the transmitted wavelength, the bit duration of the signal and the length of the link. The effects of chromatic dispersion of FCM transmissions will be shown qualitatively in Chapter 6. Dispersion compensation devices can be inserted into the link to reverse the signal degradation.

In a WDM system, the optical bandwidth of the transmitted optical signal also affects the total aggregate throughput of fiber links. The wavelength (or optical frequency) spacings of adjacent optical channels must be greater than the bandwidth of any particular channel to prevent adjacent channel cross talk after the separation of a wavelength by a WDM demultiplexor.

1.2.2 Network Design Requirements.

Assuming an acceptable physical layer link performance (acceptable error rate and bit-rate), the overall network efficiency strongly depends upon the supported network protocols, logical and physical network interconnections and traffic demands (traffic type and burstiness).

Network efficiency is most often discussed in terms of utilization. Utilization is "the fraction of channel bandwidth used by successfully transmitted messages" [CON1]. Estimations of utilization for given user demands predict the bandwidth allocation that must be made to provide service to customers. Factors that affect utilization are network capacity, fairness of bandwidth allocation, source bit rate (the rate at which users generate traffic), data burstiness (high amounts of traffic demand in a short time period), response time (delay between bandwidth allocation requests and transmission), and data loss tolerances [CON1]. Different types of traffic (voice, video, data, etc.) have competing requirements concerning these utilization-affecting factors, so the choice of protocol and network architecture is a strong function of the user demands. For more information the reader is referred to [CON1].

It will be assumed for the remainder of the presented work that, by meeting the same physical layer requirements of established optical network link designs, the network analysis of isolated links presented here will be equivalent to established models. Any differences between the established network links and FCMA links will be differences in node design and will result in changes to switching capabilities and network reconfiguration. WDM applications employing FCMA on each wavelength (representing an additional level of multiplexing over conventional WDM) are schematically demonstrated in Section 1.11. The analysis of network efficiency will not be presented as part of this thesis and will be left for future work.

1.3 An Introduction to FCMA.

FCMA uses a multilevel FSK signal in the optical domain over fiber to provide multiple access for a MAN. FCMA uses a baseband frequency shift keyed signal in the optical domain as a transmitted signal format. The demodulation scheme relies on symbol self-interference [MAC1] which is similar to Manchester coding and decoding in the context described in [PRO1].

In order to maintain consistency throughout this thesis, baseband FSK and baseband *M*-ary FSK will be referred to as FSK or *M*-ary FSK. The signal modulation is not carrier modulation or subcarrier modulation, which represents a departure from common optical FSK systems that employ one of these modulation formats. Also, any power modulated digital optical signal will be referred to as intensity shift keyed (ISK) and *M*-ary ISK (where the context requires) because the signal levels of an intermediate multilevel optical power signal are spaced evenly in the optical power domain. The term optical ASK can be used to describe a binary optical ISK signal without confusion or contradiction but ASK is inappropriate to describe multilevel optical ISK signals. The symbol used to represent optical intensity for an *M*-ary ISK signal level will be $\mathscr{I}_m$, where m is an index used to denote the symbol number.

The following subsection serves to compare FCMA to other types of coherent transmission in an effort to clarify what makes FCMA a unique solution compared to the usual coherent optical physical layer solutions.

1.3.1 FCMA, A Coherent Optical Physical Layer Solution.

Coherent optical physical layer solutions fall into two general categories based on the type of receiver that is employed, direct detection systems and local oscillator systems. Direct detection receivers rely on optical self interference to recover a baseband amplitude modulated signal and commonly use filters based on Fabry-Perot, Mach-Zehnder or

Michelson interferometers. Local oscillator receivers mix the signal bearing light with an optical local oscillator with an optical coupler and recover the baseband signal with a combination of gear that may include intermediate frequency (IF) filters, low pass filters, square law detectors, maximum likelihood detection, etc.

The biggest advantage of the local oscillator reception is that a large optical power local oscillator produces a large mixing signal that enhances the receiver sensitivity. The advantage of direct detection coherent receivers is the lack of a local oscillator which is usually an expensive, high-power, low-noise laser diode and the lack of the associated complexity of controlling the local oscillator phase via a phase locked loop (PLL).

The FCMA system falls into the category of direct detection (DD) receiver based systems. The difference between FCMA and the other types of coherent DD systems is that the passive optical filtering also demultiplexes $\log_2(M)$-multiplexed channels as well as individually recovering the baseband signals.

1.4 FCMA Transmitted Signal Format.

Like any optical fiber transmission system, the FCMA system consists of an optical fiber link that transports a signal from a transmitter to a receiver. The input and output signals are binary electrical Amplitude Shift Keyed (ASK). Unlike optical transmission systems that employ a direct conversion of electrical ASK to optical ISK, FCMA uses a series of signal format conversions at the transmitter to multiplex more than one electrical ASK channel to one optical multilevel FSK channel for transmission. At the receiver, another series of signal format conversions result in the reproduction of the input electrical ASK channels. A block diagram depiction of these signal format conversion is shown in Figure 1-3.

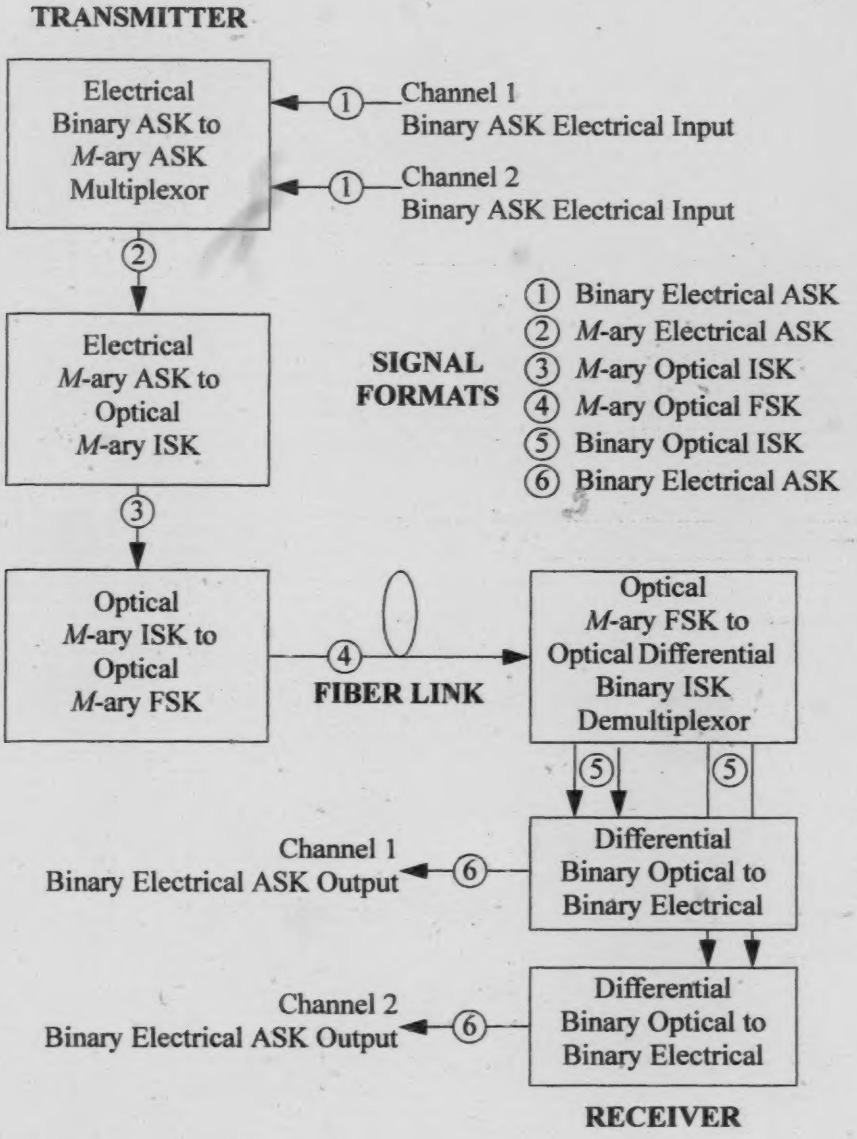
TRANSMITTER
Electrical Binary ASK to M-ary ASK Multiplexor
①
Channel 1 Binary ASK Electrical Input
①
Channel 2 Binary ASK Electrical Input
②
Electrical M-ary ASK to Optical M-ary ISK
SIGNAL FORMATS
① Binary Electrical ASK
② M-ary Electrical ASK
③ M-ary Optical ISK
④ M-ary Optical FSK
⑤ Binary Optical ISK
⑥ Binary Electrical ASK
③
Optical M-ary ISK to Optical M-ary FSK
④
FIBER LINK
Optical M-ary FSK to Optical Differential Binary ISK Demultiplexor
⑤
⑤
Channel 1 Binary Electrical ASK Output
⑥
Differential Binary Optical to Binary Electrical
Channel 2 Binary Electrical ASK Output
⑥
Differential Binary Optical to Binary Electrical
RECEIVER

Figure 1-3: A block diagram depicting successive signal conversions for a two channel FCMA link, including the transmitter and receiver.

All of the necessary signal conversions shown in Figure 1-3 will be addressed in detail in the body of this document. The conversions from the signals labelled 2, 3 and 4 in Figure 1-3 predetermine the type of optical transmitter that is employed. This choice must and will be justified. The actual transmitted signal, optical *M*-ary FSK, is a central part of this research and the properties it possesses are fundamental to the advantages of using FCMA.

1.4.1 Multilevel FSK in the Optical Frequency Domain.

FCMA is a multiple access scheme where data is coded into a multilevel frequency shift keyed (*M*-ary FSK) optical signal. The optical frequency, ν, of the transmitted signal is directly related to the logical values that it represents. In other words, the optical signal is a function of time where, in the ideal case, it takes on a specific value of optical frequency for the duration of a stated symbol time (*T*) as demonstrated by Figure 1-4 for a four level signal, where ν_0 is the base optical frequency of the signal and $\Delta\nu$ is the signal level spacing.

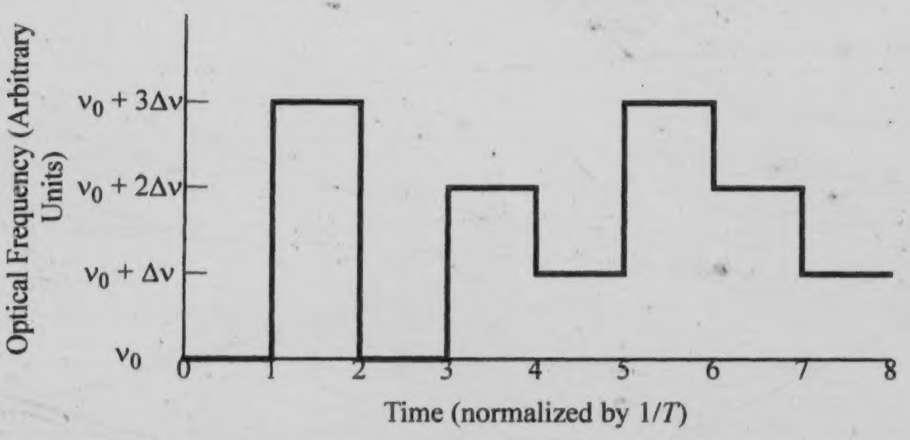

Figure 1-4: Representation of the optical frequency of an ideal four level FCMA signal for an eight symbol duration.

The optical power of this frequency based signal is the same for all values of optical frequency in the ideal case but, as will be discussed in later chapters, it is not constant for actual FCMA link symbols based on the proposed transmitter. The associated intensity, or amplitude, modulation of the optical signal turns out to be only a minor inconvenience.

For the remainder of this introductory chapter a 16 frequency level FCMA system (four binary channels multiplexed) will be discussed to demonstrate the principles underlying FCMA. Figure 1-5 shows the frequency levels that correspond to the bit level codings for such a 16 level signal.

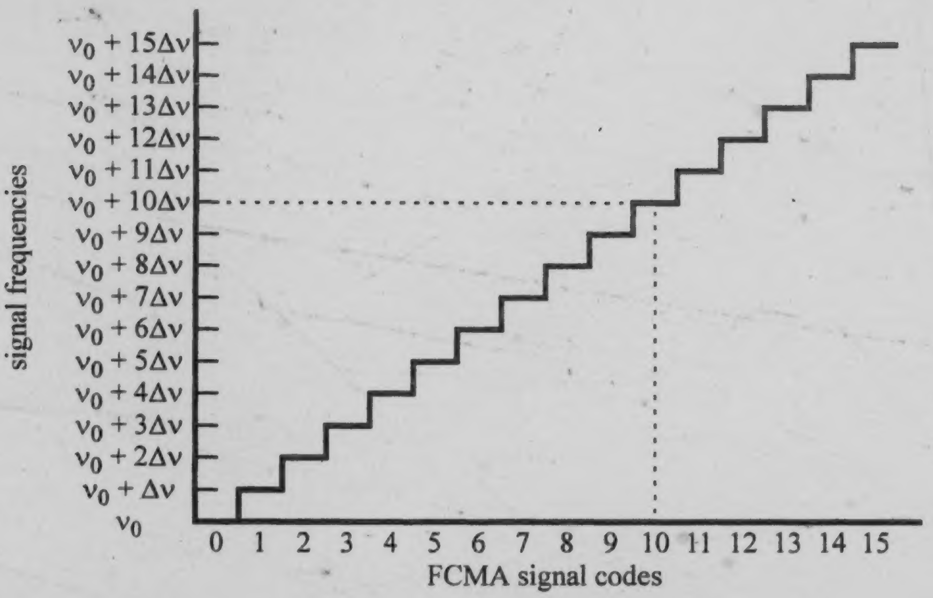

Figure 1-5: A pictorial representation of the FCMA signal codes and the frequencies that correspond to those codes for a 16 level (4 channel) FCMA system. For example, signal code 10 corresponds to an optical frequency of $\nu_0 + 10\Delta\nu$.

These 16 signal levels correspond to all possible combinations of four independent binary digits that represent the logic levels of four independent data streams (data channels) as demonstrated in Table 1-1. The optical frequency values of the optical frequency levels with respect to the base frequency, ν_0, are calculated as the transmitted FCMA code multiplied by the frequency level spacing, $\Delta\nu$.

Table 1-1: Logic levels of four independent binary channels and the corresponding FCMA codes and transmitted optical frequencies.

Transmitted Optical Frequency Level	Individual Binary Values Organized by Channel Number				Transmitted FCMA codes	
	4 MSB	3	2	1 LSB	binary	decimal
ν_0	0	0	0	0	0000	0
$\nu_1 = \nu_0 + \Delta\nu$	0	0	0	1	0001	1
$\nu_2 = \nu_0 + 2\Delta\nu$	0	0	1	0	0010	2
$\nu_3 = \nu_0 + 3\Delta\nu$	0	0	1	1	0011	3
$\nu_4 = \nu_0 + 4\Delta\nu$	0	1	0	0	0100	4
$\nu_5 = \nu_0 + 5\Delta\nu$	0	1	0	1	0101	5
$\nu_6 = \nu_0 + 6\Delta\nu$	0	1	1	0	0110	6
$\nu_7 = \nu_0 + 7\Delta\nu$	0	1	1	1	0111	7
$\nu_8 = \nu_0 + 8\Delta\nu$	1	0	0	0	1000	8
$\nu_9 = \nu_0 + 9\Delta\nu$	1	0	0	1	1001	9
$\nu_{10} = \nu_0 + 10\Delta\nu$	1	0	1	0	1010	10
$\nu_{11} = \nu_0 + 11\Delta\nu$	1	0	1	1	1011	11
$\nu_{12} = \nu_0 + 12\Delta\nu$	1	1	0	0	1100	12
$\nu_{13} = \nu_0 + 13\Delta\nu$	1	1	0	1	1101	13
$\nu_{14} = \nu_0 + 14\Delta\nu$	1	1	1	0	1110	14
$\nu_{15} = \nu_0 + 15\Delta\nu$	1	1	1	1	1111	15

1.4.2 Constructing a 16 Level Signal from Four Binary Channels.

Four binary channels of equal voltage amplitude are combined to produce a sixteen level electrical signal. The four channels are bit-wise synchronized and amplified. Channel 1 is a nominal amplitude V_{c1}. Channel 2 is amplified so that it's amplitude is twice that of Channel 1, $V_{c2} = 2\ V_{c1}$. The amplitudes of Channels 3 and 4 are amplified to values of four and eight times the amplitude of Channel 1. The channels are passively combined (multiplexed) to form a 16 level amplitude shift keyed electrical signal, as depicted in Figure 1-6.

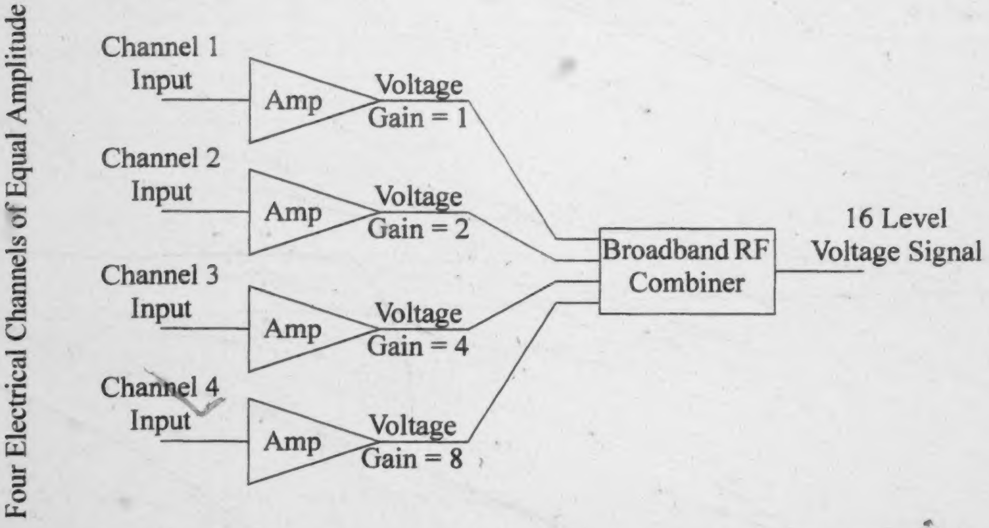
Four Electrical Channels of Equal Amplitude
Channel 1 Input
Amp
Voltage Gain = 1
Channel 2 Input
Amp
Voltage Gain = 2
Channel 3 Input
Amp
Voltage Gain = 4
Channel 4 Input
Amp
Voltage Gain = 8
Broadband RF Combiner
16 Level Voltage Signal

Figure 1-6: Circuit schematic for combining four channels of binary ASK data of equal pulse amplitude to create a 16 level voltage signal (16-ary ASK).

The conversion of this multilevel amplitude shift keyed (*M*-ary ASK) electrical signal to the transmitted multilevel frequency shift keyed (*M*-ary FSK) optical signal is the subject of Chapters 2 and 3. Passive harmonic decoding is employed at the receiver to decode the four channels.

1.5 Harmonic Decoding.

To receive the FCMA signal, the individual channels are passively demultiplexed by a set of optical Mach-Zehnder (MZ) filters; see Figure 1-7 for a schematic representation of a four channel demultiplexor.

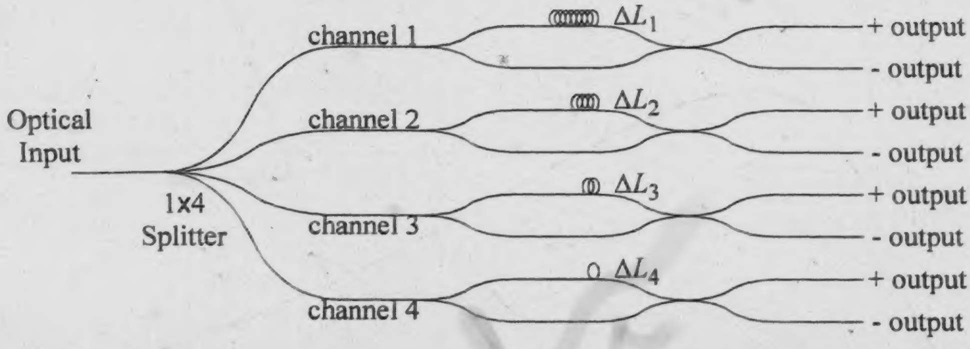

Figure 1-7: A representative schematic of a passive optical demultiplexor based on imbalanced Mach-Zehnder interferometers used for demultiplexing and decoding the four channels of a 16 level FCM signal. The imbalance (or delay) lengths are represented by ΔL_1, ΔL_2, ΔL_3 and ΔL_4.

Each Mach-Zehnder decodes one channel, passively, in the optical domain and a dedicated receiver for each channel performs an optical to electrical conversion. The use of Mach-Zehnders to demultiplex and decode a multilevel FSK signals is the central idea motivating this work and was first proposed by Dr. Ian MacDonald [MAC1].

For the four channel (16 level) FCM signal the required number of receivers is four. The recovery of the respective channel signals relies on the conversion of intensity shift keyed optical power to amplitude shift keyed electrical voltage. In order to receive optical power signals, the frequency shift keyed signal has to be converted to the intensity domain. The details of the frequency to intensity conversion are covered in Chapter 4 but the conversion can be understood using the steady state (constant frequency) transfer function of a Mach-Zehnder filter with two complementary outputs,

$$P_{MZ+}(\nu) = P_{MZmax}\frac{1+\cos\left(\frac{2\pi\mu_{eMZ}\Delta L}{c}\nu\right)}{2}, \qquad (1)$$

$$P_{MZ-}(\nu) = P_{MZmax}\frac{1-\cos\left(\frac{2\pi\mu_{eMZ}\Delta L}{c}\nu\right)}{2}, \qquad (2)$$

where $P_{MZ+/-}(\nu)$ is the output power each of two output ports, P_{MZmax} is the maximum observed output power of the filter, μ_{eMZ} is the Mach-Zehnder effective refractive index,

ΔL is the difference in path length of the two interfering paths, c is the speed of light in vacuum and ν is the optical frequency of the light.

The optical power at the output of the Mach-Zehnder is converted to voltage with a PIN diode optical receiver. The electrical waveform from P_{MZ-} is subtracted from the electrical waveform from P_{MZ+} leaving a voltage proportional to the cosine term only,

$$V_{MZ}(\nu) \propto P_{MZ}(\nu) = P_{MZ+}(\nu) - P_{MZ-}(\nu) = P_{MZmax}\cos\left(\frac{2\pi\mu_{eMZ}\Delta L}{c}\nu\right), \quad (3)$$

where $V_{MZ}(\nu)$ and $P_{MZ}(\nu)$ represent the received electrical signal voltage and optical signal power, respectively.

The frequency level spacings are determined so that the Mach-Zehnder delay is less than one symbol period, regardless of the transmitted symbol rate. How much less is a factor that impacts the performance of the system and will be discussed in detail in Chapter 4. Assuming that the frequency level spacing is 150% of the bit-rate, B, ΔL_1 (delay length for the decoder for channel 1) will be chosen to approximate the phase criterion

$$\frac{2\pi\mu_{eMZ}\Delta L_1}{c}\Delta\nu \approx \pi, \quad (4)$$

which can be rewritten using the symbol rate to become,

$$\Delta L_1 \approx \frac{c}{3\mu_{eMZ}B}. \quad (5)$$

For $\mu_{eMZ} = 1.5$ and $B = 2.488$ Gbps, $\Delta L_1 = 2.68$ cm and $\Delta\nu = 3.732$ GHz. The total delay time is 1/3 of the symbol duration. The exact value of ΔL_1 must conform exactly to the following equation for the harmonic decoder to work,

$$\frac{2\pi\mu_{eMZ}\Delta L_1}{c}\nu_0 = (2n_{MZ1} + 1)\pi, \quad (6)$$

where ν_0 is the optical frequency of the symbol representing a transmitted 0 and n_{MZ1} is an integer and represents the order of the channel 1 MZ interferometer at the frequency ν_0. Appendix A demonstrates how to determine the filter order n_{MZ} using the approximate value of $\Delta\nu$ of the transmitted signal and the absolute signal optical frequency, ν_0, which is how the values of ΔL for the different MZ decoders are determined. Appendix A also introduces a new notation for the signals which is to express the signals in a center symmetric fashion. For this 16-ary FSK signal a center symmetric reference, ν_0', can be defined as,

$$\nu_0' = \nu_0 + \frac{15}{2}\Delta\nu , \tag{7}$$

or, in the general case of an M level system,

$$\nu_0' = \nu_0 + \frac{M-1}{2}\Delta\nu . \tag{8}$$

Rewriting Equation (3) with this change of variables and using the subscript m to denote the frequency level, from Table 1-1, gives,

$$P_{MZ}(m) = P_{MZmax}\cos\left(\frac{2\pi\mu_{eMZ}\Delta L}{c}\left(\nu_0' + \left(m - \frac{M-1}{2}\right)\Delta\nu\right)\right) . \tag{9}$$

Expressing the signal frequency levels in reference to ν_0' makes it convenient to graphically represent the signal with signal space diagrams in a meaningful manner.

The other channels are decoded from the optical FSK signal with Mach-Zehnders where the optical delay lengths are related to ΔL_1 as,

$$\Delta L_2 \approx \frac{\Delta L_1}{2} , \tag{10 a}$$

$$\Delta L_3 \approx \frac{\Delta L_1}{4} , \tag{10 b}$$

$$\Delta L_4 \approx \frac{\Delta L_1}{8} \tag{10 c}$$

where ΔL_2, ΔL_3 and ΔL_4 are the respective delay lengths that decode channels 2, 3 and 4 for a 16 level signal. For the given example values, the total spectral width of a 16 level signal (15 $\Delta\nu$) with 1/3 bit overlap at 2.488 Gsps is 56 GHz which represents an inefficient use of optical bandwidth. The ratio of bandwidth to bit-rate is 5.6 for this example versus 2 for a binary ISK transmission.

1.6 Intermediate Signal Space Diagrams for FCMA.

The intent of this section is to provide the reader with an easy to follow graphical representation of all of the signal formats used in an FCMA link as shown in Figure 1-3. Special attention will be given to signal format conversions and the order in which they occur. The general FCMA link transports binary electrical ASK channels from transmitter to receiver making the actual transmitted signal format transparent to the ends of the link.

The nomenclature for this section includes a prefix on the keying designations (ASK, FSK, and ISK) of e- or o- to specify that the signal is in the electrical or optical domain, respectively. Also, the signal designations from Figure 1-3 that refer to the specific signal formats will be used. For example, a signal of type 1 will refer to Binary Electrical ASK. The general term M-ary is used for multilevel signals and M is used to represent the number of levels in such a signal.

Each of the following subsections refers to one of the blocks in the signal block diagram, Figure 1-3, representing a signal conversion. Each subsection will assume that $M = 16$, that is the combination of four binary channels.

1.6.1 $\log_2 M$ Binary e-ASK Channels to one M-ary e-ASK Channel.

A number of separate binary channels, all at the same bit-rate, are combined to one channel of multilevel amplitude shift keyed (M-ary ASK) signal as described in Section 1.4.2. The input electrical signals are represented by voltage levels and are, initially all the same amplitude. Figure 1-8 shows the signal space diagram of any of these binary signals.

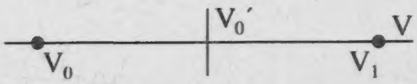

Figure 1-8: Signal space diagram of an electrical ASK signal and corresponding voltage levels. V_0 and V_1 represent the voltage levels of a binary 0's and 1's, respectively.

In the system block diagram, Figure 1-3, signals of this type are labelled 1.

The amplification of the individual binary channels, as shown diagramatically in Figure 1-6, results in changes to the levels for those channels. The combination of these signals with a passive broadband combiner results in the transformation of the four individual signals into one common signal, Figure 1-9.

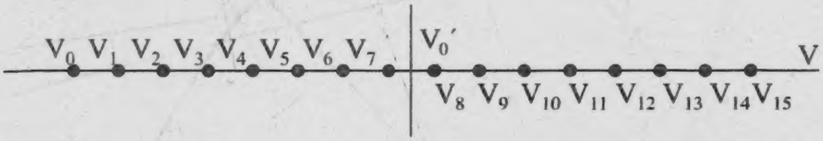
V_0 V_1 V_2 V_3 V_4 V_5 V_6 V_7
V_0'
V
V_8 V_9 V_{10} V_{11} V_{12} V_{13} V_{14} V_{15}

Figure 1-9: An equally spaced 16-level amplitude shift keyed voltage signal.

In the system block diagram, Figure 1-3, signals of this type are labelled 2. The subscripts on the voltage levels in Figure 1-9 represent the logical values listed in Table 1-1 for identically indexed optical frequency levels and V_0' represents the mean voltage.

1.6.2 *M*-ary e-ASK to *M*-ary o-ISK.

The combined 16 level voltage signal is used to linearly intensity modulate an optical signal resulting in the signal space diagram in the optical intensity domain shown in Figure 1-10.

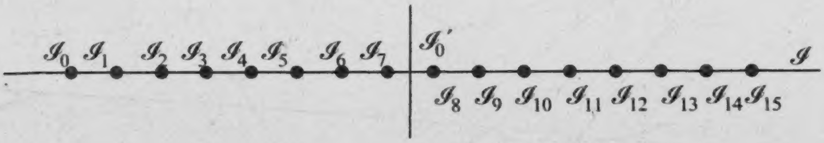
$\mathscr{I}_0$ $\mathscr{I}_1$ $\mathscr{I}_2$ $\mathscr{I}_3$ $\mathscr{I}_4$ $\mathscr{I}_5$ $\mathscr{I}_6$ $\mathscr{I}_7$
$\mathscr{I}_0'$
$\mathscr{I}$
$\mathscr{I}_8$ $\mathscr{I}_9$ $\mathscr{I}_{10}$ $\mathscr{I}_{11}$ $\mathscr{I}_{12}$ $\mathscr{I}_{13}$ $\mathscr{I}_{14}$ $\mathscr{I}_{15}$

Figure 1-10: An equally spaced 16-level intensity shift keyed optical power signal.

In the system block diagram, Figure 1-3, signals of this type are labelled 3. The subscipts on the intensity levels in Figure 1-10, $\mathscr{I}_m$, represent the logical values listed in Table 1-1 for identically indexed optical frequency levels and $\mathscr{I}_0'$ represents the mean intensity.

1.6.3 *M*-ary o-ISK to *M*-ary o-FSK.

The linearly spaced intensity shift keyed optical signal is converted to a linearly spaced frequency shift keyed optical signal with constant intensity as represented in Figure 1-11.

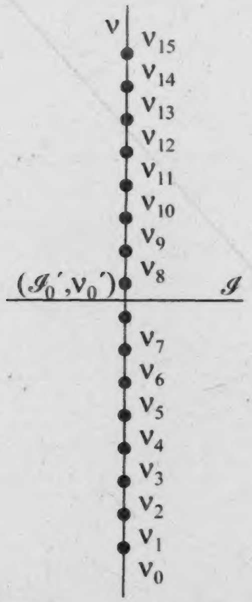

Figure 1-11: An equally spaced 16-level frequency shift keyed optical power signal.

In the system block diagram, Figure 1-3, signals of this type are labelled 4. The subscipts on the frequency levels in Figure 1-11, ν_m, represent the logical values listed in Table 1-1 for optical frequency levels and ν_0' represents the mean frequency as defined in Equation (8). $\mathscr{I}_0'$ in this diagram represents the intensity of the signal and is different from the mean intensity of the injection signal depicted in Figure 1-10. This diagram represents the ideal transmitted signal.

1.6.4 One *M*-ary o-FSK to log$_2$*M* Differential Binary o-ISK Channels.

For a four channel FCMA system, the signal optical signal is split four ways and each of these four signals is input to a Mach-Zehnder filter where the delay lengths of the filters are defined as in Section 1.5. For channel four, using ΔL_4 from Equation (10 c), the optical signals at the outputs of the dual output Mach-Zehnder filter are predicted by Equations (1) and (2) which is shown in Figure 1-12 where the p subscript refers to P_{MZ+}, the n subscript refers to P_{MZ-} and the numeric subscript represents the transmitted symbol.

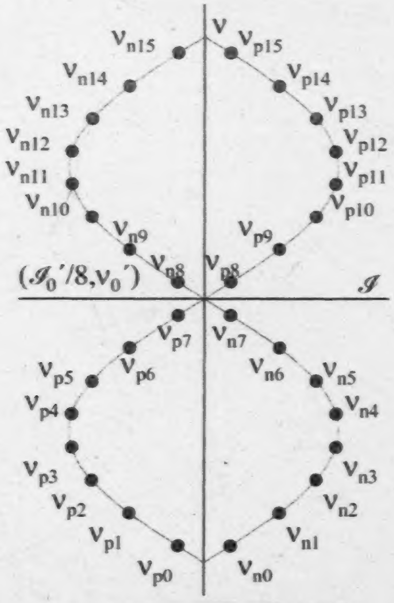
v
v_{n15}
v_{p15}
v_{n14}
v_{p14}
v_{n13}
v_{p13}
v_{n12}
v_{p12}
v_{n11}
v_{p11}
v_{n10}
v_{p10}
v_{n9}
v_{p9}
$(\mathcal{I}_0'/8, v_0')$
v_{n8}
v_{p8}
$\mathcal{I}$
v_{p7}
v_{n7}
v_{p5}
v_{p6}
v_{n6}
v_{n5}
v_{p4}
v_{n4}
v_{p3}
v_{n3}
v_{p2}
v_{n2}
v_{p1}
v_{n1}
v_{p0}
v_{n0}

Figure 1-12: An equally spaced 16-level frequency shift keyed optical power signal after being split at the receiving end of the link and passing through the Mach-Zehnder filter for channel four. Optical power is plotted on the horizontal axis and optical frequency is on the vertical axis where the symbols are represented by the numeric subscripts.

In the system block diagram, Figure 1-3, signals of this type are labelled 5.

The Mach-Zehnder filter responses for the four channel system are depicted in Figure 1-13 for four harmonically related Mach-Zehnder filters that comprise a complete set of signal decoders for a 16 level signal. It is assumed, for simplicity, that the decoders have no excess optical attenuation and that the optical power has been split evenly between the four channels. Only the P_{MZ+} values, Equation (1), for the output optical signal levels are shown.

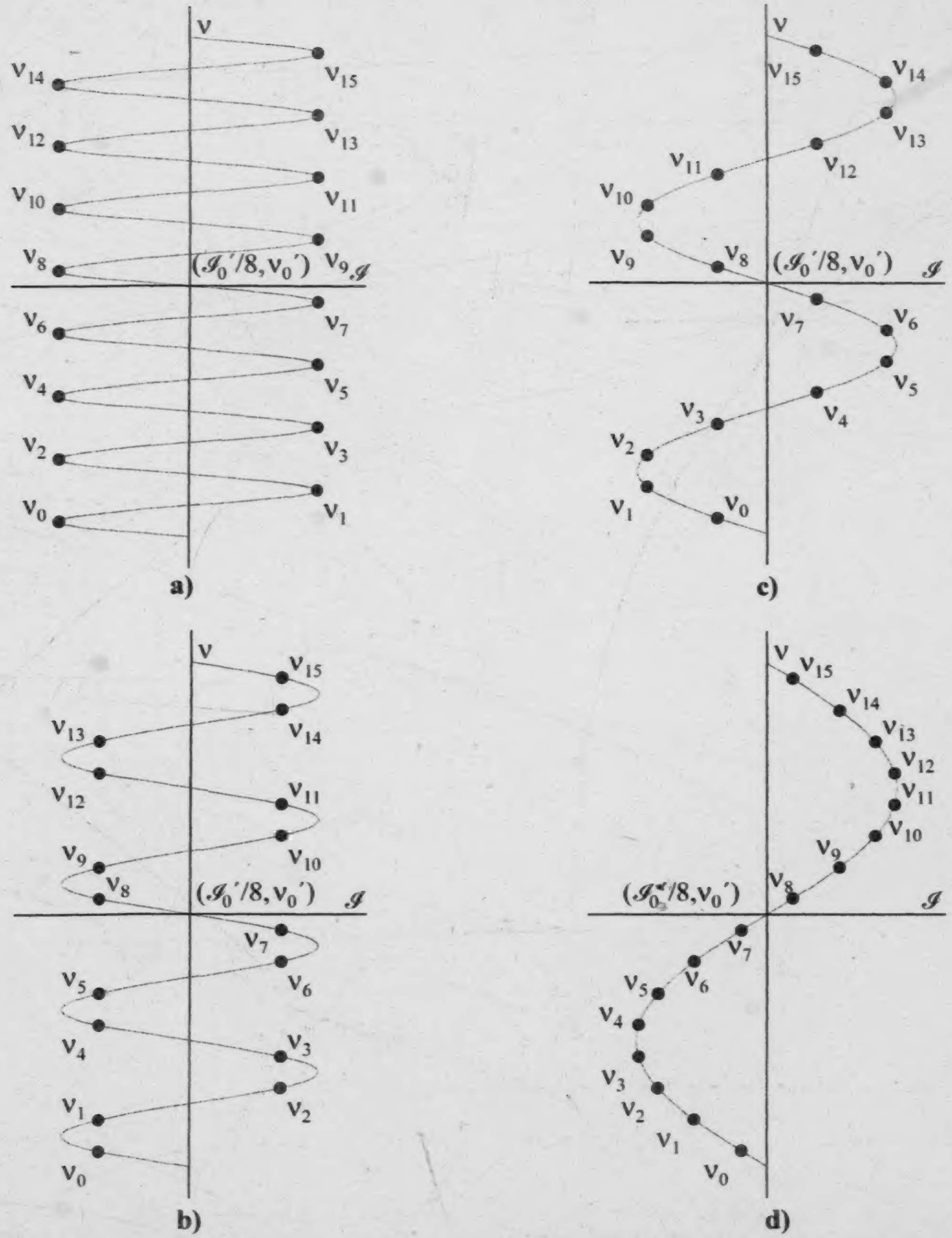

Figure 1-13: Optical frequency versus optical power of all transmitted FCMA symbols as they appear at the output of the Mach-Zehnder demultiplexor for a four channel system (the P_{MZ+} output only). **a)** channel 1. **b)** channel 2. **c)** channel 3. **d)** channel 4.

The corresponding electrical receiver power is only proportional to the output optical power of the demultiplexed optical signals. This is the means of recovering each of the electrical signals at the receiver end of the optical link.

1.6.5 Differential Binary o-ISK to Binary e-ASK.

With the appropriate choices of optical delay lengths for the respective channels, given by Equations (10 a), (10 b) and (10 c), and the relationship between optical power and receiver signal voltage, Equation (3), the electrical signal voltages can be derived for all four channels of a four channel FCMA optical link. These voltages are depicted in Figure 1-14.

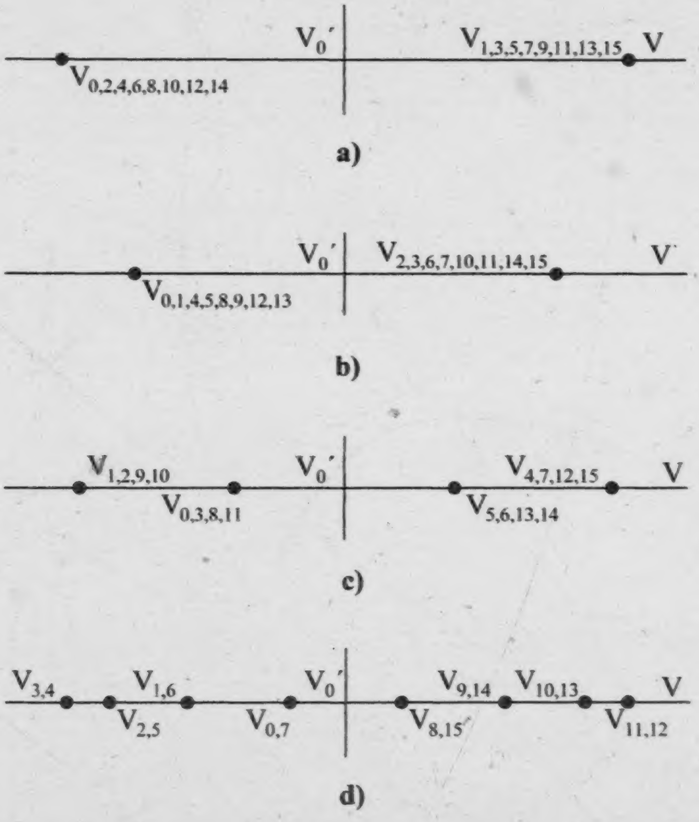

V_0'
$V_{1,3,5,7,9,11,13,15}$
V
$V_{0,2,4,6,8,10,12,14}$
a)
V_0'
$V_{2,3,6,7,10,11,14,15}$
V'
$V_{0,1,4,5,8,9,12,13}$
b)
$V_{1,2,9,10}$
V_0'
$V_{4,7,12,15}$
V
$V_{0,3,8,11}$
$V_{5,6,13,14}$
c)
$V_{3,4}$
$V_{1,6}$
V_0'
$V_{9,14}$
$V_{10,13}$
V
$V_{2,5}$
$V_{0,7}$
$V_{8,15}$
$V_{11,12}$
d)

Figure 1-14: Electrical signal voltages of all transmitted FCMA symbols as they appear at the output of the dual differential receivers for a four channel system (V_{MZ} from Equation (3)). **a)** channel 1. **b)** channel 2. **c)** channel 3. **d)** channel 4.

In the system block diagram, Figure 1-3, signals of this type are labelled 6.

For channel 1, Figure 1-14 a), the received voltage levels centered around V_0' are proportional to

$$\sin\left(\frac{3\pi}{2}\right) \quad \text{for symbols 0,2,4,6,8,10,12, and 14,}$$
$$\sin\left(\frac{\pi}{2}\right) \quad \text{for symbols 1,3,5,7,9,11,13, and 15.} \qquad (11)$$

For channel 2, Figure 1-14 b), the received voltage levels centered around V_0' are proportional to

$$\sin\left(\frac{5\pi}{4}\right) \quad \text{for symbols 0,4,8, and 12,}$$
$$\sin\left(\frac{7\pi}{4}\right) \quad \text{for symbols 1,5,9, and 13,}$$
$$\sin\left(\frac{\pi}{4}\right) \quad \text{for symbols 2,6,10, and 14,}$$
$$\sin\left(\frac{3\pi}{4}\right) \quad \text{for symbols 3,7,11, and 15.} \qquad (12)$$

For channel 3, Figure 1-14 c), the received voltage levels centered around V_0' are proportional to

$$\sin\left(\frac{9\pi}{8}\right) \quad \text{for symbols 0, and 8,}$$
$$\sin\left(\frac{11\pi}{8}\right) \quad \text{for symbols 1, and 9,}$$
$$\sin\left(\frac{13\pi}{8}\right) \quad \text{for symbols 2, and 10,}$$
$$\sin\left(\frac{15\pi}{8}\right) \quad \text{for symbols 3, and 11,}$$
$$\sin\left(\frac{\pi}{8}\right) \quad \text{for symbols 4, and 12,}$$
$$\sin\left(\frac{3\pi}{8}\right) \quad \text{for symbols 5, and 13,}$$
$$\sin\left(\frac{5\pi}{8}\right) \quad \text{for symbols 6, and 14,}$$
$$\sin\left(\frac{7\pi}{8}\right) \quad \text{for symbols 7, and 15.} \qquad (13)$$

For channel 4, Figure 1-14 d), the received voltage levels centered around V_0' are proportional to

$$\begin{array}{llll}
\sin\left(\frac{17\pi}{16}\right) & \text{for symbol 0,} & \sin\left(\frac{19\pi}{16}\right) & \text{for symbol 1,} \\
\sin\left(\frac{21\pi}{16}\right) & \text{for symbol 2,} & \sin\left(\frac{23\pi}{16}\right) & \text{for symbol 3,} \\
\sin\left(\frac{25\pi}{16}\right) & \text{for symbol 4,} & \sin\left(\frac{27\pi}{16}\right) & \text{for symbol 5,} \\
\sin\left(\frac{29\pi}{16}\right) & \text{for symbol 6,} & \sin\left(\frac{31\pi}{16}\right) & \text{for symbol 7,} \\
\sin\left(\frac{\pi}{16}\right) & \text{for symbol 8,} & \sin\left(\frac{3\pi}{16}\right) & \text{for symbol 9,} \\
\sin\left(\frac{5\pi}{16}\right) & \text{for symbols 10,} & \sin\left(\frac{7\pi}{16}\right) & \text{for symbol 11,} \\
\sin\left(\frac{9\pi}{16}\right) & \text{for symbol 12,} & \sin\left(\frac{11\pi}{16}\right) & \text{for symbol 13,} \\
\sin\left(\frac{13\pi}{16}\right) & \text{for symbol 14,} & \sin\left(\frac{15\pi}{16}\right) & \text{for symbol 15.}
\end{array} \tag{14}$$

The decision threshold for all channels is V_0' which reproduces the values in Table 1-1 for transmitted symbols being converted into the respective channel binary bit sequences.

The receiver voltages for channels 1 to 4 presented above are ideal values that depend on precisely linear signal format conversions. In general there will be non-linearities in the signal format conversions. The sources of signal format conversion non-linearities will be introduced in the next section and the effects of these non-linearities will be discussed throughout later chapters.

1.7 Comments on Signal Conversion Linearities.

All of the signal conversions that are necessary for the implementation of FCMA as described in the previous sections require linear transformations from one signal format to the next. In the context of practical implementations of these signal conversions it is easy to assume that there are problems with precisely linear transformations from one signal space to the other. Each conversion presents a unique set of challenges. Also, one or more of the signal conversions may have to be non-linear in order to achieve an optimum transmitted optical FSK signal.

Conversion from a multilevel amplitude shift keyed voltage signal to a multilevel intensity shift keyed optical signal while keeping the frequency of the optical signal constant is one such conversion that may be non-linear. It will be explained in Chapters 2 and 3 how the intensity shift keying may be accomplished with external modulation of an optical source that will be non-linear.

Conversions from a multilevel intensity shift keyed optical signal to a multilevel frequency shift keyed optical signal is also challenging and is inherently non-linear if performed by optical injection. Chapters 2 and 3 will explain the challenges presented by this signal transformation and will point out possible solutions and limitations. The combination of the signal conversion from a multilevel amplitude shift keyed voltage signal to a multilevel frequency shift keyed optical signal provides an opportunity for the two conversion non-linearities to cancel one another.

In the conversion from a multilevel frequency shift keyed optical signal to the final demultiplexed binary electrical signals (prior to any decision making circuitry), optical power losses in the Mach-Zehnder demultiplexor and any residual intensity modulation of the frequency shift keyed signal cause problems for converting the signal linearly. Problems and solutions associated with this signal conversion will be discussed in Chapters 4, 5 and 6.

Additional signal conversion concerns at the receiver are the optical power levels necessary to overcome noise and signal distortion due to chromatic dispersion. An overview of the effects of chromatic dispersion and received optical power in terms of the optical link power budget, the primary design criteria for quantifying the limitations on optical link length, is presented next.

1.8 Design Limitations of the First Generation FCMA System.

Optical links are designed from the perspective of the trade off between capacity and transmission distance. The capacity of a system is the product of the per channel bit-rate and the number of optical channels transmitted (assuming a WDM system). This discussion will be restricted to single channel transmission with the assumption that using WDM will not impact the performance of any single channel. Transmission distance in single mode optical fiber is affected by two main factors, signal distortion from chromatic dispersion and loss of optical power due to absorption and scattering in the transmission fiber. With two restrictions, that only standard single mode non-dispersion shifted fiber (NDSF) is used and the FCMA links will not employ dispersion compensation, the design specifications can be limited to a manageable level of analysis.

1.8.1 Chromatic Dispersion Limitations.

Chromatic dispersion in single mode optical fiber is a physical property, determined by both the material refractive indices and the fiber geometry, where longer wavelengths see a higher effective index of refraction which translates into an increased propagation time for longer wavelengths. Any optical data transmission has a spectral width that is at least on the order of the transmission bit-rate or symbol rate, even when the transmission carrier (optical source) has a vanishingly small linewidth. For long transmission distances the signal becomes distorted due to phase shifts caused by chromatic dispersion in the transmission fiber. If the signal is propagated far enough the data will be irrecoverable no matter how much optical power is available at the receiver.

For an FCMA signal, the negative effect of dispersion is especially important. Adjacent symbols are represented by different optical frequencies (wavelengths). These adjacent symbols travel at different group velocities and begin to overlap immediately. The adjacent symbol overlap leads to intersymbol interference (ISI) and is a potential cause of errors at the receiver. This potential source of errors will be addressed in more detail in Chapter 6. For now, some assumptions will be made to qualitatively assess the limitations that dispersion places on the transmission distance for FCMA based fiber optic communication links.

Section 1.5 outlined a bit-rate dependent frequency symbol spacing for a four channel (16 level) FCM signal. The largest frequency deviation between two adjacent symbols will be for symbol transitions from 0 to 15 or from 15 to 0. For a symbol rate of 2.488 Gsps the maximum frequency difference between adjacent symbols is 56 GHz, and for a symbol rate of 0.622 Gsps the maximum frequency difference is 14 GHz, where the MZ delay time is 1/3 of the bit period for channel 1. Assuming that the maximum tolerable overlap between adjacent symbols in 25% of the bit period, T, the maximum transmission distance can be estimated. Here it will be assumed that the transmission fiber is non-dispersion shifted fiber (NDSF) with a linear dispersion coefficient of approximately 17 ps/nm/km for wavelengths near 1550 nm and that unlimited optical power is available.

For the case of 2.488 Gsps the frequency separation for the maximum frequency difference between adjacent symbols is 56 GHz (0.45 nm) and 25% of the bit period is approximately 100 ps. The appropriate formula for calculating the time delay for dispersion effects follows as

$$\tau_d = \tau_d' L_d \Delta\lambda , \qquad (15)$$

where τ_d is the differential propagation time for two different wavelengths, τ_d' is the linear dispersion coefficient, L_d is the distance travelled and $\Delta\lambda$ is the difference in wavelength. For the stated conditions at 2.488 Gsps, L_d at the assumed dispersion limit is approximately 13 km.

For 0.622 Gsps and the same 150 % symbol separation assumption made in Section 1.5, the wavelength spread is approximately 0.11 nm for maximum frequency difference between adjacent symbols and the maximum allowable overlap time is now approximately 400 ps. The dispersion limited transmission distance at 0.622 Gsps is approximately 215 km.

In general, the dispersion limited transmission distance, $L_{\text{disp. limit}}$, varies in inverse proportionality to the square of the symbol rate [PENX1], B,

$$L_{\text{disp. limit}} \propto \frac{1}{B^2} , \qquad (16)$$

assuming that the maximum allowable overlap time of adjacent symbols scales linearly with symbol rate.

These estimated transmission distance limits due to dispersion are for transmission on non-dispersion shifted fiber. Dispersion shifted fiber (DSF) and non-zero dispersion shifted fiber (NZDSF) have linear dispersion coefficients that are less than one-third of the non-dispersion shifted fiber linear dispersion coefficient in the wavelength region around 1550 nm. For these fibers, the dispersion limited transmission distance will at least triple.

These distance limits can be increased further by using dispersion compensation devices.

A complete analysis of limitation of transmission distance would have to include the specifics of the optical to electrical signal conversion of the receiver in terms of received signal to noise ratio which varies with received optical power. The receiver signal to noise ratio also depends on the electrical transfer function of the receiver, this analysis will be deferred to Chapters 5 and 6. The performance of the optical transmission link is very dependent on the received optical power, therefore, it is important to calculate how much optical power has to be launched at the transmitter end to overcome the losses encountered in the fiber link.

1.8.2 Optical Power Budgeting, the Link Budget.

The input optical power required by an optical receiver is a function of the signal to noise ratio of the incoming optical signal, the amount of noise generated in the receiver, signal distortion from the optical transmission path and signal distortion from the transfer function of the receiver electronics. Assuming, for simplicity, that the signal distortion from the optical transmission path is negligible and the signal to noise ratio of the incoming optical signal is sufficiently high, the calculation of the required optical power at the receiver, the receiver sensitivity, is a function of the properties of the receiver and the incident power only. These assumptions make possible a demonstrative calculation of the allowable optical signal loss a function of optical fiber link length and the properties of the passive Mach-Zehnder demultiplexor. The allowable optical signal loss for a given transmitted optical power in a fiber optic link is the link power budget.

The optical power loss for an FCM link is divided between the optical fiber attenuation and the power loss of the passive Mach-Zehnder based demultiplexor. For any FCM link the passive Mach-Zehnder based demultiplexor appears as fixed power loss. The optical power loss of the Mach-Zehnder based demultiplexor heavily influences the link budget because it directly results in reduced link length.

As depicted in the representative schematic of the Mach-Zehnder based decoder, Figure 1-7, the incoming signal at the input of the decoder is split between four optical paths. If the optical power is split evenly between the four Mach-Zehnder filters, the required optical power at the input to the decoder is determined by channel 4. In Figure 1-13 d) it can be seen that the difference in optical power between symbols ν_7 and ν_8, which represent a 0 and a 1 for channel 4, is the smallest optical power difference between any two symbols that need to be distinguished. If the incoming data stream were to consist of only symbols 7 and 8, the optical signal power at the receiver for this symbol pattern would have to be greater than the receiver sensitivity. For a receiver on one output of the Mach-Zehnder decoder, the optical powers of symbols 7 and 8 are

$$\frac{P_{MZmax}}{2}\left(1-\sin\left(\frac{\pi}{16}\right)\right), \quad \text{and}$$
$$\frac{P_{MZmax}}{2}\left(1+\sin\left(\frac{\pi}{16}\right)\right), \tag{17}$$

and half of the difference between these optical powers is

$$\frac{P_{MZmax}}{2}\sin\left(\frac{\pi}{16}\right), \tag{18}$$

which has to be greater than the receiver sensitivity.

With the assumption that the power is split evenly among the separate channel decoders and this split is otherwise lossless, the input optical power to the power splitter is four times that of the input optical power to the Mach-Zehnder for channel 4,

$$\mathscr{P}_0' = 4P_{MZmax}. \tag{19}$$

Setting the receiver sensitivity, S_R, to the optical power given by Equation (18), the optical power at the input to the demultiplexor, $\mathscr{P}_0'$, is

$$\mathscr{P}_0' = \frac{(8S_R)}{\left(\sin\left(\frac{\pi}{16}\right)\right)}. \tag{20}$$

The multiplicative factor relating the receiver sensitivity to the input power of the decoder is approximately 16 dB. Given that the attenuation of standard single mode NDSF is approximately 0.2 dB/km, this is equivalent to 80 km of transmission distance. A loss of 16 dB in the demultiplexor section of the transmission system severely limits the utility of this modulation format. It will be shown in Chapter 6 that an optimum choice of power splitting ratio for channels 1 through 4 at the input to the Mach-Zehnders and the use of a dual differential receiver can effectively reduce this number by approximately 4.5 dB.

1.8.3 Summary of Design Limitations.

A combination of chromatic dispersion and optical attenuation determine the maximum possible optical communications network link length. Implementation of the FCM modulation format to achieve as near ideal transmission as possible will be a determining factor in the maximum possible bit rate and the insertion loss of the harmonic decoder will be minimized to maximize link length. The receiver sensitivity will also limit the maximum achievable link loss. Achieving an optimum combination of transmitter, harmonic decoder, and receiver will maximize the transmission distance and transmitted symbol rate, therefore various hardware options need to be considered.

1.9 Hardware Implementation Options.

The hardware implementation options can be broken down into three building blocks: signal generation requires a transmitter, separating the channels requires a demulitplexor, and a receiver is necessary to recover the transmitted information.

1.9.1 Transmitter Options.

The basic requirements of the transmission section of an FCMA system (see Figure 1-3 and the Section 1.4 for a functional description) are as follows:

1) the optical source must have a narrow linewidth.
2) equal frequency spacing of symbols in the frequency domain.
3) sharp transitions between adjacent symbols and maintenance of stability of frequency throughout any particular symbol.
4) keeping the optical power constant at all times.

Three options to achieve FCM transmission are direct modulation of a laser diode, external modulation of a laser diode and modulation by external optical injection in a laser diode. External modulation of a laser diode to produce a stable FCM waveform was excluded as an option due to the technical challenge it presents and design restrictions that it introduces. The other two options will be compared in Chapter 2 and it will be shown that external optical injection shows the most promise of being employed in the generation of FCM waveforms.

1.9.2 Harmonic Decoder Options.

The basic requirements of the harmonic decoder based demultiplexor section of an FCMA system are as follows:

1) low insertion loss.
2) optimization for maximum signal self interference.
3) optimization of power splitting ratios to maximize the effective receiver sensitivity.

Three options to create an FCM harmonic decoder are using free space optics, fiber optics, and integrated planar lightwave circuit (PLC). The all fiber solution was rejected due to difficulties in maintaining polarizations with standard fiber couplers. The other two solutions each have advantages and disadvantages and will be compared in Chapter 4.

1.9.3 Receiver Options.

The basic requirements of the receiver section of an FCMA system are as follows:

1) maximizing receiver sensitivity.
2) reducing the effects of optical interference between adjacent symbols.

A PIN diode based receiver was chosen over an Avalanche Photodiode (APD) for the sake of design simplicity. Two options for PIN diode based receiver designs for an interferometric receiver are the single PIN diode and dual differential PIN diode receiver. Dual differential receivers give a 3 dB gain in electrical signal to noise ratio (SNR) and this is the reason that a dual differential PIN based receiver was chosen for the FCMA system, see Chapter 5.

1.9.4 Implementation Option Summary.

An outline of the implementation strategy for the first generation of FCMA systems has been presented above. An external optical injection or direct modulation based transmitter with either a free space or PLC based interferometric harmonic decoder and a dual differential PIN diode based receiver are chosen as the technologies that will be explored in the building of a prototype FCMA system. An additional intent of this research is to demonstrate the potential of this choice of technological options. In the next section a list of goals will be presented, and if these are accomplished there will be sufficient evidence that FCMA is a viable technology.

1.10 Goals of the First Generation FCMA System.

The goals of the first generation FCMA system are eightfold:

1) Construction of the FCMA transmitter using only fiber compatible components.

2) Demonstration of frequency modulation by optical injection in distributed feedback (DFB) and Fabry-Perot (FP) semiconductor laser diodes.

3) Demonstration of the generation of a binary frequency shift keyed signal of known modulation depth corresponding to odd multiples of the multilevel signal separation $\Delta\nu$.

4) Studying the effectiveness of frequency decoding by Mach-Zehnder interferometers and identify relevant limitations.

5) The design, construction and testing of a set of four harmonically-related integrated Mach-Zehnder interferometer filters.

6) The design and construction of a dual differential receiver.

7) Characterization of the performance of a link using binary frequency shift keying.

8) Demonstration of symbol rates equal to OC-12 (622 Mbps), OC-48 (2.488 Gbps) and Gigabit Ethernet (1.25 Gbps).

If these goals can be accomplished, the potential applications of this technology offer advantages over current network physical layer options. A brief overview of physical layer architectures is presented in the following section.

1.11 FCMA Metropolitan Area Networks.

As an illustration of the utility of network design using FCMA, this section will provide a general survey of possible FCMA based network configurations. The discussion will not address details about protocols and network management.

Each network possibility will be pictorially represented and discussed. The first diagram will be a simple single FCM transmission over a single link and subsequent diagrams will increase in complexity, culminating in a diagram of a bidirectional bus network constructed from multiple FCMA links. All of the functionality that is labelled transmitter in Figure 1-3 will be represented in the following diagrams by the standard symbol Tx. All of the functionality that is labelled receiver in Figure 1-3 will be represented in the following diagrams by the standard symbol Rx. A four channel multiplexing level is used for each network application that is presented.

1.11.1 A Single FCMA Link.

The single optical link based on the FCMA system includes a four channel multiplexing transmitter, a single mode optical fiber (transmission medium), and a four channel demultiplexing receiver. Figure 1-15 depicts a schematic diagram of a single FCMA link. The electrical signals enter the transmitter at the left and exit the receiver on the right. The optical signal is carried on a single mode fiber that connects the transmitter to the receiver. The electrical signals are all at the same data rate at both the input and the output. The single wavelength optical signal has the same symbol rate as each of the input channels but multiplexes their signals onto a common carrier where four bits share each symbol period, as previously described.

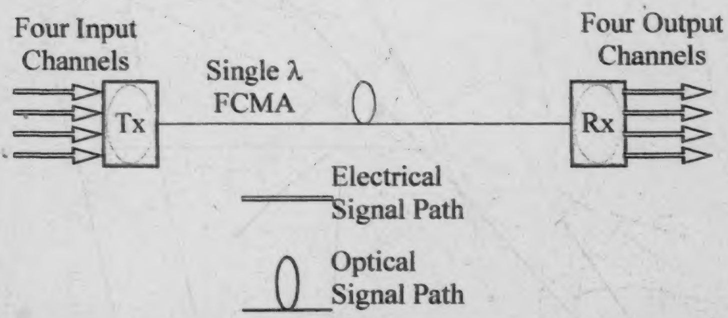
Four Input Channels
Single λ FCMA
Four Output Channels
Tx
Rx
Electrical Signal Path
Optical Signal Path

Figure 1-15: The diagram depicts the most basic functional representation of a single four-channel FCMA link. There are four electrical channels that are multiplexed at the transmitter (Tx), transmitted over a fiber optic link on a single wavelength (λ) and demultiplexed into four output electrical channels at the receiver (Rx).

Figure 1-15 is one of the basic building blocks that will be used in the following proposals of optical network architectures and optical network functions. Other building blocks for networks based on FCMA are the electrical cross-connect network node and the head-end switch. The electrical cross-connect network node will be introduced next.

1.11.2 An Electrical Cross-Connect Network Node.

The electrical cross-connect network node is a junction of two (or more) incoming FCMA links and two (or more) outgoing FCMA links. Figure 1-16 depicts the electrical and optical connections that are inside the cross-connect.

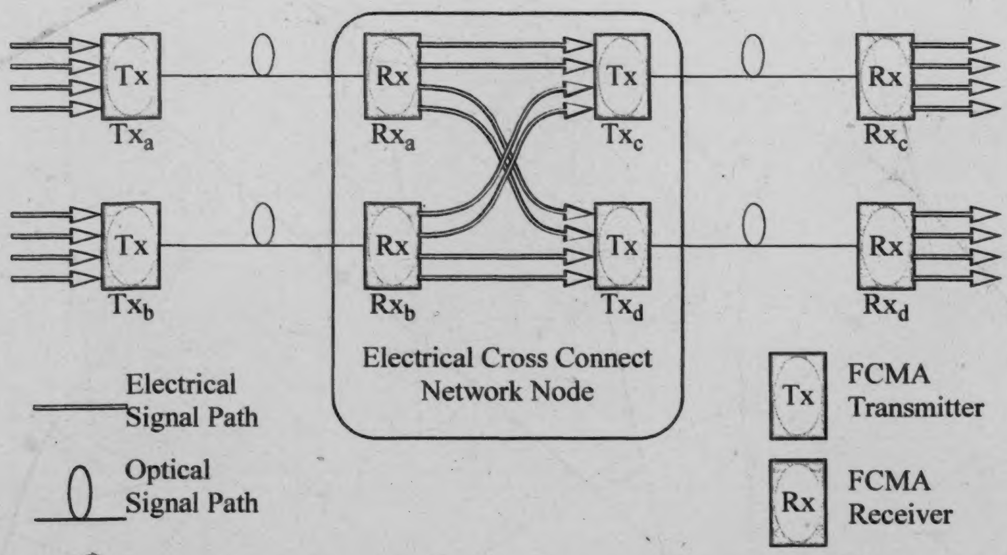
Tx
Txa
Rx
Rxa
Tx
Txc
Rx
Rxc
Tx
Txb
Rx
Rxb
Tx
Txd
Rx
Rxd
Electrical Cross Connect Network Node
Electrical Signal Path
Optical Signal Path
Tx
FCMA Transmitter
Rx
FCMA Receiver

Figure 1-16: A diagram depicting the electrical and optical connections that cross connect two pairs of FCMA links. Transmitters and receivers are labelled Tx and Rx respectively, with subscripts to denote the manner in which they are connected.

Tx_a and Tx_b are multiplexing transmitters that are not co-located, but the receivers Rx_a and Rx_b for the links on the left in Figure 1-16 are co-located. The signal channels originating at Tx_a and Tx_b are demultiplexed at the electrical cross connect network node. Two of the channels from Tx_a are sent to Tx_c and Tx_d and two of the channels from Tx_b are sent to Tx_c and Tx_d. Tx_c and Tx_d transmit these channels to their respective receivers, Rx_c and Rx_d, that are not co-located. Thus, there are four sets of logical connections in this diagram that are connected by two physical connections without any electrical data processing required to correctly route the signals. Using SONET standard signal multiplexing as an comparative example, the eight respective TDM signals (four from each path) would have to be received, buffered, demultiplexed and (once the header information is interpreted) remultiplexed, buffered and transmitted. These operations require a large electrical processing overhead and software control. By contrast, once it is configured, the FCM cross-connect is transparent to its internal electrical function.

The cross-connect can be modified easily to provide for local access. Any number of the electrical channels internal to the cross-connect can be routed in or out of the cross-connect to route traffic to users that are in the local vicinity. This function is shown in Figure 1-17.

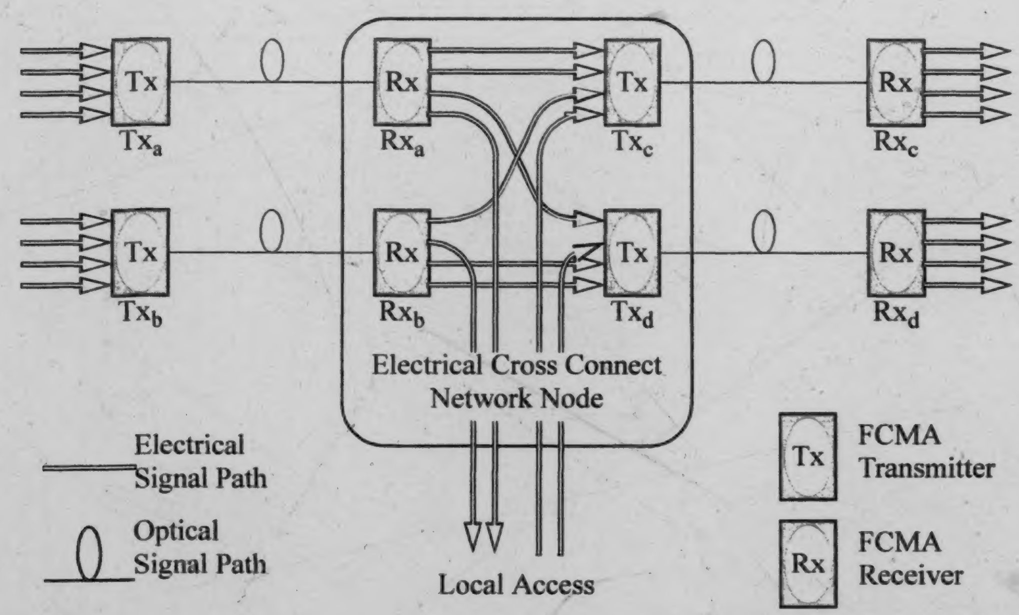
Tx
Txa
Tx
Txb
Rx
Rxa
Rx
Rxb
Tx
Txc
Tx
Txd
Rx
Rxc
Rx
Rxd
Electrical Cross Connect
Network Node
Electrical
Signal Path
Optical
Signal Path
Local Access
Tx
FCMA
Transmitter
Rx
FCMA
Receiver

Figure 1-17: A diagram representation of an electrical cross connect network node that provides local access.

This local access can be assigned in granularities of 1/4 the aggregate bit rate of one optical channel without decoding the routing information of the remaining 3/4 of the optical signals. Another advantage is that the decoding that is necessary takes place at a frequency that is 1/4 of the equivalent bit-rate for the received optical channel.

1.11.3 Head-End Switching.

FCMA networks have a built in means of performing switching without changing the network hardware configuration and without decoding the addressing information for a particular channel that has been multiplexed onto an FCM signal. Figure 1-18 depicts a hypothetical network hardware deployment that has two optical FCM signals entering from the left side of the diagram and two optical FCM signals leaving on the right side of the diagram, each on individual fibers.

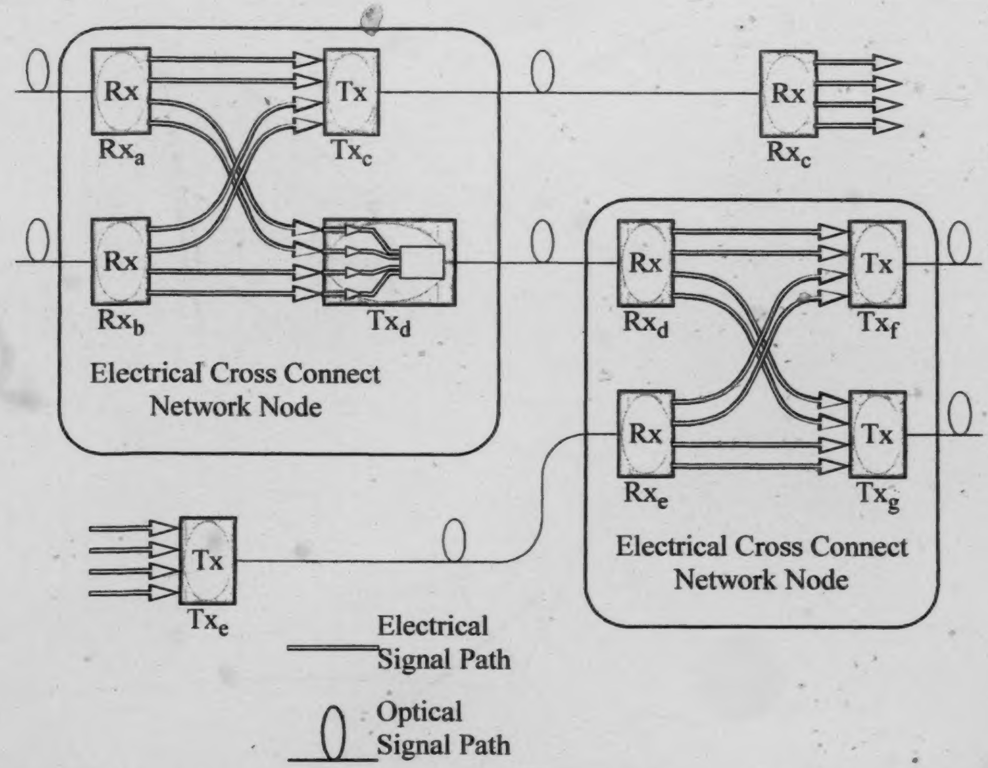
Rx
Tx
Rx$_a$
Tx$_c$
Rx
Rx$_c$
Rx
Rx$_b$
Tx$_d$
Electrical Cross Connect
Network Node
Rx
Tx
Rx$_d$
Tx$_f$
Rx
Tx
Rx$_e$
Tx$_g$
Electrical Cross Connect
Network Node
Tx
Tx$_e$
Electrical
Signal Path
Optical
Signal Path

Figure 1-18: An example of a more complex network connectivity that shows the internal electrical multiplexing elements of one of the transmitters, Tx$_d$. Figure 1-19 will show the details of what is happening inside of Tx$_d$.

In Figure 1-18, a channel from Tx$_a$ (which is not shown) will be routed from the fourth channel emerging from Rx$_a$ to the second input of Tx$_d$. The channel is remultiplexed and retransmitted to Rx$_d$, where it emerges from Rx$_d$ on the second channel and is passed along to Tx$_f$ and retransmitted again. If at some time the gains of the electrical multiplexor internal to Tx$_d$ are reconfigured, as depicted in Figure 1-19, the channel that previously emerged from Rx$_d$ on the second output will now appear at the third output and be transmitted by Tx$_g$ to a different location.

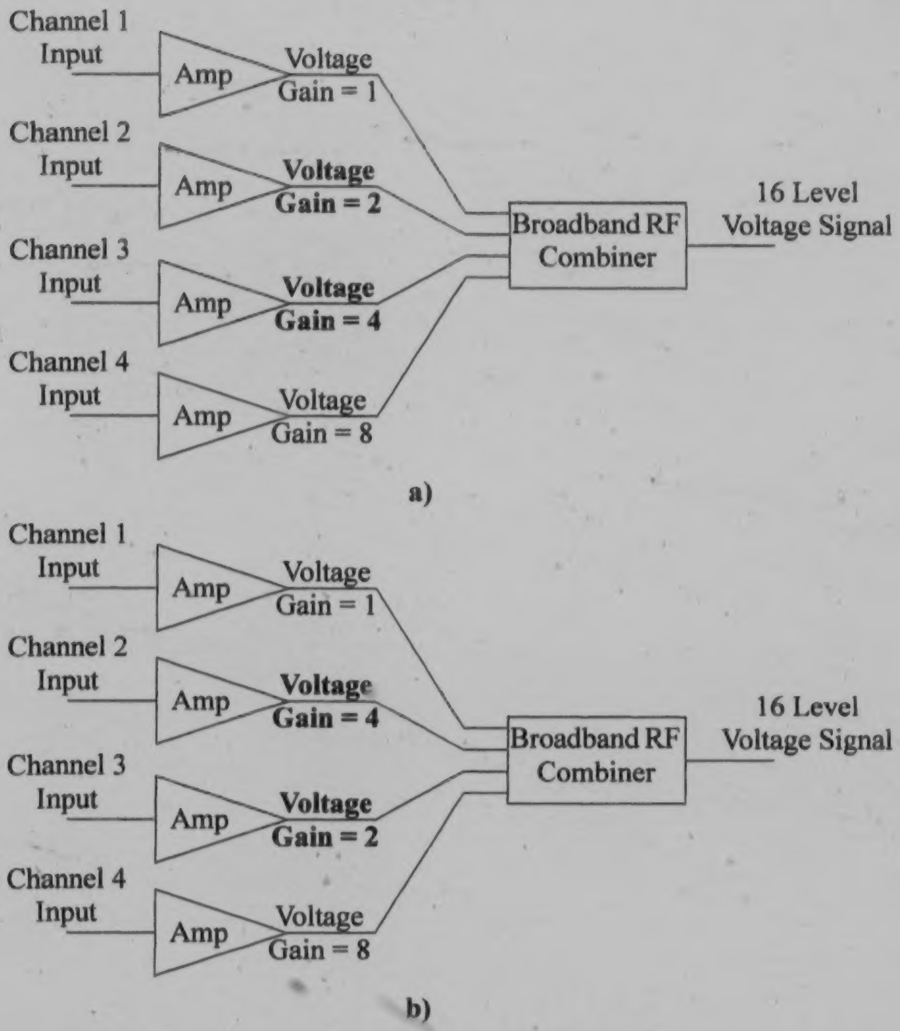
Channel 1 Input
Amp
Voltage Gain = 1
Channel 2 Input
Amp
Voltage Gain = 2
Channel 3 Input
Amp
Voltage Gain = 4
Channel 4 Input
Amp
Voltage Gain = 8
Broadband RF Combiner
16 Level Voltage Signal
a)
Channel 1 Input
Amp
Voltage Gain = 1
Channel 2 Input
Amp
Voltage Gain = 4
Channel 3 Input
Amp
Voltage Gain = 2
Channel 4 Input
Amp
Voltage Gain = 8
Broadband RF Combiner
16 Level Voltage Signal
b)

Figure 1-19: A diagrammatical representation of what is necessary for Tx_d to perform switching of 1/4 of its aggregate data from Tx_f to Tx_g as depicted in Figure 1-18 without decoding the addressing information of the constituent channels. **a)** represents the initial gain configuration and **b)** represents the gain configuration after switching.

One consequence of performing this switching is that the third output of Rx_d will have to be transmitted by Tx_f in Figure 1-18.

The examples that have been presented to this point have only one optical channel transmitted on each fiber. Better use of the bandwidth available on any fiber can be accomplished using Wavelength Division Multiplexing (WDM). The section that follows will explain an example that demonstrates FCMA combined with WDM.

1.11.4 FCMA with WDM.

Wavelength Division Multiplexing (WDM) is a common technology used in fiber optic communication networks. Any signal format that can be transmitted optically on fiber can be multiplexed and demultiplexed optically using WDM technology. Using WDM to combine and separate FCM signals transmitted on different wavelengths requires adding the appropriate optical filters at the physical locations where the channels are combined and separated.

Figure 1-20, below, shows a simple WDM link that combines two FCM channels onto one fiber link.

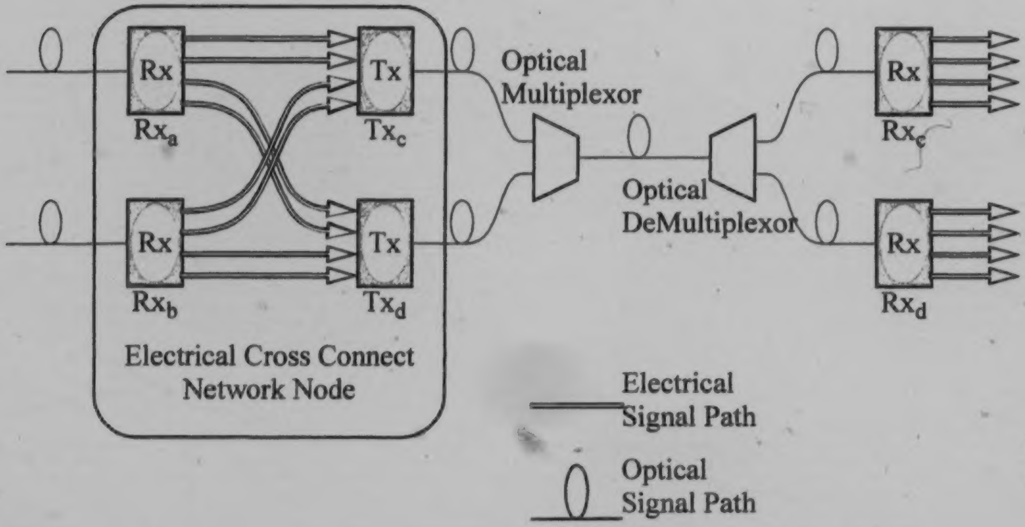
Rx
Rxa
Tx
Txc
Rx
Rxb
Tx
Txd
Electrical Cross Connect Network Node
Optical Multiplexor
Optical DeMultiplexor
Rx
Rxc
Rx
Rxd
Electrical Signal Path
Optical Signal Path

Figure 1-20: A two optical channel example of co-directional wavelength division multiplexing of FCM signals on different wavelengths.

The transmitters that are wavelength combined on a common fiber are shown to be co-located at an electrical cross connect network node. It is assumed that the transmitted signals are on different wavelengths and are combined with the optical multiplexor at the electrical cross connect network node site. The optical link carries the two wavelengths an unspecified distance at the end of which the channels are separated by the optical demultiplexor. The receivers for the two channels are shown in a manner that does not impose the restriction that they are co-located, and the signals are not necessarily retransmitted or terminated in the manner that they are shown.

Assuming the total bandwidth estimated for the four OC-48 channel FCM signal (~56 GHz), it is likely that more than two channels can be transmitted over a common fiber. The analysis of how many channels could be combined on one fiber is beyond the scope of this work and will not be explored.

Building a MAN based on a bus architecture, as was discussed for DQDB in Section 1.1.4, could be realized with one fiber for each direction or bi-directional WDM on a common fiber, as will be briefly discussed in the following section.

1.11.5 Bi-directional Bus Architecture.

A bi-directional bus can be realized on single fiber links using WDM to manage the directionality of two different wavelengths travelling in opposite directions on the same fiber. Figure 1-21 shows a two wavelength bi-directional bus network node and the two WDM multiplexor/demultiplexor units that would be standard equipment for realizing a bi-directional bus. A bus network based on the WDM building block depicted in Figure 1-21 would consist of a concatenation of these building blocks.

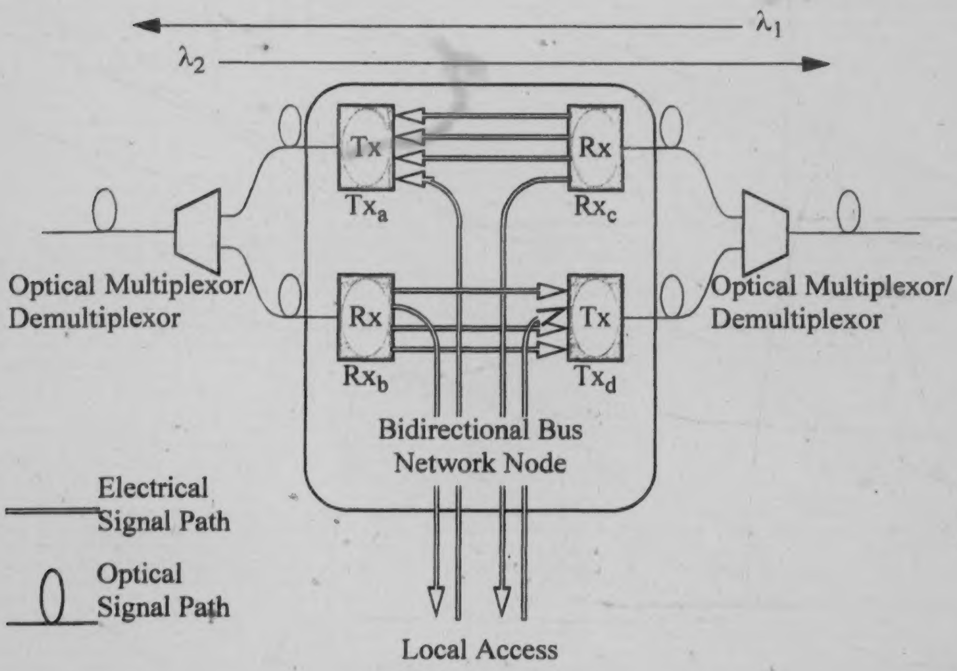
λ1
λ2
Tx
Txa
Rx
Rxc
Rx
Rxb
Tx
Txd
Optical Multiplexor/
Demultiplexor
Optical Multiplexor/
Demultiplexor
Bidirectional Bus
Network Node
Electrical
Signal Path
Optical
Signal Path
Local Access

Figure 1-21: A two optical channel example of bi-directional wavelength division multiplexing of FCM signals on different wavelengths. Concatenation of network nodes and links of this type creates a bidirectional bus network.

By terminating only part of the aggregate bandwidth of the total transmitted FCM signal at any node, four independent virtual bus architectures can be physically realized with a single wavelength that offer different physical and logical connections for each multiplexed part of the FCM signal. Also, what is shown in the diagram, Figure 1-21, has the fourth part of the left-travelling FCM signal paired with the second part of the right-travelling signal terminating at the local access point to demonstrate that the bi-directional bus is not restricted to using the same multiplexed part of the FCM signal for both directions.

Combining this bus architecture, regardless of what signal format is multiplexed by FCMA, with the electrical cross connect function and adding multiple wavelengths in each direction could be used to create a generalized mesh architecture with physical and logical connections being made at the sub-wavelength granularity scale. This realization of a sub-wavelength mesh network architecture does not require time domain demultiplexing to access the aggregate bandwidth of single optical channels in pieces smaller than the per wavelength data throughput,

1.11.6 Network Summary.

From the discussions presented throughout Section 1.11 it can be seen that FCMA can be deployed in a variety of existing network architectures including everything from single-channel single-fiber spans to generalized mesh networks with multiple WDM channels.

1.12 Summary of Chapter 1 and Chapter by Chapter Overview.

Some basic concepts were introduced pertaining to optical MAN design and physical layer architectures of these optical networks. Existing MAN technologies and transmission formats are a technological merging of the LAN, where Ethernet is dominant, and the WAN, where SONET and ATM are popular. The background for FCMA, what it is, how is it different from existing transmission methods, how it works, and how to implement it as a physical layer, was presented as well as an overview technology choices that may be used to implement FCMA. Finally, the network configurations possible with FCMA were discussed and the advantages FCMA brings to a communication network are directly derived from these configurations.

Moving forward from Chapter 1, Chapter 2 is a theoretical investigation of the limitations encountered when attempting to use semiconductor laser diodes to transmit signals for FCMA links. The theory of semiconductor laser rate equations will be reviewed and integration results obtained by the Runge Kutta method will be presented to compare transmitter design options.

Chapter 3 will provide some experimental verification of the optical modulation methods as proposed in Chapter 2. More details of the design of an FCM transmitter will be described in Chapter 3, including the necessity of polarization control.

Chapter 4 will cover the design of the harmonic optical decoder that demultiplexes the FCM signal into it's constituent channels. Chapter 5 will provide design details for the dual differential receiver used to recover these constituent channels.

Using the theoretical and experimental results of Chapters 2 through 5, Chapter 6 will be concentrated on predicting the performance of the overall design with the components described in preceding chapters. Only calculated results will be presented.

The last chapter, Chapter 7, will review the material that has been presented in the form of a summary and draw conclusions based on the work completed and offer suggestions with respect to ideas for improvement and future work.

Chapter 2. Semiconductor Laser Theory for Frequency Shift Keying.

Semiconductor lasers are a class of opto-electronic devices that exhibit light amplification by stimulated emission of radiation. Lasers, in general, consist of an optical gain medium confined to the interior of a resonant optical cavity. Semiconductor lasers have a semiconductor gain medium and feedback provided by end mirrors or Bragg gratings, or both. It is the amplification of radiation by the optical gain medium and the subsequent interaction of this amplified radiation with the properties of the resonant optical cavity that one can use to develop numerical models in order to gain insight into the operation of semiconductor lasers. This chapter provides the necessary background information for numerical modelling of semiconductor lasers and to clearly demonstrate the development of a numerical model that accurately describes the dynamics of a semiconductor laser subjected to the injection of charge carriers or an external optical signal. By doing this, one can compare the dynamics of current injection versus optical injection and their respective effectiveness in generating optical FSK signals. This will be accomplished by following an evolution of laser rate equations, equations used to describe the operation of lasers, from a set of equations for a single-longitudinal-mode semiconductor laser to a more complex set of equations describing simultaneous injection of coherent and non-coherent light into a multiple-longitudinal-mode semiconductor laser. These rate equations can be integrated and the results of the integration will be analyzed and discussed.

This investigation of laser rate equations will provide information pertaining to the effectiveness of baseband FSK signal generation such as available output modulation depth and signal distortion due to relaxation oscillation and non-linearity of the FSK signal transfer function (from either current or optical injection). Laser rate equations for electrical and optical injection describe the dynamic operation of the laser and are used to estimate the optimum injection rate, input modulation depth, and the laser bias current. In the case of optical injection, the optimum injected laser frequency also must be estimated.

It is the comparison of the frequency response of a semiconductor laser for carrier injection versus photon injection that will be dealt with in this chapter. A large frequency-modulation depth is desirable, but signal quality in terms of the shape of the frequency modulation is also important. The associated intensity modulation, an undesirable consequence of the laser modulation for FSK signals must be examined also.

2.1 The Mathematical Description of Laser Frequency Response.

Frequency shifts of oscillating modes of a semiconductor laser can be represented mathematically by their relation to the charge carrier density in the gain medium of the lasing cavity [PETE1],

$$2\pi(\nu - \nu_{th}) = \frac{1}{2}\alpha g_n(n - n_{th}), \tag{21}$$

where ν is the oscillation frequency of a lasing mode, ν_{th} is the oscillation frequency of a particular lasing mode at threshold, α is the linewidth enhancement factor, g_n is the derivative of the semiconductor gain with respect to carrier number, n is the carrier number in the gain region of the semiconducting medium (in the laser), and n_{th} is the threshold value of carrier number in the laser. In the reference, [PETE1], there is another factor in the right hand side of this equation, the group velocity of the lasing mode. In the equation system that was used here, the gain is normalized to the group velocity so it does not appear in Equation (21).

The steady state value of the carrier number for a laser biased above threshold is a monotonically increasing function of DC laser bias current. For these conditions (where α and g_n are both positive parameters), the oscillation frequency is also a monotonically increasing function of bias current. This effect is known as *adiabatic* chirp.

The transient response of a semiconductor laser to quick changes of injected current (with rise times on the order of ns for most semiconductor lasers) produces an additional corresponding lasing frequency change, called *transient* chirp. Because of the interaction of photons and charge carriers in the laser cavity, an oscillation occurs, known as relaxation oscillation, that behaves like an underdamped feedback system. The charge carrier number oscillates as a function of time and so does the lasing frequency.

In order to generate an FSK signal that closely resembles the signal depicted in Figure 1-4 (a square wave response in the lasing frequency) the signal produced by the FCMA transmitter requires linear adiabatic chirp and a minimization of transient chirp. A fast rise time (much less than the symbol period) is also required for the frequency response. Rate equation analysis of the laser dynamics will be used to investigate the scope and limitations of baseband FSK signal generation.

2.2 Semiconductor Laser Rate Equations.

An extensive body of literature is available on the subject of laser rate equations for single- and multiple-longitudinal-mode semiconductor lasers, lasers coupled to external cavities, and lasers subject to external injection [AG1,AG2,CARE1,CARE2,CARE3,COR1,HO1,LA1,MARE1,MARE2,MEC1,MOH1, OS1,PETE1,PETI2,SHU1,TR1,WH1]. The content presented in this chapter is based on the work of Schunk and Petermann[SHU1], and, where it is necessary, modifications to the theory presented in their paper will be explained. Semiconductor laser rate equations are based on theoretical derivations for the interaction of photons and charge carriers (electrons and holes) in a direct band gap semiconductor material as well as phenomenological corrections to account for experimentally observed effects, such as gain compression and optical losses due to scattering in the laser active region, that are not obvious results of theoretical analysis. The equations take the form of coupled first-order non-linear differential equations for the charge carrier density, n, and the number of photons in the lasing modes, S_l, where l is an index that runs over the number of longitudinal modes included in the model. This theoretical development applies to Fabry-Perot (FP) lasers, although Distributed Feedback (DFB) lasers can be modelled by the same equations with some modifications [MOH1,TR1].

The equation for the charge carrier number, n, Equation 35 of [SHU1], follows,

$$\frac{dn}{dt} = \frac{I(t)}{q} - \frac{n}{\tau_n} - \sum_l g_{rl} g(n, S) S_l + \text{Noise Terms}, \tag{22}$$

where

$$g(n, S) = \left(\frac{1}{\tau_p} + g_n(n - n_{th})\right)\left(1 - \kappa_s \sum_l S_l\right), \tag{23}$$

and $I(t)$ is the injected current as a function of time, t, q is the electron charge, τ_n is the carrier lifetime, g_{rl} is the gain reduction factor for the lth mode, τ_p is the photon lifetime and κ_s is the gain compression factor. The summations are over the number of modes in the model. The first two terms on the right hand side (RHS) of Equation (22) combine to represent the change in charge carrier density due to current injection and all modes of electron and hole recombination that do not result in stimulated emission. The third term is the stimulated emission term, it is proportional to the number of photons in each of the lasing modes. The noise terms are not used in any of the calculations in this chapter.

For each of the lasing modes, in a laser without optical injection, a first order differential equation for the number of photons oscillating in the lth mode, S_l, inside the laser cavity can be written,

$$\frac{dS_l}{dt} = \left(g_{rl} g(n, S) - \frac{1}{\tau_p}\right) S_l + R_s + \text{Noise Terms}, \tag{24}$$

where the only new variable, R_s, is the amount of spontaneous emission coupled to the lasing mode. In general the value of R_s is different for each mode, but it will be assumed to be the same for all modes for simplicity. The first term on the RHS of Equation (24) represents the effects of semiconductor gain on the lth mode of the laser oscillation and the noise terms are not used in any of the calculations in this chapter.

Integration of Equations (22) and (24) by the Runge Kutta method calculates the dynamic behaviour of semiconductor lasers. The dynamics of the laser for an arbitrary electrical current can be observed by varying the injection current, $I(t)$.

The phase of the lasing modes in the absence of optical injection is determined solely by Equation (21) and is calculated from the results of the Runge Kutta integration.

When optical injection is added to the set of equations, a modification of the photon number equation is necessary, Equation (24) becomes

$$\frac{dS_l}{dt} = \left(g_{rl}g(n,S) - \frac{1}{\tau_p}\right)S_l + R_s + 2\kappa_c\sqrt{S_l S_l^{in}}\cos(-\phi_l) + \text{Noise Terms}, \qquad (25)$$

where κ_c is the coupling factor for the injected optical signal, S_l^{in} is the number of photons injected into the laser, and ϕ_l is the phase of the lth oscillation mode of the laser. It will be assumed that the phase of the injected signal is constant, which means that the optical frequency of the injected signal does not change. A general expression that replaces the phase term in the cosine that accounts for changes in injected signal phase is

$$-\phi_l \Rightarrow \phi_{ml} - \phi_l, \qquad (26)$$

where ϕ_{ml} is the phase of the injected signal. Note that Equation (25) is Equation (24) with one extra term to account for the optical injection.

The phase of the lth oscillation mode of the laser must be calculated along with the photon number as follows,

$$\frac{d\phi_l}{dt} = \frac{1}{2}\alpha g_{rl} g_n (n - n_{th}) - 2\pi(d_l + d_{sl}) + \kappa_c\sqrt{\frac{S_l^{in}}{S_l}}\sin(-\phi_l) + \text{Noise Terms}, \qquad (27)$$

where α is the linewidth enhancement factor, d_l is the optical frequency detuning of the injected light from the free running mode frequency, and d_{sl} is the optical frequency detuning of the free running mode frequency from its threshold value. The detunings are defined by the relations

$$d_{sl} = \nu_{sl} - \nu_{thl} \qquad (28)$$

and

$$d_l = \nu_l^{in} - \nu_{sl}, \qquad (29)$$

where ν_{thl} is the optical frequency of the free running mode at threshold, ν_{sl} is the free running optical frequency for the mode when the laser bias is above threshold, and ν_l^{in} is the optical frequency of the injected optical signal.

One important distinction must be made for modelling laser with optical injection, only the modes that are subject to optical injection must obey Equations (25) and (27), every other mode obeys Equation (24) where the optical frequency of these "free-running" modes can be determined by Equation (21).

In these semiconductor laser rate equations the conventional notation for the electric field is a normalization to the number of photons in the optical cavity at any given time. Written explicitly, the photon number is related to the electric field by this equation,

$$S_l = |E_l|^2, \tag{30}$$

where E_l is the full complex electric field of the photons inside the cavity and $|\ |^2$ denotes the product of the argument and its complex conjugate.

To understand how the behaviour of the semiconductor lasers is modelled through simulations, a discussion of the simulation parameters and the modelling method will be necessary. The next section introduces the simulation parameters and some subsidiary equations that will be necessary to model a laser effectively. The section following that will briefly describe the modelling method.

2.3 Laser Parameter Values and Subsidiary Equations.

The laser parameter values and subsidiary equations used in the simulations performed for this chapter are based on [SHU1], with additional information from [CARE1,HO1]. The parameter values are typical for InGaAsP Fabry-Perot lasers at 1550 nm wavelength. A list of the parameter values is presented in Table 2-1.

Some of the parameters listed in Table 2-1 are present in the rate equations of Section 2.2, and some of the parameters in the rate equations are calculated from these values. The subsidiary equations in the following section show how to derive the values of the remaining equation parameters from the parameters with values listed in Table 2-1. The optical frequency, the optical power (inside and outside of the laser facet), and the gain compression factor will be discussed individually.

Table 2-1: Initial parameter values for laser rate equation integration..

Laser Parameter	Symbol	Value	Unit
photon lifetime	τ_p	2	ps
(charge) carrier lifetime	τ_n	2	ns
linewidth enhancement factor	α	6	
gain derivative with respect to carrier number	g_n	3660	s^{-1}
threshold carrier number	n_{th}	calculated	
spontaneous recombination coefficient (rate)	R_s	calculated	s^{-1}
side mode suppression ratio	γ_{sms}	~ 10 - 30	dB
gain compression coefficient	κ_p	3 - 6	W^{-1}
facet loss	α_m	calculated	m^{-1}
group refractive index	μ_g	4.5	
lasing wavelength(s)	λ_l	~ 1550	nm
resonator length	L	300	μm
facet reflectivities	R_m	0.32	
scattering loss (inside the laser cavity)	α_s	calculated	m^{-1}
carrier number at transparency	n_0	2×10^8	
inversion factor	n_{sp}	2.5	

2.3.1 General Subsidiary Equations.

Some of the parameters in Table 2-1 will be treated as free parameters; the photon lifetime, the carrier lifetime, the linewidth enhancement factor, the derivative of the gain with respect to the carrier number, the sidemode suppression ratio, the gain compression coefficient, the group refractive index, the lasing wavelengths, the resonator length, the facet reflectivities, the carrier number at transparency, and the inversion factor. Parameters that need to be calculated prior to running Runge Kutta integration based computer simulation of the rate equations include the mirror loss, the threshold gain, the scattering loss, the threshold carrier number, the threshold current and the spontaneous emission coefficient. Additional parameters must be calculated as described in following sections of this chapter, but the information necessary to calculate the values of these parameters is provided in this section.

It is customary to represent the loss of photons from the facets of the laser by a loss parameter that is distributed throughout the lasing cavity. Assuming that the facet reflectivities are equal, represented by R_m, the facet loss, α_m, can be written as,

$$\alpha_m = -(\ln R_m)/L. \tag{31}$$

At transparency the rate of stimulated emission equals the rate of reabsorption for the bulk semiconductor, therefore the net gain of the semiconductor is zero. There are additional losses to consider in the case of a laser represented by the mirror loss and scattering loss. The total additional loss above transparency, α_l, is the sum of these two terms,

$$\alpha_l = \alpha_m + \alpha_s. \tag{32}$$

At the onset of threshold, the gain equals the total loss which defines the threshold gain, g_{th}, as,

$$g_{th} = v_g \alpha_l, \tag{33}$$

where v_g is the group velocity. The threshold gain defines the photon lifetime, τ_p, directly, so when the photon lifetime is used as a known parameter, the threshold gain can be calculated,

$$g_{th} = \frac{1}{\tau_p}. \tag{34}$$

Assuming that the known parameters are the threshold gain (via the photon lifetime), the cavity length and the mirror reflectivity, the scattering loss can be treated as a calculated parameter,

$$\alpha_s = \frac{v_g}{g_{th}} - \alpha_m . \tag{35}$$

The threshold carrier number, n_{th}, can be calculated knowing the threshold gain, the transparency carrier number and derivative of the gain with respect to the carrier number (assumed to be linear),

$$g_n(n_{th} - n_0) = g_{th} . \tag{36}$$

The threshold current can then be calculated using Equation (22), the carrier number rate equation, assuming steady state operation at threshold with no photons in the lasing modes,

$$\frac{I_{th}}{q} - \frac{n_{th}}{\tau_n} = 0 . \tag{37}$$

The spontaneous emission coefficient (the rate of spontaneous emission into a lasing mode) can be calculated from the spontaneous emission inversion factor and the photon lifetime as in the following equation, [SHU1],

$$R_s = \frac{n_{sp}}{\tau_p} . \tag{38}$$

These general subsidiary equations apply to all calculations and simulations performed for any results within this chapter and are equally applicable to either current injection or photon injection being used as a modulation mechanism. The manner in which the laser oscillation frequency is treated for current injection modulation or photon modulation is different, and will be discussed next.

2.3.2 Laser Oscillation Frequency.

When a semiconductor laser is not subject to coherent optical power injection, the optical frequency of the oscillation is determined only by the dynamics inside and the physical attributes of the laser cavity. When a semiconductor laser is subject to coherent optical power injection, the laser can be forced to oscillate at the frequency of the injected light, which, in general, will be different from the solitary laser situation (without photon injection). It is important to distinguish between these cases and explicitly define the meanings of the parameters used to represent the optical frequency in the rate equations.

A DC biased semiconductor laser will have an oscillation frequency defined with respect to the threshold value of oscillation frequency by Equation (21). This frequency detuning is represented by d_{sl} in Equation (27). For steady state operation of a laser without optical injection the laser emits at an optical frequency defined by this detuning. The first term on the RHS of Equation (27) in combination with d_{sl} are the terms that represent the internal self balancing of the laser oscillation frequency and the changes in charge carrier number within the active region of the laser. d_l in Equation (27) and the term involving the injected optical power, S_l^{in}, represent the external driving forces from the optical injection. The laser would operate at a point that balances the optical frequency and the carrier number in the absence of optical injection, but with optical injection all these terms must balance (at least for a DC optical power injection).

For a given electrical DC bias the oscillation frequency detuning in the absence of injection can be determined from Equation (21) and a steady state calculation. Once the value of d_{sl} has been determined for a given set of simulation parameters and bias current, d_l and S_l^{in} can be chosen and the dynamics of the semiconductor laser can be calculated via Runge Kutta integration. For all calculations performed for this work, d_{sl} and d_l will be assumed to be constants.

Calculation of the oscillation frequency shift, or adiabatic chirp, relies on Equation (21) but the mechanisms that are responsible for adiabatic chirp are not obvious, with gain compression playing a key rôle. Gain compression and it's effects on laser oscillation frequency are the subject of the next section.

2.3.3 Gain Compression.

Gain compression is a phenomenological addition to the laser rate equations that compensates numerical calculations for gain non-linearities at high values of laser output power. The consequence of not having a gain compression term in laser rate equations, along with neglecting spontaneous emission contributions to the lasing modes, is that the adiabatic chirp of the lasing frequency is removed, the lasing frequency does not change with the bias current operating point of the laser. This can be verified by removing these terms, as well as any optical injection terms and noise terms, and solving for the carrier number, n, for a DC electrical bias current. An easy means of expressing the relationship between ν and S is provided by Petermann [PETE1],

$$2\pi(\nu - \nu_{th}) = \frac{1}{2}\alpha\left(\frac{d(\ln S)}{dt} + \frac{1}{\tau_p}\left(\kappa_s S - \frac{n_{sp}}{S}\right)\right), \tag{39}$$

where the reference notation has been converted to the notation used here and the spontaneous emission enhancement factor of the reference is assumed to be 1 (see Chapter 2 of [PETE1] for a discussion of spontaneous emission enhancement factor). This is Equation (21) expressed in terms of the photon number and it can be seen that without gain compression, $\kappa_s = 0$, and spontaneous emission, $n_{sp} = 0$, the only variation in optical frequency is a dynamic variation.

For high output power, from a laser with parameter values similar to those used here, $S \sim 10^7$, and assuming typical values of κ_s ($\sim 10^{-7}$) and n_{sp} (~ 2.5), the gain compression term clearly dominates the adiabatic chirp behaviour of semiconductor lasers. The adiabatic chirp is directly proportional to the product of the linewidth enhancement factor and the gain compression coefficient, so by enhancing this product large adiabatic shifts can be achieved. The linewidth enhancement factor is laser structure dependent [KOB1,KOC1,OS1], but the optimum value has not been used here in these calculations. A working assumption is that a value of 6 is reasonable.

The gain compression factor, κ_s, as included in the rate equations is a convenient shorthand expression for the experimentally observable gain compression factor, denoted κ_p. The relationship between the two is a straightforward equality,

$$\kappa_s = \frac{1}{2}h\nu v_g \alpha_m \kappa_p , \tag{40}$$

where h is Planck's constant, ν is the optical frequency of the mode, and κ_p is the gain compression expressed in units of inverse Watts (see [PETE1]). Values of κ_p for InGaAsP lasers range from 1 to 5 W^{-1} [PETE1].

2.3.4 Optical Powers Inside and Outside of the Laser.

The optical power exiting one facet of the laser cavity at the optical frequency of one of the lasing modes, ν_l, can be calculated from the number of photons inside the laser cavity in that lasing mode,

$$P_l^{out} = \frac{1}{2} h \nu_l v_g \alpha_m S_l . \tag{41}$$

Conversely, the inverse of the relation converts an optical power incident on one facet of the laser into an equivalent photon number outside the laser facet,

$$S_l^{in} = \frac{2 P_l^{in}}{\hbar \omega_l^{in} v_g \alpha_m} . \tag{42}$$

Another factor is necessary to account for the facet reflectivity and to normalize the injection rate to the round trip cavity time for optically injected photons, see [HO1] or [SHU1] for details. The injection coupling coefficient, κ_c, converts the instantaneous value of the electric field (i.e.; square root of the photon number) of the photons outside the laser facet into an equivalent electric field amplitude distributed over the cavity and is given as

$$\kappa_c = \frac{(1 - R_m)}{\tau_L \sqrt{R_m}} , \tag{43}$$

where the facet reflectivities are again assumed to be equal and τ_L is the round trip cavity time defined by,

$$\tau_L = \frac{2L}{v_g} . \tag{44}$$

2.3.5 Section 2.3 Summary.

All the information necessary to calculate the dynamic behaviour of semiconductor lasers has been presented in this section. What is needed is a numerical method to perform the calculation. The Runge Kutta method is one means to solve coupled differential equations [PRE1], such as semiconductor rate equations, as is discussed in the following section.

2.4 Semiconductor Laser Modelling using the Runge Kutta Method.

The Runge Kutta method is a means of solving a set of first order differential equations by approximating the derivatives of the set of variables and multiplying by a given step of an integrand, such as time. The results are new initial values for the set of variables that become the starting conditions for another integration step.

There are a number of variations of the Runge Kutta method, the one employed here uses a fifth order Runge Kutta step to evaluate the integration. There are more powerful and less powerful versions of this method, so, to validate the accuracy of this method applied to semiconductor lasers, a number of similar simulations from published papers were repeated [CARE1,HO1] and the fifth order Runge Kutta was deemed to be more than adequate. The source code used in this work was based on the routines published in 'Numerical Recipes in FORTRAN'[PRE1].

The code for this Runge Kutta routine is written in such a way that the core of the calculation code never changes, no matter what set of equations need to be solved. The routines that are modified are for loading the parameter values into the relevant variables, calculation of the derivatives, and saving the values of any calculated parameters upon completion of the integration.

The next section describes the application of the Runge Kutta method to the modelling of a single-mode semiconductor laser and presents the results of simulations for lasers subject to electrical current modulation.

2.5 Free-Running Single-Mode Semiconductor Lasers.

A free-running single-mode semiconductor laser is a laser that is not subject to external optical injection, either from another laser or an external reflector (external cavity), and has only one mode of oscillation. Single-mode here means both laterally single-moded and longitudinally single-moded. Such a laser reacts only to changes in electrical drive current.

Equations (22) and (24), with $l = 1$ and $g_{r1} = 1$, are used to calculate the response of the laser to the electrical input, $I(t)$. The results, optical power and optical frequency, of an example simulation of a DC biased laser, $I(t)$ = constant, biased at twice the threshold current are plotted as functions of time in Figure 2.1 and Figure 2.2.

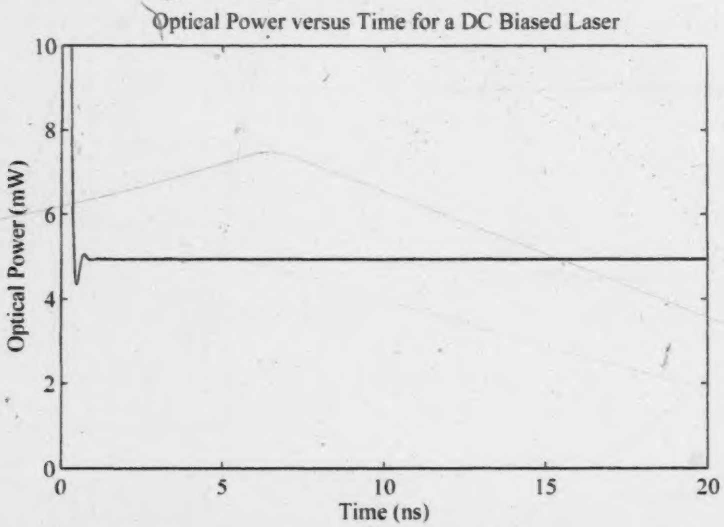

Figure 2.1: Optical power output from one facet of a DC biased laser, biased at twice threshold, as a function of time.

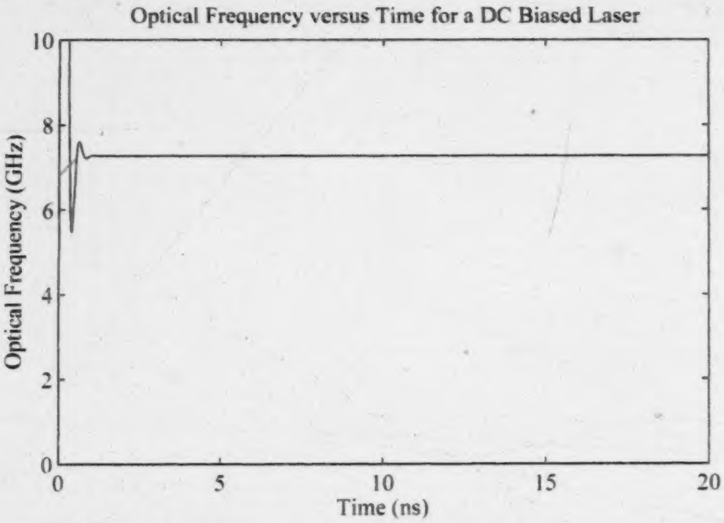

Figure 2.2: Optical frequency offset from the threshold oscillation frequency of a DC biased laser, biased at twice threshold, as a function of time.

The starting values for the photon number and the carrier number are 24000 and 466660000, respectively, and the value of the gain compression coefficient for this calculation is 6 W^{-1}. The values of all of the remaining simulation parameters are as listed in Table 2-1. The integration step size is varied depending on the length of the simulation, it is calculated so that it is less than 250 fs and total number of steps is a power of 2. The variations in optical power and frequency for times less than 1 ns on the example simulation plots result from a relaxation from the initial conditions to the proper steady state values for power and frequency at the given bias current.

Repeated simulations with different bias currents provides the steady state optical power and frequency offset from the threshold value of oscillation frequency as a function of injected current. When optical power versus injected current (the LI transfer curve) and frequency offset versus injected current (the νI transfer curve) are plotted then the bias and modulation currents can be chosen to produce an frequency code signal. Simulated predictions of the LI and νI transfer curves are presented in the next section.

2.5.1 Continuous Wave Operation.

Continuous wave operation of a semiconductor laser means it is operated in a steady state manner with no changes in any external influence. For the continuous wave operation of a single-mode semiconductor laser, the injected current is held at a constant DC bias. Simulations were run for a variety of bias currents and the steady state output optical power and frequency were tabulated. Runge Kutta simulations were performed with bias currents from 110% of the threshold current to 300% of the threshold current in 10% steps. The values of optical power and frequency were calculated by averaging over the last 10 ns of the 20 ns duration simulations. The values of the simulation parameters for the LI and νI curves in this section are as presented in Table 2-1. Two values of gain compression were used, 3 and 6 W^{-1}, to illustrate the effects that this parameter has on the behaviour of a semiconductor laser. The threshold current for the lasers that were simulated, for both values of gain compression, was 24.6 mA.

The output optical power from one facet is plotted against the bias current, which is normalized to the threshold current, in Figure 2.3 for both values of gain compression.

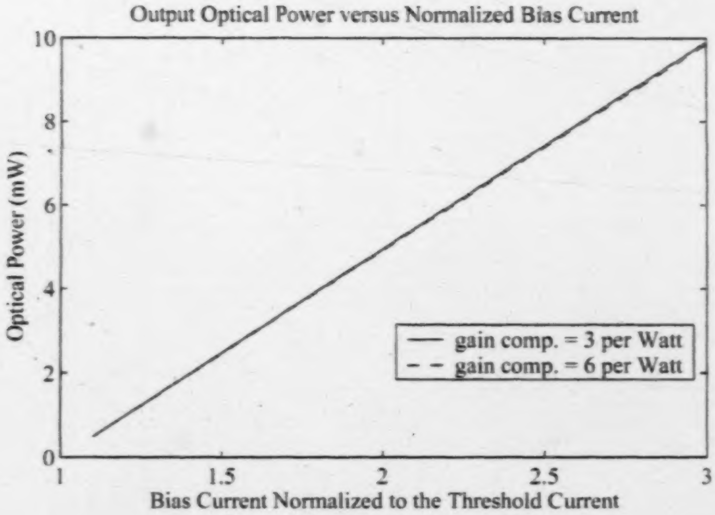

Figure 2.3: Output optical power versus normalized bias current (bias current divided by the threshold current) for gain compressions of 3 and 6 W^{-1}.

Doubling the gain compression has very little effect on the output optical power for DC biased lasers. The effects that gain compression has on the output of the semiconductor laser will be noticeable when the frequency response of the semiconductor laser is examined with respect to the gain compression. A figure of merit can be derived from plots like Figure 2.3, the optical power modulation efficiency, in mW/mA, is calculated from the slope of these graphs.

The output optical frequency offset from the threshold value is plotted against the bias current, which is normalized to the threshold current, in Figure 2.4 for both values of gain compression.

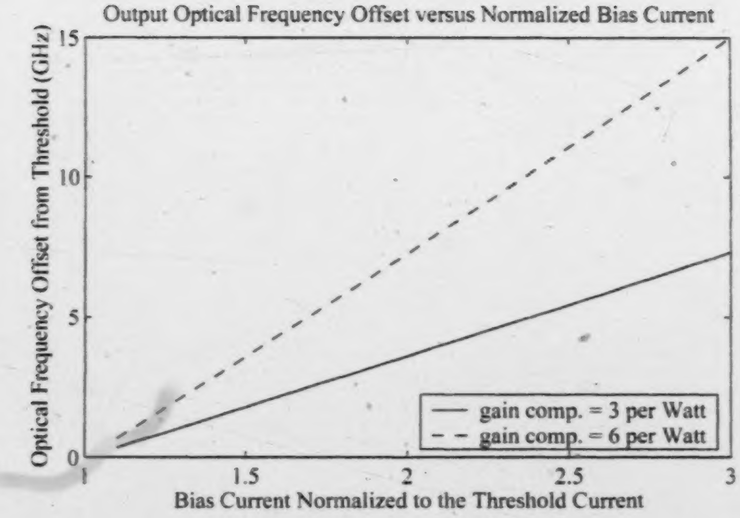

Figure 2.4: Output optical frequency offset from the threshold frequency versus normalized bias current (bias current divided by the threshold current) for gain compressions of 3 and 6 W^{-1}.

Doubling the gain compression effectively doubles the optical frequency offset from the threshold frequency for a given bias current for DC biased lasers. This effect is consistent with what is predicted for steady state operation by Equation (39). Another figure of merit can be derived from plots like Figure 2.4, the optical frequency modulation efficiency, in GHz/mA, is calculated from the slope of these lines.

The semiconductor laser rate equations that have been used to produce these results do not include temperature variations with bias current, therefore, the change in optical frequency with bias current is what is expected for the contribution due to changes in carrier number in the active region of the laser only (as in most simulations based on rate equations). The variations of optical frequency with laser temperature are quite dramatic for semiconductor lasers [GO1,KOB1,SHA1]. In fact, the oscillation frequency of a semiconductor laser is dominated by temperature effects when the bias current is changed. The influence that temperature has on the oscillation frequency of semiconductor lasers will be discussed in more detail in the next section when electrical modulation is introduced to the Runge Kutta simulations.

The ratio of the optical frequency offset to the output power as a function of bias current is of interest because it effects the signal quality for the FCMA based transmission system (which will be discussed in later chapters). The figure of merit is the frequency offset to output power ratio and it is a function of bias current for a DC biased laser, see Figure 2.5.

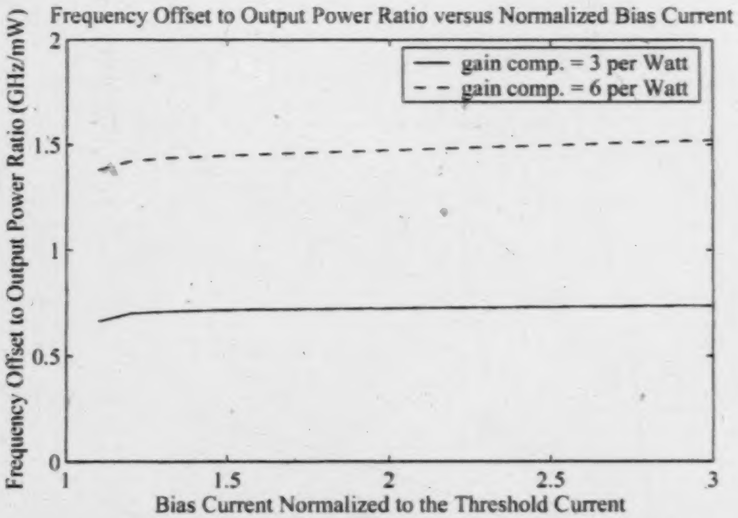

Figure 2.5: Optical frequency offset to output optical power ratio versus laser bias current for gain compressions of 3 and 6 W^{-1}.

For values of gain compression of 3 and 6 W^{-1}, the frequency offset to output power ratios are approximately 0.75 and 1.5 GHz/mW, respectively. This means that for lasers with higher gain compression, the optical frequency varies more with respect to output optical power for changes in drive current.

The results presented in this section have been for DC values of injected current. It is by changing the current that signals are optically transmitted from semiconductor lasers. The DC performance predicts the modulation efficiency of the laser, the amount of current necessary to produce the required change in optical frequency or power to generate the optical signal, but the laser has dynamic properties when modulated with high frequency signals that require real time calculations. The next section addresses what happens when semiconductor lasers are electrically modulated at high data rates.

2.5.2 Electrically Modulated Semiconductor Lasers.

A binary bit sequence in a typical optical transmissions system is intensity shift keyed where a time period of high intensity represents the transmission of a bit with value 1 and a time period of low intensity represents the transmission of a bit with value 0. In analogy to the intensity shift keyed optical system, a binary frequency shift keyed optical system uses two values of optical frequency to represent the bits with values 1 and 0. Typically, bits are transmitted with equal times and in sequence (synchronously) to form a transmitted data stream, or a transmission signal. Changing the electrical current of a semiconductor laser changes the output optical power and the output optical frequency, in this manner a binary amplitude shift keyed electrical signal is transferred to the optical domain to become an optical ISK signal or an optical FSK signal.

A general formula for electrical modulation of semiconductor lasers with a signal consisting of *M*-levels is

$$I(t) = \begin{cases} I_b - m_i(I_b - I_{th}) + \dfrac{2b_{k-1}m_i}{M-1}(I_b - I_{th}) + \\ \dfrac{2(b_k - b_{k-1})m_i}{M-1}(I_b - I_{th}) sin^2\left(\dfrac{\pi(t-(k-1)T)}{2t_r}\right) \\ \qquad (k-1)T \le t < (k-1)T + t_r \\ I_b - m_i(I_b - I_{th}) + \dfrac{2b_k m_i}{M-1}(I_b - I_{th}) \qquad (k-1)T + t_r \le t < kT \end{cases}, \quad (45)$$

where I_b is the bias current of the laser, m_i is the modulation index of the signal, b_k is the value, from 0 to M-1, of the kth symbol where k is a positive integer that represents the timeslot of the a particular symbol in the symbol sequence, t_r is the rise time of the signal and T is the duration of one symbol. This is a raised cosine signal where the modulation index is defined in terms of the bias current and threshold current such that the maximum excursion of the drive current from the bias current is $m_i(I_b - I_{th})$. The symbol to symbol transition point, by this definition, does not occur at integer multiples of the bit period from the start of the signal at $t = 0$, it occurs at an offset equal to one half of the rise time later. This was done for mathematical simplicity as it does not affect the integration results.

The modulation of the laser leads to conversion of the current signal to a signal in optical power and frequency. A binary signal is represented by setting $M = 2$ in Equation (45). The results from a Runge Kutta simulation, output optical power and frequency offset, for a laser with a gain compression of 6 W^{-1} biased at twice threshold, with a modulation index of 50%, a bit period of 1 ns (1 Gbps), and a bit rise time of 0.1 ns, are presented in Figures 2.6 and 2.7, respectively.

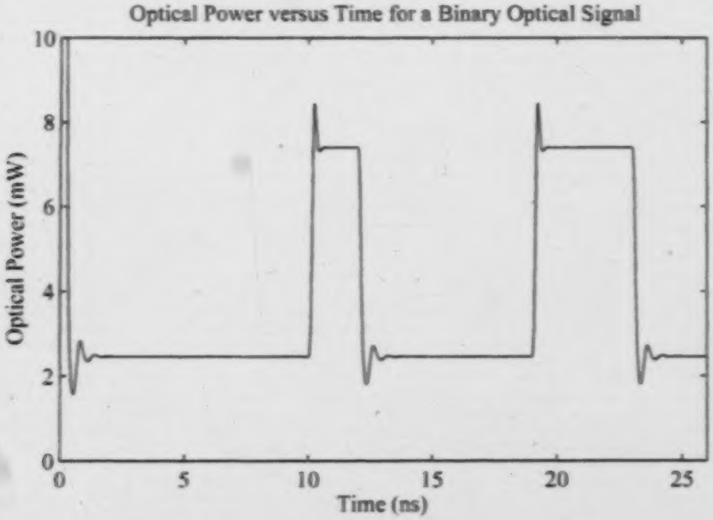

Figure 2.6: An example calculation result of the output optical power for a binary signal by current modulating a semiconductor laser, with a gain compression of 6 W^{-1}.

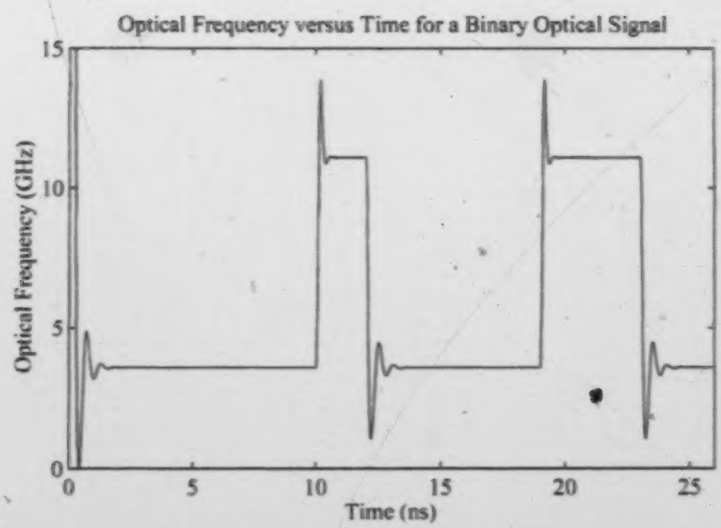

Figure 2.7: An example calculation result of the output optical frequency offset from threshold for a binary signal by current modulating a semiconductor laser, with a gain compression of 6 W^{-1}.

The optical power and frequency offset for binary modulation transition between the values predicted by the LI and νI transfer curves, Figures 2.3 and 2.4, with oscillation following each transition that are damped after ~ 1 ns. These damped oscillations are the relaxation oscillations of the laser. The appearance of relaxation oscillations on this type of modulated signal is explained as follows: When the laser is subjected to fast changes of input current, on a timescale roughly equal to the carrier lifetime, relaxation oscillations of the laser power and frequency result. When the rate of injection of electrical carriers is faster than the rate of stimulated emission the number of electrons and holes in excited states in the active region increases. The increased number of available carriers in the excited states increases the rate of stimulated emission. The number of photons increases rapidly, which decreases the number of excited charge carriers. The number of photons eventually decreases and the build-up of charge carriers begins again. The oscillation amplitude decreases with time for a step input of current because the oscillations are naturally damped. The result of a fast decrease in laser current is similar; changes in the photon number in the laser cavity lag behind the changes in charge carrier numbers. Relaxation oscillations occur even for DC biased lasers, but their effect on output optical power and optical frequency is not easily noticed in this case. When the optical spectrum of a DC biased semiconductor laser is measured (with enough sensitivity) there are small spectral peaks on either side of the laser mode frequency at +/- the relaxation oscillation frequency (the frequency at which relaxation oscillation manifest) from the laser mode frequency, see plots in [HE1,PETI1,PETI2,VA1].

For the optical power and frequency offset shown in Figures 2.6 and 2.7, the relaxation oscillations for a downward signal transition are plotted together on an expanded time-scale in Figure 2.8.

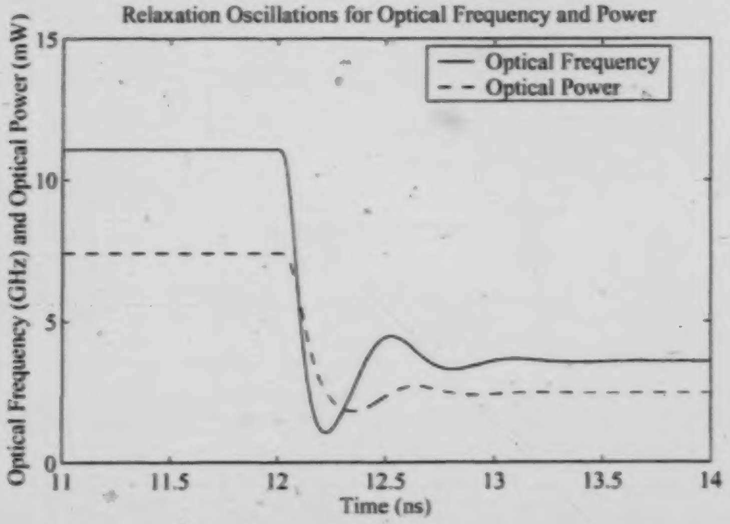

Figure 2.8: An expanded view of a high to low bit transition for the optical power and optical frequency offset for the example calculation result plots of Figures 2.6 and 2.7 highlighting the relaxation oscillations.

The oscillations in optical frequency, related to the decreased drive current through the number of carriers, precede the changes in optical power, related to the number of photons in the laser, as predicted by the preceding argument.

For a gain compression of 3 W^{-1}, the same bit sequence was simulated and the results of the same downward signal transition are shown in Figure 2.9.

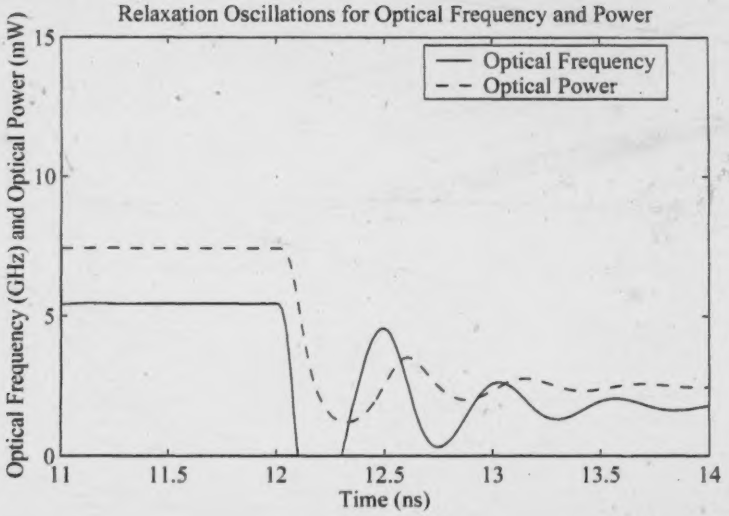

Figure 2.9: An expanded view of a high to low bit transition for the optical power and optical frequency offset for an example calculation with the same bit sequence as Figures 2.6 and 2.7, but a gain compression of 3 W^{-1}, highlighting the relaxation oscillations.

The damping time for relaxation oscillations is much longer for a lower value of gain compression, even though the relaxation oscillation frequency is almost equal in the two cases, Figures 2.8 and 2.9.

The dynamic response of semiconductor lasers to current modulation produces changes in optical power and optical frequency that can be used to transfer an electrical signal to an optical signal. Both adiabatic and transient chirp are present in Gbps signals produced by current modulation. Transient chirp and subsequent relaxation oscillations are effects that decrease the quality of the optical signal. Adiabatic chirp is not as much of a problem and for FCMA signal generation is an absolute necessity.

Gain compression has a strong effect on modulation performance of directly modulated semiconductor lasers. Increasing the gain compression increases the damping of relaxation oscillations and increases the adiabatic frequency shift. For ISK transmission signals this increased adiabatic chirp may not be the best, but for the FCM signal it is an advantage.

One drawback of direct current modulation of semiconductor lasers is the frequency shift effect due to temperature changes in semiconductor lasers at low frequencies. A transfer function in reference [KOB1] suggests low pass filter like response with a 3 dB corner at ~1 MHz for temperature dependent frequency modulation. The temperature induced chirp effects introduce bit pattern dependent optical frequency changes due to the presence of low frequency signal components. For many signal types, such as SONET with low frequency components at multiples of 8 kHz, this type of frequency modulation would be imposed on the output optical signal. The result, for this application, would be that the output frequency of the laser would no longer accurately represent the intended FCM signal.

These temperature effects were not included in the rate equations that were used calculate the transient response of semiconductor laser presented in this section, a more powerful set of equations is required. But, since these temperature effects are so detrimental to the FCMA system, direct modulation of the semiconductor lasers will no longer be considered here except as a bench mark for performance of other methods of modulation.

Overcoming pattern dependent effects and transient chirp in today's optical communication systems is typically accomplished through the use of an external (optical) modulator, Lithium Niobate or semiconductor electro-optic devices or semiconductor electro-absorption modulators are the most common. Both of these types of devices produce chirp in the signals they generate. A short discussion on the application of these modulators to the generation of optical FCMA signal generation is discussed in the following section.

2.5.3 A Note on External Modulation of Semiconductor Lasers.

The two types of high-speed optical external modulators that will be discussed here are electro-optic modulators and electro-absorption modulators. In order to produce FCM signals with an external modulator, the phase of the input light has to be modified to produce an output with distinct frequency levels. This is accomplished by continuously changing the phase of the input light such that the wavelength of the input light is either continuously and constantly shortened or lengthened.

In the case of an high speed electro-optic modulator, a high speed phase modulator, a voltage ramp applied to the travelling wave electrode of such a device would produce a change in the input optical frequency [CARE4,KOY1]. Modulation with electro-optic devices is possible, but impractical. A long sequence of identical symbols would require a very long voltage ramp, which would likely exceed the maximum rated voltages of such devices for the frequency shifts mentioned in Chapter 1 Also, at symbol transitions, the drive voltage would have to be quickly returned to the start voltage of the next symbol which would produce very large dynamic chirp effects in the output optical frequency.

Phase modulation, and hence frequency modulation, can be produced using electro-absorption modulators via the Kramers-Kronig relations. Frequency shifts are related to the rate of change of the loss of the absorption region of the EA modulator [CHIN1,CHIN2,KOY1]. The electro-absorption modulator has the same problems as the electro-optic modulator for creation of FCM signals.

Another means of creating FCM signal must be found. Optical injection in semiconductor lasers is a possible method of modulating semiconductor lasers to produce these signals. Using optical injection for the creation of FCM signals involves at least two modes of the semiconductor laser and the interaction of these modes via the carrier population. A short discussion of multi-mode semiconductor lasers precedes the investigation optical injection applied to FCM signal generation.

2.6 Semiconductor Lasers that are not Single-Moded.

Complications arise when attempting to model semiconductor lasers that are not single-moded. When modelling the operation of multi-mode semiconductor lasers, the gain and threshold current of the different modes are different in general. In the analysis presented here the threshold current will be assumed to be the same for all laser modes, as is done in [PETE1] or [SHU1]. Also, following the rate equations in [SHU1], the different optical gains of the different modes can be included in the model.

The development of equations that relate the gains of the sidemodes to the main mode of the semiconductor laser use the observable sidemode suppression ratio from experiment. Measuring the relative intensities of the sidemodes with respect to the main mode of the laser when the laser is DC biased and using this information, along with the gain of the main mode and the inversion factor, the gains of the sidemodes are calculated. The equations for calculating the gain of sidemodes using the sidemode suppression ratio will be stated here, for a discussion of the relevance of these equations the reader is referred to [SHU1]. The gain reduction factor, g_{rl}, for the laser sidemode with index l is calculated from the measurable sidemode suppression ratio, $\gamma_{sms,l}$, the inversion factor, n_{sp}, and the number of photons in the main mode of the laser, S_1,

$$g_{rl} = \frac{S_1 - n_{sp}/\gamma_{sms,l}}{S_1 - n_{sp}}. \tag{46}$$

For DFB lasers, typical values of gain suppression ratio are of the order of 20 to 30 dB or higher. For FP lasers there may be many modes above threshold with a variety of gains, with sidemode suppression ratios ranging from a few dB to 40 dB or higher. Calculation of the sidemode suppression ratio is the last piece of information necessary to successfully calculate the steady state and dynamic response of semiconductor lasers to optical injection.

2.7 Optical Injection in Semiconductor Lasers.

Optical injection in a semiconductor laser is accomplished by focusing light onto the facet of the laser from another light source, potentially another laser. Some of this injected light will couple into the laser active region and will be guided by the waveguiding properties of the laser. If the light is within the gain spectrum of the semiconductor material, it will affect the number of charge carriers through stimulated emission. It is through the carrier interactions, mediated by the gain of the laser, that the injected light influences the natural emission characteristics of the laser. The changes in dynamic behaviour of lasers modulated by optical injection are an increase in the modulation bandwidth of the laser [MEN1,SE1,SI1,YAS1] and a suppression of the relaxation oscillations [OL1] when compared to current injection modulation. Linewidth reduction can also be a result of optical injection, but only in specific circumstances [MOG1].

There are reported uses of directly current modulated semiconductor lasers for binary FSK, phase shift keying (PSK) or differential phase shift keying (DPSK) communication systems with optical filtering and direct detection reception [EM1,GO1,MAJ1,MAJ2,MAL1,SHI1,VO1,VO2,WOO1]. On close inspection of the simulations or experiments described in these papers the frequency content of the transmitted bit patterns is limited so that there is no appreciable signal energy or all of the signal energy is in the thermal frequency modulation region. This limitation is sometimes due to the application of a line coding scheme to the data and sometimes due to the use of an artificially short, repetitive bit sequence. The exception to the above statements is [CHRY1], where a laser with an extremely large linewidth enhancement factor is directly current modulated to produce a binary FSK signal while avoiding the thermal modulation distortion. Details on the specific type of laser were not provided.

Optical injection is immune to thermal chirp effects due to the fact that the energy that is dissipated as heat in the laser, due to the electrical current, remains unchanged as the bias current remains unchanged. This fact has been exploited for all optical wavelength conversion [DUR1,MI1].

In the rate equations for photon number, Equation (25), and phase, Equation (27), for a laser with optical injection, the injected optical signal is represented by the injected photon number, S_l^{in}, while in experimental situations the known quantity is the incident optical power, P_l^{in}. The injected optical power will be used as the input parameter to the Runge Kutta simulation of lasers with optical injection, where the conversion between the optical power incident on the laser facet and the photon number incident on the laser facet is provided by

$$S_l^{in} = \frac{2P_l^{in}(t)}{\hbar\omega_l^{in} v_g \alpha_m}. \tag{47}$$

A theoretically necessary addition to this formula, which converts a rate of photon arrival to a quantity of photons, is the coupling coefficient, κ_c from Equation (43), which converts the electric field of number of photons outside the laser facet into an electric field for the number of photons that are coupled to the lasing mode within one round trip transit time of the laser cavity. Neither Equation (43) nor (47), taken in isolation, have physical meaning in terms of the optical injection but, together, they provide the correct conversion from external incident optical power to internal photon number.

The theoretical analysis, through the rate equations, will be used to gain insight into optical injection in two types of semiconductor lasers, Fabry-Perot (FP) lasers and Distributed Feedback (DFB) lasers. The analysis of DFB lasers will be presented first followed by the analysis of FP lasers.

2.8 Optical Injection in DFB Semiconductor Lasers.

An assumption for modelling DFB lasers will be that there is one dominant lasing mode with one or more sidemodes. In this model for optical injection in DFB semiconductor lasers two modes will be considered, the main mode of the laser, which would be the dominant mode in the absence of optical injection, and one sidemode of the laser. The main mode of the laser is allowed to oscillate without optical injection. The sidemode is under the influence of external optical injection from an external laser with an optical frequency detuning, d_I.

The gain of the main mode is the gain of the dominant mode with $g_{r1} = 1$, and the gain of the sidemode, g_{r2}, is calculated from Equation (46) for different values of sidemode suppression in the neighbourhood of 30 dB. The optical frequency of the injection into the sidemode of the laser is detuned in the manner discussed in Sections 2.2 and 2.3.2.

The injected optical signal is from another laser, the master laser, it is coherent and consists of a single optical frequency, and it may be modulated. The DFB laser, the slave laser, is isolated from the master laser with an optical isolator. The physical realization of this optical circuit is depicted in Figure 2.10. The slave laser is always DC biased above threshold. Simulation results will be presented and discussed for DC optical injection, in the next section, and for modulated injected power, in sections that will follow.

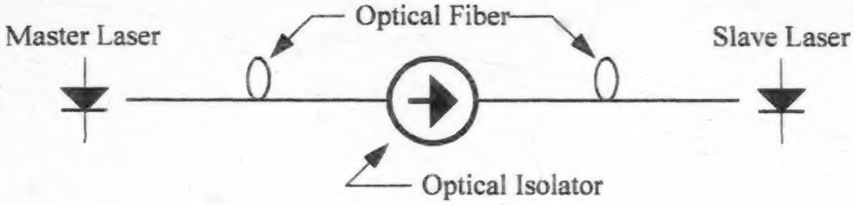

Figure 2.10: Schematic diagram of an optical injection system that uses a master/slave laser arrangement.

2.8.1 Continuous Wave Optical Injection in DFB Lasers.

As in the case of the solitary semiconductor laser, the simulation analysis will begin with steady state input; the injected optical signal is not modulated. The input parameters are the same as for the solitary laser with a gain compression coefficient of 6 W^{-1}. The optical detuning of the injected light from the free running laser mode frequency will be restricted to the range of +/- 25 GHz. Given that the simulated laser is 300 μm long and the group refractive index is 4.5, the mode spacing of the Fabry-Perot modes of the DFB laser is approximately 100 GHz. 25 GHz represents about 25% of the mode spacing which is within the range of validity for this type of calculation according to [HO1]. The incident optical power will be allowed to be any optical power less than 10 mW. The sidemode suppression will not be larger than 40 dB.

The dynamic optical behaviour of laser with external optical injection are quite different than electrically driven lasers. Optical injection can result in instability of the laser modes. The stability of semiconductor lasers with optical injection into the dominant mode of the laser is the subject of many papers [BORI1,GAL1,LI1,MOH1]. Modelling lasers with injection into sidemodes has been performed [GO2,JO1,LU1,MOH1,WH1], but with limited attention to the stability properties. The stability of semiconductor lasers with optical injection into sidemodes will be investigated in this section and throughout the remainder of this chapter. The types of instabilities seen in lasers with optical injection into their sidemodes are quite similar to the instabilities resulting from optical injection into the main mode, including oscillations of the output optical power and frequency or, in extreme cases, self pulsation of the slave laser. An example of oscillations induced by DC optical power injection is demonstrated by Figure 2.11, the optical power of the free-running (dominant) mode and the injected mode, and Figure 2.12, the optical frequency of the free-running mode only.

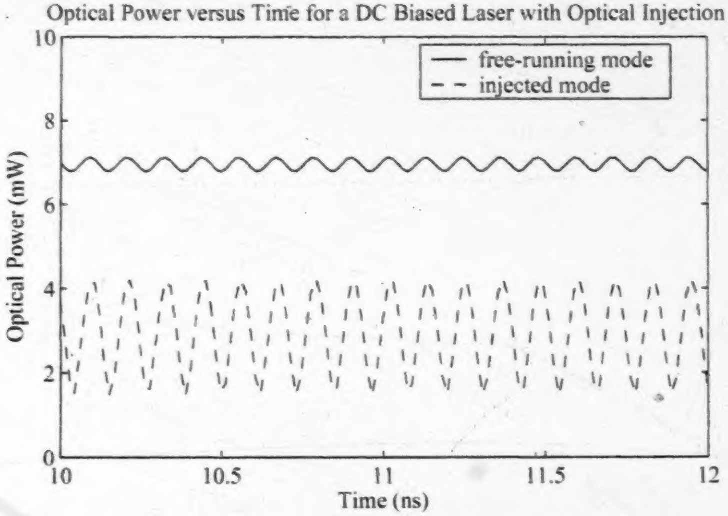

Figure 2.11: Instability (oscillation) of the optical power output from one facet for two modes of a DC biased DFB laser, biased at three times threshold, with DC optical injection as a function of time.

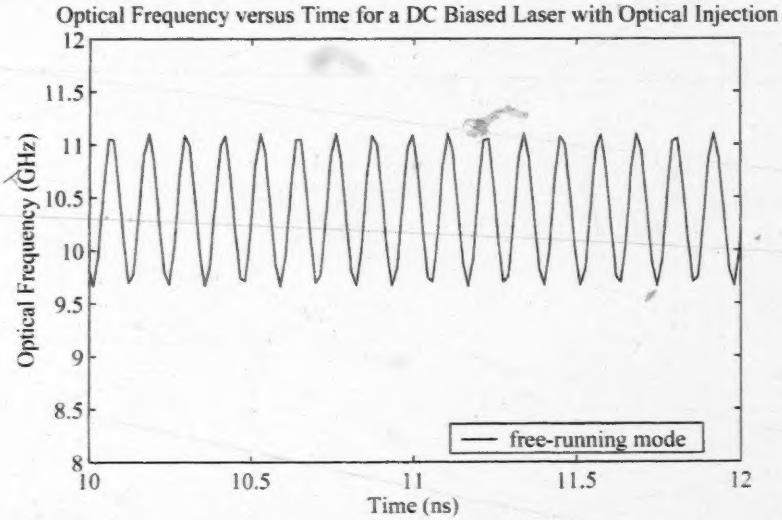

Figure 2.12: Instability (oscillation) of the optical frequency, offset from the threshold oscillation frequency, for the dominant mode of a DC biased DFB laser, biased at three times threshold, with DC optical injection as a function of time.

The simulation was for a laser biased at twice threshold, a gain compression of 6 W^{-1}, an injected optical frequency detuning of 5 GHz and a sidemode suppression of 30 dB and the incident injected optical power was 0.2 mW. The frequency of the oscillation is ~ 8.5 GHz.

Another example demonstrates self-pulsation induced by DC optical power injection (as in [WI1]) where the optical power of the free-running (dominant) mode and the injected mode are shown in Figure 2.13 and the optical frequency of the free-running mode only is shown in Figure 2.14.

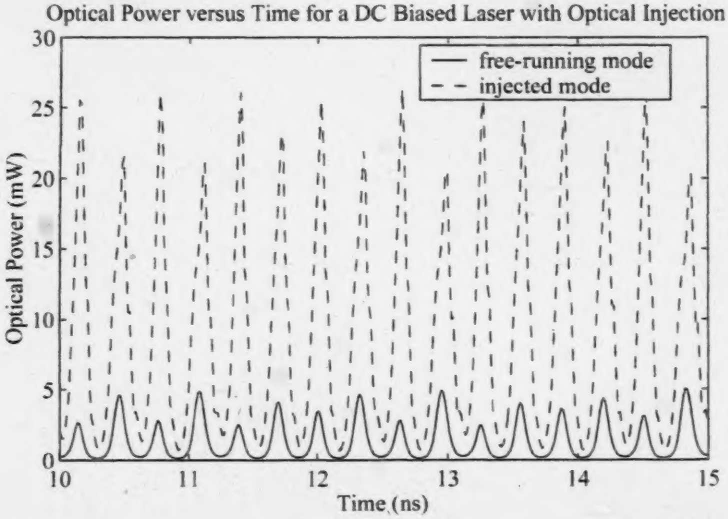

Figure 2.13: Self-pulsation of the optical power output from one facet for two modes of a DC biased DFB laser, biased at three times threshold, with DC optical injection as a function of time.

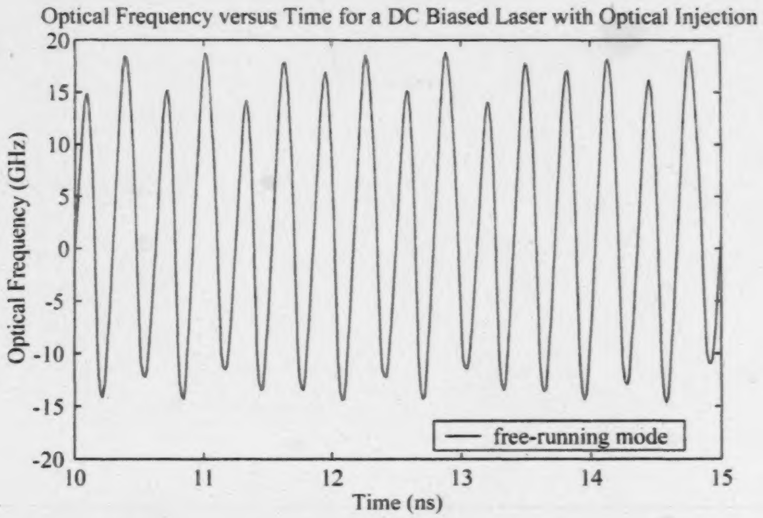

Figure 2.14: Optical frequency offset from the threshold oscillation frequency during self-pulsation for the dominant mode of a DC biased DFB laser, biased at three times threshold, with DC optical injection as a function of time.

The simulation was for a laser biased at twice threshold, a gain compression of 6 W^{-1}, an injected optical frequency detuning of -5 GHz and a sidemode suppression of 30 dB and the incident injected optical power was 0.5 mW. The self-pulsation is periodic with a repetition frequency of about 3 GHz.

Instabilities, like those presented in the previous two examples, are not conducive to generation of high-quality digital signals. The combination of input parameters that will produce a stable, high-quality output need to be found. For given values of sidemode suppression, gain compression and laser bias current, the root mean square deviation of the optical frequency of the free-running mode can be plotted as a function of injected optical power, with optical frequency detuning as a parameter, to find the ranges of parameters that result in stable operation of the laser. As with these calculations, all further calculations in this section will use a gain compression of 6 W^{-1}.

For a DFB slave laser that is biased at three times the threshold current, with a sidemode suppression of 30 dB, the root mean square deviation of the optical frequency of the free-running mode is plotted as a function of incident injected optical power of 0.1 mW, 0.2 mW, 0.5 mW, 1 mW, 2 mW and 3 mW, for negative frequency detunings, Figure

2.15. The output optical frequency is stable for low injection powers and optical detunings that are less than 0 where the RMS value of the optical frequency is zero.

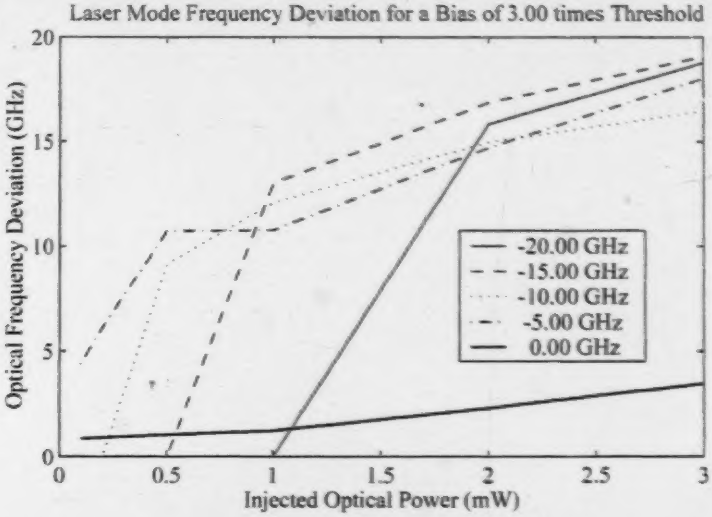

Figure 2.15: Root mean square deviation of the free-running optical frequency of a DFB laser as a function of incident injected optical power for a sidemode suppression of 30 dB and five values of injected frequency detuning.

For positive frequency detunings the stability is plotted for the same incident optical powers, Figure 2.16.

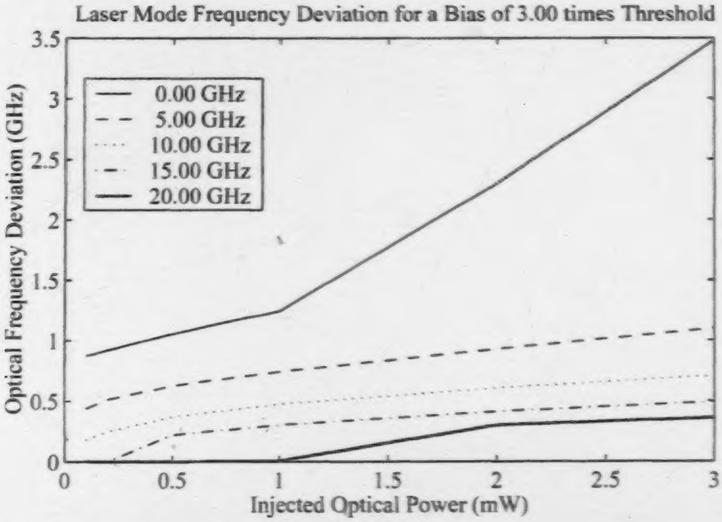

Figure 2.16: Root mean square deviation of the free-running optical frequency of a DFB laser as a function of incident injected optical power for a sidemode suppression of 30 dB and five values of injected frequency detuning.

The output optical frequency is stable for low injection powers and optical detunings that are larger than 10 GHz.

The root mean square deviation of the optical frequency of the free-running mode is plotted as a function of incident injected optical power with a sidemode suppression of 20 dB and biased at three times threshold, for negative frequency detunings, Figure 2.17.

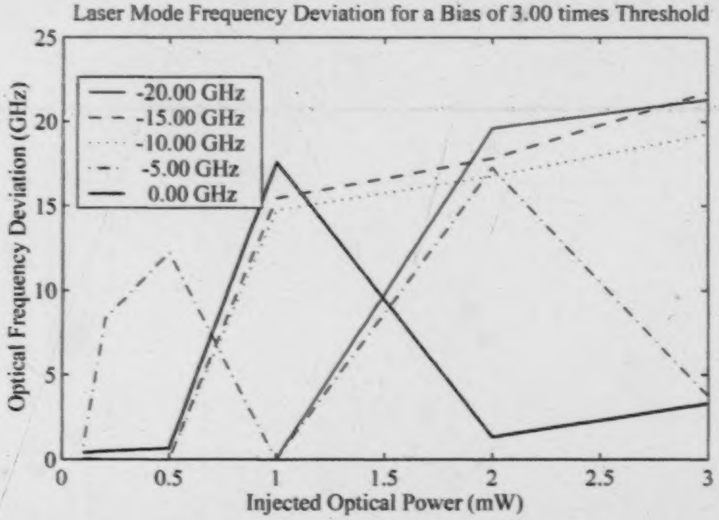

Figure 2.17: Root mean square deviation of the free-running optical frequency of a DFB laser as a function of incident injected optical power for a sidemode suppression of 20 dB and five values of injected frequency detuning.

The output optical frequency is stable for low injection powers and optical detunings that are less than -5 GHz. For positive frequency detunings the frequency deviation is plotted in Figure 2.16.

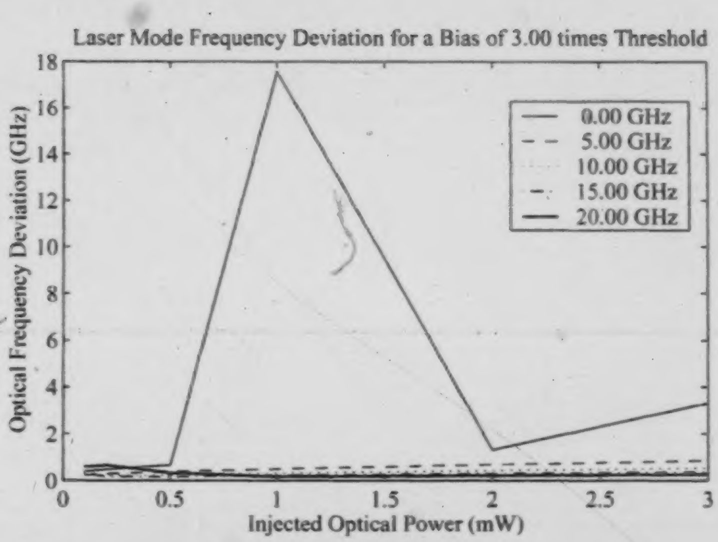

Figure 2.18: Root mean square deviation of the free-running optical frequency of a DFB laser as a function of incident injected optical power for a sidemode suppression of 20 dB and five values of injected frequency detuning.

The output optical frequency is unstable optical detunings that are positive when the sidemode suppression is 20 dB.

In the section on modulation by optical injection, Section 2.8.2, it will be demonstrated that the magnitude and frequency of the relaxation oscillations depends strongly on the sidemode suppression. The amplitude of the relaxation oscillations due to modulation by optical injection is smaller for larger values of the sidemode suppression. For this reason the remainder of this section will show results for 30 dB sidemode suppression.

To illustrate the degree of stability for injection at negative detunings and a sidemode suppression of 30 dB, Figures 2.19 and 2.20 show the Runge Kutta simulation results for output optical power (for both modes) and the optical frequency for the free-running mode for a detuning of -20 GHz and an incident injected optical power of 1 mW. The output optical power and frequency of the free-running mode are constant functions of time for this injected optical power.

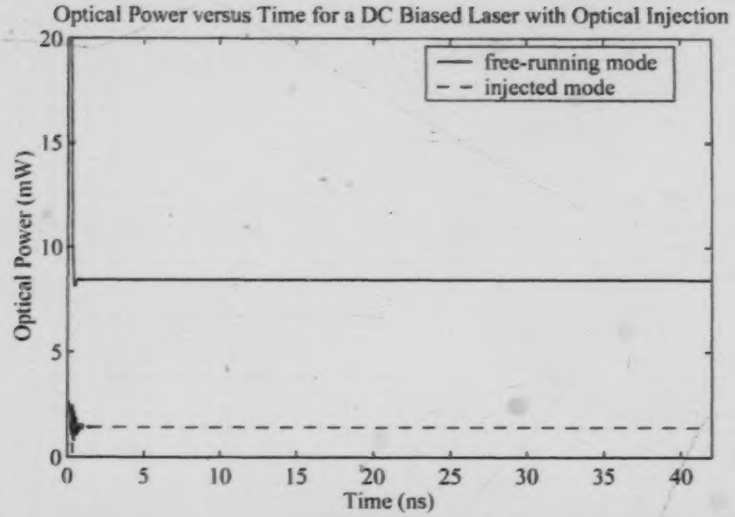

Figure 2.19: Optical power output from one facet of a DC biased laser, biased at three times threshold, with 1 mW incident optical injection power and a detuning of -20 GHz as a function of time.

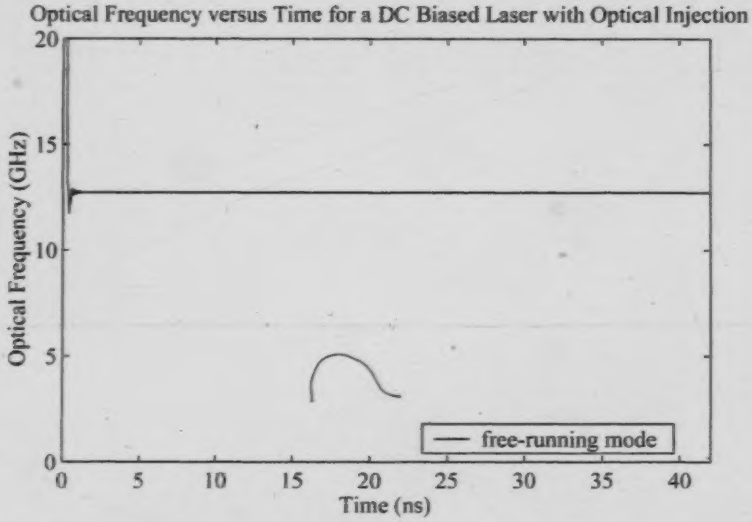

Figure 2.20: Output optical frequency offset for the free-running mode of a DC biased laser, biased at three times threshold, with 1 mW incident optical injection power and a detuning of -20 GHz as a function of time.

The available frequency modulation depth (of the free-running mode) is large for negative frequency detunings for the 30 dB sidemode suppression. For a selection of optical frequency detunings from -25 to -15 GHz, the optical power (time averaged over 10 ns) of the free-running mode of the slave laser is plotted as a function of the incident injected optical power, with frequency detuning as a parameter, Figure 2.21.

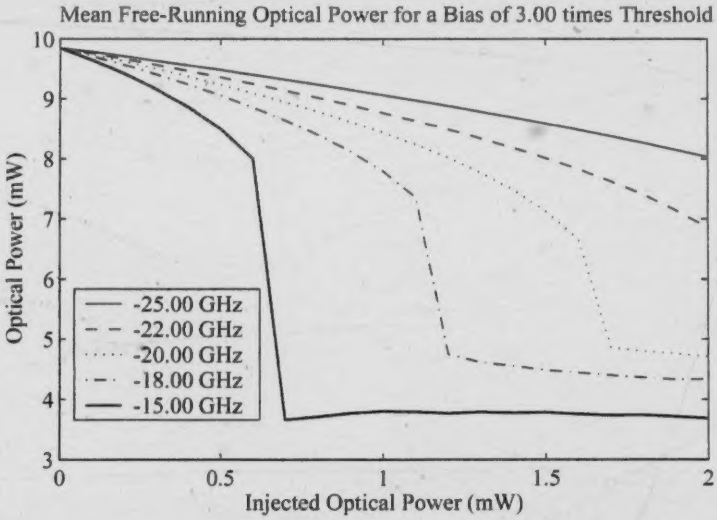

Figure 2.21: The time averaged optical power of the free-running mode of the semiconductor laser plotted as a function of incident injected optical power with a sidemode suppression of 30 dB and biased at three times threshold. Various optical frequency detunings are shown. The horizontal sections for detunings of -15, -18 and -20 GHz detunings are for unstable operation.

The optical power of the free-running mode decreases monotonically as a function of injected optical power until the laser becomes unstable, then the time average of the optical power remains near the same value for increased injected powers. As the detuning is decreased from -15 to -25 GHz, the injected optical power required to destabilize the laser increases.

For the same conditions, the optical frequency offset of the free-running mode is plotted as a function of the incident injected optical power, with frequency detuning as a parameter, Figure 2.22.

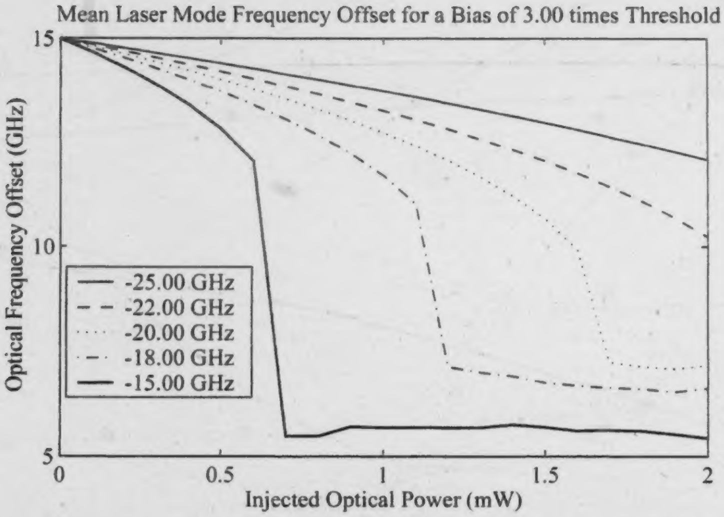

Figure 2.22: The time averaged optical frequency offset from threshold of the free-running mode of the semiconductor laser plotted as a function of incident injected optical power with a sidemode suppression of 30 dB and biased at three times threshold. Various optical frequency detunings are shown. The horizontal sections for detunings of -15, -18 and -20 GHz detunings are for unstable operation.

The profiles of these curves are very similar in shape to the optical power curves, Figure 2.21, and the frequency offset also decreases as a function of the injected optical power where the higher detunings require higher injected power to reach the same induced frequency change.

Also of note is the fact that the range of the output optical power and frequency offset is dependent on the detuning as functions of injected optical power.

All of these calculations were performed at bias currents that are three times the threshold value, this was done because there is a dependence on of the available frequency modulation depth on the bias current and three times threshold is near the maximum available depth for the simulation parameters that were used. Also, an excessively high bias current is unphysical since semiconductor lasers can "burn out" when the current is increased too much. For currents that do not result in immediate failure of the laser, the laser lifetime is a decreasing function of bias current, therefore the laser cannot be biased at too high of a current if a long lifetime is desired. A bias of four times threshold will be used as an upper limit in this analysis; this will be adequate to demonstrate the operational characteristics of lasers with optical injection without dealing with laser lifetime any further.

The optical power and optical frequency changes for the free-running mode are monotonically decreasing functions of injected power when the laser is operating in the stable region of injection operation. The injected optical powers of 0 and the maximum injected optical power for stable operation define the limits of optical power modulation and optical frequency modulation for lasers with optical injection. The maximum optical power and optical frequency ranges for the free-running mode can be found by comparing simulations without injection to simulations with the maximum injected optical power. For the same laser parameters and with a sidemode suppression of 30 dB and a gain compression of 6 W^{-1}, the DC output optical power of the free-running mode from one facet of the laser is plotted as a function of the bias current, normalized to the threshold current, for detunings of -15, -20 and -25 GHz at the maximum injected optical power and without injection, see Figure 2.23.

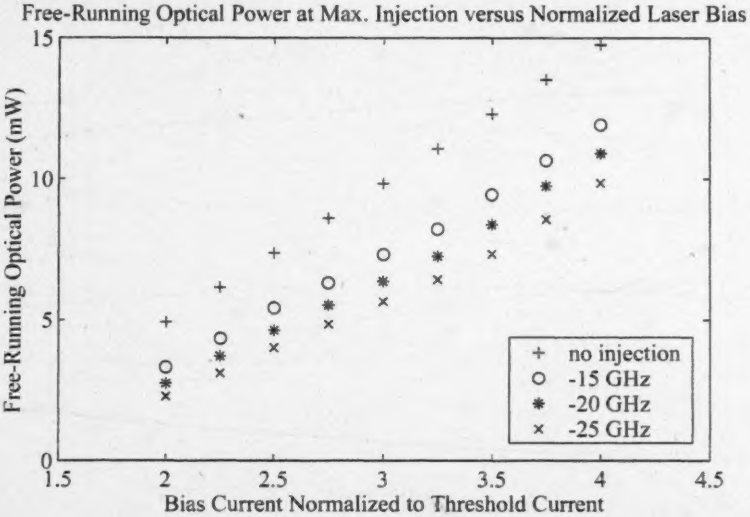

Figure 2.23: The output optical power of the free-running mode from one facet of the laser with the maximum amount of incident injection power for laser bias currents between two and four times threshold with injection detuning as a parameter. The output power of this mode without injection is included to demonstrate the effect of the injection.

The change in optical power is larger for frequency detunings further from 0 and larger for higher bias currents. The difference in optical power between the case without injection and the case of maximum injected optical power does not increase indefinitely as the bias current is increased as can be seen in Figure 2.24 where this differential optical power for the free-running mode is plotted.

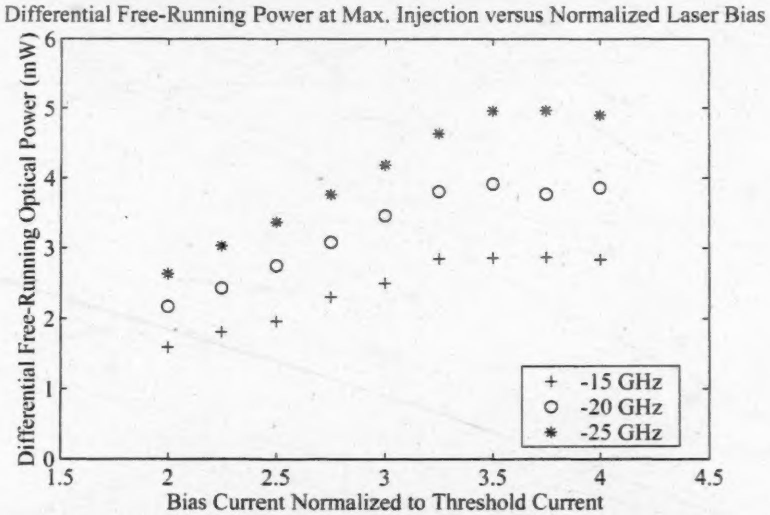

Figure 2.24: The optical powers from Figure 2.23 are replotted as the difference between the free-running optical power without injection minus the free-running optical power at maximum injection for the same frequency detunings and normalized laser biases.

The differential output optical power over the range of stable optical injection reaches a maximum as the bias current is increased for all of the optical detunings shown in Figure 2.24. The maximum is reached at a lower bias current for detunings that are closer to the free-running mode frequency.

The optical frequency shift that occurs for the free-running mode due to optical injection is influenced in a similar manner to the output optical power; the maximum difference in optical frequency from the free-running optical frequency increases as the bias current is increased until it reaches a maximum. This difference in optical frequency for the two extremes of injected optical power will be referred to as the maximum (available) frequency modulation depth and is plotted as a function of normalized bias current in Figure 2.25.

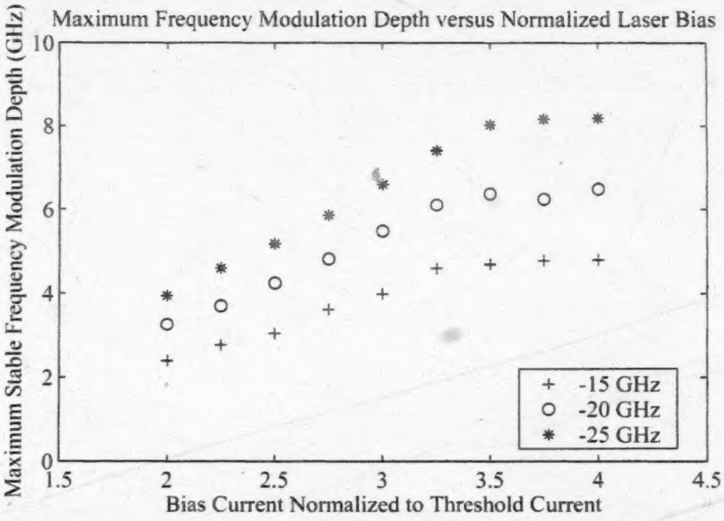

Figure 2.25: The maximum frequency modulation depth of the free-running mode of the laser for laser bias currents between two and four times threshold. The injection frequency detuning is a parameter.

As with the free-running mode output optical power, the output optical frequency difference is enhanced by injecting at detunings further from the free-running mode oscillation frequency.

The total output power of the laser, from both the injected mode and the free-running mode, is approximately constant independent of the amount of light injected into the laser, Figure 2.26.

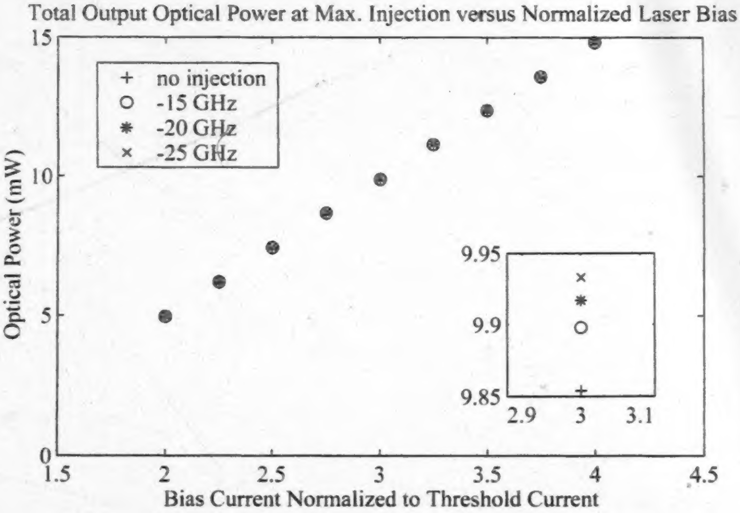

Figure 2.26: The total output optical power (free-running and injected modes) from one facet of the laser with the maximum amount of incident injection power for laser bias currents between two and four times threshold with injection detuning as a parameter. The output power of the free-running mode without injection is included to demonstrate the effect of the injection.

When the bias current is held constant and the total output power of the laser remains constant, the temperature of the laser does not change. The result is that bit pattern dependent frequency modulation effects, compared to the case of the electrically driven semiconductor laser, are substantially reduced. Experimental evidence of this will be provided in Chapter 3.

The maximum incident injected optical power while maintaining laser stability for the same set of laser bias currents is shown in Figure 2.27. The injected optical power required to reach the maximum change in the free-running mode frequency does not change much with the laser bias current but the stable operation frequency range (modulation depth) does increase with bias current.

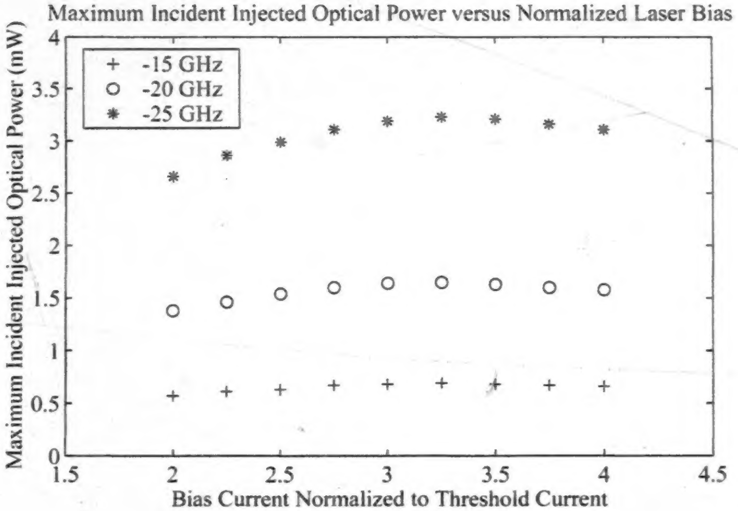

Figure 2.27: The maximum incident injected optical power at the facet of the laser for bias currents between two and four times threshold with injection detuning as a parameter.

Using the results from this section, particularly the stable operating range and the maximum incident injected optical power, the transient effects of injecting intensity shift keyed signals into a DFB laser near a sidemode can be investigated.

2.8.2 Modulation of DFB Lasers by Optical Injection.

The dynamic response of the DFB laser to the injection of a binary ISK modulated signal will be demonstrated in this section. The results shown here and in Section 2.5.2 can be used for the comparison of the modulation of DFB lasers by optical injection to current injection modulation and a more complete comparison will be provided near the end of this chapter.

A schematic diagram of the physical situation these calculations are intended to simulate is shown in Figure 2.28.

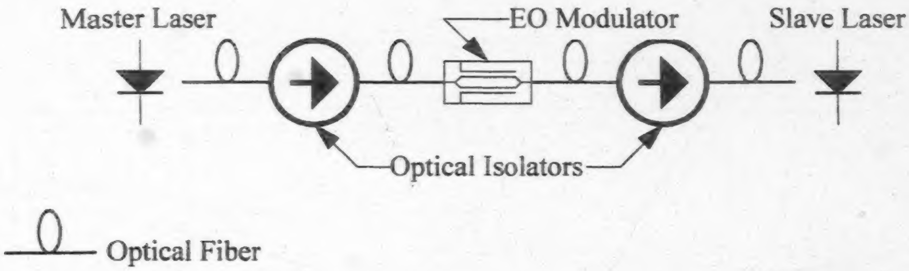

Figure 2.28: Schematic diagram of an optical injection system that uses a master/slave laser arrangement that uses an electro-optic modulator to modulate the injected signal.

The light from the master laser is modulated with an electro-optic (EO) Mach-Zehnder (MZ) modulator and injected into the slave laser. The isolators are necessary to eliminate unwanted back reflections into the lasers and coupling from the slave laser to the master laser.

For a straightforward comparison of electrical current modulation and optical modulation of the slave laser diode the same pulse shape is used for the optical modulation as was used for current modulation, see Equation (45),

$$P_l^{in}(t) = \begin{cases} \bar{P}_l^{in} - m_i\bar{P}_l^{in} + \dfrac{2b_{k-1}m_i}{M-1}\bar{P}_l^{in} + \\ \qquad \dfrac{2(b_k - b_{k-1})m_i}{M-1}\bar{P}_l^{in} sin^2\left(\dfrac{\pi(t-(k-1)T)}{2t_r}\right) & \\ \qquad\qquad (k-1)T \le t < (k-1)T + t_r \\ \bar{P}_l^{in} - m_i\bar{P}_l^{in} + \dfrac{2b_k m_i}{M-1}\bar{P}_l^{in} & (k-1)T + t_r \le t < kT \end{cases}, \quad (48)$$

where $\bar{P}_l^{in}$ is the mean optical power and all of the other parameters are the same as their previous definitions except the modulation index. The modulation index is defined in terms of the injected optical power such that largest deviation from the average of the maximum and minimum power symbols is the modulation index multiplied by this average, $m_i\bar{P}_l^{in}$. The optical frequency, and therefore the phase, of the injected optical signal is assumed to be constant for these calculations, which is not accurate in general. A dual drive MZ modulator can be biased in such a way as to create a signal that is chirp free everywhere except at bit transitions.

A binary signal is represented by setting $M = 2$ in Equation (48). The results from a Runge Kutta simulation, output optical power and frequency offset, for a laser with a gain compression of 6 W^{-1} biased at three times threshold, a sidemode suppression of 30 dB, an optical detuning of -20 GHz, a mean incident injected optical power of 0.75 mW, with a modulation index of 95%, a bit period of 1 ns (1 Gbps), and a bit rise time of 0.1 ns, are presented in Figures 2.29 and 2.30, respectively. The response of the DFB laser to the input optical injection has different features than the current modulation examples presented earlier, Figures 2.6 and 2.7. The effects of relaxation oscillations are reduced and there is a new type of feature for high output power in the free-running mode, the optical power increases quickly part of the way to the steady state high power value and follows an approximately exponential rise from there. The optical frequency of the free-running mode also has this type of slow relaxation to steady state at high values of frequency offset. This behaviour can be compared to the published results of [HU1].

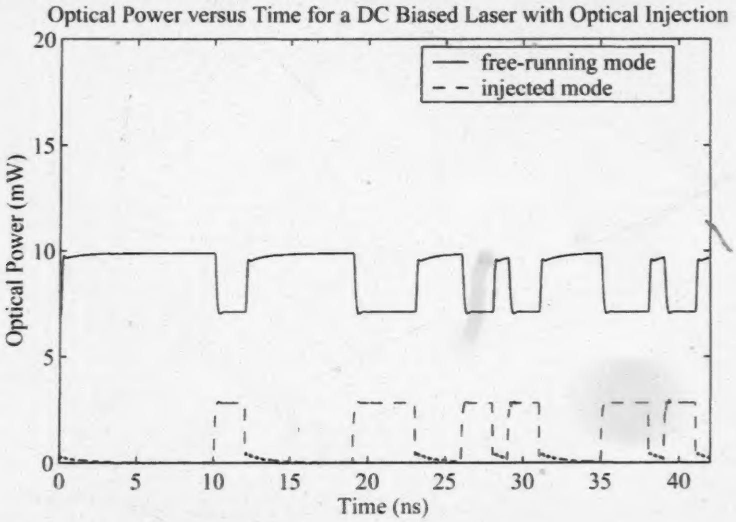

Figure 2.29: An example calculation result of the output optical power for a binary signal by optical injection modulating a DFB laser.

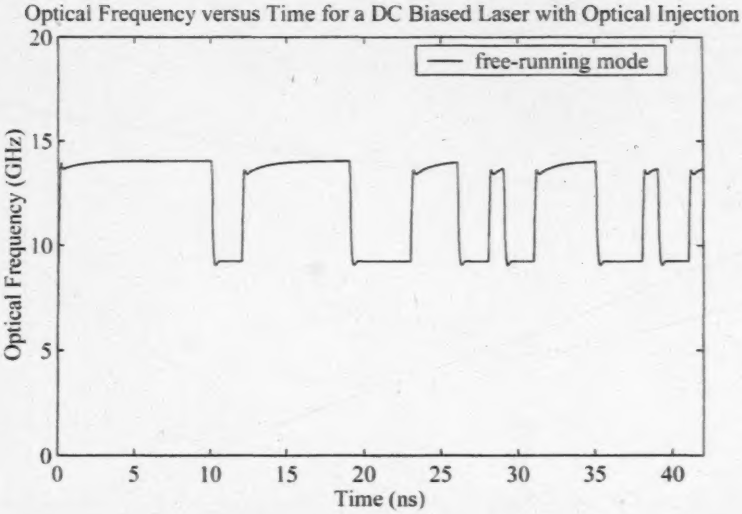

Figure 2.30: An example calculation result of the output optical frequency offset from the threshold frequency for the free-running mode of a DFB laser for a binary signal by optical injection modulation.

The DFB laser with optical injection in a sidemode can be used as a means to produce FSK signals with frequency modulation depths of up to 8 GHz for binary signals. The preceding analysis will be repeated for Fabry-Perot (FP) lasers in the following sections to determine the range of use of this type of laser. The DFB and FP lasers will be compared in terms of available frequency modulation depth and other performance impacting parameters to determine which type of laser would be more suitable for FCM signal generation.

2.9 Optical Injection in FP Semiconductor Lasers.

Fabry-Perot (FP) lasers are inherently multimode lasers because they lack an extra mode selectivity influence like the Bragg grating in DFB lasers. In order to produce an FCM signal with an FP laser, the laser must operate with a single, dominant, free-running mode, in addition to the sidemode that is used for optical injection. One mode can be forced to dominate the output spectrum of a multi-mode FP laser by injecting additional spontaneous emission into the laser in the spectral vicinity of the desired dominant mode.

This method of forced modal domination in FP lasers has been proposed and experimentally verified for low cost Passive Optical Network (PON) applications to provide low cost direct modulation transmitters [KIMY1]. A schematic representation of the optical circuit proposed for use here is presented in Figure 2.31.

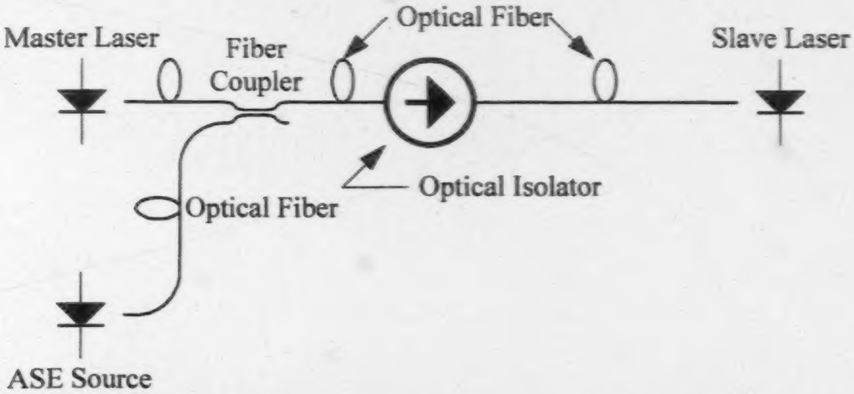

Figure 2.31: Schematic diagram of an optical injection system that uses a master/slave laser arrangement with additional Amplified Spontaneous Emission (ASE) injection.

The reasoning behind using the Amplified Spontaneous Emission (ASE) injection in this application is not only to provide suppression of unwanted sidemodes in the output signal spectrum, but also to reduce mode partition noise effects in the output signal. The suppression of mode partition noise via optical injection has been studied extensively [CARE2,HE2,IW1,PETE2] and will not be discussed here. The downside of injecting spontaneous emission into a laser is an increase in linewidth of the forced dominant lasing mode. The dynamic linewidth will be calculated in Section 2.10 and the effects of linewidth on FCMA system operation will be discussed in Chapters 4 and 6.

The FP laser static and dynamic behaviour will be analyzed with the same equations that were used to model DFB lasers. The differences are that the natural sidemode suppression ratios used to simulate the FP laser will be much lower and additional noise must be added to the dominant FP mode. The sidemode suppression ratio is easily changed by modifying the input parameters, whereas increasing the amount of spontaneous emission for one mode can be accomplished by increasing n_{sp} for that mode. Increasing n_{sp} for the dominant mode is unphysical in general, but in the case of simulating the behaviour of the laser with the equations contained in this chapter it will work because the rate of spontaneous emission for the *l*th mode, $R_{s,l}$, is the only parameter that is calculated from the spontaneous inversion factor.

2.9.1 Incoherent Optical Injection in FP Lasers.

As a precursor to studying the effects of simultaneous coherent and incoherent injection in FP lasers, the effect of only incoherent injection will be described. Incoherent optical injection into the dominant mode of the FP laser will increase the sidemode suppression ratio of the laser. In the results presented in this section the simulation parameters that were used to model the DFB laser will be carried over for direct comparison; the linewidth enhancement factor will be chosen to be 6, the gain compression will be set to 6 W^{-1}, and the laser will be biased at three times the threshold current. The important results of constant incoherent optical power injection into the main laser mode are the modifications to the sidemode suppression ratio of the main lasing mode to the nearest sidemode. For original sidemode suppression ratios of 3, 6, 10 and 15 dB, the modified sidemode suppression ratios for increasing the spontaneous emission spectral density by factors of 10, 100 and 1000 (the Relative Spontaneous Emission Spectral Density or RSESD) are presented in Figure 2.32.

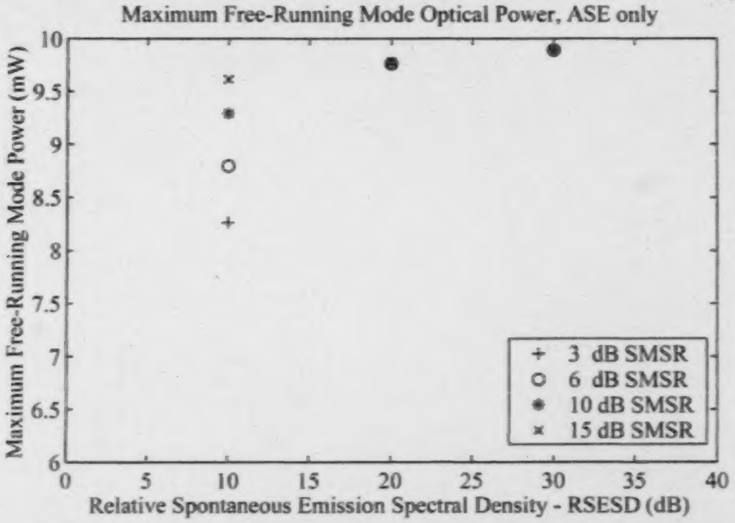

Figure 2.32: The sidemode suppression ratio with spontaneous emission injection is plotted against the original sidemode suppression ratio of the laser with the Relative Spontaneous Emission Spectral Density (RSESD) as a parameter.

The sidemode suppression ratio is dominated by the original sidemode suppression ratio when the spontaneous emission spectral density is increased by a factor less than the original sidemode suppression ratio; i.e., the case of 15 dB sidemode suppression ratio when the spontaneous emission spectral density is increased by 10 dB. The spontaneous emission spectral density dominates the sidemode suppression ratio when the spontaneous emission spectral density is increased beyond the original sidemode suppression ratio; i.e., the instances when the spontaneous emission spectral density is increased by greater than 10 dB.

The sidemode suppression ratios that are achieved by injection of spontaneous emission injection into FP lasers affect the conversion efficiency of the coherent sidemode optical injection that is proposed for generation of FCM signals.

2.9.2 Simultaneous Coherent and Incoherent Optical Injection in FP Lasers.

Injection of incoherent light into the main mode of an FP laser increases the sidemode suppression ratio which enables the use of coherent light injection into a neighbouring sidemode to produce transmission signals for optical FCM based communication systems. An examination of the range of injected signal power and injected optical detuning for different values of original sidemode suppression ratio and increased spontaneous emission spectral density will provide insight into the value of this signal generation approach.

The behaviour of FP lasers subjected to optical injection is very similar to the behaviour discussed previously for DFB lasers. When the injected optical power in the sidemode is relatively small, the laser is stable; i.e., the optical powers and frequencies of the free-running and injected modes reach steady state values and remain constant. When the injected optical power is increased beyond a certain point, the output powers and frequencies of the modes begin to oscillate or the laser operates in a pulsation mode. These behaviours define the usable limit of optical injection.

Similar results were obtained for FP lasers as were obtained with DFB lasers with respect to the large injected optical frequency detuning required to produce large shifts in the free-running mode optical frequency. The analysis was restricted to optical detunings of -15, -20 and -25 GHz detuning from the free-running mode frequency for the sidemode. In addition, only two modes were considered in the model, the forced dominant free-running mode and the sidemode that is used for optical injection, because the optical injection levels were chosen to be high enough to limit the effects of the other free-running modes of the FP laser. The original sidemode suppression ratios that were used for calculations were 3, 6, 10 and 15 dB and the spontaneous emission injection rate increased the spontaneous emission spectral density by factors of 10, 20 and 30 dB. The benchmark cases used for the analysis are calculations with only incoherent injection into the main mode and the maximum coherent injection into the sidemode, before instability occurs, were used to determine the maximum available frequency modulation depth as previously described for DFB lasers.

The maximum available frequency modulation depth of the free-running mode of the laser is plotted as a function of original sidemode suppression ratio where the relative spontaneous emission spectral density (RSESD) equal to 10, Figure 2.33.

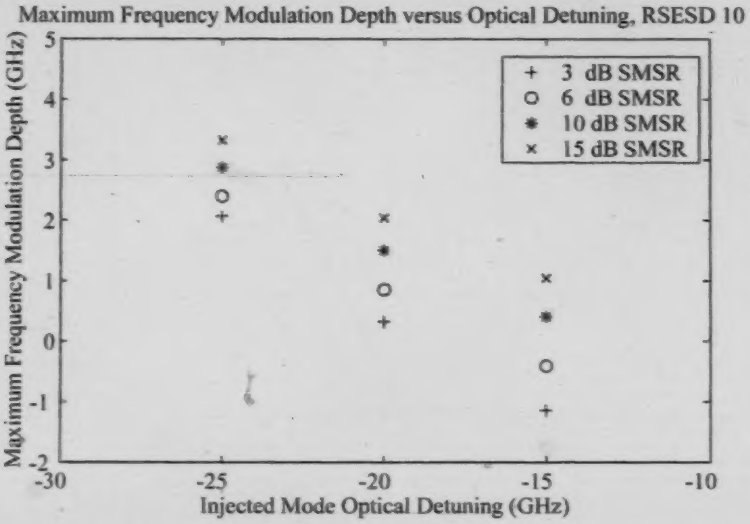

Figure 2.33: Maximum frequency modulation depth of a Fabry-Perot laser with RSESD = 10 for the main mode and coherent optical injection into a sidemode with the original sidemode suppression ratio as a parameter.

The maximum available frequency modulation depth increases as the injected light is detuned further from the natural resonance frequency of the slave laser sidemode and also increases as the original sidemode suppression ratio is increased. A curious result for low original sidemode suppression (3 and 6 dB) and the detuning of -15 GHz is that the polarity of the frequency shift induced by the optical injection is different than all of the other results that have been previously presented, the optical frequency of the free-running mode increases instead of decreasing.

When the RSESD is increased to 100 or 1000, the polarity of the free-running mode frequency shift is always the same polarity and is maximum for large injection frequency detunings and original sidemode suppression ratio, Figures 2.34 and 2.35. The overall maximum frequency shift available for the FP type laser was found to be just under 5 GHz when RSESD = 1000 and the optical injection detuning is -25 GHz and the original SMSR is 15 dB.

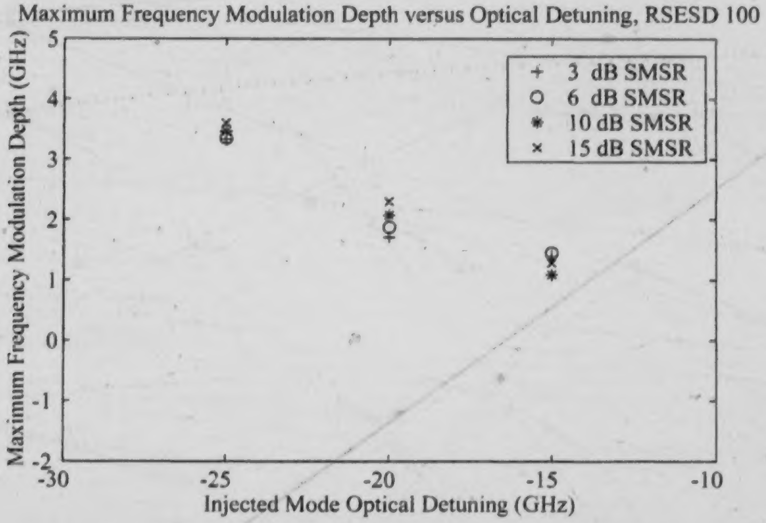

Figure 2.34: Maximum frequency modulation depth of a Fabry-Perot laser with RSESD = 100 for the main mode and coherent optical injection into a sidemode with the original sidemode suppression ratio as a parameter.

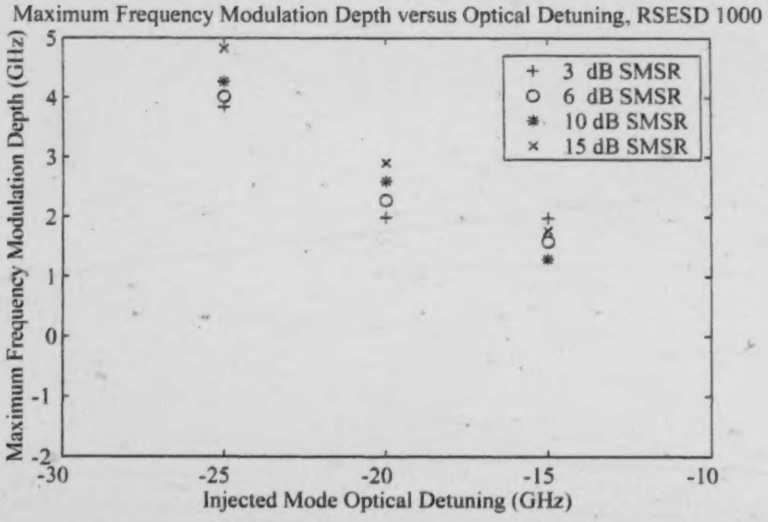

Figure 2.35: Maximum frequency modulation depth of a Fabry-Perot laser with RSESD = 1000 for the main mode and coherent optical injection into a sidemode with the original sidemode suppression ratio as a parameter.

The change in optical power of the free-running mode in the slave FP laser for the RSESD values simulated are shown in the following graphs, Figures 2.36, 2.37 and 2.38.

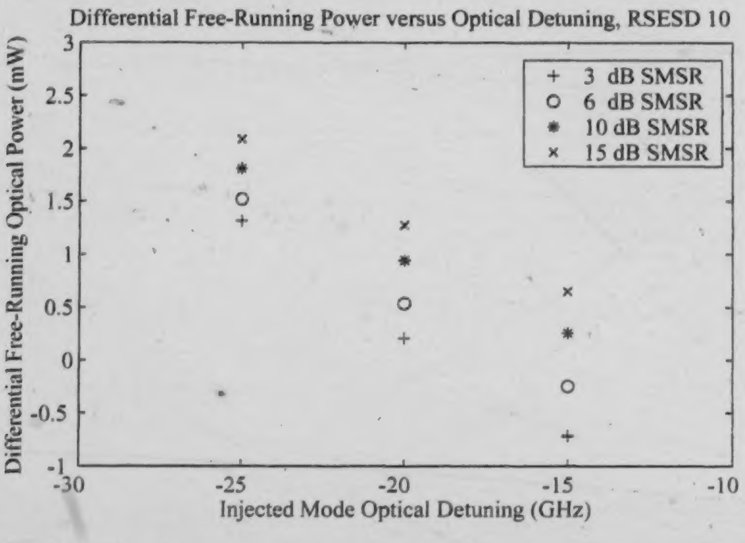

Figure 2.36: Maximum change of free-running mode optical power due to coherent side-mode injection with different amounts of spontaneous emission injection into the main mode. RSESD (= 10) refers to the relative spontaneous emission spectral density.

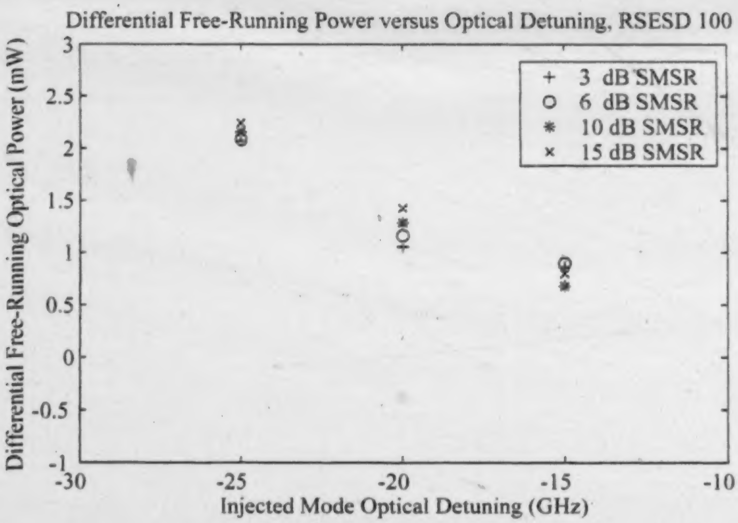

Figure 2.37: Maximum change of free-running mode optical power due to coherent side-mode injection with different amounts of spontaneous emission injection into the main mode. RSESD (= 100) refers to the relative spontaneous emission spectral density.

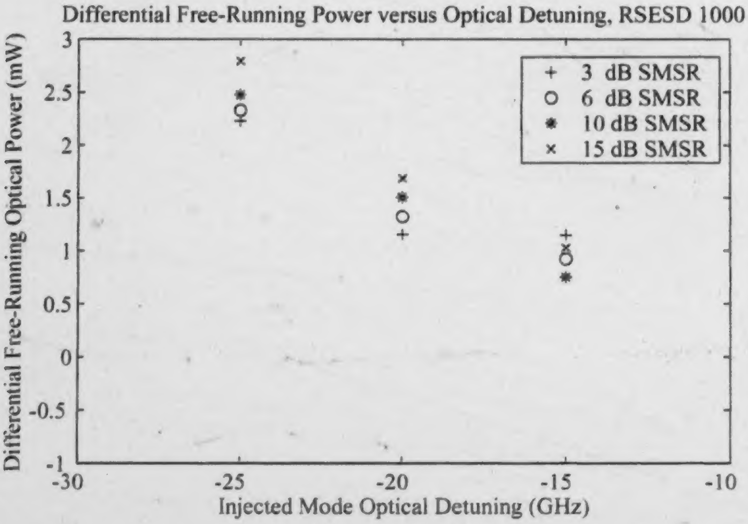

Figure 2.38: Maximum change of free-running mode optical power due to coherent side-mode injection with different amounts of spontaneous emission injection into the main mode. RSESD (= 1000) refers to the relative spontaneous emission spectral density.

These changes represent the decrease in the output power in the free-running mode of the slave FP laser when the maximum amount of injected optical power is incident on the facet of the laser. The output power of the free running mode in these cases is not shown, but can be estimated by subtracting these changes from the results presented in Figure 2.32 for the output optical power in the free-running mode in the absence of optical injection into the sidemode.

The results presented in this section dealt with the application of DC coherent injection into the sidemode, the next section investigates the effects of modulated light being injected into the slave FP laser.

2.9.3 Modulation of FP Lasers by Optical Injection.

Simulation of the dynamic behaviour of FP lasers when the input is a binary bit sequence of injected optical power is performed by the same method as was used for the DFB laser as described in Section 2.8.2. The schematic diagram is similar to the DFB injection diagram, Figure 2.28, with the exception that spontaneous emission must be coupled to the slave laser, Figure 2.39.

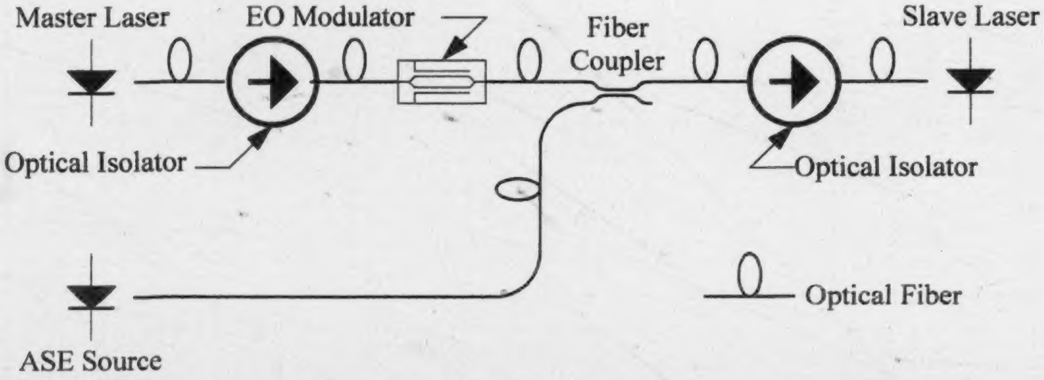

Figure 2.39: Schematic diagram of an optical injection system that uses a master/slave laser arrangement that uses an electro-optic modulator to modulate the injected signal, including an ASE source to select and stabilize the dominant mode of the slave laser.

The optical pulse waveform shape for the injected light from the master laser is provided by Equation (48), which is the same waveform that was used to simulate the dynamics for the DFB laser.

All of the results for the calculations for FP lasers will be for the maximum available frequency modulation depth as investigated in the previous section. The relevant modulation depth that was used, m_i in Equation (48), is 0.99 (or 99% modulation) with a mean injection power of 1.09 mW.

The modulation of the free-running mode optical frequency, as can be seen in Figure 2.40, is has very similar features compared to the simulation results of the DFB laser, see Figure 2.30.

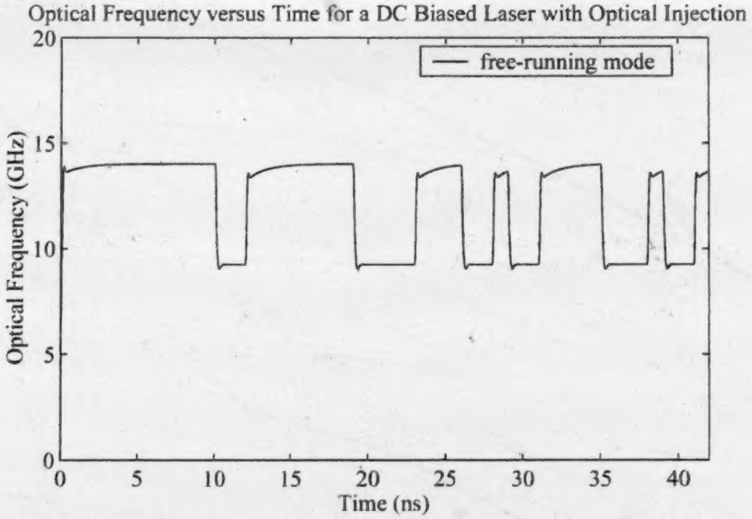

Figure 2.40: An example calculation result of the output optical frequency offset from the threshold frequency for the free-running mode of a FP laser for a binary signal by optical injection modulation with RSESD = 1000.

. Simulated results for the FP laser output optical power in both the free-running mode and the sidemode with injection are depicted in Figure 2.41 for binary modulated optical injection. The output optical powers for the modes of the FP laser have similar feature when compared to the DFB results in Figure 2.29.

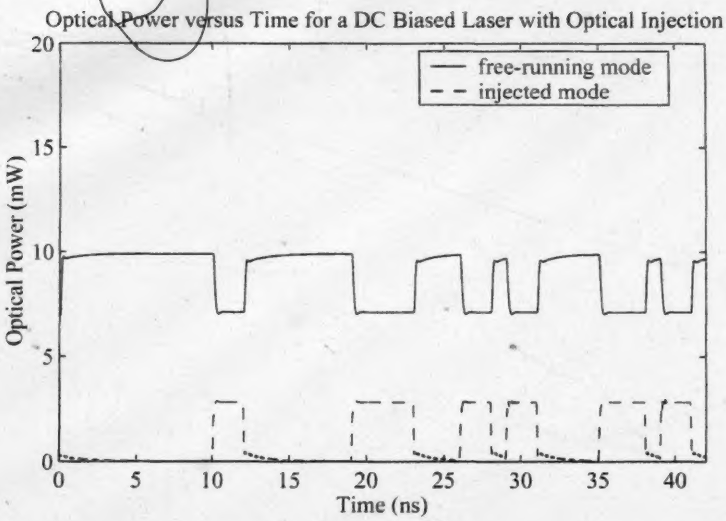

Figure 2.41: An example calculation result of the output optical power for a binary signal by optical injection modulating a FP laser with RSESD = 1000.

The maximum available frequency shift for the FP laser simulated here was found to be less than 5 GHz. No attempt was made to find the optimum bias current for the FP laser, as was done for the DFB laser, for reasons that will be explained in the following section that compares the performance of DFB and FP lasers with optical injection.

2.10 Comparison of DFB to FP Lasers with Optical Injection.

Comparing the DFB and FP lasers with optical injection as FCM signal sources will be made qualitatively with regard to three performance related factors; available frequency modulation depth, waveform quality and linewidth.

From the simulation result obtained at 3 times the bias current, the DFB laser has the advantage of a slightly larger available frequency modulation depth, attributed to the inherently larger sidemode suppression ratio for this type of laser.

With regard to the output waveform in terms of response time and waveform distortion due to the modulation method, both relaxation oscillations and phase relaxation at low injection power, are similar for both types of lasers. This factor does not preferentially indicate one type of laser.

The performance consideration that has not been given attention yet is the linewidth of the free-running mode of the lasers. The DFB lasers will retain a low linewidth when modulated by optical injection, but the FP laser linewidth is expected to broaden due to the additional spontaneous emission that has been added to the lasing cavity in order to select the output lasing mode.

The full width at half maximum (FWHM) spectral width of a lasing mode, $\Delta\nu_{FWHM,l}$, in a semiconductor laser is given by the following equation [OSINSKI],

$$\Delta\nu_{FWHM,l} = \frac{h\nu_l v_g \alpha_m g_{th} n_{sp}}{8\pi P_l^{out}}(1+\alpha^2). \tag{49}$$

In the reference, this equation has $\Delta\nu_{FWHM,l}$ proportional to the square of the group velocity. Again, this is due to the choice of whether or not the gain is normalized to the group velocity.

Using Equations (34), (38) and (41), the FWHM laser mode linewidth reduces to

$$\Delta\nu_{FWHM,l} = \frac{R_s}{4\pi S_l}(1+\alpha^2), \tag{50}$$

which is a common expression as can be found in [AG2,HE3,KAZ1,OS1], sometimes modified for the effects of external cavities. The formula holds for FP and DFB lasers as discussed in [OS1]. In the case of spontaneous emission injection into the FP laser free-running mode, R_s is replaced with the product of the natural spontaneous emission rate and the relative spontaneous emission spectral density (RSESD) factor R_R,

$$\Delta\nu_{FWHM,l} = \frac{R_R R_s}{4\pi S_l}(1+\alpha^2). \tag{51}$$

The linewidth will increase linearly proportional to the relative spontaneous emission spectral density. For the sample calculation presented in Section 2.9.3 for the FP laser, the instantaneous value of the linewidth is plotted as a function of time using Equation (51), Figure 2.42.

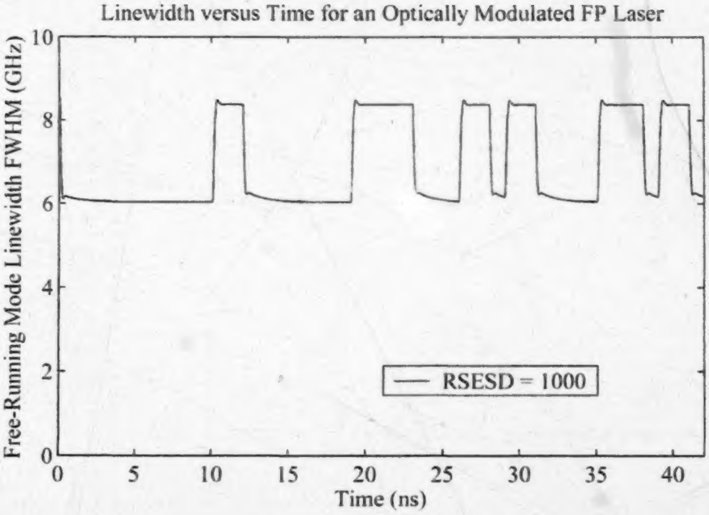

Figure 2.42: The linewidth of a FP laser with binary modulated optical injection in a sidemode and RSESD = 1000 for the free-running mode as a function of time.

The linewidth of the FP laser mode with external injection of spontaneous emission is varies from ~6 GHz to ~8.5 GHz for the above example. The linewidth of this signal is larger than separation of the logic levels, ~5 GHz, and will render the PF laser modulation method useless for high levels of spontaneous emission injection. Since the efficiency of the modulation depth is related to the level of spontaneous emission injection, the FP laser is a poor candidate for FCM signal generation.

When the same calculation is performed for the optical injection modulated DFB laser the linewidth is not increased like the FP laser, Figure 2.43.

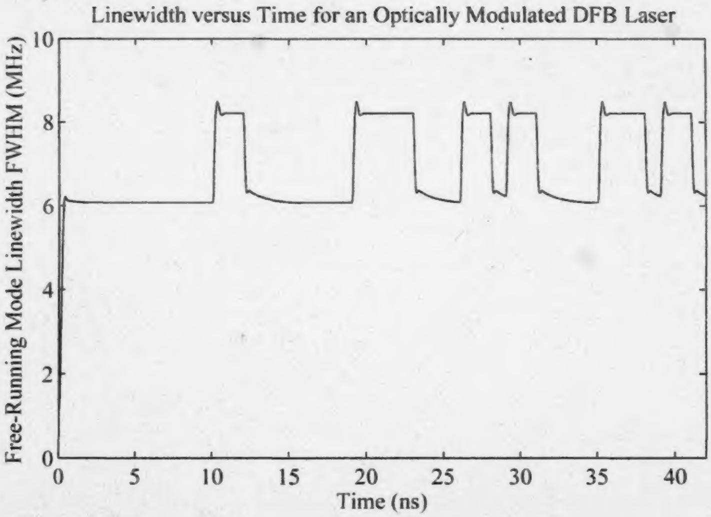

Figure 2.43: The linewidth of a DFB laser with binary modulated optical injection in a sidemode and for the free-running mode as a function of time.

The linewidth of the free-running mode of the DFB laser varies from ~6 MHz to ~8.5 MHz for the example presented above. This should be low enough to recover the signal at the receiver. The reasoning behind this assertion is as follows. For a laser with a linewidth of 1-10 MHz, the coherence length is on the order of tens of meters in free-space or glass devices (fiber, planar lightwave circuits, etc.). The time delays for self-interference considered for the FCM signal are on the order of nanoseconds which correspond to delay lengths of centimeters. The self-interference is not expected to broaden the frequency spectrum of the FCM signal at the receiver significantly due to linewidth related effects if the linewidth of the laser is kept to a few MHz or less, which is reasonable for DFB lasers [MOG2].

This linewidth argument applies to the DFB laser with either electrical or optical injection modulation as the means to produce an FCM signal. The choice between these two modulation methods has to be made at this point. A comparison of the electrical and optical injection modulation methods is the subject of the next section.

2.11 Comparison of Electrically versus Optically Modulated Lasers.

When choosing between electrically versus optically modulated laser sources for generation of FCM transmission signals, three performance factors will be considered; thermal bit patterning effects, immunity to relaxation oscillations and signal distortion.

The optical injection modulation, since it doesn't change the temperature of the diode laser junction, will not cause thermal effects at lower frequencies due to the temperature dependence of the refractive index of the laser. This is a key factor since correct reception of the signal at the receiver depends on absolute frequency accuracy of the signal because the interferometers that precede the receivers are an immutable feature of the FCMA architecture. It would be almost impossible to adjust the receiver interferometers for fast (~100 kHz) fluctuations in the absolute optical frequency of the incoming signal. This consideration suggests a preference for optical injection modulation.

Optically modulated lasers have better immunity to relaxation oscillations as can be seen from the results presented so far in this chapter. The steady values of optical frequency throughout the duration of a transmitted signal will play a key role in the proper reception of the FCM signal. This consideration also suggests a preference for optical modulation.

Optically modulated lasers have odd relaxation feature at high to low injected power transition. This consideration favours the electrical modulation option, but is not as important as the two previously stated influences.

For the reasons stated here, optical modulation will be pursued as the method for generation of the FCM signal. The next section presents and discusses the efficiency with which optical modulation can be used to generate multilevel frequency shift based FCM signals and introduces some limitations.

2.12 Generation of Multilevel FCM Signal with DFB Lasers.

The response of the DFB laser to external optical injection, as demonstrated in Figure 2.22, is a non-linear function of injected optical power. Since the linearity of the injected optical power to output optical frequency conversion is important, as introduced in Section 1.7, if the linearity of the conversion can be improved by any means the FCMA system performance will benefit.

The non-linearity of the conversion curve can be qualitatively described in terms of the injected optical power and the optical frequency detuning. As the injected optical power increases, the difference between the injected optical frequency and the natural cavity resonance of the nearest laser mode decreases. This increases the gain for the injected light in a non-linear fashion [HO1], which has the effect of pulling the cavity resonance even closer to the injected optical frequency. The inverse gain curve as it is presented in the reference behaves like a raised sinusoid, which can be approximated as a quadratic when the detuning is within 25% of the overall mode spacing of the slave laser. It is with this in mind that the idea of using the near quadratic dependence of the output optical power from a MZ EO modulator near the peak of its voltage driven transfer function that provides a means to improve the linearity of the conversion of a linearly-spaced multilevel input voltage signal (to the MZ EO modulator) to a linearly-spaced multilevel optical frequency shift keyed signal.

The MZ EO modulator, as functionally depicted in Figure 2.28, must be biased above the 3 dB point of its output power transfer curve. The optical injection waveform that will be used for calculating the dynamic response of the slave DFB laser to the injected optical power will be a raised sinusoid, where it will be assumed that the voltage waveform (which may be dual drive) can be appropriately scaled to the transfer function of the MZ EO modulator to produce the following injected optical power as a function of time,

$$P_l^{in}(t) = \begin{cases} \overline{P}_l^{in}\left(1 + \sin\left(\varphi_{os} + \frac{2b_{k-1} - M + 1}{M-1} m_i\left(\frac{\pi}{2} - \varphi_{os}\right)\right)\right) + \\ \quad \left(\sin\left(\varphi_{os} + \frac{2b_k - M + 1}{M-1} m_i\left(\frac{\pi}{2} - \varphi_{os}\right)\right) - \right. \\ \quad \left. \sin\left(\varphi_{os} + \frac{2b_{k-1} - M + 1}{M-1} m_i\left(\frac{\pi}{2} - \varphi_{os}\right)\right)\right)\overline{P}_l^{in} sin^2\left(\frac{\pi(t-(k-1)T)}{2t_r}\right) \\ \qquad (k-1)T \le t < (k-1)T + t_r \\ \overline{P}_l^{in}\left(1 + \sin\left(\varphi_{os} + \frac{2b_k - M + 1}{M-1} m_i\left(\frac{\pi}{2} - \varphi_{os}\right)\right)\right) \\ \qquad (k-1)T + t_r \le t < kT \end{cases} . \quad (52)$$

In this equation, both $\overline{P}_l^{in}$ and m_i are redefined and φ_{os} is a phase offset for the MZ EO modulator transfer function (in radians) and is always positive and less than $\pi/2$. $\overline{P}_l^{in}$ now represents the optical power if the MZ EO modulator would be biased at the 3 dB point, or the mean available modulated power. The modulation index is defined as the maximum excursion between the MZ EO bias point, given by φ_{os}, and the maximum output power from the modulator, with an applied phase of $\pi/2$. This equation is controlled by linear offsets in phase of the argument of a standard MZ EO modulator which adequately describes the operation of such modulators.

Simulation results presented in this section will show that the linearity of the conversion can be controlled by changing the phase offset and the frequency level spacing can be controlled by virtue of the modulation index. The new injected optical power equation, Equation (52), is used as the input to the laser rate equations for optical injection and the output signal frequency levels are found for four, eight, or sixteen level signals using a histogram of the frequency waveform to find the peak frequencies in the signal.

The DFB laser is biased at 350% of the threshold current and the injected optical frequency detuning is set to -25 GHz to maximize the frequency conversion range. All of the other laser parameters are as previously used to simulate the DFB laser. The FCM signal frequency levels were calculated for a range of MZ EO modulator phase offset from 0.5 to 1.25 radians and the results are presented in Figure 2.44.

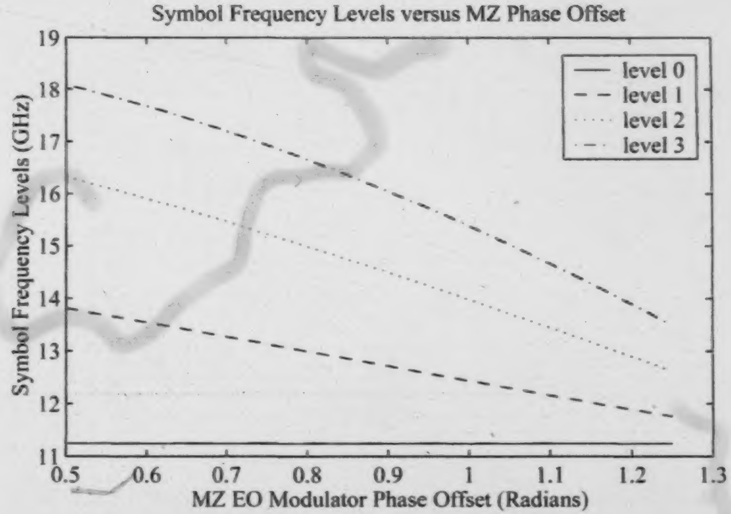

Figure 2.44: The frequency levels of a four level FCM signal referenced to the threshold value of the free-running laser mode frequency as a function of the MZ EO modulator phase offset with a modulation index of 99% as defined in Equation (52).

The frequency spacing between adjacent frequency levels was calculated as an intermediate step in evaluating the linearity of the signal conversion and these results are presented in Figure 2.45.

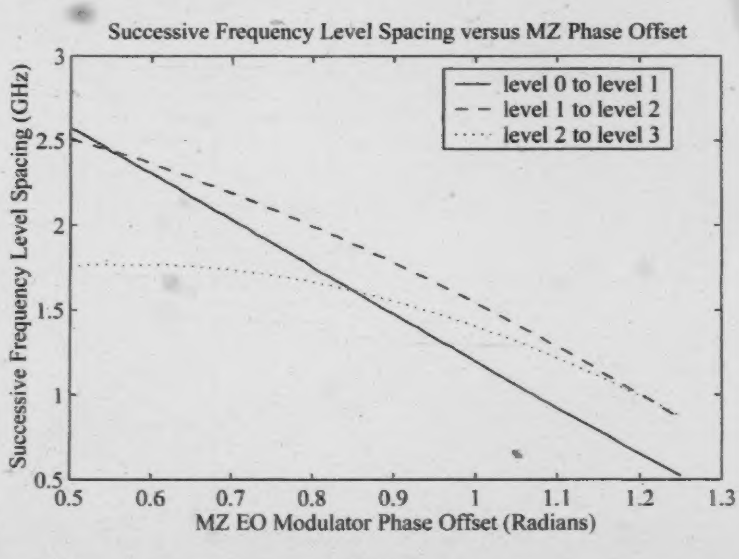

Figure 2.45: The frequency difference between successive frequency levels of a four level FCM signal as a function of the MZ EO modulator phase offset with a modulation index of 99% as defined in Equation (52).

The frequency spacings between adjacent frequency levels of the FCM signal are not simultaneously equal to each other for any value of the MZ EO modulator phase offset, but some values of phase offset produce frequency levels that are close to being equally spaced.

The mean frequency level spacing of the FCM frequencies is what will be used to choose the modulation parameters when the lowest symbol value and the highest symbol value are centered exactly on the peaks of the MZ decoder response with the lowest FSR at the receiver. The mean frequency level spacings for four level FCM signals generated with modulation indices of 80% and 99% and a range of MZ EO modulator phase offsets are shown in Figure 2.46.

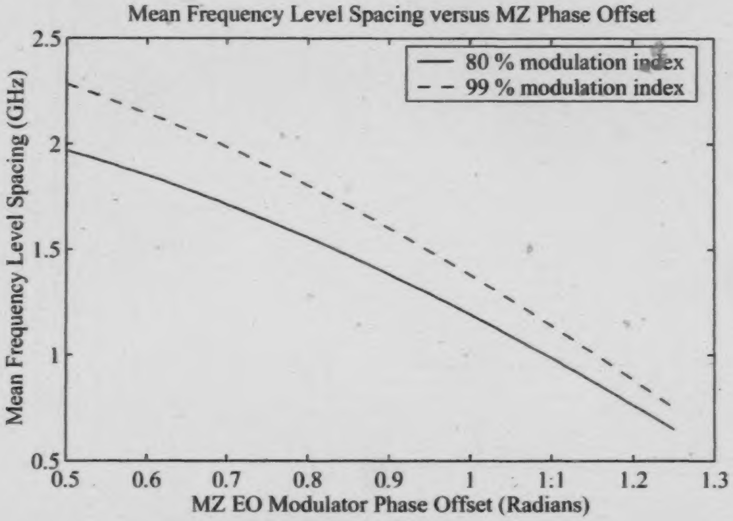

Figure 2.46: The mean frequency level spacing of a four level FCM signal as a function of the MZ EO modulator phase offset Simulation results for modulation indices of 99% and 80% are shown.

A wide range of mean frequency level spacings are available by changing the MZ EO modulator phase offset and keeping a constant modulation index. Lowering the modulation index has the effect of decreasing the mean level spacing, but when the linearity is defined as the maximum difference between the actual frequency level spacings and the mean frequency level spacing, lowering the modulation index becomes advantageous. The absolute frequency difference, referred to as the frequency level spacing error, is plotted against the MZ EO modulator phase offset for modulation indices of 80% and 99% in Figure 2.47.

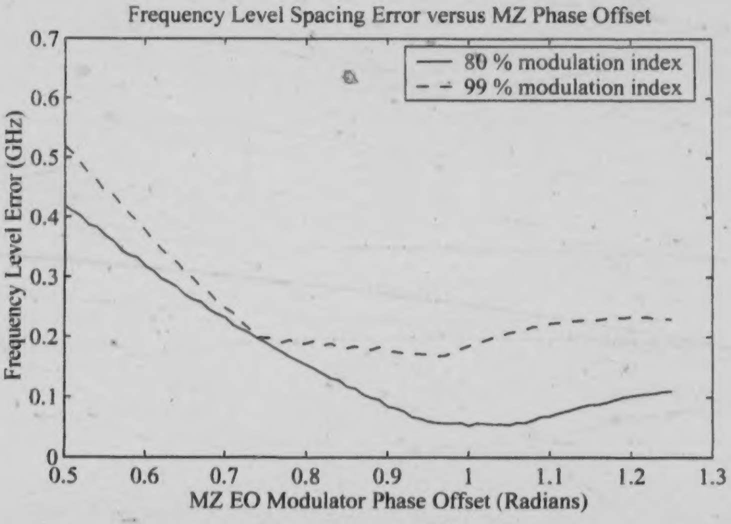

Figure 2.47: The largest absolute deviation of all three frequency level spacings from the mean frequency level spacing versus the phase offset of the MZ EO modulator. Simulation results for modulation indices of 99% and 80% are shown.

If this error is plotted as a percentage of the mean frequency level spacing, the advantage becomes even more noticeable, Figure 2.48.

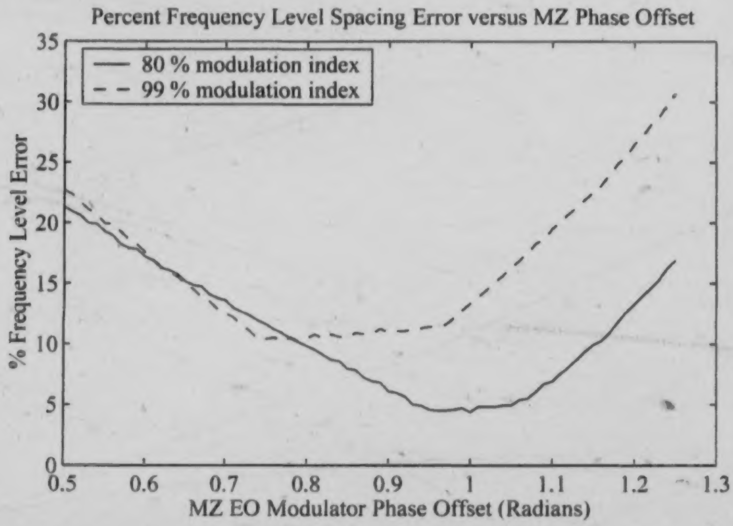

Figure 2.48: The largest deviation of all three frequency level spacings from the mean frequency level spacing as a percentage of the mean frequency level spacing versus the phase offset of the MZ EO modulator. Simulation results for modulation indices of 99% and 80% are shown.

The frequency level spacing errors of the FCM signal can be quite small if the correct bias point of the MZ modulator and modulation index are chosen. The non-linearity of the converted signal can be as low as 5% for frequency level spacings of 1.25 GHz and as low as 10% for frequency level spacings of 2 GHz for four level FCM signals.

These same simulation conditions were applied to an eight level input signal. The corresponding mean frequency level spacing, as an average over the seven spacings between eight levels, repeats the general shape of Figure 2.46 and is plotted as a function of the MZ EO modulator phase offset in Figure 2.49.

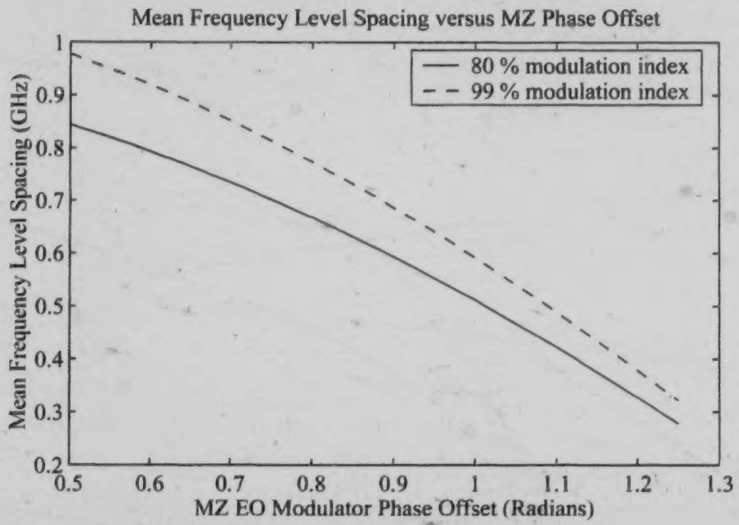

Figure 2.49: The mean frequency level spacing of a eight level FCM signal as a function of the MZ EO modulator phase offset Simulation results for modulation indices of 99% and 80% are shown.

The frequency level spacing error as a percentage of the mean frequency level spacing has a sharper minimum for an eight level signal than it does for a four level signal, see Figure 2.50.

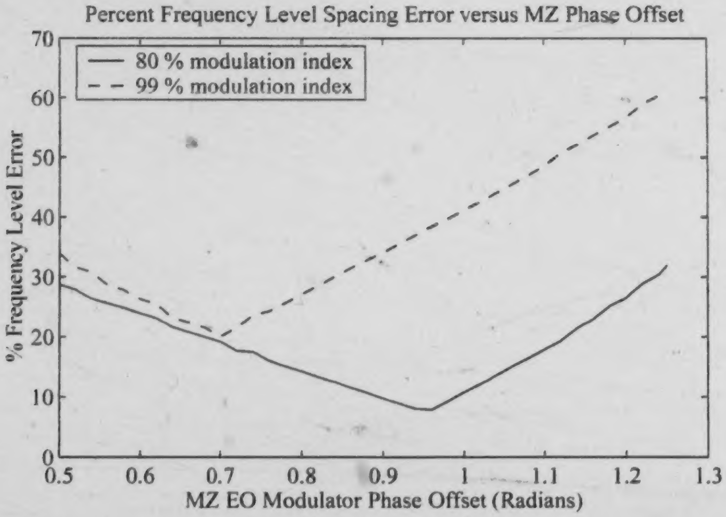

Figure 2.50: The largest deviation of all seven frequency level spacings from the mean frequency level spacing as a percentage of the mean frequency level spacing versus the phase offset of the MZ EO modulator. Simulation results for modulation indices of 99% and 80% are shown.

The 99% modulation index results for the eight level signal frequency level spacing error show that the minimum percentage error is ~ 20% compared to ~ 10% for the four level signal, but for 80% modulation index the minimum error is still less than 10%. The linearity degrades as more frequency levels are added to the composite FCM signal.

A simulation assessment for 16 level FCM signals will not be done as part of this chapter, the reasoning will be explained in the following section, Section 2.13, which deals with the limits of this method of generating FCM signals.

The combination of mean frequency level spacing and linearity defined by the percent error of the frequency level spacing relative to the mean spacing determines the maximum data throughput of the FCM system when the signal is generated via optical injection in DFB laser sidemodes. The following section briefly summarizes the data formats and maximum data throughput possible using the results of this section.

2.13 Data Throughput Limits using Optical Injection in DFB Lasers.

The total frequency range required for *M*-ary FCM signals, $\Delta\nu_{total}$, can be derived by rewriting the equations of Section 1.5 for a general fractional delay for the first channel of the combined FCM signal where $L_{\Delta T}$ is the longest delay time as a fraction of the symbol period, *B*, for the Mach-Zehnder decoder,

$$\Delta L_1 \approx \frac{c}{\mu_{eMZ} B} L_{\Delta T}, \qquad (53)$$

where typical values of $L_{\Delta T}$ are 1/4, 1/3 or 1/2 and

$$\Delta\nu_{total} = \frac{1}{2TL_{\Delta T}}(M-1). \qquad (54)$$

For SONET data rates OC-12 and OC-48 as well as Gigabit Ethernet, the total frequency ranges required for multiplexing 1, 2, 3, and 4 channels onto one optical carrier an FCM signal format are tabulated in Table 2-2.

Table 2-2: Required total frequency excursions for FCM signals with different transmission formats, bit overlap times and number of frequency levels. The entries in bold are frequency ranges that are considered to be within the reach of the optical injection modulation method. The entries in italics are attainable with moderate increases in the linewidth enhancement factor and/or the gain compression coefficient.

Transmission Format	Native Bitrate (Gbps)	Delay as a Fraction of the Bit Duration	Level Spacing (GHz)	Total Frequency Range Required for M-ary FCM Signals $M = 2, 4, 8, \text{or } 16$			
				2	4	8	16
OC-12	0.622	1/4	1.244	**1.244**	**3.732**	*8.708*	18.66
		1/3	0.933	**0.933**	**2.799**	**6.531**	14.00
		1/2	0.622	**0.622**	**1.866**	**4.354**	*9.330*
Gigabit Ethernet	1.25	1/4	2.500	**2.500**	**7.500**	17.50	37.50
		1/3	1.875	**1.875**	**5.625**	13.13	28.13
		1/2	1.25	**1.250**	**3.750**	*8.750*	18.75
OC-48	2.488	1/4	4.976	**4.976**	14.93	34.83	74.64
		1/3	3.732	**3.732**	11.20	26.12	55.98
		1/2	2.488	**2.488**	**7.646**	17.42	39.32

The bold entries in the above table are considered to be attainable frequency ranges using the DFB/MZ EO modulator optical injection system. The italicized frequency range entries may be reached with a DFB laser by increasing the linewidth enhancement factor and/or the gain compression coefficient. Increasing these physical parameters of the laser should not be too difficult since they are generally considered to be degradations in lasers and much effort has been expended in the past to reduce them. For all of the remaining entries, another modulation method must be found.

The maximum throughput summarized by transmission format is as follows:

1) Three OC-12 format channels with a maximum throughput of 1.866 Gbps of data may be transmitted using FCMA.

2) Two OC-48 format channels with a maximum throughput of 5.976 Gbps of data may transmitted using FCMA.

3) Two Gigabit Ethernet channels with a maximum bit-rate of 2.5 Gbps and a maximum throughput of 2 Gbps of data may be transmitted using FCMA.

This concludes the investigation of rate equation analysis to choose a preferred modulation method and predict potential FCMA throughput. A summary of Chapter 2 is given in the following section.

2.14 Summary of Chapter 2.

Chapter 2 employed Runge Kutta integration of the laser rate equations to investigate the feasibility of using electrical current modulation and optical injection modulation of laser diodes for the generation of optical FCM signals. Direct current modulation was excluded from consideration due to pronounced relaxation oscillations and bit patterning effects induced by thermal modulation of laser refractive index.

Optical injection was proposed as an alternative to electrical injection to modulate the laser diode. Both FP and DFB laser were investigated as potential signal sources. The DFB laser was found to be the preferred laser type because it has a modulation depth without artificially increasing the laser linewidth through spontaneous emission injection, as was proposed for the FP laser.

The use of optical injection limits per channel bit-rate and number of channels because it has a limited available frequency modulation depth and the linearity of the optical power injection to output optical frequency conversion curve is less than perfect.

Chapter 3 presents experimental results of fiber optics implementations of both FP and DFB lasers with optical injection.

Chapter 3. Optical Injection Laser Transmitters.

The effectiveness of the optical transmitter design depends on availability of a set of laser qualities in the same laser, as was discussed in detail in Chapter 2. The desirable qualities can be paraphrased with the following list:

- The center (oscillation) frequency of the laser can be changed (shifted) quickly, on the order of <100 ps.
- The center frequency shift can be several GHz in magnitude.
- Shifting of the center frequency does not result in excessive frequency oscillations (damped relaxation oscillations).
- Center frequency shifts should not be accompanied by corresponding changes in optical power, or optical power changes should be minimized.

In theory, using optical injection into a sidemode of the laser to modify the central optical frequency of a free-running laser can provide optical frequency modulation performance that closely matches these requirements. This chapter provides experimental evidence to support the predictions of Chapter 2.

One Fabry-Perot (FP) laser and one distributed feedback (DFB) laser were tested experimentally. The experimental setups will be described and the results will be presented for measurements of the frequency shifts induced through optical injection as well as background information and experiments to help put the results into context.

The first section of this chapter introduces some basic experimental considerations necessary to perform injection experiments using semiconductor lasers.

3.1 Experimental Considerations for Laser Injection.

A diagram of a basic master/slave optical injection laser system is shown below in Figure 3-1.

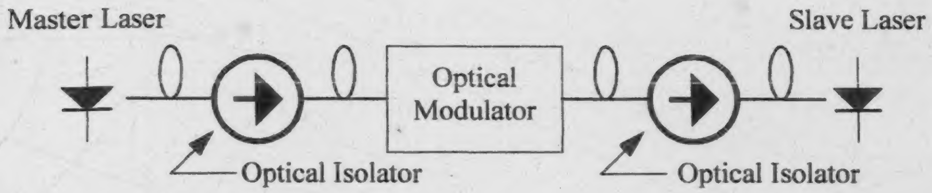

Figure 3-1: Schematic diagram of a general optical injection system that uses a master/ slave laser arrangement.

The light from the master laser is modulated by a modulator and optically coupled to the slave laser and the isolators prevent reverse coupling from the slave laser into the master laser. Other components will be necessary in experiments to perform measurements on optical powers and optical frequencies as well as control the polarization of the master laser light entering the optical modulator and entering the slave laser. Adding these components introduces loss between the master laser and the slave laser so amplification may be necessary to overcome losses in the transmitter system. Because of the addition of these components to the optical system the isolators should be placed as close to the lasers as possible to prevent the slave laser from coupling back to the master laser and to prevent reflections from optical components from feeding back into the lasers. The use of the isolators in this way will help maintain the stability of the lasers.

The polarization of the light from the master laser must be controlled to a high degree to ensure that when it enters the slave laser it is polarized correctly, in the same direction as the sidemode into which it is being injected. This is accomplished by using polarization maintaining fiber wherever possible. However, the isolators, tap couplers, splitters, couplers, filters, amplifiers, and pump laser WDM couplers are pigtailed with standard (non-polarization maintaining) fiber making it impossible to guarantee that the master laser light is polarized in the correct direction for the injection into the laser and coupling to the modulator. Fiber-loop polarization controllers can be used to modify the polarization of the light but the polarization also needs to be measured. This involves careful placement of polarization maintaining fibers in the optical circuit and frequent free-space measurements of the polarization of the master laser light.

The most important element in the design of an optical injection FSK transmitter is the slave laser. Two implementations of slave lasers were investigated; Fabry-Perot lasers and Distributed Feedback lasers. The experiments and results for these two alternatives are presented in the next two sections, Sections 3.2 and 3.3.

3.2 Optical Injection Fabry Perot FSK Transmitter.

Because of the structure of Fabry-Perot semiconductor lasers, particularly the broad range of reflection from the mirrors and the wide gain spectrum (up to several tens of nanometers), the laser can oscillate in many modes simultaneously over a large optical spectrum. These modes draw on the same pool of electrons and holes in the semiconductor for their individual optical gains and, therefore, the gain (optical output power) of any particular mode is influenced by the gains (optical output powers) of all of the other modes. Some consequences of this fact will be discussed later in Section 3.2.2.

A simplified semiconductor Fabry-Perot laser structure is depicted in Figure 3-2 to demonstrate how the optical energy is confined to the gain region of a semiconductor laser.

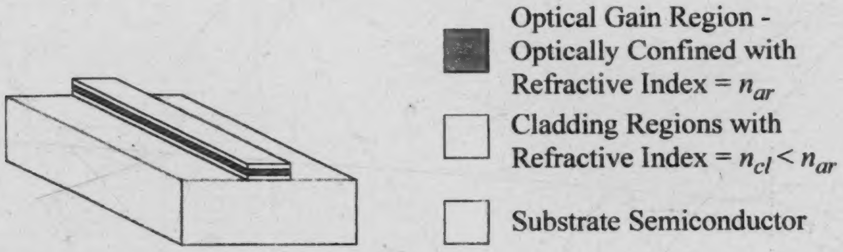
▨ Optical Gain Region - Optically Confined with Refractive Index = n_{ar}
☐ Cladding Regions with Refractive Index = $n_{cl} < n_{ar}$
☐ Substrate Semiconductor

Figure 3-2: A depiction of the optical confinement properties of a typical Fabry-Perot semiconductor laser.

The refractive index difference between the optical gain region, or active region, with index n_{ar} and the cladding regions, with indices such that $n_{cl} < n_{ar}$, is what provides optical confinement in the laser which is necessary for high gain. The electrical carriers, electrons and holes, can be confined to the gain region as well by creating heterojunctions in the semiconductor, but in general what is needed is a simple p-n (diode) junction. Heterojunction lasers have higher gain than simple diode junction lasers due to the lack of carrier diffusion out of the optical waveguide.

Photons confined to the waveguide active region of a semiconductor laser will either be reflected or transmitted by the semiconductor to air interfaces, called the laser facets, at either end of the waveguide structure. This is depicted in Figure 3-3.

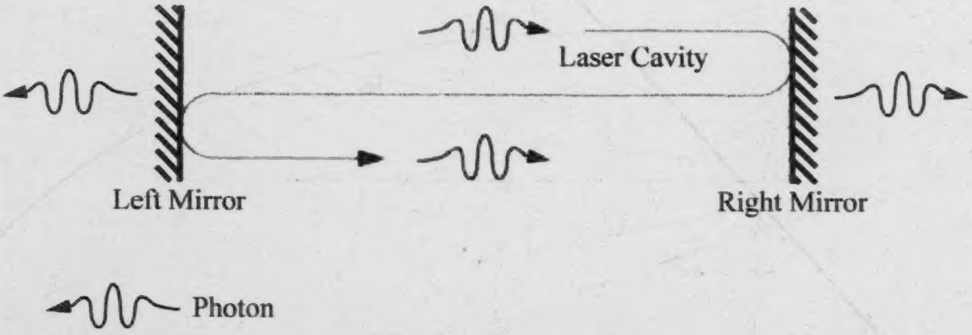

Figure 3-3: A functional diagram of a Fabry Perot Laser. The photons depicted internal to the laser cavity are shown to be "in phase" after one round trip in the cavity.

The round trip transit time and the propagation velocity determine the oscillation wavelengths/frequencies of the modes, any wavelength that sees a total round trip phase that is a multiple of 2π will oscillate if the gain for that wavelength is greater than the loss.

These phase and gain conditions must also be upheld for successful optical injection into semiconductor lasers. The inherent qualities of semiconductor FP lasers that make them unusable for standard high-speed transmission system light sources also inhibit their use in this application. One of these concerns, mode partition noise, will be better explained in Section 3.2.2 which will follow a section describing the spectral properties of the FP laser that was used in the experiments presented in this chapter.

3.2.1 Free-Running Fabry-Perot Laser Mode Spectrum.

The laser that was used for experimental attempts at creating an FCM signal was an 800 μm long InGaAsP semiconductor laser with a gain peak near 1550 nm when the laser temperature was maintained near 15 °C. The laser was packaged and pigtailed with standard 9 μm single mode fiber at both facets by Nortel Networks. The coupling efficiencies of laser power from the laser to the fiber and from the fiber to the laser were not calibrated, the significance of this fact will become apparent in later sections.

The optical spectrum was measured over temperature and at various bias currents, up to 50 mA. The laser spectrum for a bias current of 25 mA is shown in Figure 3-4 for temperatures ranging from 13 °C to 20.2 °C.

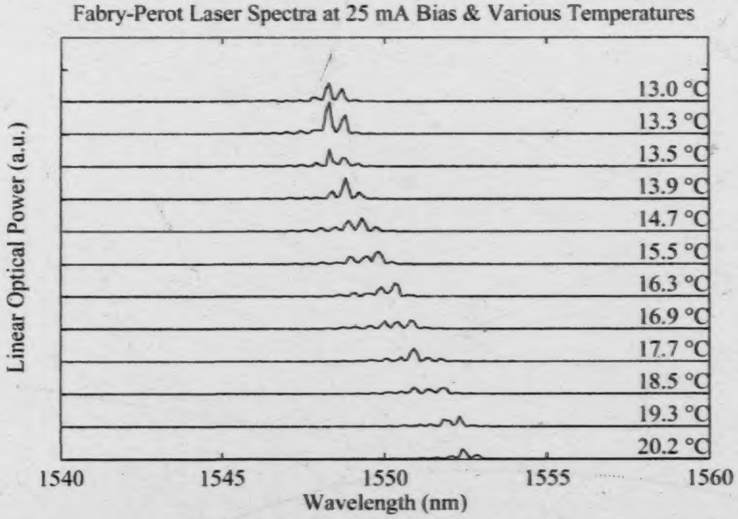

Figure 3-4: The free-running FP laser spectrum at 25 mA bias current is shown with laser temperature as a parameter. The spectra were measured with a monochromator.

The threshold current for this lasers is ~20 mA so the laser is biased slightly above threshold. The graph shows that only a few lasing modes (3 or 4) are significantly above threshold at any of the measurement temperatures. Also shown by the figure is the characteristic shift of the optical gain to longer wavelength at higher temperatures.

The laser spectrum for a bias current of 35 mA is shown in Figure 3-5 for temperatures ranging from 13 °C to 20.2 °C. This graph shows that more lasing modes (up to 7 or 8) are significantly above threshold at any of the measurement temperatures at the higher bias current. Again shown by the figure is the characteristic shift of the optical gain to longer wavelength at higher temperatures.

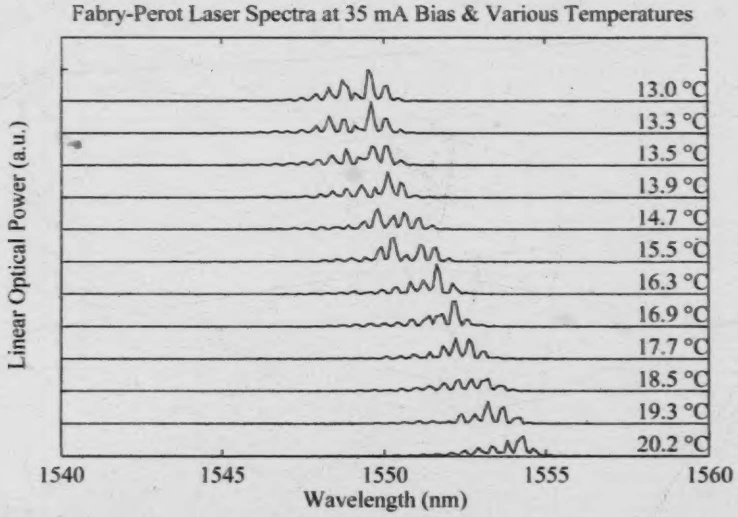

Figure 3-5: The free-running FP laser spectrum at 35 mA bias current is shown with laser temperature as a parameter. The spectra were measured with a monochromator.

The laser spectrum for a bias current of 45 mA is shown in Figure 3-6 for temperatures ranging from 13 °C to 20.2 °C.

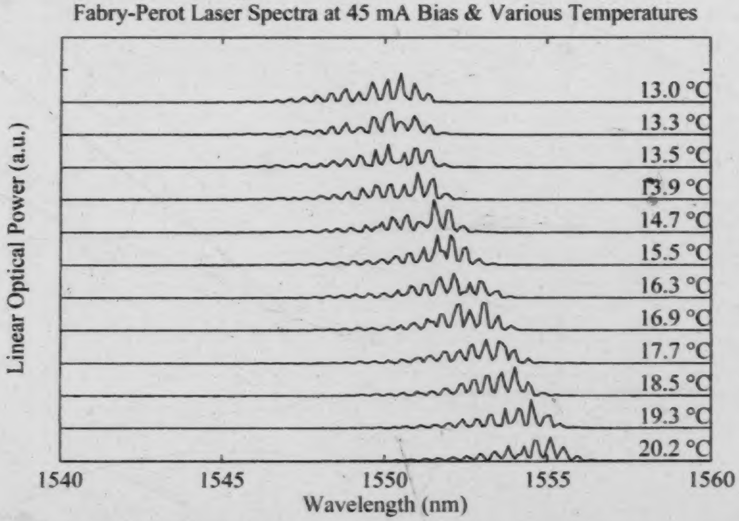

Figure 3-6: The free-running FP laser spectrum at 45 mA bias current is shown with laser temperature as a parameter. The spectra were measured with a monochromator.

These spectra show that even more lasing modes are significantly above threshold compared to the lower bias currents. Again shown by the figure is the characteristic shift of the optical gain peak to longer wavelength at higher temperatures.

Another observation that can be made by examining Figures 3-4 to 3-6 is the shift of individual modes to slightly higher wavelength as the temperature increases due to thermal expansion of the laser cavity affecting the round trip phase condition for oscillation. What cannot be seen from these figures is the shift to lower wavelength (higher optical frequency) of individual modes when the bias current is increased which is due to the electrical carrier density induced change in the index of refraction of the laser.

A conclusion that can be drawn from Figures 3-4 to 3-6 is the change of the dominant mode wavelength of several nanometers with respect to bias current. If the laser were to be directly modulated with current injection, the dominant mode would switch during transitions from low to high and high to low current causing what is known as mode hopping. Mode hopping, when combined with the effects of fiber dispersion, is the one main reason that semiconductor FP lasers cannot be used for Gigabit line-rate transmission over significant (> 1 km) transmission distances [SA1].

Another significant reason that semiconductor FP lasers cannot be used for Gigabit line-rate transmission is the spectral width of the output light. Optical fibers are dispersive and optical spectrums several nanometers wide would be irretrievably distorted after travelling only a few kilometers.

A performance affecting property of semiconductor lasers that is not obviously observable in the graphical information presented in this section is mode partition noise. The performance degradation due to this property will be discussed in the following section.

3.2.2 Mode Partition Noise in Semiconductor FP Lasers.

Mode partition noise is an instability in the spectrum of a semiconductor laser caused by thermal fluctuation of the electrical carriers, electrons in the conduction band and holes in the valence band. The instantaneous distributions of these carriers over the available states determines the instantaneous gain that any particular wavelength of light in the cavity of the laser will see. In room temperature lasers, the distribution of the electrical carriers concentrates at the peak gain on average, but there is significant probability that for small amounts of time the carrier distribution will be higher for stimulated emission energies of another mode. This causes a short transition of the main mode of the semiconductor laser to a mode that is not at the average peak gain and thus causes a fluctuation in output power. Mode partition noise affects lasers that are DC biased and externally modulated in addition to those that are directly modulated, therefore, this impairment will always affect optical transmission systems.

In addition to optical power fluctuations, the corresponding change of the dominant lasing mode will alter the received waveform of a fiber optic system due to the dispersion of the fiber. Mode partition noise can be reduced, and mode hopping can also be reduced, by injecting spectrally-narrow uncorrelated light into the laser cavity [KIMY1]. Injecting light from a spontaneous emission source, such as a light emitting diode (LED) or an optically pumped Erbium doped fiber, that has been spectrally narrowed via optical filtering is investigated as means to produce optical power and mode stability in semiconductor FP lasers in the next few sections.

3.2.3 Spontaneous Emission Injection and Mode Stabilization.

Injection of spontaneous emission into a semiconductor FP laser while injecting a coherent intensity shift keyed (ISK) signal and allowing for the transmission of the FCM signal from the FP laser requires an optical system like the one shown in Figure 3-7.

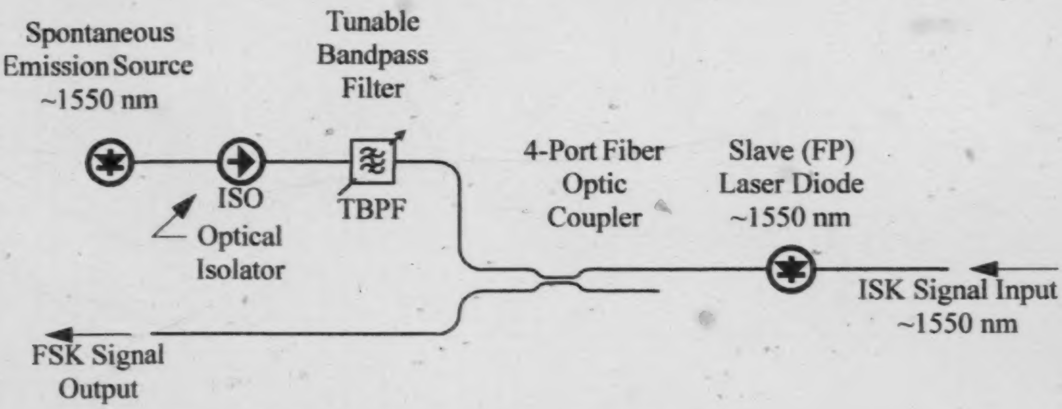
Spontaneous
Emission Source
~1550 nm
Tunable
Bandpass
Filter
ISO
Optical
Isolator
TBPF
4-Port Fiber
Optic
Coupler
Slave (FP)
Laser Diode
~1550 nm
ISK Signal Input
~1550 nm
FSK Signal
Output

Figure 3-7: A general depiction of the co-injection of a coherent signal and a narrow band spontaneous emission source into a laser diode.

The optical system has two input ports and one output port and is a functional equivalent to Figure 2.31. The coupling intensity of the ISK signal should be maximized because, as the results of Chapter 2 suggest, several milliWatts of optical power may be needed to shift the optical frequency of the slave laser sufficiently for FCM signal generation. The intensity of the spontaneous emission source or the output FCM signal can be increased through optical amplification without much difficulty.

The narrow band spontaneous emission source was constructed in the manner shown in Figure 3-8.

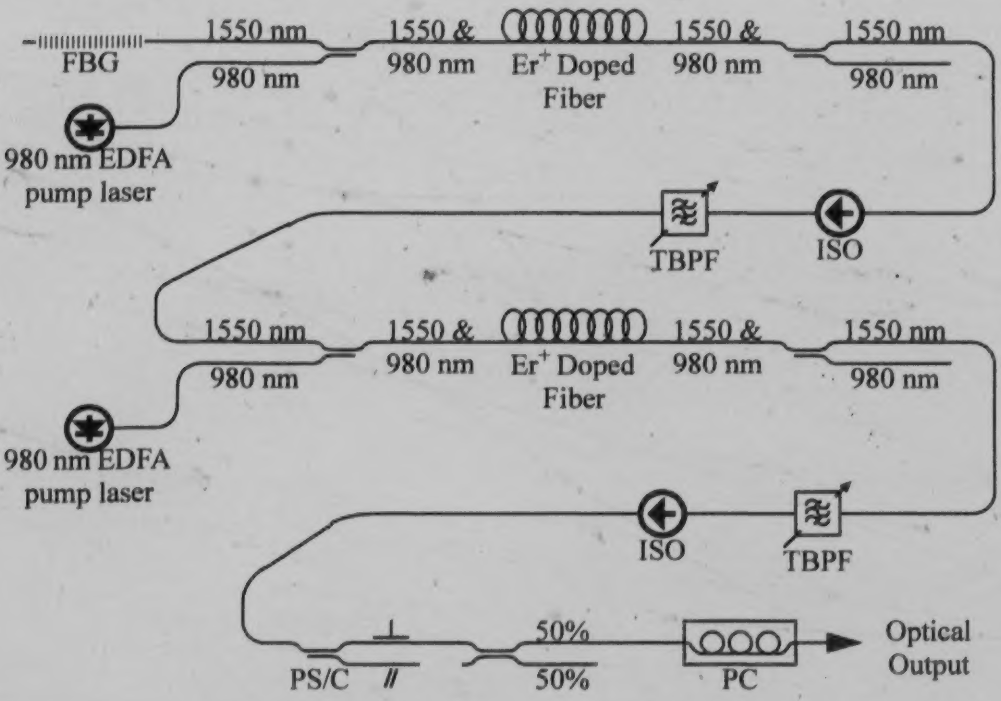
FBG
1550 nm
980 nm
980 nm EDFA pump laser
1550 & 980 nm
Er⁺ Doped Fiber
1550 & 980 nm
1550 nm
980 nm
TBPF
ISO
1550 nm
980 nm
980 nm EDFA pump laser
1550 & 980 nm
Er⁺ Doped Fiber
1550 & 980 nm
1550 nm
980 nm
ISO
TBPF
PS/C
⊥
//
50%
50%
PC
Optical Output

Figure 3-8: The optical schematic of the narrow band spontaneous emission light source.

At the top of Figure 3-8 there is an erbium doped fiber amplifier (EDFA) with a fiber Bragg grating (FBG) connected to one end of the amplifier. The feedback provided by the FBG is narrow band, with a bandwidth of approximately 0.2 nm, so the EDFA amplifies this noise and this light as well as background noise appear at the output of the EDFA. The light is then isolated (ISO) and filtered with a tunable bandpass filter (TBPS) and amplified again by a second EDFA. This light is then filtered and isolated again and coupled into a polarization splitter/combiner (PS/C). The function of the PS/C is to provide injection of noise power of only one polarization into the slave laser which will be aligned to the polarization of the free-running modes of the slave laser via the polarization controller (PC). The 50/50 coupler in the bottom right hand corner of Figure 3-8 serves the same purpose as the four port fiber optic coupler in Figure 3-7.

The optical spectra of the EDFA at the top of Figure 3-8 with and without the FBG connected to it are shown in Figure 3-9.

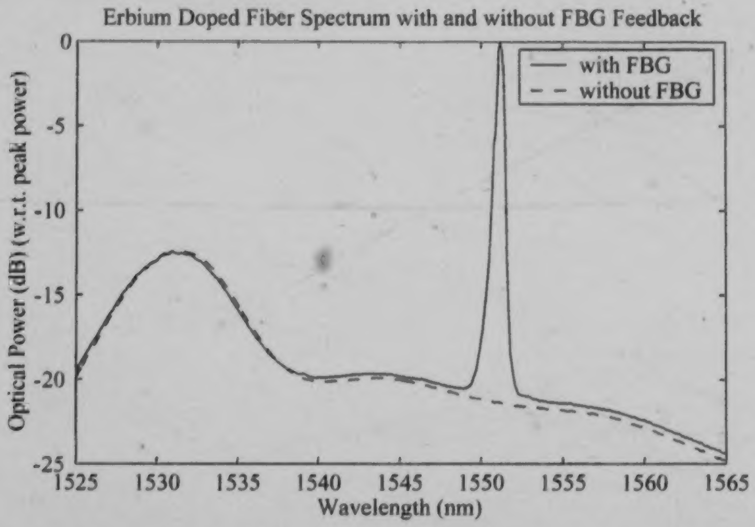

Figure 3-9: The optical spectrum of the spontaneous emission source (EDFA) used to produce the narrow band spontaneous emission injected into the FP laser. The spectrum with and without the feedback from the fiber Bragg grating (FBG) filter is shown.

The optical spectrum of the EDFA is modified by providing narrow band feedback via the FBG and effectively produces a noise peak around 1551 nm.

When the original noise is filtered and amplified again, the spectrum does not change too much as can be seen in Figure 3-10. But, as can also be seen in Figure 3-10, the post filtering of the noise spectrum, by the final tunable filter, limits the optical power outside of the filter bandwidth to be about 35 dB down from the peak noise spectral density.

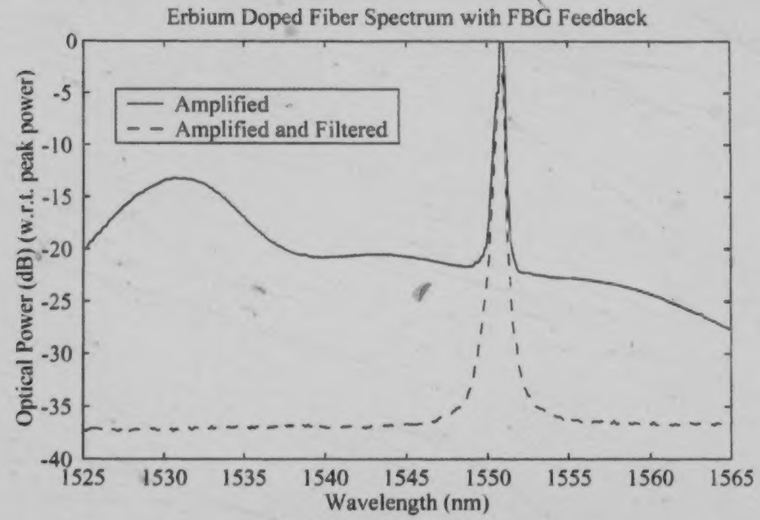

Figure 3-10: The optical spectrum of the spontaneous emission source after amplification and filtering which becomes the narrow band spontaneous emission injected into the FP laser.

When this final noise spectrum is examined closely it can be seen to be very narrow at the peak, see Figure 3-11.

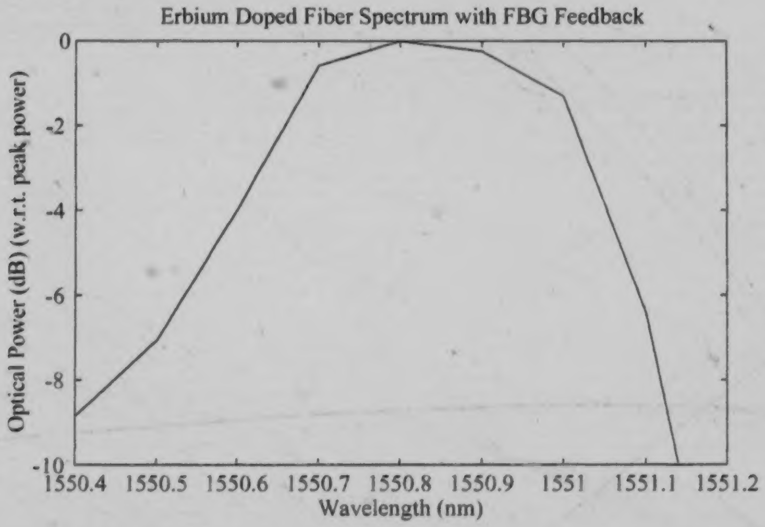

Figure 3-11: A close up view of the amplified and filtered spontaneous emission optical spectrum shown in Figure 3-10.

This measurement was made with a monochromator with a resolution limit of approximately 0.17 nm at the finest setting so the actual spectral width of the spontaneous emission spectrum is expected to be less than 0.3 nm at 3 dB down from the peak.

Any optical power measurements that were made during experiments on the injected spontaneous emission power were done using the rejected light from the PS/C as shown in Figure 3-12.

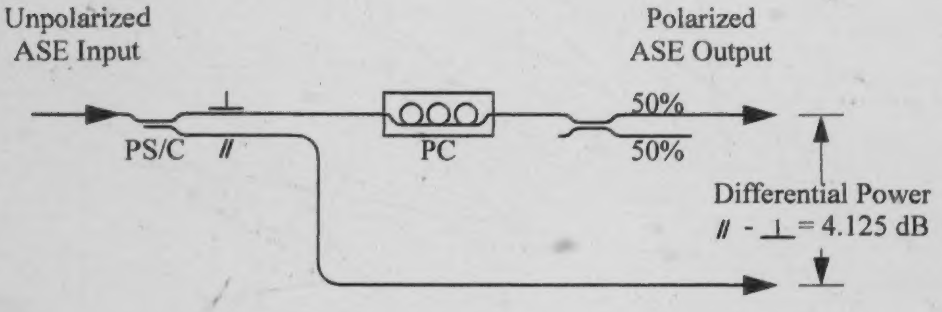

Figure 3-12: Experimental setup for ASE injection power calibration. A Hewlett Packard optical power meter was used to measure the optical power.

The PS/C was assumed to be equal loss for either polarization port and the spontaneous emission source was assumed to have no polarization dependence. The calibration of this optical circuit indicated that the optical power launched into the fiber pigtail of the slave laser was 4.125 dB less than the measured optical power at the other port of the PS/C.

The injection of the spontaneous emission into the slave FP laser causes the laser to oscillate preferably in one mode near the peak of the spontaneous emission noise spectrum, as demonstrated in the following figure, Figure 3-13. Figure 3-13 also demonstrates that increasing the injected spontaneous emission power allows the mode nearest to the peak of the injected spectrum to dominate more completely as would be expected.

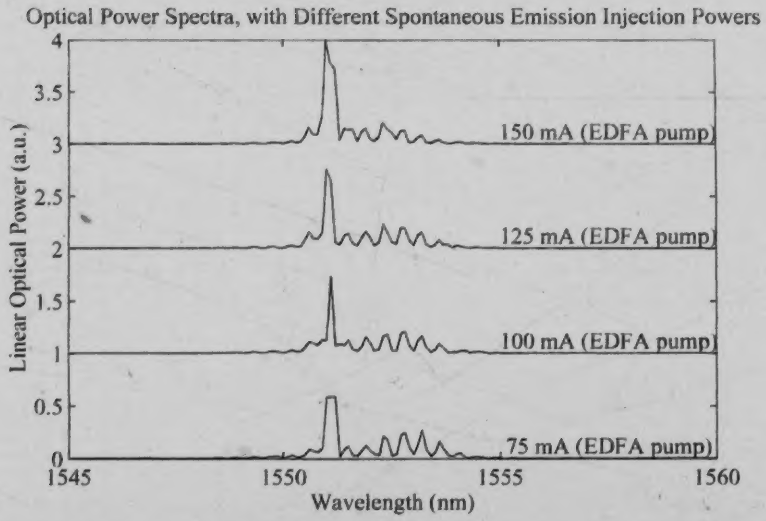

Figure 3-13: The optical spectrum of the FP laser with constant temperature, 17.5 °C, and 40 mA bias current with spontaneous emission injection power as a parameter (controlled via the pump current for the EDFA).

When the injected optical power from the spontaneous emission source is held constant and the temperature (i.e., gain peak wavelength) of the slave laser is changed, the dominant mode of the slave laser will still be the mode nearest the peak of the injected spontaneous emission spectrum, Figure 3-14.

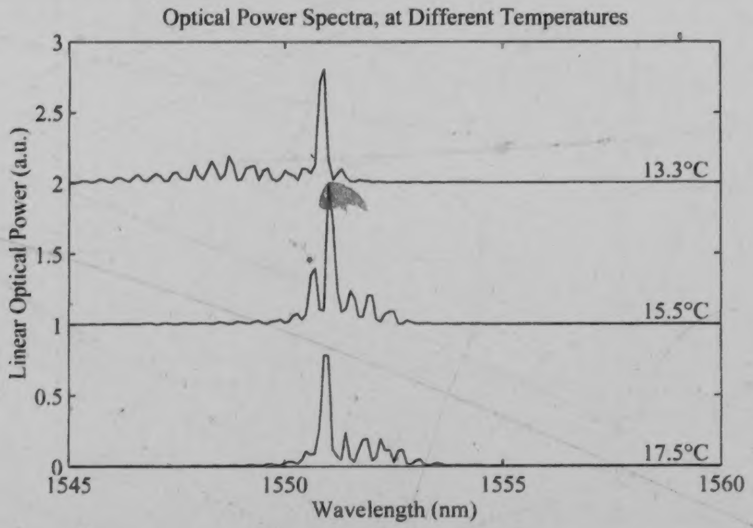

Figure 3-14: The optical spectrum of the FP laser with constant spontaneous emission injection power and 40 mA bias current with temperature as a parameter.

The injected noise allows the noise driven mode to dominate more clearly if the gain peak of the laser is not near the spectral peak of the injected light.

When the bias current is varied, as shown in Figure 3-15, similar results are found, the laser oscillates preferably in the mode nearest the spectral peak of the injected light.

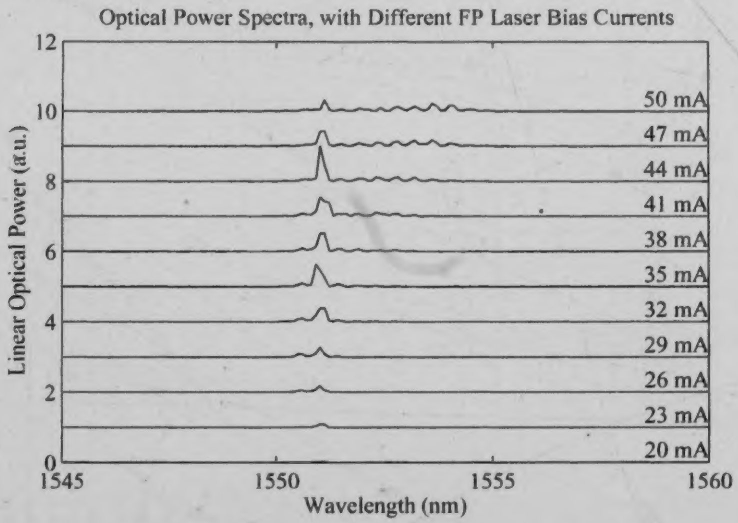

Figure 3-15: The optical spectrum of the FP laser subject to spontaneous emission injection power (EDFA pump laser biased at 150 mA) at a constant temperature, 17.5 °C, plotted with FP bias current as a parameter. Scanned with a monochromator.

The injected optical power, the laser temperature and the laser bias are all of the independent variables that were able to change in these experiments and changing any one of the three does not change the fact that the spontaneous emission injection causes the slave laser to oscillate preferentially in the mode nearest to the peak of the injected spectrum.

The next section describes the optical system that was used to inject coherent light into the slave laser.

3.2.4 Injection of Laser Light.

The modulation method for generating the FCM signal involves injecting an ISK modulated signal from a master laser into a slave laser. As was shown in Chapter 2, an multilevel ISK signal with unequal power spacing between successive levels is required to produce a frequency shifted output with nearly equal frequency level spacings. A Mach-

Zehnder modulator can be used to produce such a multilevel signal if it is used to modulate a DC biased laser. Figure 3-16 shows the basic implementation of the optical circuit that is necessary to produce the coherent injection signal.

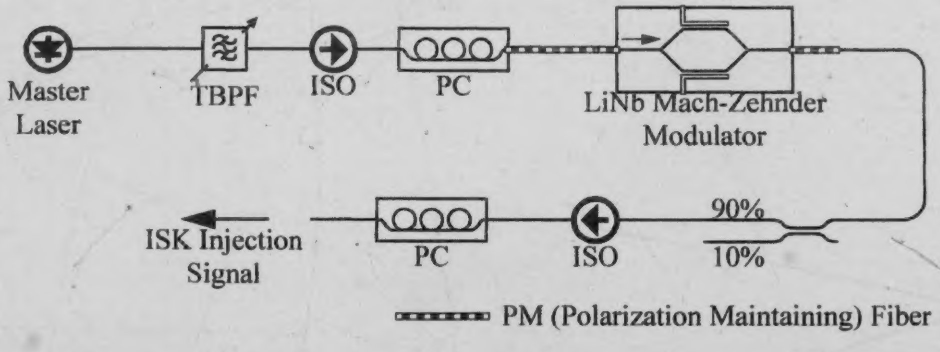
Master Laser
TBPF
ISO
PC
LiNb Mach-Zehnder Modulator
90%
10%
ISO
PC
ISK Injection Signal
PM (Polarization Maintaining) Fiber

Figure 3-16: The optical schematic of the optical circuit necessary to generate the ISK injection signal. (TBPF = tunable bandpass filter, ISO = optical isolator, PC = polarization controller)

The total loss of all of the components between the master laser and the output of this optical system is greater than 10 dB. If the master laser can produce a maximum of a few milliWatts of optical power at it's output fiber, the injected signal power will never be sufficiently powerful to create the frequency shifts in the slave laser as predicted in Chapter 2. Adding an optical amplifier can overcome this problem at the expense of additional noise, as shown in Figure 3-17.

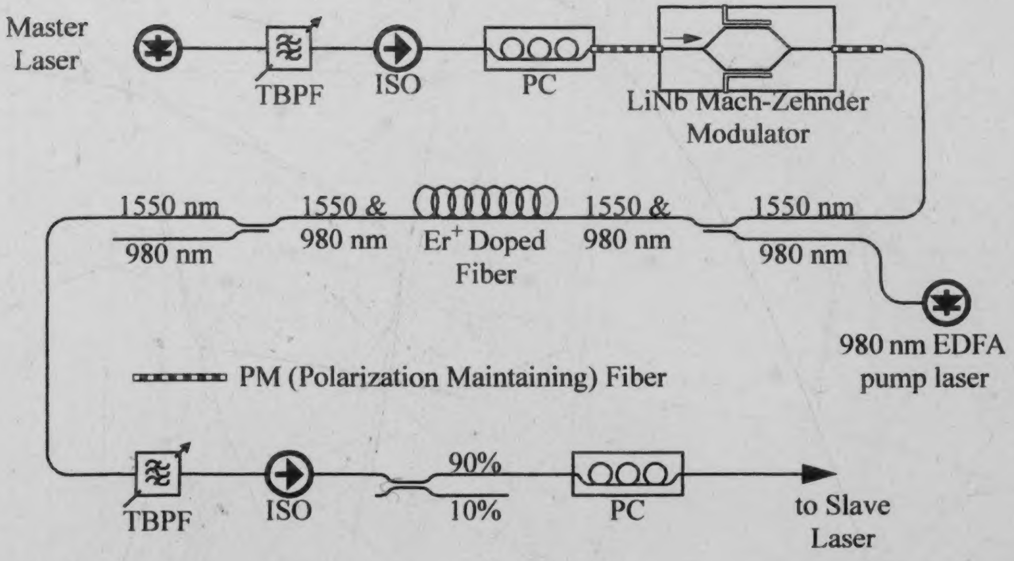
Master Laser
TBPF
ISO
PC
LiNb Mach-Zehnder Modulator
1550 nm
980 nm
1550 & 980 nm
Er$^+$ Doped Fiber
1550 & 980 nm
1550 nm
980 nm
980 nm EDFA pump laser
PM (Polarization Maintaining) Fiber
TBPF
ISO
90%
10%
PC
to Slave Laser

Figure 3-17: The optical schematic of the ISK signal generation system including an optical amplifier to increase the strength of the injection.

The addition of the amplifier requires that a bandpass filter be inserted after the amplifier to limit the ASE injection into the slave laser. The system depicted in Figure 3-17 was used for the experiments discussed in this chapter involving coherent injection. This coherent injection system and the narrow-band spontaneous emission source are combined to produce stable frequency shifts in semiconductor FP laser which is the subject of the following section.

3.2.5 Co-injection of Spontaneous Emission and Laser Light.

Connection of the optical systems shown in Figure 3-8 (the narrow-band spontaneous emission source) and Figure 3-17 (the ISK signal generator) to the two pigtails of the slave laser is shown schematically inFigure 3-18.

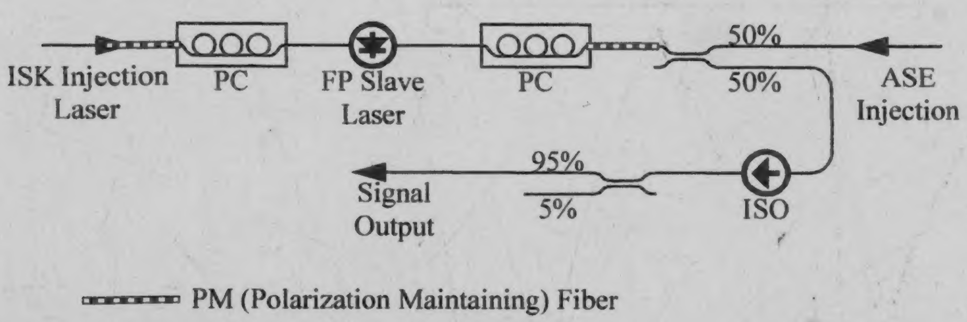

Figure 3-18: An optical schematic showing the connections of the narrow-band spontaneous emission source (ASE Injection) and the ISK signal source to the slave laser. Also shown is the isolated output port where the FCM signal will appear.

The coherent light and the ASE are injected into opposite facets of the slave laser. The generated FCM signal comes out of both ends of the laser, but the 50% fiber coupler on the ASE injection side is used to extract the output signal from the injection systems. The FCM signal is then isolated, to prevent feedback into the slave laser from components following the isolator, and a 5% optical tap is used to split off part of the signal for measurements of the optical spectrum during tests.

The optical spectrum of the slave FP laser was measured with a monochromator when both coherent and ASE were injected into the slave laser cavity, the measurement result is displayed in Figure 3-19. In Figure 3-19 the spectral peaks near 1551 nm are one mode of the slave laser that has been selected via the injection of the ASE and the calibration tone at 1550.79 nm. The peak near 1553.5 nm is the coherent injection light. The FP modes appear stable. The spectral resolution of the monochromator is insufficient to resolve spectral features like sidebands due to relaxation oscillations so no definite statement on the mode stability can be made.

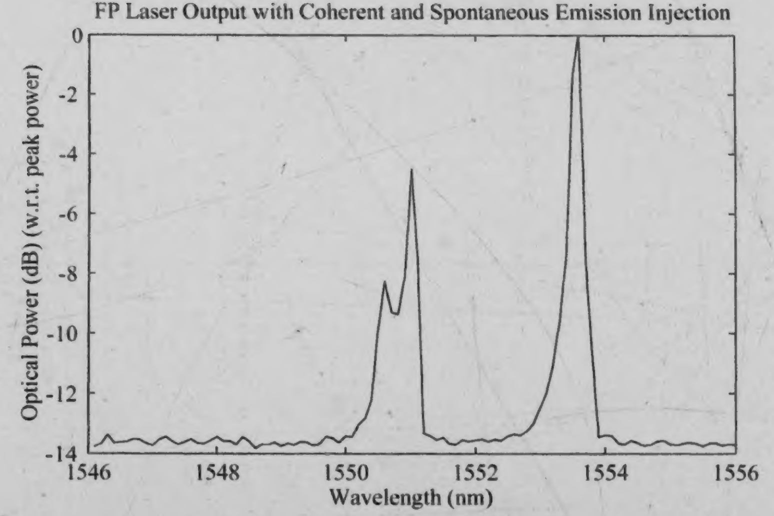

Figure 3-19: The optical spectrum of the FP laser with spontaneous emission injection near 1550.8 nm and coherent (laser) injection near 1553.5 nm with a calibration wavelength at 1550.79 nm. Measured with a monochromator.

When the coherent injection power is changed while holding the ASE injection power constant, the predicted mode shift occurs, see Figure 3-20.

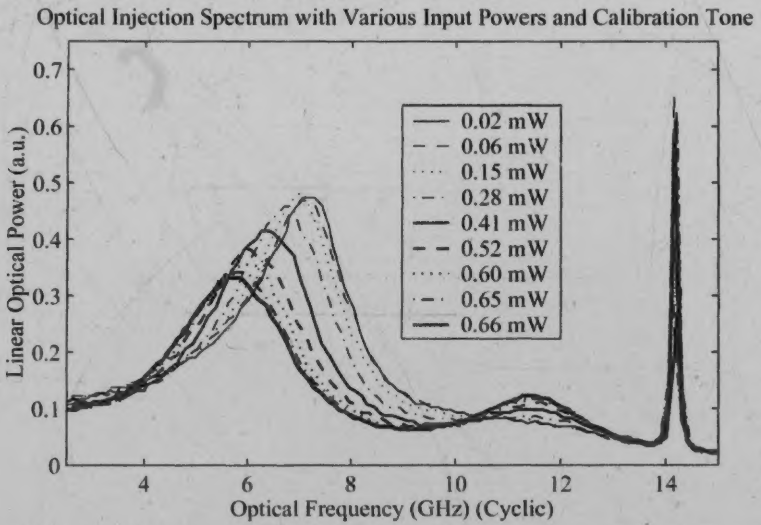

Figure 3-20: The optical spectrum of the FP laser as measured with a 40.4 GHz FSR tunable Fabry-Perot filter. The injected laser light is shown at approximately 14 GHz in the figure. The free-running FP laser mode shift is shown as a function of injected laser power.

The spectrum was measured with a tunable fiber-Fabry-Perot (FFP) filter with a free spectral range (FSR) of 40.39 GHz at wavelengths near 1550 nm and a finesse of approximately 400, which means that the spectral width of the filter is approximately 100 MHz. Because of the cyclic nature of the FFP, all of the light appears at the output of the filter when it is scanned through one FSR in optical frequency. The peak at the right hand side of Figure 3-20 is actually two laser peaks overlapped, one is the coherent injection laser and the other is a calibration laser source from a fiber DFB laser at 1550.79 nm. The fact that these two peaks overlap almost identically for all of the scans means that the injected laser wavelength did not change significantly throughout the tests. The wide peaks that shift left and diminish as the injected optical power is increased are the measurements of the dominant free-running slave laser mode. This consistent shift toward lower optical frequency and optical power is exactly what was predicted by the theory presented in Chapter 2. Two unfortunate limitations in the performance of these experiments were that the detuning of the coherent injection from the nearest slave laser Fabry-Perot mode and the actual power injected into the slave laser cavity could not be measured due to limitations of the measurement equipment. The optical powers shown in Figure 3-20 are the optical powers that were present in the fiber pigtail of the slave laser, the fiber to laser coupling efficiency was unknown and could not be measured. Due to these limitations the theory presented in Chapter 2 can be considered to be qualitatively verified but not correct in an exact sense.

Figure 3-20 qualitatively verifies the results of Section 2.10 with respect to the prediction that injection of spontaneous emission into the slave laser will substantially increase the linewidth of the laser modes where the spontaneous emission is spectrally significant. When the slave laser is free of spontaneous emission injection the individual modes appear to be as narrow as the calibration mode shown in Figure 3-20, with linewidths too narrow to resolve with a FP filter with a spectral resolution of 100 MHz. The linewidth of the spontaneous emission assisted mode is greater than 2 GHz full width at half maximum (FWHM) which is consistent with the spectral width predicted in Figure 2.42 within an order of magnitude.

.The experiment described above was performed many times, each time the laser temperature was changed which changed the detuning of the coherent injection from the nearest slave laser FP mode. The absolute optical frequency detuning of the coherent injection from the slave laser mode could not be measured, so the measured frequency shifting of the free-running mode will be presented relative to an arbitrary offset which maintains the calibration laser source in the spectral scans at the same optical frequency. Twelve spectral scans at different optical frequency detunings are shown in Figure 3-21.

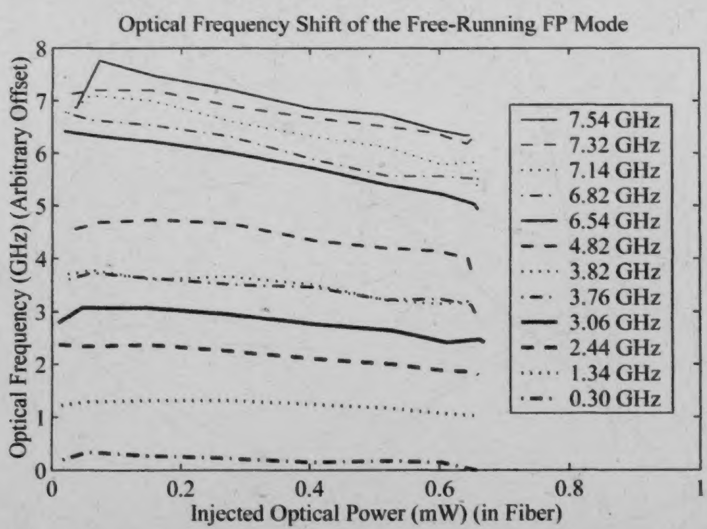

Figure 3-21: The center frequency of the free-running FP laser mode as a function of injected optical power (in the fiber) for various values of optical frequency offset. The values in the legend were derived from linear least squares fits to the lines in the figure at 0 injected optical power.

Increasing the injected optical power decreases the free-running optical frequency by as much as 2 GHz with less than 0.7 mW incident in the fiber pigtail of the slave laser with an efficiency of 2.86 GHz/mW. Figure 3-21 identifies the different experimental results via the optical frequency (relative to the arbitrary offset) that would be expected without optical injection as derived from linear least squares fitting to each individual curve in the graph. The slope of the curves in the graph can be derived from the same least squares fit and is the conversion efficiency of optical power to optical frequency shift of the optical injection which is plotted versus the derived optical frequency offsets in Figure 3-22.

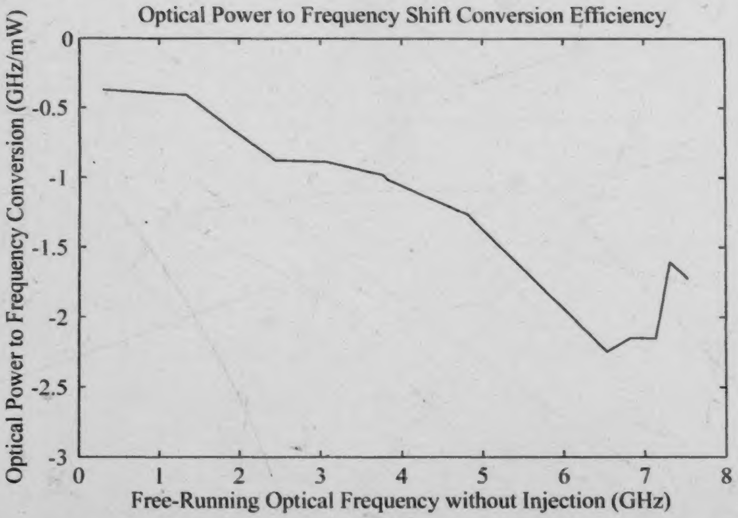

Figure 3-22: The conversion efficiency of the free-running FP laser mode shift in GHz/mW of injected optical power (in the fiber) as a function of the free-running optical frequency without optical injection (offset arbitrarily).

For negative optical detunings, the injected laser light should be at a lower optical frequency than the free-running frequency of the nearest laser mode. The linear conversion efficiency at low injection power should be higher for low detunings from the results in Chapter 2, the opposite is seen in Figure 3-22 where lower optical detunings should occur for lower free-running optical frequencies (since the frequency of the injected laser mode does not change).

One relevant conclusion that can be drawn from the results of this section is that the co-injection experiments did not cause significant instabilities in the slave laser due to the absence of relaxation oscillation side-bands in Figure 3-20. All of the results presented so far have been for steady state optical injection where the injected laser light was not modulated, the following section describes the experiments that were conducted when the laser injection was modulated.

3.2.6 Frequency Modulation of the Slave Laser.

When the master laser is modulated with the EO MZ modulator and co-injected with the narrow-band ASE the result is the modulation of the slave laser. Figure 3-23 shows the basic experimental test setup for modulating the slave laser.

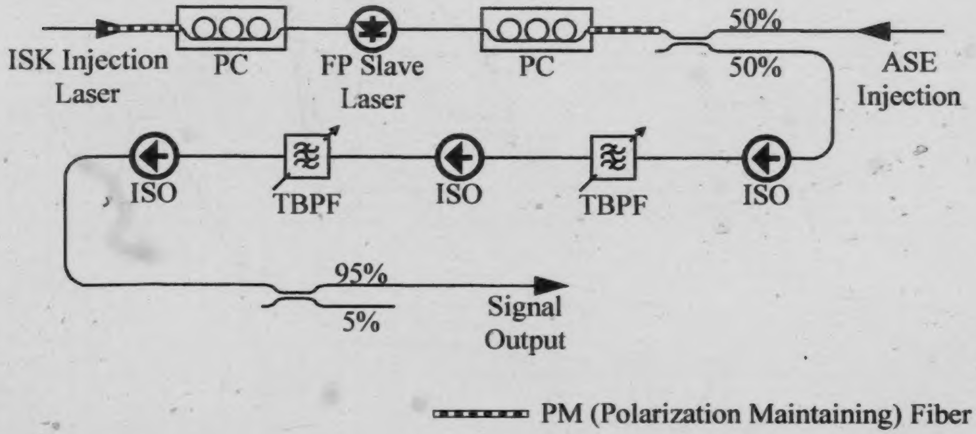

Figure 3-23: The FP slave laser shown with ASE injection and ISK injection where the output light is filtered twice and isolated to allow only the free-running (FCM signal) mode to appear at the signal output.

The optical schematics Figures 3-8 and 3-17 are implied to be connected to the input ports of Figure 3-23 and are not completely shown except for the polarization controllers at the end of each of the optical systems. The 50/50 coupler that was shown as part of the narrow band ASE system is shown here as where the slave laser output light will emerge. The isolators and the tunable band pass filters maintain the stability of the slave laser and provide a means to filter out the amplified ISK injection signal. The signal output should consist of only the frequency-modulated free-running mode of the slave laser.

The problem of too little optical power at the output occurs in the output of the system shown in Figure 3-23, making optical amplification necessary. Figure 3-24 provides the schematic of the signal output optics with optical amplifiers inserted after the desired FCM signal has been separated from the ASE injection signal.

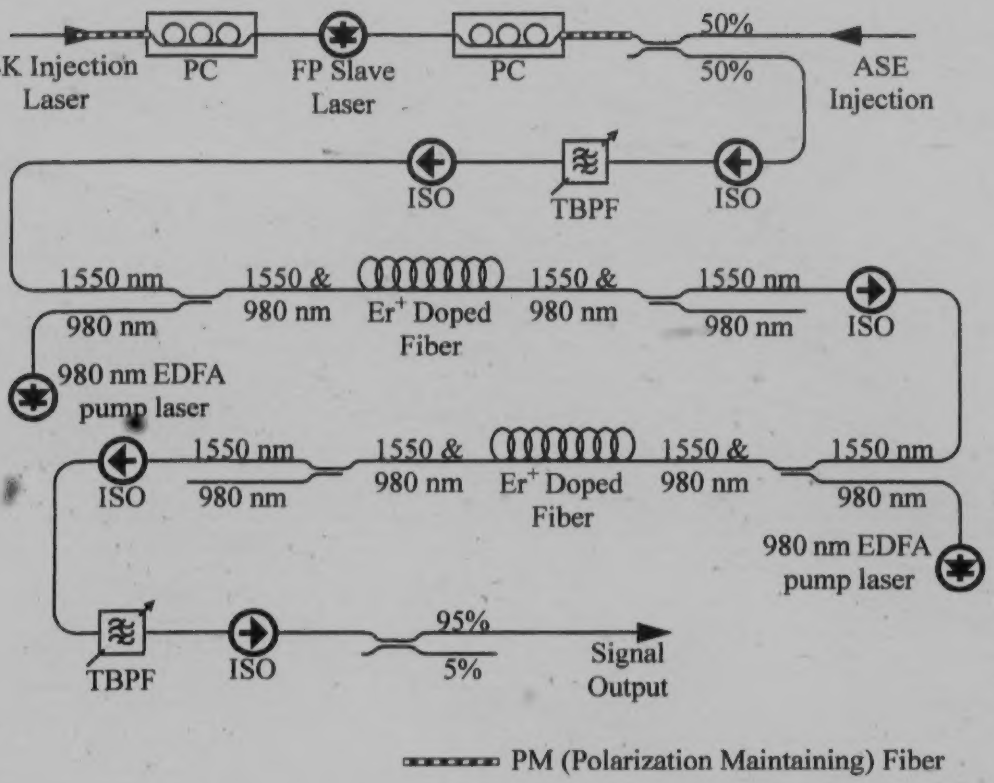
ISK Injection Laser
PC
FP Slave Laser
PC
50%
50%
ASE Injection
ISO
TBPF
ISO
1550 nm
980 nm
1550 & 980 nm
Er$^+$ Doped Fiber
1550 & 980 nm
1550 nm
980 nm
ISO
980 nm EDFA pump laser
ISO
1550 nm
980 nm
1550 & 980 nm
Er$^+$ Doped Fiber
1550 & 980 nm
1550 nm
980 nm
980 nm EDFA pump laser
TBPF
ISO
95%
5%
Signal Output
PM (Polarization Maintaining) Fiber

Figure 3-24: The FP slave laser shown with ASE injection and ISK injection where the output light is filtered, amplified and filtered again, as well as isolated, to allow more power of the free-running (FCM signal) mode to appear at the signal output.

The insertion of two optical amplifiers and two additional isolators made it possible to get several mW of signal power at the output at the expense of adding noise in the spectral vicinity of the signal.

Experiments were conducted using these optical arrangements as attempts to generate a binary FCM signal with an FP slave laser. The results of these tests were inconclusive as to whether or not the FCM signal was being generated correctly with optical injection.

3.2.7 Summary of Injection in FP Lasers.

Narrow-band spontaneous emission injection allows mode domination in FP lasers for the free-running mode nearest the spectral peak of the injected spectrum. The drawback of using noise to achieve spectral domination is the increase in the spectral width of the dominant mode.

The co-injection of spontaneous emission and coherent light into different and non-central modes of a DC biased FP laser produces frequency shift in the free-running mode where the shifting magnitude is related to the intensity of the optical injection. The efficiency of the shift depends on the relative spectral location of the injected coherent light to the free-running mode spectrum of the slave laser.

Tests that were conducted to prove that the FCM signal could be generated using FP lasers via the method described in previous sections were inconclusive.

Some of the tests performed on FP lasers were repeated using a DFB laser (without ASE injection). The following section provides background for understanding these tests and presents the test results.

3.3 Optical Injection Distributed Feedback FSK Transmitter.

In contrast with FP lasers, DFB lasers have the advantage that the primary source of feedback is provided by the semiconductor/air interface at the ends of the laser (acting as mirrors) with a secondary feedback source provided by a grating etched internally in the confining optical waveguide that forms the laser gain cavity, see Figure 3-25. The effective index of refraction of the DFB laser varies regularly in the direction of light propagation within the laser produce a grating of pitch Λ_g within the laser cavity. The relative phase of the grating with respect to the laser facets affects the spectral and stability properties of the laser, the details of which will not be discussed.

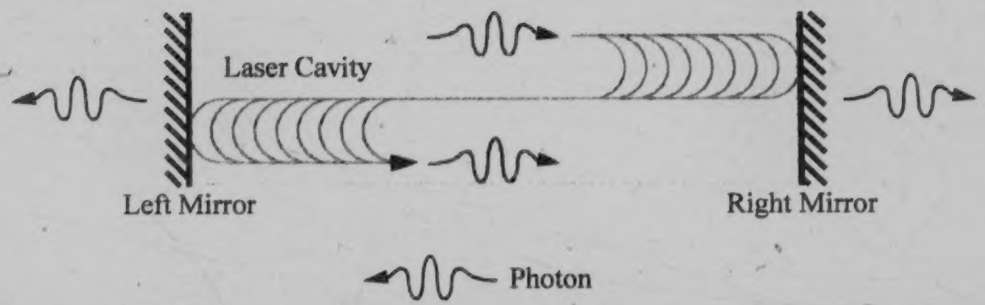

Figure 3-25: A functional diagram of a Distributed Feedback Laser showing that some feedback is due to reflections within the optical cavity with the ends of the laser (mirrors) providing the same feedback as they do in FP lasers.

The facets of the laser can be positioned with respect to the grating in such a way that the output spectrum will be strongly single moded and the wavelength of the oscillation will be close to the pitch of the internal grating. Some residual Fabry-Perot modes will exist within the gain-bandwidth of the laser and may be present several nanometers (up to tens of nm) away from the dominant mode depending on the position of the semiconductor gain peak. An example spectrum of the DFB semiconductor laser that was used for the experiments in this chapter is provided in at 14.9°C with a bias current of 50 mA.

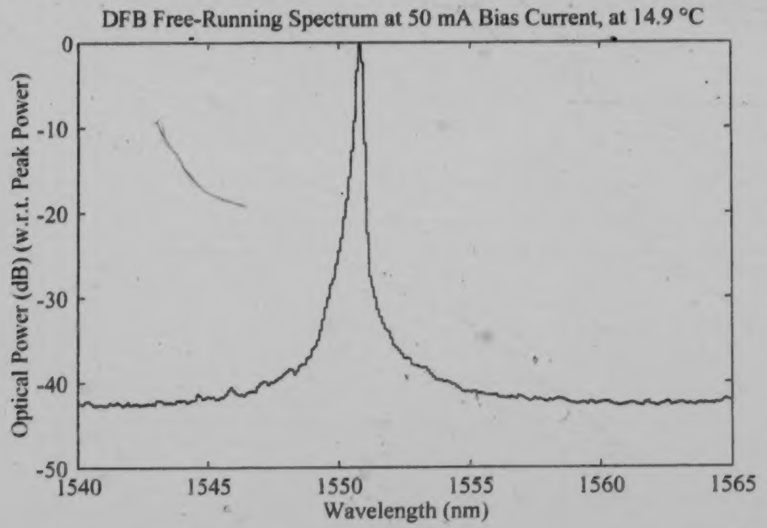

Figure 3-26: The free-running spectrum of the DFB slave laser biased at 50 mA and at 14.9 °C.

The spectrum shows one strong mode at approximately 1551 nm and several smaller modes can be seen on the lower wavelength side of the main peak at powers that are about 40 dB lower than the main mode power, these are residual FP modes of the DFB laser.

Regardless of whether or not the Fabry-Perot resonances of the DFB laser have sufficient gain to lase on their own, injection into the laser in spectral regions that are above transparency can experience net gain. It is the influence of the feedback due to facet reflections for injection of wavelengths that are not close to the Bragg grating pitch that determines the effectiveness of the injection. When the injected power and wavelength are correctly chosen with respect to the natural interference that occurs for an FP mode, stable oscillation at that wavelength in the DFB laser will result. The dominant free-running mode and the injected mode can oscillate together. The following section describes this co-oscillation in more detail.

3.3.1 Injection of Laser Light into Residual FP Modes of DFB Lasers.

The experiments that were conducted to assess the performance of the DFB laser when a constant optical power was injected into the laser cavity into a residual sidemode (Fabry-Perot mode) of the laser used a similar optical setup as was used for the FP laser, see Figure 3-27. The main difference between the DFB tests and the FP tests is the absence of the injection of spontaneous emission. The free-running output signal is filtered (to remove the injected wavelength), isolated and amplified. The facet reflectivities were asymmetric on the DFB slave laser. The facet that was used as the output in Figure 3-27 had a reflectivity of ~90%, which led to low output power and required the use of optical amplifiers again. The facet where the injected signal was incident had a normal reflectivity (~30%) and was used for injection since it yields a greater coupling efficiency.

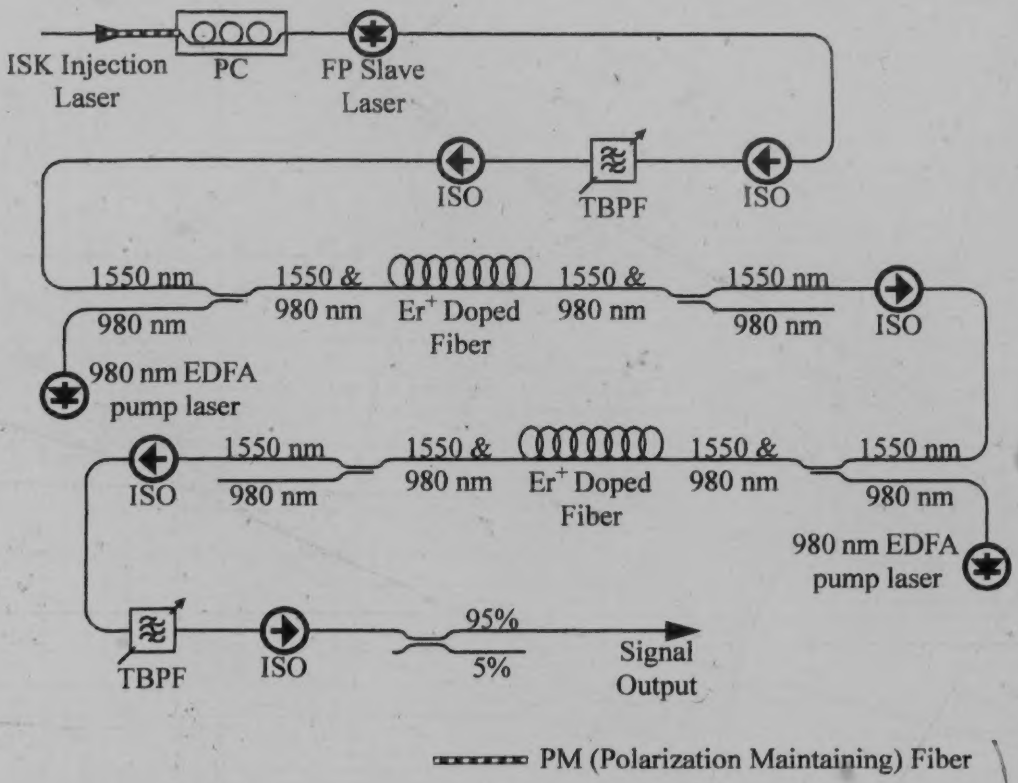
ISK Injection Laser
PC
FP Slave Laser
ISO
TBPF
ISO
1550 nm
980 nm
1550 & 980 nm
Er$^+$ Doped Fiber
1550 & 980 nm
1550 nm
980 nm
ISO
980 nm EDFA pump laser
ISO
1550 nm
980 nm
1550 & 980 nm
Er$^+$ Doped Fiber
1550 & 980 nm
1550 nm
980 nm
980 nm EDFA pump laser
TBPF
ISO
95%
5%
Signal Output
PM (Polarization Maintaining) Fiber

Figure 3-27: The DFB slave laser shown with the ISK injection where the output light is filtered, amplified and filtered again, as well as isolated, to allow more power of the free-running (FCM signal) mode to appear at the signal output.

When the coherent injection power is increased in the DFB slave laser, the predicted mode shift occurs, see Figure 3-28. The injection wavelength for these tests is 1553.4 nm which is at a slightly higher optical frequency compared to the FP injection experiments and which can be seen by noting the fact that the injected mode is tuned slightly higher than the calibration tone in the spectrum measurements. The spectrum was measured with the same tunable fiber-Fabry-Perot (FFP) filter as was used for the FP measurements.

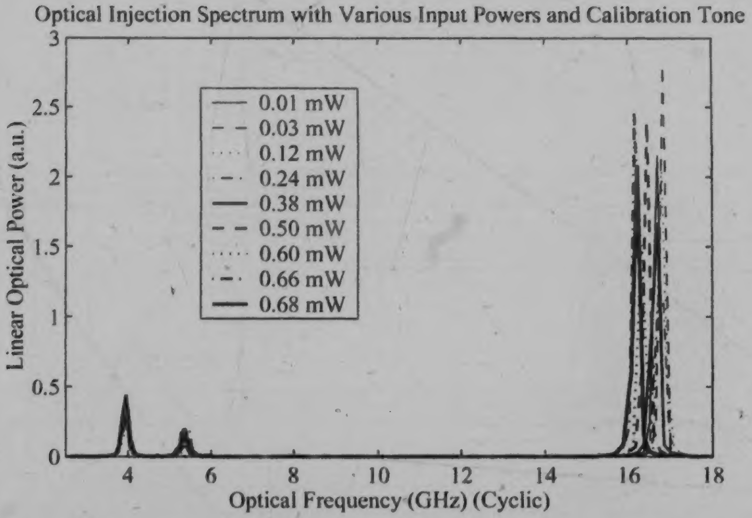

Figure 3-28: The optical spectrum of the DFB laser as measured with a 40.39 GHz FSR tunable Fabry-Perot filter. The injected laser light is shown at approximately 5.3 GHz in the figure. The free-running DFB laser mode shift is shown (on the right near 16 GHz) as a function of injected laser power. The calibration wavelength is near 4 GHz.

The peaks at the left hand side of Figure 3-28 are the injection laser and the other is a calibration laser source from a fiber DFB laser at 1550.79 nm. The fact that these two peaks are separated by the same difference in optical frequency for all of the scans means that the injected laser wavelength did not change significantly throughout the tests. The peaks on the right side of the figure that shift left and diminish as the injected optical power is increased are the measurements of the dominant free-running slave laser mode. The shift toward lower optical frequency is what was predicted by the theory presented in Chapter 2, although it is not seen as clearly as it was for the FP laser. Again, the limitations in the performance of these experiments were that the detuning of the coherent injection from the nearest slave laser Fabry-Perot mode and the actual power injected into the slave laser cavity could not be measured due to limitations of the measurement equipment. The optical powers shown in Figure 3-20 are the optical powers that were present in the fiber pigtail of the slave laser, the fiber to laser coupling efficiency was unknown and could not be measured. Due to these limitations the theory presented in Chapter 2 can be considered to be qualitatively verified but not correct in an exact sense.

Figure 3-28 qualitatively verifies the results of Section 2.10 with respect to the prediction that injection of coherent optical power into the DFB slave laser will not greatly increase the linewidth of the free-running modes. The spectral width change of the free-running mode is not measurable in the results of Figure 3-28, with linewidths too narrow to resolve with a FP filter with a spectral resolution of 100 MHz.

The experiment described above was performed many times, each time the laser temperature was changed which changed the detuning of the coherent injection from the nearest slave laser FP mode. The absolute optical frequency detuning of the coherent injection from the DFB slave laser mode could not be measured, so the measured frequency shifting of the free-running mode will be presented relative to an arbitrary offset which maintains the calibration laser source in the spectral scans at the same optical frequency. Three spectral scans at different optical frequency detunings are shown in Figure 3-29

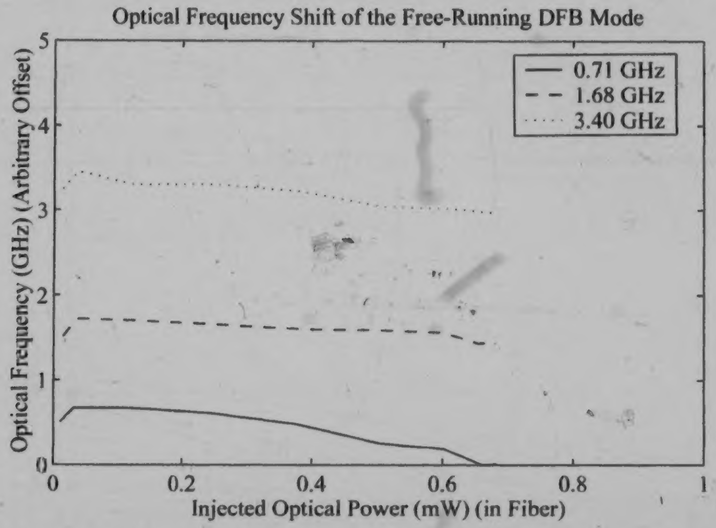

Figure 3-29: The center frequency of the free-running DFB laser mode as a function of injected optical power (in the fiber) for various values of optical frequency offset. The values in the legend were derived from linear least squares fits to the lines in the figure at 0 injected optical power.

Increasing the injected optical power decreases the free-running optical frequency by as much as 0.7 GHz with less than 0.7 mW incident in the fiber pigtail of the slave laser. Figure 3-29 identifies the different experimental results via the optical frequency (relative to the arbitrary offset) that would be expected without optical injection as derived from linear least squares fitting to each individual curve in the graph. The slope of the curves in the graph can be derived from the same least squares fit and is the conversion efficiency of optical power to optical frequency shift of the optical injection which is plotted versus the derived optical frequency offsets in Figure 3-30.

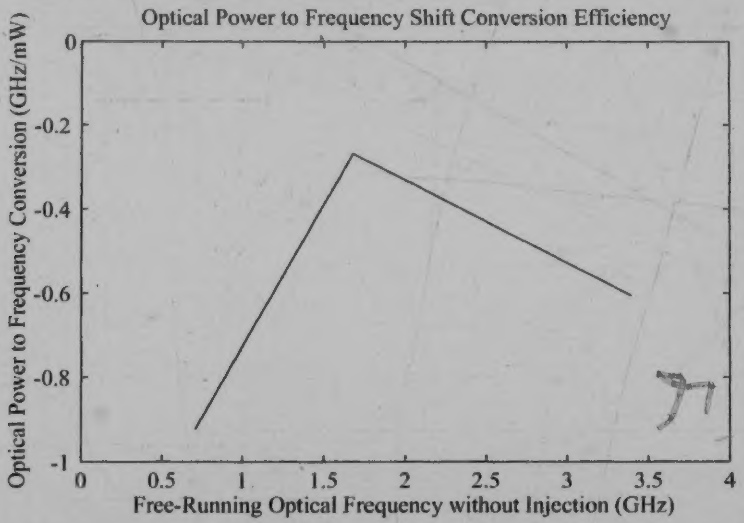

Figure 3-30: The conversion efficiency of the free-running DFB laser mode shift in GHz/mW of injected optical power (in the fiber) as a function of the free-running optical frequency without optical injection (offset arbitrarily).

For negative optical detunings, the injected laser light should be at a lower optical frequency than the free-running frequency of the nearest laser mode. The linear conversion efficiency at low injection power should be higher for low detunings from the results in Chapter 2 but, with only three results presented in Figure 3-30, it is inconclusive whether the trend has been verified or not.

These experiments on coherent injection into DFB lasers did not cause significant instabilities in the slave laser due to the absence of relaxation oscillation side-bands in Figure 3-28. The results in this section were for steady state optical injection into the DFB laser where the injected laser light was not modulated. There were no modulation experiments performed on DFB lasers, so the next section will summarize this chapter.

3.4 Summary of Optical Injection Experiments.

The experiments described in this chapter demonstrate that optical injection of coherent light into semiconductor laser cavities can result in shifts in the lasing frequency of the semiconductor laser that depend on the optical power of the injected light. This phenomenon was suggested by the results of the numerical simulations derived from rate equation analysis presented in Chapter 2, where this laser frequency shift was predicted for both Fabry-Perot (FP) and distributed feedback (DFB) lasers.

The results of experiments conducted on the FP laser discussed in Section 3.2 suggest that the conversion efficiency of injected optical power to free-running laser mode frequency shift can be greater than 2 GigaHertz per milliWatt of injected optical power. The experiments were conducted for low levels (less than 1 mW) of incident optical power, where incident in this context refers to the optical power in the fiber pigtail coupled to the laser facet. The power to frequency conversion efficiency is expected to be non-linear as a function of input optical power, but this could not be confirmed through any of the experiments that were conducted because of a lack of available optical power.

The results of experiments conducted on the DFB laser discussed in Section 3.3 suggest that the conversion efficiency of injected optical power to free-running DFB laser mode frequency shift is less than the FP laser conversion efficiency at a maximum of about 0.7 GigaHertz per milliWatt of injected optical power. The lack of available optical power again limited the scope of the experiments, but the results agree in general with the predictions of Chapter 2

The experimental results apparently contradict the predictions of Chapter 2 in one regard, the measured efficiency of the power to frequency conversion does not seem to increase with a decrease in optical detuning. But, since the absolute detuning of the optically injected light could not be determined with these experimental setups, this fact must be investigated further to provide irrefutable evidence to prove that there is a contradiction.

The laser frequency shifts of both FP and DFB lasers were measured with specific and attainable, but not necessarily optimum, conditions with DC optical injection only. The original intent of this experimental work was to optimize the injection conditions and perform experiments with injection of optical ISK signals and observe the generated FSK signals. This would require more experimental time. Discussion of necessary steps to modulation experiments is left to Chapter 7 where future work is discussed.

Chapter 3 concludes the discussion of the laboratory experiments conducted with optical injection. All further discussion of the performance of FCMA systems will rely on the results presented in Chapter 2 to generate input optical waveforms for assessment of the designs of the harmonic decoder based FCMA demultiplexor and the optical receiver, discussed in Chapter 4 and Chapter 5 respectively.

Chapter 4. Mach-Zehnder Interferometer Harmonic Decoders.

Passive demultiplexing and decoding of the optical FCM signal is accomplished using a set of harmonically related Mach-Zehnder interferometers, which was introduced in Section 1.5. The Mach-Zehnder (MZ) interferometer is an optical device with many applications such as optical spectral width measurement [BA1] or non-invasive sensors [HN1]. In communications, passive Mach-Zehnders have been used to decode differential binary signals for coherent transmission systems [EL1,KIMO1,MAJ3,MAL1,TO1,VO1,VO2] and electro-optic Mach-Zehnders are used as external modulators for ASK, PSK, and single-side-band (SSB) optical signal generation. The simplicity of the MZ is what makes it an attractive tool. A general free-space model of the MZ interferometer is shown in Figure 4-1.

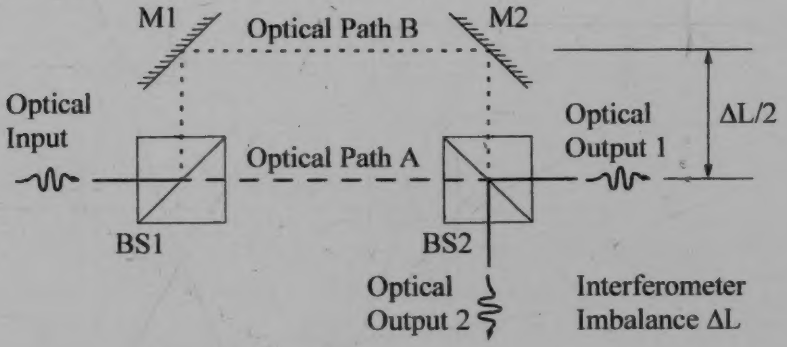

Figure 4-1: General optical layout of a free-space Mach-Zehnder interferometer with a path length difference of ΔL between Optical Path B and Optical Path A. (M1 and M2 are mirror 1 and 2, BS1 and BS2 are beam splitter 1 and 2.)

Mach-Zehnder interferometers can also be thought of as optical filters where, for an optical input of constant power and frequency with continuous phase, the optical power at one output of a lossless interferometer, P_{MZ+}, is calculated from the following function of input power and optical frequency,

$$P_{MZ+}(\nu) = P_{MZmax}\frac{1+\cos\left(\frac{2\pi\mu_{eMZ}\Delta L}{c}\nu\right)}{2}, \tag{55}$$

where P_{MZmax} is the input power, μ_{eMZ} is the index of refraction of the material in the arms (the two optical paths), c is the speed of light in vacuum, ΔL is the path length difference and ν is the input optical frequency. Equation (55), the DC response of the Mach-Zehnder interferometer, is an ideal equation and is limited in calculation capability. Equations used to model MZs in real applications must include the optical loss imbalance of the respective interferometer arms as well as accounting for any time dependency inherent in the input optical signal's power, frequency or phase. Analyses of these effects are presented in Sections 4.2 and 4.4 and applied to the decoding of the optical FCMA signal.

The passbands of the DC response are equally spaced in frequency with maxima ($P_{MZ+} = P_{MZmax}$) at

$$\frac{\mu_{eMZ}\Delta L}{c}\nu = integer, \tag{56}$$

which means that the free spectral range (FSR_{MZ}) is given by

$$FSR_{MZ} = \frac{c}{\mu_{eMZ}\Delta L}. \tag{57}$$

The minima ($P_{MZ+} = 0$) located exactly between successive maxima or, in other words, are located one half of the FSR from each maximum. A frequency shift keyed binary signal with the appropriate choice of mark and space optical frequencies (and constant optical power) can be converted to an amplitude shift keyed signal with a Mach-Zehnder interferometer.

Mach-Zehnder interferometers for modern signal processing applications, such as the application described in this document, are compact monolithic integrated devices. An integrated device was designed and fabricated for testing, but a free-space Mach-Zehnder, with variable delay length between the arms, was designed and constructed in case of fabrication problems with the integrated version. Also, the free-space interferometer allows interruption either (or both) of the optical signal paths without damaging the device and can be used to measure the effects of non-ideal transmitted signal characteristics, such as signal power fluctuation, insitu.

The response of the Mach-Zehnder interferometer to a general optical signal will be introduced in the context of demultiplexing Multilevel (*M*-ary) FSK signals as an introduction to the design of the experimental MZs, Section 4.1. Following this introduction, the free-space interferometer design will be presented with an explanation of the device function, Section 4.2. The integrated Mach-Zehnder devices are discussed in Section 4.3. A more specific description of the demultiplexing operation of the *M*-ary FSK signal will be presented in Section 4.4 that will include calculations of the response of the free-space and integrated MZ demultiplexors using Runge Kutta simulation results from Chapter 2. A brief introduction to the effects of phase noise on the output signals of MZ interferometers is the subject of Section 4.5, which is followed by a chapter summary, Section 4.6.

4.1 Interference for a Mach-Zehnder Interferometer.

The derivation of the interference equations for an MZ interferometer based on the free-space model for input with constant optical frequency and power and also with an arbitrary input will be presented in the following two sections. Figure 4-2 explicitly defines the terminology for each of these discussions by identifying the variables for electric field and optical power that will be used in the derivations.

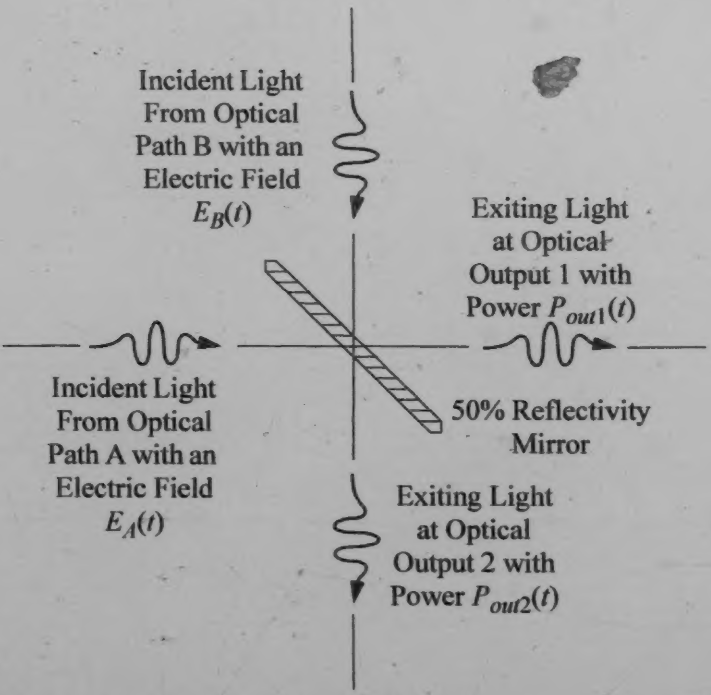
Incident Light
From Optical
Path B with an
Electric Field
$E_B(t)$
Exiting Light
at Optical
Output 1 with
Power $P_{out1}(t)$
Incident Light
From Optical
Path A with an
Electric Field
$E_A(t)$
50% Reflectivity
Mirror
Exiting Light
at Optical
Output 2 with
Power $P_{out2}(t)$

Figure 4-2: Schematic diagram of a 50% optical power splitter employing a partially reflective mirror. Input electric fields are $E_A(t)$ and $E_B(t)$ and the exiting light is denoted by optical powers $P_{out1}(t)$ and $P_{out2}(t)$.

The physical significance of the derived output powers, $P_{out1}(t)$ and $P_{out2}(t)$, for the case of constant incident amplitude and frequency for the incident electric fields, $E_A(t)$ and $E_B(t)$, will be shown to be a special case of the more general derivation for arbitrary incident amplitude and frequency. In both derivations, the electric field amplitude will be normalized to be the square root of the total input optical power, which is assumed to be split equally between the two arms of the MZ, and it will be assumed that the MZ is lossless.

4.1.1 Equal Incident Amplitudes and Constant Optical Frequency.

For the case of equal amplitudes of electric field in both optical paths of the interferometer, the incident electric field from optical path A, $E_A(t)$, and optical path B, $E_B(t)$, can be written as

$$E_A(t) = \frac{A_0}{\sqrt{2}} e^{-i\omega t} e^{-i\phi_t} \tag{58}$$

and

$$E_B(t) = \frac{A_0}{\sqrt{2}} e^{-i(\omega t - \omega\tau_{\Delta L})} e^{-i\phi_r}; \tag{59}$$

respectively, where A_0 is a constant electric field amplitude and $\tau_{\Delta L}$ is the additional transit time for light travelling along path B. The additional phases that appear in these equations, ϕ_t and ϕ_r, are there to account for the phase of the transmitted and reflected beams relative to the incident beam when the light interacts with the first beam splitter. The transit time difference, $\tau_{\Delta L}$, can be expressed in terms of the geometry of the MZ and the refractive indices of the materials in the optical paths if the index of refraction is integrated along the optical paths as in the following formula,

$$\tau_{\Delta L} = \int_B \frac{\mu(L)}{c} dL - \int_A \frac{\mu(L)}{c} dL, \tag{60}$$

where $\mu(L)$ is the refractive index along the optical path (either A or B) at position L and the integrals are evaluated from where the light is split to where the light recombines.

For a lossless 50% reflectivity mirror at the recombination beam splitter of the MZ interferometer, the equations describing the reflected and transmitted values of electric fields are,

$$E_{A1}(t) = \frac{A_0}{2} e^{-i\omega t} e^{-i2\phi_t} \tag{61}$$

for path A transmitting to output 1,

$$E_{A2}(t) = \frac{A_0}{2} e^{-i\omega t} e^{-i(\phi_t + \phi_r)} \tag{62}$$

for path A reflecting to output 2,

$$E_{B1}(t) = \frac{A_0}{2} e^{-i\omega t} e^{i\omega\tau_{\Delta L}} e^{-i2\phi_r} \tag{63}$$

for path B reflecting to output 1, and

$$E_{B2}(t) = \frac{A_0}{2} e^{-i\omega t} e^{i\omega\tau_{\Delta L}} e^{-i(\phi_t + \phi_r)} \tag{64}$$

for path B transmitting to output 2.

To obtain the output power transfer function from the MZ interferometer for output 1, Equations (61) and (63) are added and multiplied by the complex conjugate of this sum and the result is

$$P_{out1} = \left|E_{A1}(t) + E_{B1}(t)\right|^2 = \frac{A_0^2}{2}[1 + \cos(\omega\tau_{\Delta L} - 2(\phi_t - \phi_r))]\,. \tag{65}$$

The equation for the output optical power from output 2 is calculated from Equations (62) and (64) which gives the following result,

$$P_{out2} = \left|E_{A2}(t) + E_{B2}(t)\right|^2 = \frac{A_0^2}{2}[1 + \cos(\omega\tau_{\Delta L})]\,. \tag{66}$$

These equations hold for arbitrary input light at arbitrary incident angles, with respect to the mirror surfaces, as long as the reflectivity at that particular incident angle is 50% and the incident angles are the same for the splitting beam cube and the recombining beam cube.

Equations (65) and (66) were derived under the assumption that the interferometer was lossless, which means that, for any particular input frequency of light, the total output power should equal the total input power to conserve energy. This fact restricts the relative phase of the reflection and transmission of the light and the difference in phase between ϕ_t and ϕ_r must be identically 90°. The converse of this statement is that when the relative phase between transmission and reflection at the beam splitter cubes is not identically 90° the MZ interferometer cannot be lossless.

The generic equations presented at the beginning of the chapter that describe the relationship between FSR and the maxima of the response, Equations (55) and (57), must be modified to account for general phase differences between the transmissions and reflections of the beam splitter cubes. General phase differences result in what seem like arbitrary relationships between the MZ FSR and maxima of the response functions. Fortunately, for FCM signals, shifting the maxima of the MZ response to match the incoming signal will not change the FSR much, because the order of the MZ interferometers are high enough, and the signals can still be decoded. What will be shown later, in Sections 4.2 and 4.4, is the measurement of a real MZ interferometer where this phase condition is nearly met.

When the amplitude or frequency, or both, of the light entering the interferometer change as a function of time, these equations are no longer valid. The following subsection explains what modifications need to be made to the derivation to include time variations of the input signal.

4.1.2 MZ Interferometer Response to an Arbitrary Signal.

An arbitrary input optical signal is defined here as a signal that varies in both optical power and frequency but has continuous phase. The definitions of the optical electric fields that are incident on the mirror, as shown in Figure 4-2, are

$$E_A(t) = \frac{A_0(t)}{\sqrt{2}} e^{-i\phi(t)} e^{-i\phi_r} \tag{67}$$

and

$$E_B(t) = \frac{A_0(t-\tau_{\Delta L})}{\sqrt{2}} e^{-i\phi(t-\tau_{\Delta L})} e^{-i\phi_r}, \tag{68}$$

where discontinuities in the amplitude and frequency of the optical signal are allowed. The condition of continuous phase imposes the following equation that relates the phase to the optical frequency,

$$\phi(t) = \int_0^t \omega(t')dt', \tag{69}$$

where $\phi(0) = 0$.

The output from the MZ interferometer is squared modulus of the sum of the interfering electric fields,

$$P_{out1} = \left|E_{A1}(t) + E_{B1}(t)\right|^2, \tag{70}$$

which is the result for output 1 only. Evaluating the modulus squared of the above equation yields the general result that includes the substitution of Equation (69),

$$P_{out1} = \left(\frac{A_0(t)}{2}\right)^2 + \left(\frac{A_0(t-\tau_{\Delta L})}{2}\right)^2 + \frac{A_0(t)A_0(t-\tau_{\Delta L})}{2}\cos\left(\int_{t-\tau_{\Delta L}}^{t} \omega(t')dt' - 2(\phi_t - \phi_r)\right). \qquad (71)$$

The optical output power at output 2 is given by the following equation,

$$P_{out2} = \left(\frac{A_0(t)}{2}\right)^2 + \left(\frac{A_0(t-\tau_{\Delta L})}{2}\right)^2 + \frac{A_0(t)A_0(t-\tau_{\Delta L})}{2}\cos\left(\int_{t-\tau_{\Delta L}}^{t} \omega(t')dt'\right). \qquad (72)$$

These equations do not include the effect of different losses in different paths of the interferometer and the effect of phases other 90° between transmissions and reflections. The different MZ designs, free-space and integrated, impose different loss and phase modifications to the output power equations and will be investigated after discussions of the respective designs. The design of the free-space MZ is presented in the following section.

4.2 Design of the Free Space Mach-Zehnder Interferometer.

All of the components of the prototype FCMA system were to be built using fiber pigtailed components with the exception of the Mach-Zehnders. The free space MZ operates as a single-mode fiber compatible optical system. The FSK signal enters the interferometer from a cleaved fiber pigtail and is collimated by an objective. This collimated beam of light passes through the interferometer and is focused by objectives into two single-mode fiber pigtails, one for each interferometer output. Coupling from a single-mode fiber into a free space optical system and back into single-mode fibers is a difficult mechanical problem. The diameter of the core of single mode fiber is ~9 μm and the numerical aperture is ~0.14 for wavelengths in the 1550 nm region. Mechanical stability of the hardware components of the interferometer has to be high.

Minimizing the cumulative optical power loss for the optical signal passing through the interferometer is another concern, as is having the ability to precisely align the interfering beams of light at the combining surface of the beam splitter. The subsequent subsections address these important design criteria for free space Mach-Zehnder interferometers.

4.2.1 Optical Component Layout.

The free space Mach-Zehnder interferometer that was designed for this project was based on an equilateral triangle layout, see Figure 4-3.

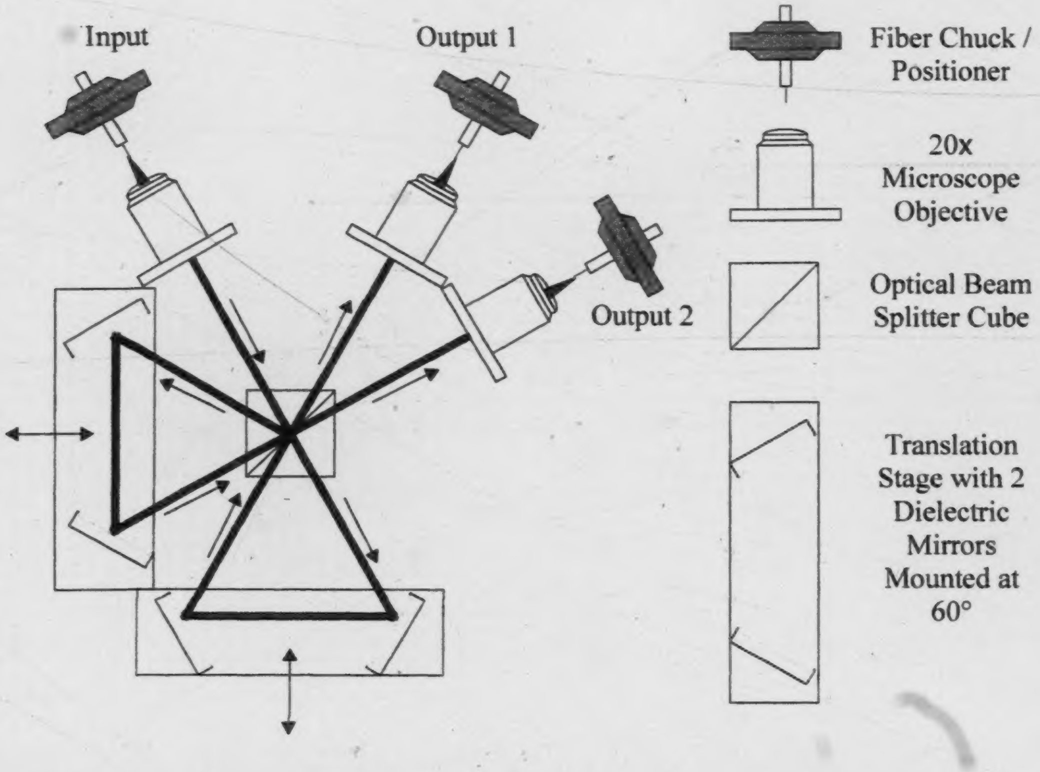
Input
Output 1
Output 2
Fiber Chuck / Positioner
20x Microscope Objective
Optical Beam Splitter Cube
Translation Stage with 2 Dielectric Mirrors Mounted at 60°

Figure 4-3: Optical component layout of a free-space Mach-Zehnder interferometer based on an equilateral triangle geometry (shown in plan view looking from above the optical table). The arrows show the direction the light travels along the optical paths in thick lines.

There are advantages to using this interferometer. First, any reflections from the faces of the beam splitter cube will not be colinear with any of the optical paths. Second, both arms of the Mach-Zehnder are independently adjustable to optimize path difference between the respective arms. Third, it is possible to get very low path length differences between the respective arms which is prohibited in the layout depicted in Figure 4-1 by the physical dimensions of the beam splitter cubes and the mirrors. The disadvantage of this arrangement is that it requires a beam splitter cube that has the same reflectivity and transmissivity at two different angles. In the most common beam splitter designs, the reflection from the 50/50 mirror in the splitter will only be 50/50 for light entering at normal incidence with respect to the beam splitter face. For the experiments that were conducted the beam splitter was approximately 50/50 only at normal incidence, so any analysis that is presented will consider the effects of asymmetry between reflections and transmissions. The origins of power and phase asymmetry between reflections and transmissions from metallic or dielectric partial mirrors are well explained, as in [BORN1] for example, and will not be covered here.

There are requirements for choosing appropriate optical components for a free-space interferometer and some specific concerns that apply to building this particular interferometer. Then next section addresses these requirements and concerns.

4.2.2 Optical Component Specifications.

Collimation of the light emanating from the fiber pigtail has to be done with a lens or objective with a numerical aperture that is larger than the numerical aperture (NA) of the fiber. Also, the magnification of the collimation optics has to produce a beam of light with diameter that does not exceed the physical dimensions of any of the reflecting surfaces used in the interferometer. For these reasons, a 20**x** objective with an NA equal to 0.4 was used and produced a beam of ~1 mm diameter. To provide symmetry between input and output fiber couplings, identical objectives were used at the output end of the interferometer.

The fiber chucks that were used to hold the input and output fibers were true chucks that clamped down on the 900 μm buffer of the fiber. The fiber was cleaved less than 3 mm from the end of the buffer, so the fiber was mechanically constrained with a low risk of wobbling.

The mirrors in the arms of the MZ interferometer were high reflectivity dielectric front surface mirrors that were optimized for use with infrared light in the 1550 nm region.

The splitting ratio of the beam splitter cube is not quite 50/50 for the designed normal incidence, and definitely not 50/50 for arbitrary incident angles. Also, the splitting ratio is different for orthogonal polarizations. As well, without being able to tell from the manufacturers data, the relative phase of the reflected beam to the transmitted beam is also assumed to be polarization dependent. The asymmetry of the splitting ratio can be compensated with a neutral density filter, but the polarization effects could only be dealt with by controlling the input polarization with a fiber compatible polarization controller.

Once the MZ was designed and built, the free spectral range and optical power transmission and reflection coefficients could be measured. These measurements are described in the next section.

4.2.3 Operation of the Free-Space Mach-Zehnder Interferometer.

The intent of building this free-space MZ interferometer was to have a backup device in case the integrated MZ decoder did not work correctly. This interferometer was designed such that the optical delay length could be easily changed and could obtain very low values without significant realignment. Calibration of the free-space MZ interferometer was performed in terms of the optical power response to a signal that varied in optical frequency, the FSR could be derived from this calibration.

A temperature stabilized DFB laser was modulated at a frequency of 1 kHz to produce a signal that varied sinusoidally in optical frequency. This signal was fed into the free-space MZ polarized parallel to the optical bench and the optical power was measured at the output, as depicted in Figure 4-4.

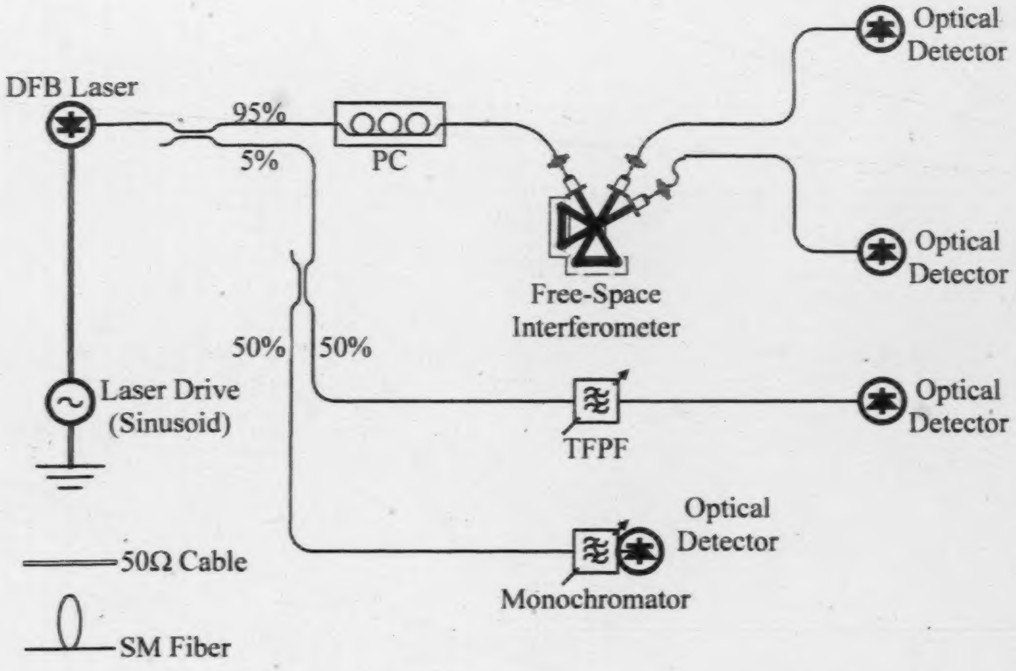
DFB Laser
95%
5%
PC
Optical Detector
Optical Detector
Free-Space Interferometer
50%
50%
Laser Drive (Sinusoid)
TFPF
Optical Detector
Optical Detector
Monochromator
50Ω Cable
SM Fiber

Figure 4-4: The optical schematic for measuring the free spectral range of the free-space MZ interferometer. (TFPF = tunable Fabry-Perot filter, SM = single mode)

The optical power at the outputs of the MZ interferometer were measured by Newport optical power meters which produce an electrical waveform proportional to the received optical power. These waveforms were captured on a Tektronics digital oscilloscope and the traces were analyzed to extract information about the phase offset of transmissions versus reflections for the interference of the input light. The monochromator and the tunable Fabry-Perot filter (TFPF) were used to monitor the wavelength of the input light to ensure that the optical frequency waveform was stable. The Fabry-Perot filter can also be used to find the FSR of the MZ interferometer since it's FSR is known (40.39 GHz).

The measurement described in this section enabled measurement of the FSR of the MZ interferometer but this is only part of what needs to be calibrated to understand the operation of the device. The magnitudes of the reflections and transmissions at the angles of incidence that were used must also be known. The next two sections describe the reason that the optical power coefficients are important and how these values were determined.

4.2.4 The Signal Power Budget.

For a beam splitter based MZ interferometer, the output optical powers depend on the amplitudes and phases of the reflections and transmissions. In analogy to the derivations presented in Sections 4.1.1 and 4.1.2, the following derivation will use the same notation and supplement the equations with the reflectances and transmittances at the relevant incident angles.

The angle of incidence is 30° to the normal of the cube face and refracts to ~15° inside the cube, ultimately hitting the partially reflective mirror at ~25° to the mirror normal, as shown in Figure 4-5.

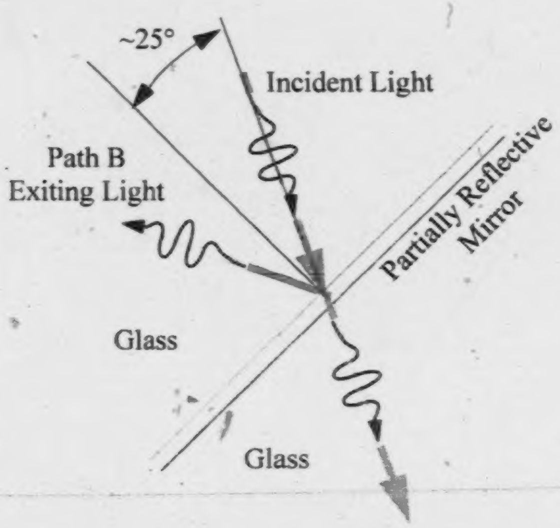

Figure 4-5: Light that is input to the free space interferometer is shown to be partially reflected by the partially reflective mirror of the beam splitter cube.

Light exits the beam splitter cube from two of the faces where it will refract to the original 30° to the cube face normal. The transmitted electric field (Path A) is related to the incident electric field by

$$E_A(t) = t_{25}A_0(t)e^{-i\phi(t)}, \quad (73)$$

where t_{25} is the transmission coefficient at 25° to the reflecting surface, including reflection losses at the cube surfaces. The reflected electric field (Path B) is similarly related to the incident electric field by

$$E_B(t) = r_{25}A_0(t-\tau_{\Delta L})e^{-i\phi(t-\tau_{\Delta L})}, \quad (74)$$

where r_{25} is the reflection coefficient at 25° to the reflecting surface, including reflection loss at the cube surfaces. Equation (74) also includes an arbitrary time delay, $\tau_{\Delta L}$, with respect to Equation (73).

The light returns to the beam splitter cube after being reflected by dielectric mirrors and is incident on the beam splitter on two faces with 30° angles of incidence to the respective faces. The two beams refract upon entering the cube and will be at ~65° off the normal of the partially reflective mirror, as shown in Figure 4-6.

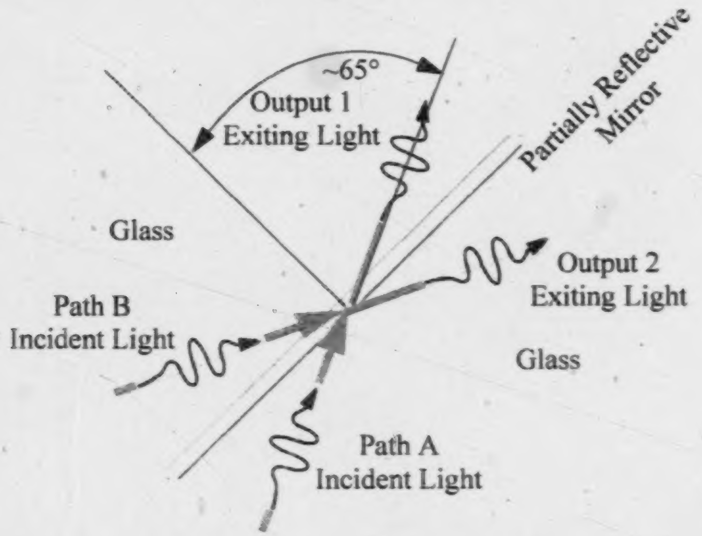

Figure 4-6: Light re-enters the beam splitter cube of the free space interferometer and is forced to interfere at the by the partially reflective mirror of the beam splitter cube producing two output light beams.

Expressions for the transmitted and reflected parts of the two incident beams including the transmission and reflection coefficients of the partially reflective mirror at 65° incidence are

$$E_{A1}(t) = t_{65}t_{25}A_0(t)e^{-i\phi(t)}, \tag{75}$$

for light entering from path A of Figure 4-6 and exiting at output 1,

$$E_{A2}(t) = r_{65}t_{25}A_0(t)e^{-i\phi(t)}, \tag{76}$$

for light entering from path A and exiting at output 2,

$$E_{B1}(t) = r_{65}r_{25}A_0(t-\tau_{\Delta L})e^{-i\phi(t-\tau_{\Delta L})}, \tag{77}$$

for light entering from path B and exiting at output 1, and

$$E_{B2}(t) = t_{65}r_{25}A_0(t-\tau_{\Delta L})e^{-i\phi(t-\tau_{\Delta L})}, \tag{78}$$

for light entering from path B and exiting at output 1.

The output power exiting at output port 1 of Figure 4-6 is found by combining the results of Equations (75) and (77),

$$\begin{aligned} P_{out1} &= \left|E_{A1}(t) + E_{B1}(t)\right|^2 \\ &= \left|t_{65}t_{25}A_0(t)e^{-i\phi(t)} + r_{65}r_{25}A_0(t-\tau_{\Delta L})e^{-i\phi(t-\tau_{\Delta L})}\right|^2. \end{aligned} \tag{79}$$

The output power exiting at output port 2 is evaluated in a similar manner from Equations (76) and (78). Evaluating the modulus squared of the sum of these equations yields the general result that includes the substitution of Equation (69),

$$\begin{aligned} P_{out1} = {} & T_{65}T_{25}(A_0(t))^2 + R_{65}R_{25}(A_0(t-\tau_{\Delta L}))^2 + \\ & 2|t_{65}||t_{25}||r_{65}||r_{25}|A_0(t)A_0(t-\tau_{\Delta L})\cos\left(\int_{t-\tau_{\Delta L}}^{t} \omega(t')dt' + \phi_{ttrr}\right), \end{aligned} \tag{80}$$

where

$$t_{65}t_{25}r^*{}_{65}r^*{}_{25} = |t_{65}||t_{25}||r_{65}||r_{25}|e^{-i\phi_{ttrr}}, \tag{81}$$

and for output 2 of the interferometer

$$P_{out2} = R_{65}T_{25}(A_0(t))^2 + T_{65}R_{25}(A_0(t-\tau_{\Delta L}))^2 + \\ 2|t_{65}||t_{25}||r_{65}||r_{25}|A_0(t)A_0(t-\tau_{\Delta L})\cos\left(\int_{t-\tau_{\Delta L}}^{t} \omega(t')dt' + \phi_{trtr}\right), \tag{82}$$

where

$$t_{25}r_{65}t^*{}_{65}r^*{}_{25} = |t_{65}||t_{25}||r_{65}||r_{25}|e^{-i\phi_{trtr}}. \tag{83}$$

These are general equations for beam splitter based MZ interferometers where the phases of the transmission or reflection coefficients can be changed to any angle.

For beam splitter based MZ interferometers, one must rely on the relative phases of reflections and transmissions to be well behaved in order to get good performance. For optimum performance the phase difference for the cosine arguments of Equations (80) and (82) must be exactly π.

4.2.5 Experimental Values for Beam Splitter Equation Coefficients.

The coefficients for Equations (80) and (82) were found by measuring the response of the MZ interferometer to input light. The non-cosine terms could be found from measuring the response of the device while blocking one or the other port to get the static magnitude responses of either of path A or path B. For input light at 1550 nm, the values for these terms of the equations are

$$T_{65}T_{25} \approx 0.06245, \tag{84 a}$$

$$R_{65}R_{25} \approx 0.1280, \tag{84 b}$$

$$R_{65}T_{25} \approx 0.3805 \tag{84 c}$$

and

$$T_{65}R_{25} \approx 0.01830. \tag{84 d}$$

The magnitude of the interference term can also be found the same types of measurements and the coefficient value is

$$|t_{65}||t_{25}||r_{65}||r_{25}| \approx 0.0869\,. \qquad (85)$$

The cumulative phases of all of the reflection and transmission terms are very difficult to measure individually, but the difference of the phase terms can be found from interference experiments where a DFB laser is modulated at low frequency and the output is measured as a function of time. At low frequency (1 kHz was used), the DFB output power varies sinusoidally with a sinusoidal drive current and, due to thermal frequency chirp effects in the laser cavity, so does the output optical frequency of the DFB. By recording the response of the MZ interferometer with an oscilloscope for the two outputs and curve fitting to the oscilloscope traces, the relative phases of the two outputs can be found to be

$$\phi_{trtr} - \phi_{ttrr} \approx 3.151\,, \qquad (86)$$

for light at ~1550 nm in wavelength.

Only the relative phase is important because phase offsets can be compensated by slightly modifying the center frequency of the input optical signal or the delay length by small amounts. The values presented in this section will be used in the following sections and chapters to calculate the overall system performance using the free-space beam splitter MZ interferometer as a harmonic decoder. A description of the integrated (planar) MZ interferometer is presented in the next few sections, which will be followed by simulated responses to simulated input for MZ harmonic decoders.

4.3 Design of the Integrated Mach-Zehnder Interferometers.

The design of the integrated MZ interferometer was based on a planar Silicon OxyNitride (SiNO) material system because of the wide range of available refractive indices and low absorption loss [BON1,WOR1]. The design incorporated four independent MZ devices fed from the same input with harmonically related FSRs. The MZ with the largest delay time was designed to delay an Gigabit Ethernet bitrate signal by 1/3 of the bit time. Using the large range of refractive indices and an air-clad ridge waveguide structure, tight waveguide bends were possible and the four MZ devices were integrated into an area slightly larger than 2 cm^2. The drawback of using the air-clad waveguides was that single-mode guides have a large numerical aperture.

The following sections describe the design of the integrated MZ devices in detail, beginning with the layout of the photomask that was used to fabricate the waveguide structure.

4.3.1 Device Layout.

The four harmonically related MZ interferometers were fed from a common input waveguide, the input light was split equally between four waveguides using a multimode interference (MMI) 1x4 coupler where each of these waveguides each fed one of the four MZ devices. Figure 4-7 shows the layout of one of the devices that was included on the photomask.

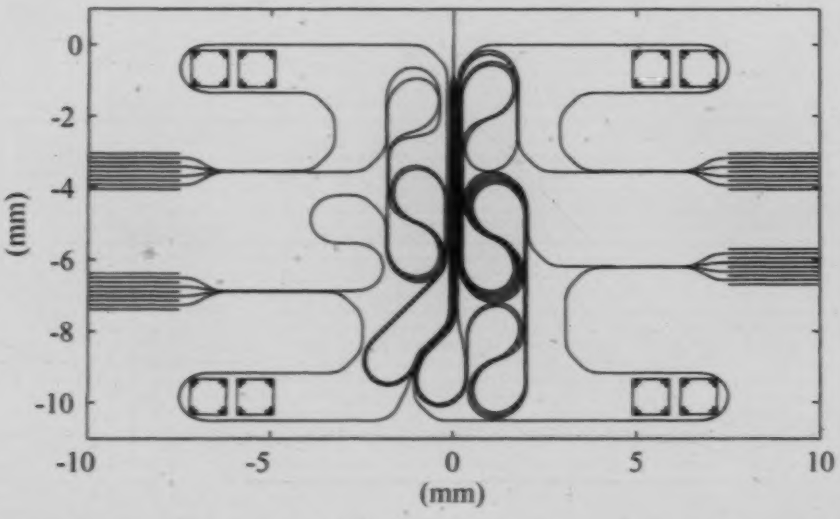

Figure 4-7: An example device layout for the photomask. This device has four MZ interferometers that have a common input.

In Figure 4-7 the input is at the top which is split four ways by the 1x4 MMI section directly beneath it. These four output waveguides fan-out to a spacing of 50 μm before entering four 1x2 MMI splitters. These splitters are the separation point for each of the four MZ devices, the output waveguides fan-out from here to a spacing of 25 μm. Two pairs of waveguides go to the left and two pairs go to the right as shown at the bottom of

Figure 4-7.

The MZ interferometers on the right have the two smallest FSRs. One waveguide from each of these waveguide pairs is routed around to the edge of the device area where they make U-shaped turns around some square features, whose purpose will be explained later. The other two waveguides coil around each other and all of these waveguides are then routed to their respective recombination 2x4 MMI couplers. The two outputs of the 2x4 MMI couplers that are closest to the central axis of the coupler are correctly positioned for receiving the interfering 1550 nm light, the other two outputs are monitor ports for thermal monitoring which will be explained later.

The MZ interferometers on the left have the larger FSRs. These waveguides are routed in a similar manner as was described in the previous paragraph to end up at their respective recombination MMI 2x4 couplers.

This mask layout was written to a text file from Matlab code that generates CIF compatible photomask layout commands. The Matlab code was written in such a way that the delay lengths were calculated harmonically from one MZ length and the layout adjusted dynamically to accommodate any length change by altering this one input parameter. The file was converted from CIF to GDSII that was written to a chrome on quartz photomask by e-beam lithography at Nortel Networks.

The resulting photomask was to be used to fabricate the waveguide devices using standard photolithographic techniques. Descriptions of the desired properties of the waveguide devices follow in the next three sections.

4.3.2 Waveguide Parameters.

The waveguides were etched from layers of Silicon OxyNitride (SiON) that were deposited on silicon wafers. The refractive indices of the top layer (the guiding layer) and the substrate layer were 1.55 and 1.5, respectively. The single mode waveguides that connected the couplers and splitters were 2 μm high by 2.5 μm wide, as depicted in Figure 4-8.

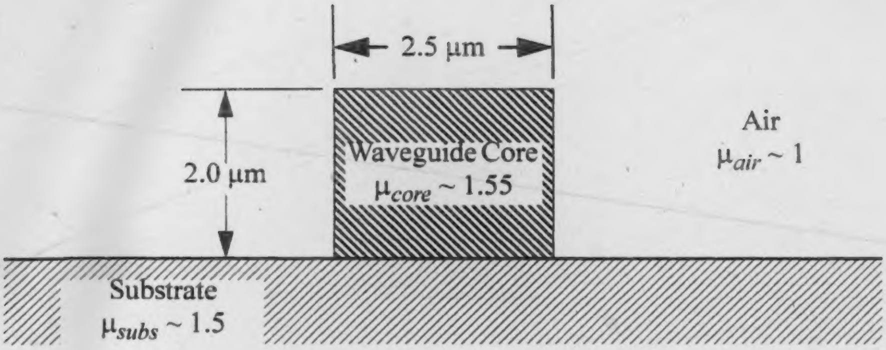

Figure 4-8: A scale drawing of the single mode waveguide sections of the harmonically related MZ interferometer devices that were fabricated. The waveguide core is 2 μm high by 2.5 μm wide with a refractive index of 1.55, and the substrate has a refractive index of 1.5.

Waveguides with these dimension and refractive indices are very tightly confining for 1550 nm light, the propagating waveguide mode does not extend very far into the air or the substrate. With such tight confinement to the waveguide, the numerical aperture will be very high.

The waveguide supports two modes, one with vertical polarization and one with horizontal polarization, each of which is the lowest order mode for it's respective polarization. Modes in waveguides like this are not truly transverse electric or transverse magnetic modes, so these modes will be referred to as vertical, with variable subscripts containing V, and horizontal, with variable subscripts containing H. A numerical mode solver, FWave, was used to obtain the electric field profiles and effective indices for both modes. The effective index of the vertically polarized mode was found to be 1.50271 and the effective index of the horizontally polarized mode was found to be 1.50157.

Two test lengths of 57.5 mm and 57 mm were used for the longest delay length interferometer. The other interferometer lengths were calculated as 1/2, 1/4 and 1/8 of these values. The length was calculated to accommodate tests for OC-12, Gigabit Ethernet and OC-48 bit rates where the Gigabit Ethernet delay length for the longest delay interferometer is roughly equal to the test length for a fractional bit delay time of 1/3.

The numerical aperture, NA, of the waveguide was found by finding the 1/e mode diameters of the electric field or electrical displacement (whichever is continuous) in the vertical and horizontal directions for both modes along lines that pass through the peak electric field for both modes. The distance between the 1/e points was used in an approximation formula for the divergence angle of a focused Gaussian beam, therefore, the NA of the waveguide is only a rough approximation because of the non-Gaussian shape of the waveguide modes. The numerical apertures and diffraction angles for the waveguide mode are listed in Table 4-1.

Table 4-1: Numerical apertures and divergence angles for the single mode waveguides for the integrated MZ harmonic decoder.

Waveguide Mode Polarization	Diffraction Direction	Numerical Aperture	Diffraction Angle
Vertical	Vertical	0.402	24°
	Horizontal	0.439	26°
Horizontal	Vertical	0.382	22°
	Horizontal	0.465	28°

Waveguides with these parameters were used to connect the splitters and couplers that are necessary to make the MZ devices and light had to be coupled in and out of these waveguides at the edges of the substrates. The following section discusses the design of the splitters and couplers that were used which are a special class of planar waveguide devices called multi-mode interference (MMI) couplers.

4.3.3 Multi-mode Interference Devices.

The basic theory for multi-mode interference (MMI) couplers was taken from [SO1] and the equations will not be repeated here. Using calculated multi-mode waveguide widths the effective indices of the MMI couplers were found by using FWave to solve for the electric field profiles within the multi-mode guiding sections. A width of 15.21 μm was used for the 1x4 splitter and the four 1x2 splitters and a width of 18.27 μm was used for the 2x2 combiners. Table 4-2 lists the effective index and interference beat length, L_π, that were found for the two multi-mode waveguide widths.

Table 4-2: The effective refractive indices and modal beat lengths of the multi-mode interference (MMI) couplers.

Waveguide Mode Polarization	Mode	Effective Refractive Index	Propagation Constant (μm)$^{-1}$ (using 1.55 μm)	Beat Length, L_π (μm)
MMI width of 15.21 μm				
Vertical	Fundamental	1.5260128	6.185949	316.1
	Next	1.5235609	6.176010	
Horizontal	Fundamental	1.5235128	6.175815	323.5
	Next	1.5211172	6.166104	
MMI width of 18.27 μm				
Vertical	Fundamental	1.5262615	6.186957	456.3
	Next	1.5245632	6.180073	
Horizontal	Fundamental	1.5237523	6.176786	462.1
	Next	1.5220750	6.169987	

The lengths of the couplers were chosen according to the rules provided in Table 1 of the reference with an extra consideration, the MMI couplers would work for 980 nm light as well as 1550 nm. The 980 nm light was not used in any of the experiments and will not be discussed except in Section 4.3.6. The MMI couplers and their lengths are listed in Table 4-3 where it is interesting to note that the lengths were chosen to be the approximate average of the lengths of the two polarizations.

Table 4-3: MMI coupler physical lengths for 1x4 and 1x2 splitters and 2x2 combiners.

MMI type	Fraction of the Beat Length for 1550 nm light	Physical Length (μm)
MMI width of 15.21 μm		
1x4 splitter (center fed)	33/16 $L\pi$	664
1x2 splitter (center fed)	33/8 $L\pi$	1328
MMI width of 18.27 μm		
2x2 combiner (offset fed)	7/2 $L\pi$	1615

For related calculations, two methods were used to find the vertical effective refractive indices. The core effective index in the vertical direction can be solved for analytically via the slab waveguide mode equations. The effective index in the vertical direction outside of the waveguiding region cannot be obtained by analytic means because there it isn't a slab type of structure. The effective index in the vertical direction, referred to as the '*y*' direction, can be found through a weighted average of the dielectric constant using the ratio of the electric displacement and the electric field (from the FWave calculation) as the weighting function. The following equation for the effective refractive index in the 'y' direction, n_{effy},

$$n_{effy} = \sqrt{\frac{\int D dy}{\int E dy}}, \tag{87}$$

is to be evaluated along a vertical line at a fixed horizontal coordinate. This procedure was verified by applying it to the core of the broad MMI waveguides and comparing the result to the analytical solution. The analytical solutions for effective indices in the vertical direction for slab waveguides with the indices of refraction and vertical dimension given in Figure 4-8 are 1.52688 for horizontal polarization and 1.52444 for vertical polarization. Evaluation of Equation (87) for the numerical mode solutions at the center of the 15.21 μm wide MMI waveguide yield values of 1.52687 and 1.52427 for horizontal and vertical polarization, respectively, and for the 18.27 μm wide MMI waveguide the horizontal and vertical polarization effective refractive indices are 1.52681 and 1.52425, respectively.

Matlab code was written that used the effective waveguide width based on calculations of the effective indices of the waveguides via FWave. A spatial harmonic series was calculated by discrete Fourier transform methods and propagated the length of the MMI section where an inverse discrete Fourier transform was used to calculate the output electric field profile. These calculations were compared to a BPM simulation that used vertical effective indices calculated via the electric field distributions as calculated by FWave.

Connecting the MMI couplers and providing the required delay length for the harmonic decoding was accomplished in a relatively small substrate region. Novel waveguide bends had to be used, these bends are the subject of the following section.

4.3.4 Novel Bending Architecture.

A novel means of bending a waveguide through an angle of 180° or greater was used in the layout of the photomask. This bend architecture is based on a parametric curve in cylindrical coordinates that is calculated using the formula

$$r_C = 1 + \alpha_C cos^2 \phi_C, \tag{88}$$

where r_C and ϕ_C are the usual cylindrical coordinates and α_C is the parameter that changes the angle that is subtended by the curve. α_C is greater than or equal to 1/2 for angles of 180° or more. If the curve is plotted over the full 2π range of ϕ_C, there will be four points on the curve where the curvature of the function is zero (one in each quadrant), with the exception that when α_C is 1/2 there are only two points of zero curvature, which can be seen in Figure 4-9.

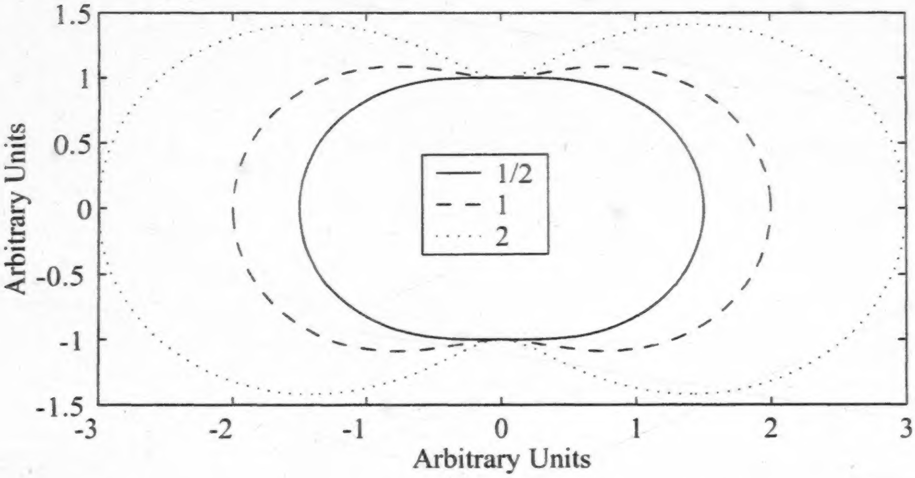

Figure 4-9: Example plots of waveguide bend functions that subtend angles greater than or equal to 180° with values of α_C of 1/2, 1 and 2. Only part of the curve is used for the waveguide bend.

The importance of having zero curvature points is that the function (waveguide bend) can be mated to a straight portion of waveguide and have no mode conversion loss at the mating point. Generally speaking, the waveguide (with bends included) will have a minimized loss as long as the curvature and rate change of curvature are continuous functions of the position along the waveguide. Specifically, the loss in waveguides depends strongly on the absolute curvature that the guided mode encounters. Example calculations of waveguide bend losses are presented in the following section for waveguide bends of various functional forms.

4.3.5 Waveguide Bend Loss Calculations.

The waveguide losses were calculated based on a slab waveguide bend loss approximation [BOY1] where the indices of refraction of the slab waveguide structure are the vertical effective indices evaluated as slab effective indices inside and outside of the core of the waveguide. The mathematical concepts will not be discussed here.

Evaluation of the effective indices in the vertical direction for the single mode waveguides was performed using Equation (87) and numerical mode profile solutions for both vertical and horizontal polarized modes. The results of these calculations for the vertically polarized mode with respect to the horizontal position transverse to the direction of propagation in the waveguide are graphed in Figure 4-10, where the center of the waveguide is at zero in the figure.

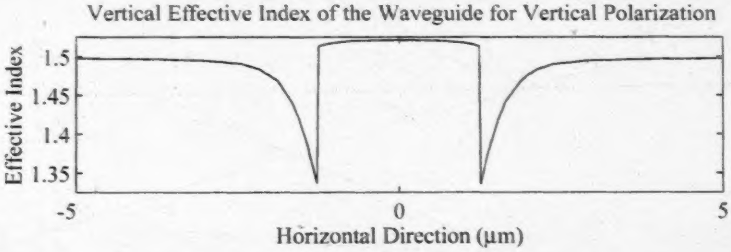

Figure 4-10: The vertical effective refractive index for vertically polarized light with a wavelength of 1550 nm in a waveguide structure with refractive indices and dimensions shown in Figure 4-8.

Since the effective vertical index of refraction does not vary much within the core region of the waveguide, the center value for effective indices can be used. Outside of the core region of the waveguide, the effective index, as evaluated here, varies considerably since the proportions of the mode that are in the substrate and air are strong functions of the distance from the core. In this region the index of refraction can be weighted by the electric field in similar manner as was done for finding the vertical effective index to approximate the effective index outside of the core guiding region with one number. The electric field is integrated in the vertical direction, and this integrated electric field is used along with an integrated displacement field (calculated using the effective index) in a horizontal analogue of Equation (87) to find the average vertical effective index outside of the core region. As can be seen in Figure 4-11, the electric field decays quite rapidly outside of the waveguiding region, so the effective index should be dominated by the lower values shown in Figure 4-10.

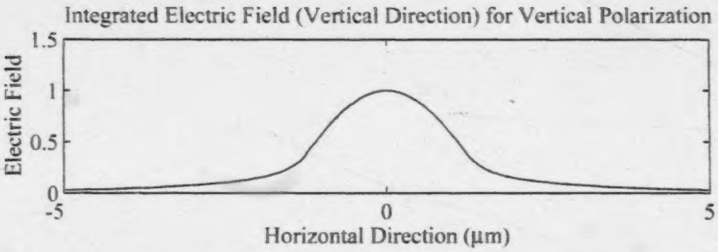

Figure 4-11: The integrated vertical electric field profile of the single mode waveguide for vertically polarized light. The core of the waveguide is centered at 0 in the figure and extends +/- 1.25 μm in either direction.

The core and cladding effective indices of refraction that are used in the slab waveguide bend loss approximation are provided in Table 4-4.

Table 4-4: The effective refractive indices used to calculate the bend loss of the single-mode waveguide for both polarizations.

Waveguide Mode Polarization	Region	Effective Refractive Index
Vertical	Core	1.521345
	Cladding	1.462242
Horizontal	Core	1.522435
	Cladding	1.469161

The waveguide bending loss for a circular shaped bend was calculated as a benchmark to evaluate the bend loss efficiency of the types of bends that were used in the design of the waveguide MZ decoder. The calculation was performed for a quarter circle where the direction of the output with respect to the input subtends and angle of 90°. The result of this calculation was multiplied by 30 to better compare the losses incurred by the multiple bends that are present in the real device. Values of the loss as a function of bend radii from 75 to 2000 μm are shown in Figure 4-12.

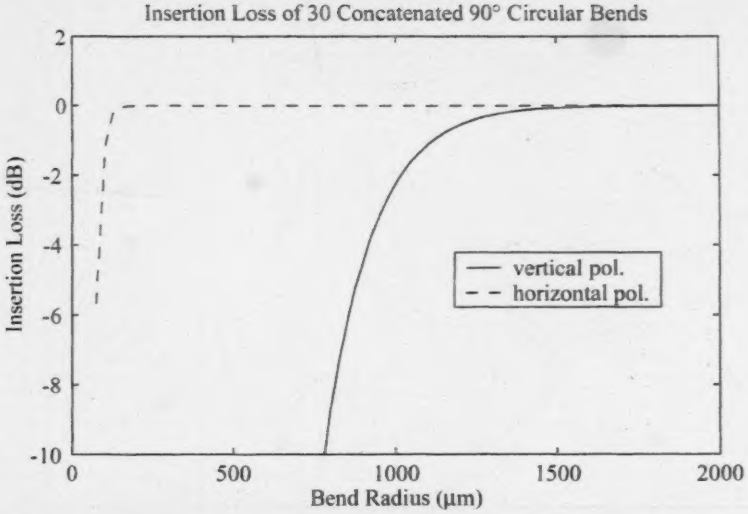

Figure 4-12: The insertion loss of 30 concatenated quarter circle waveguide bends for both vertical and horizontal polarized light, not including mode mismatch loss.

These loss calculations do not include the mode mismatch loss of mating two waveguide sections with an abrupt change in radius of curvature. The results of the calculations for the waveguide structure used here has a large difference in loss for the two polarizations, effectively creating a polarizer for bend radii of less than 1 mm.

Cosine is a function that has periodic points with zero curvature at odd multiples of $\pi/2$. The cosine function from $-\pi/2$ to $\pi/2$ has zero curvature at both ends and, if the height is chosen correctly, subtends an arc of 90°. Bends of this type were not used in the mask layout but are included here as calculated benchmarks for the cosine bends that were used in the MZ decoder. For this benchmark the loss for 15 concatenated bends that subtend an angle of 90° each is plotted as a function of minimum bend radius of the cosine curve from 75 to 2000 μm, Figure 4-13.

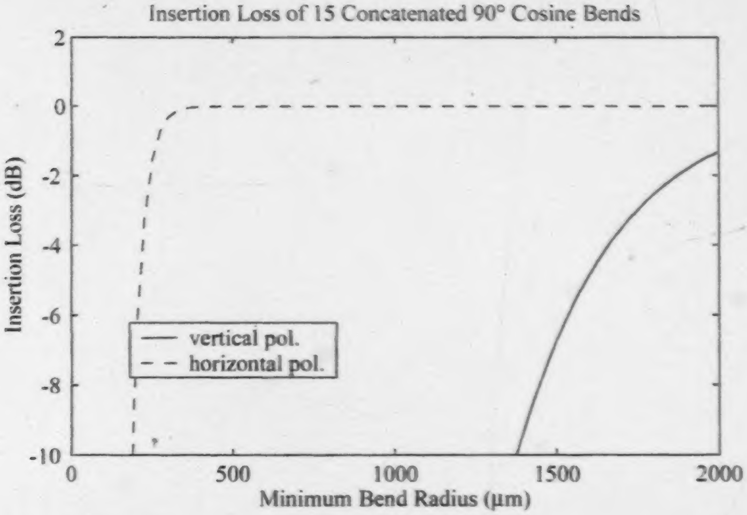

Figure 4-13: The insertion loss of 15 concatenated 90° cosine waveguide bends for both vertical and horizontal polarized light.

The horizontal polarization shows very little loss for moderate minimum bend radii of greater than 0.5 mm. Light of vertical polarization will be cutoff effectively by passing it through a large number of this type of bend.

Two cosine bends that subtend arcs of 45° each can be concatenated to subtend a total arc of 90°. It is a slightly larger structure than a single 90° cosine bend but has better performance for equivalent minimum bend radius. Cosine bends with 45° direction changes were used in the MZ decoder any time the direction of the waveguide needed to change by an angle of 45°, 90° or 135°. The loss incurred when 30 successive bends of 45° are concatenated (equivalent to 15 90° direction changes) is plotted as a function of minimum bend radius from 75 to 2000 μm, Figure 4-14.

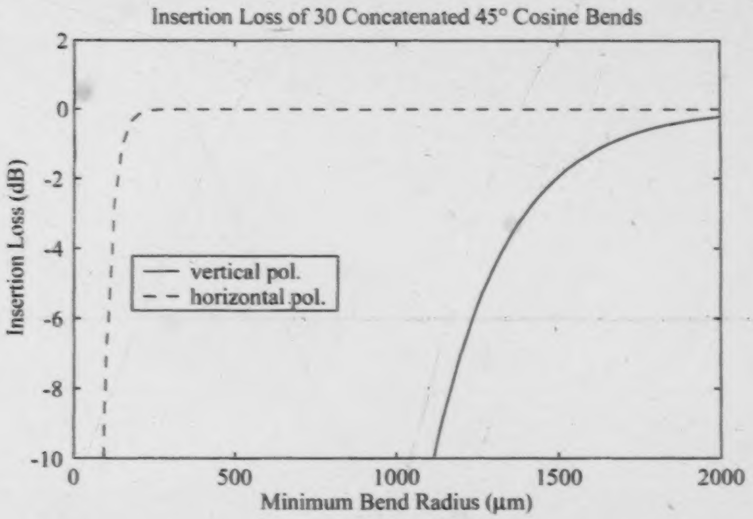

Figure 4-14: The insertion loss of 30 concatenated 45° cosine waveguide bends for both vertical and horizontal polarized light.

The total loss induced by the 30 concatenated 45° cosine bends has similar differences for the two polarizations as the previous examples, although the performance of the 45° bend is better than the 90° bend for the same aggregate direction change.

The bends with the functional form discussed in Section 4.3.4 that subtend arcs of greater than 180° have slightly superior performance when compared to circular bends with the same minimum bend radius, with the added benefit of having zero curvature at the end points. The values that are shown, Figure 4-15, for the loss in these bends are for the largest subtended angle that was used for the integrated MZ device.

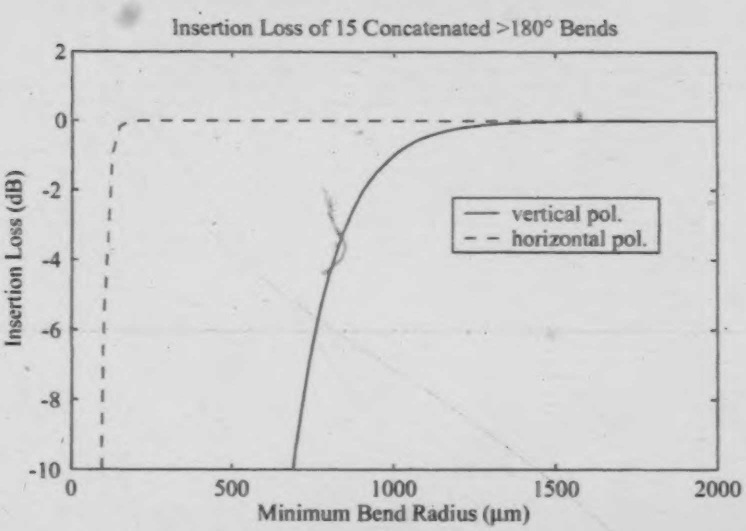

Figure 4-15: The insertion loss of 15 concatenated bends for the waveguide bends with the functional form given by Equation (88) for both vertical and horizontal polarized light. The parameter α_C takes on the value for the bends that were used in the MZ decoder.

The performance of this type of bend is slightly more efficient than the circular bend, even though the angle subtended by concatenating 30 quarter circle bends is less than the aggregate angle subtended for the values shown in Figure 4-15. Again the polarization effects that affected the performance of the other types of bends are present here.

The integrated MZ decoder was designed with minimum bend radii of 600 μm for any type of waveguide bend. The bends on the optical chip will not support vertically polarized light but, because the input polarization was to be controlled in the testing, it did not matter. As well, the number of waveguide bends that were 45° cosines and derived from Equation (88) were less than the number used to generate the theoretical loss curves, so no appreciable losses were expected from the waveguide bends.

At the output coupler of each of the individual MZs on the chip the phases of the light in each pair of optical paths are related. The length of these optical paths was calculated before the mask was laid out but small variations in refractive index and the difference in propagation constant for bent waveguides versus straight waveguides make it nearly impossible to fabricate a perfect device. The length of one of each of the paired waveguides must be controlled in length to adjust the relative phases at the output couplers. The control of the path length differences was going to be implemented through heating and cooling sections of waveguide, the next section discusses this proposed thermal control.

4.3.6 Thermal Control.

The square features in each corner of the MZ chip layout, Figure 4-7, were intended for thermal control. The usual method of employing thin film heaters was not considered in this design due to the lack of a cladding layer above the waveguides on which to place the heaters without interfering in the optical propagation. The intent was to use bulk thermal heating with solid state thermo-electric devices that would be mounted on small blocks of copper and attached to the glass on these square features with thermally conductive epoxy. One of the solid state thermo-electric drives would have been a heater and the other would have been a cooler, thus enabling push pull control of the FSR and peak passing wavelengths of the MZ decoder. This feature was not tested.

The decoders were also co-designed to pass 980 nm light, this additional signal was going to be used as a set point regulator that would be independent of the 1550 nm signal light. The recombination of the 980 light in the final MMI coupler would route this light to extra monitor ports that were placed at the edges of the coupler and not into the signal ports, as can be seen in Figure 4-7. This feature was not tested either. Regardless of whether or not the path lengths of the arms of the individual MZs could be well regulated, the phase of the light coupling to the output waveguides of the MMI combiner is another factor that would influence the received signal extinction. Recombination phase errors are briefly described in the following section.

4.3.7 Recombination Phase Errors.

Assuming that the MZ decoder imbalances could be tuned to achieve maximum signal power extinctions at the decoder output, there are other influences from the recombining MMI couplers that could degrade the performance of the MZ decoders. In a similar manner to the free-space interferometer, there is a residual phase offset incurred in MMI combiners that happens when the MMI coupler is not the exact dimensions or refractive indices that it was designed to be. Device fabrication errors in the width, height or index of refraction of the MMI couplers all cause the same general result, the length of the MMI will be incorrect for perfect interference at the output waveguides. For a theoretically perfect 2x2 MMI combiner length, the cross coupled images of the input light are exactly 90° out of phase where the extinction ratio of the output signal can reach it's theoretical maximum. When the combiner length is not at the theoretically calculated value the phase at the output waveguides is not 90° and the extinction of the output signal will have similar behaviour to the free-space MZ interferometer.

Fabrication errors of these waveguide devices influence the device performance, the results of the fabrication of these devices is discussed in the following section.

4.3.8 Integrated Mach-Zehnder Decoder Fabrication.

The integrated MZ decoder was fabricated using photolithography at the Alberta Microelectronics Center. Two layers of SiNO were deposited on Silicon substrates, the first was a 10 μm thick layer with a refractive index of 1.5 and the second layer was the waveguide layer, 2 μm thick with a refractive index of 1.55. The waveguide devices were etched out of this layering.

When the devices were delivered, they were wrapped in filter paper and set in Petrie dishes. When the wafer chips were inspected, using a video camera, with a zoom lens or microscope objective, and a video capture system, numerous damaged areas were found. A picture of a typical damaged area is shown in Figure 4-16. The frequency of the damage to the wafer chips limited the testing that could be done on the integrated MZ decoder. Testing attempts are described in the following section.

Figure 4-16: An example of a damaged area on an integrated MZ harmonic decoder wafer. Three waveguides run vertically through the picture, they are chipped off the substrate and surrounded by debris.

4.3.9 Tests of the Integrated Mach-Zehnders.

Out of 16 fabricated devices, two devices were found to each have one Mach-Zehnder without broken waveguides. The waveguide faces were polished at the input and output edges of the wafers. Figure 4-17 shows a polished waveguide end from one of the samples.

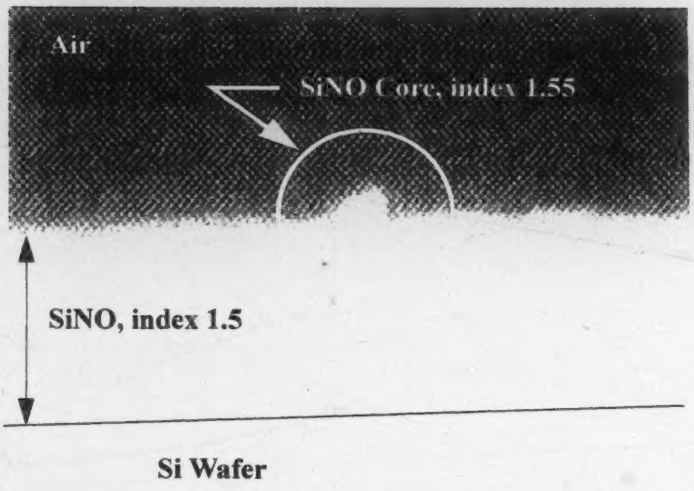

Figure 4-17: A photograph of a polished input waveguide on an integrated MZ harmonic decoder wafer. All of the layers are identified and the core of the waveguide is in the circle in the center of the photo.

During testing attempts, one device fell off of the vacuum chuck in the test jig and was damaged beyond use. The other device was found to have a defect in the waveguide very near the input of the device which scattered the light out of the waveguide. The design of the integrated MZ harmonic decoder could not be tested without fabricating more devices which, considering the cost of the fabrication and the availability of the free-space interferometer, was not done.

4.3.10 Coupling and Propagation Loss Estimates for PLC MZs.

The input and output coupling losses of optical waveguide devices are typically high, especially for waveguides with high refractive index differences. Coupling from standard single mode fiber is inhibited by the mode field mismatch and free-space coupling using lenses is difficult to optically align.

The coupling losses from standard single-mode fiber to the planar waveguide can be estimated using a two dimensional overlap integral, where the mode in the single-mode fiber is assumed to have a mode diameter of 9.0 μm and a Gaussian field profile. For the vertically polarized mode the calculation predicts and insertion loss of 9.0 dB and for the horizontally polarized mode the insertion loss should be 8.3 dB. If tapered fibers were used to reduce the mode diameter to 4 μm the mode coupling insertion losses would be 3.4 dB and 2.9 dB for the vertical and horizontal modes, respectively.

Coupling to standard single-mode fiber from the planar waveguide can be estimated using a Gaussian mode profile with a 1/e radius that is the ratio of the single-mode fiber numerical aperture to the numerical aperture of the waveguide. For the vertically polarized mode the coupling insertion loss is estimated to be 7.8 dB and the coupling loss for the horizontally polarized mode is estimated to be 8.4 dB. Fiber with a higher refractive index difference between the core and the cladding, hence higher numerical aperture, could be used at the output to reduce the output coupling loss.

Coupling light into the waveguides with free-space optics requires matching the numerical aperture of the lens system to the numerical aperture of the waveguide. A numerical aperture of at least 0.4 is necessary given the results presented in Table 4-1. Attempts to couple light to the waveguides with a high numerical aperture microscope objective were made, but the tests were unsuccessful.

Estimates of the optical power loss that would be expected for these MZ decoders can be made assuming one additional piece of information, the loss per centimeter of waveguide. The per centimeter loss of waveguides made from SiON is typically in the range of 0.1 to 1.0 dB/cm, [BON1,WOR1]. The longest optical path from input to output for the four channel harmonic decoder is less than 10 cm, for which a rough estimate of the loss is 1 to 10 dB for the waveguide loss. Combining this loss with the coupling loss estimates presented earlier for the horizontal polarization (8.3 and 8.4 dB) and accounting for 6 dB for the 1x4 channel-wise optical power split, as well as neglecting bend losses for the horizontal polarization and assuming that there are no excess losses associated with the splitting and combining MMI devices, the total loss for the most lossy optical path is 23.7 to 32.7 dB. This total loss is unacceptable. If the estimates for input and output coupling losses are reduced to the estimate given for the mode reducing fiber pigtail (2.9 dB each) the range of losses reduces to 13.8 to 22.8 dB for the most lossy optical path. 13.8 dB is still an unacceptable loss for a single channel passing through the harmonic decoder. The per channel losses of the 1x4 splitter can be chosen to favour some channels over the others to optimize the optical power distribution and balance the channel by channel BER performance. This analysis will be covered as part of Chapter 6.

Another interesting consequence of the optical power loss per centimeter of the SiON waveguides is that the optical powers at the two input ports of the combining MMI devices will be unequal given an equal split at the input end of the MZ decoders. The loss difference between the arms for the longest delay channel for devices with 5.7 cm delay length would range from 0.57 to 5.7 dB, assuming the loss range given above. The effects of such a power mismatch at the input to the interfering part of the MZ decoder are shown in detail for the free-space MZ decoder later in this chapter and will not be discussed further for the integrated devices other than to say that, conveniently, the MZ with the largest loss due to the delay is the channel that requires the least input optical power due to the optical frequency to power signal conversion.

None of the waveguide device tests were successful in producing results, so none of the theoretical predictions could be verified experimentally. All of the work presented in the remainder of this thesis will be associated with ideal MZ decoders or the free-space MZ decoder that was built. The next section presents and discusses calculated responses for the ideal and free-space decoders.

4.4 Simulated Response of the MZ to the FCM Signal.

The laser simulations discussed in Chapter 2 provide the starting point for the calculations in this section. The DFB with optical injection simulations produce optical power and optical frequency as output responses to the optical power waveform that is input. The electric field of this output is taken to be the square root of the optical power to simplify the calculations in this section. Also, the optical frequency of the signal will be modified using the derived symbol frequencies to determine a reference optical frequency for the signal so that it produces the correct output signal. This is done by setting the symbol levels to correctly correspond to the desired maximum and minimum optical powers of the MZ decoder and the FSR is set for the designed symbol rate.

In the interference equations, the optical circular frequency, $\omega(t')$, can be replaced by a somewhat arbitrary frequency offset, ω_{DC}, and a term that represents the FCM signal levels, ω_S, such that the integral in the interference equations can be replaced by a cumulative phase difference, $\Delta\phi_\tau(t)$, between the signal and the delayed signal.

$$\begin{aligned} \int_{t-\tau_{\Delta L}}^{t} \omega(t')dt' &= \int_{t-\tau_{\Delta L}}^{t} (\omega_{DC} + \omega_S(t'))dt' \\ &= \omega_{DC}\tau_{\Delta L} + \int_{t-\tau_{\Delta L}}^{t} \omega_S(t')dt' \\ &= \omega_{DC}\tau_{\Delta L} + \Delta\phi_\tau(t) \end{aligned} \tag{89}$$

For a particular transmitted signal and harmonic decoder channel the values of ω_{DC} and $\tau_{\Delta L}$ can be negotiated through a control mechanism that would adjust $\tau_{\Delta L}$ such that $\Delta\phi_\tau(t)$ is optimized. The optimization of $\tau_{\Delta L}$ results in changing the positions of the maxima of the MZ response without large changes in the FSR and is chosen such that ω_{DC} corresponds to a particular output condition when $\Delta\phi_\tau(t) = 0$. This will be discussed in the following sections that consider the response of ideal MZ and free-space MZ interferometers to simulated FCM signals.

4.4.1 Ideal MZ Decoder Response to the FCM Signal.

An ideal MZ decoder is one which has no loss, equal power splitting and recombination and the relative phases of transmissions with respect to reflection obey the ideal relationship

$$\phi_t - \phi_r = \frac{\pi}{2}. \tag{90}$$

From Equations (71) and (72) of the MZ, the following equation can be written for the difference of the received electrical signals (in terms of optical powers) at the receiver, neglecting the receiver transfer function,

$$P_{1-2} = -(A_0(t)A_0(t-\tau_{\Delta L}))\cos\left(\int_{t-\tau_{\Delta L}}^{t} \omega(t')dt'\right). \tag{91}$$

Equation (89) can be modified with the following equation for choosing the harmonic decoder delay time,

$$\omega_{DC}\tau_{\Delta L} = 2n_{MZ}\pi + \frac{\pi}{2}, \tag{92}$$

which is substituted into Equation (89) which is substituted into the argument of the cosine with the following result,

$$P_{1-2} = (A_0(t)A_0(t-\tau_{\Delta T}))\sin(\Delta\phi_{\tau}(t)). \tag{93}$$

It is this equation that is used to evaluate the baseline performance of a MZ harmonic decoder with respect to the input FCM signal. Runge Kutta evaluations of the laser rate equations for the DFB laser with the parameters that were used in Section 2.12, with the optical injection signal generated with EO MZ phase offsets and modulation indices (as defined in Section 2.12) that are optimized for linear FCM signal generation, provide the input to Equation (93).

The effects of the choice of symbol overlap, hence delay time, can be compared by generating signals with different mean frequency level spacing. For an 8-ary (3 channel) FCM signal at an OC-12 symbol rate the chosen phase offsets and modulation indices for the injected optical signal are 0.875 radians and 0.84 for a fractional bit overlap of 1/2 and 0.950 radians and 0.98 for a fractional bit overlap of 1/3, both with a peak input optical power of 1.6 mW. The results of evaluating Equation (93) using these Runge Kutta simulations for the input optical field amplitudes and frequencies are plotted as eye diagrams (for each channel and both fractional overlaps) for 127 random symbols in Figure 4-18, where the received optical power is in arbitrary units.

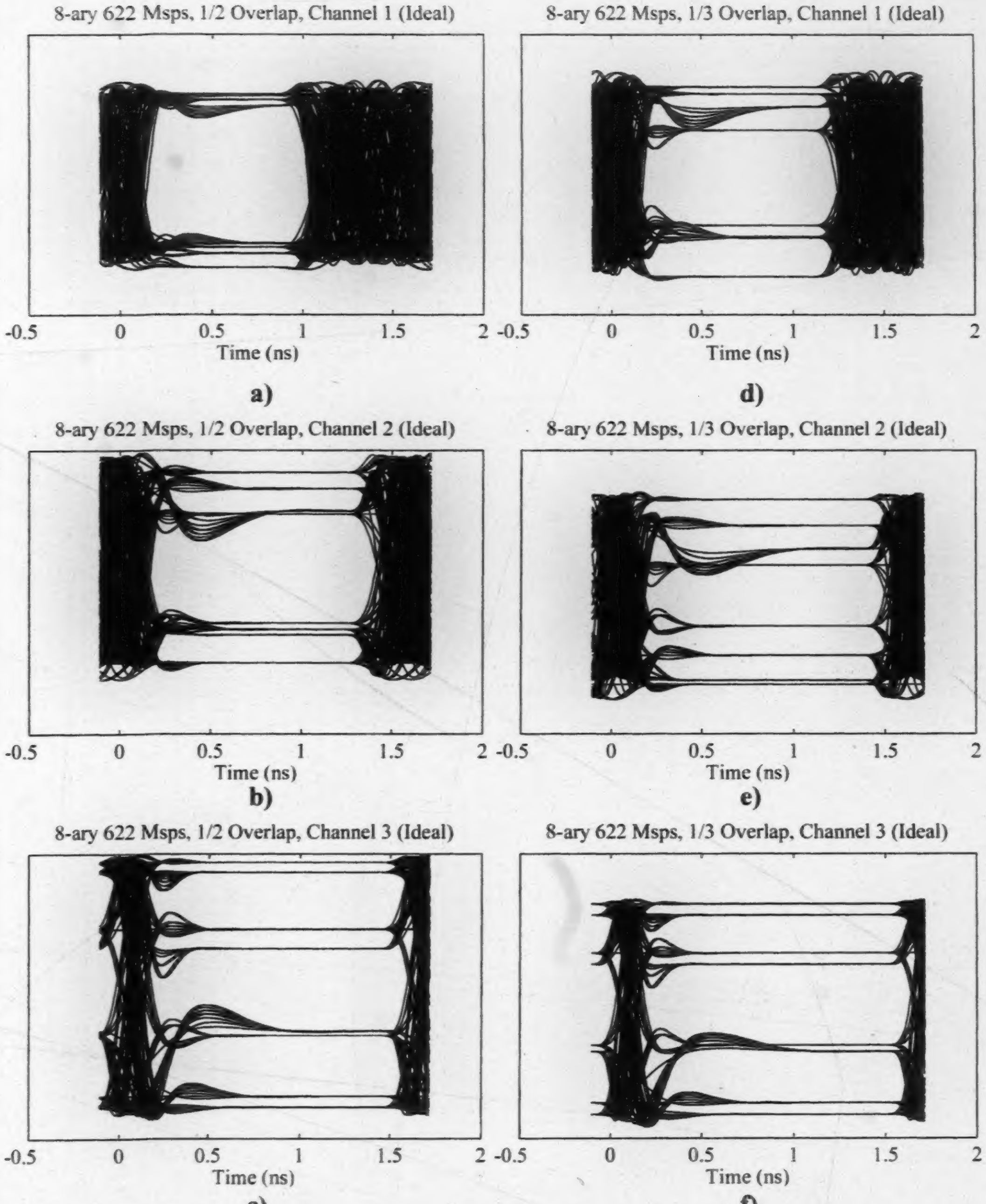

a) **d)** **b)** **e)** **c)** **f)**

Figure 4-18: Six eye diagrams depicting the difference between 1/2 bit overlap and 1/3 bit overlap for all three channels of an 8-ary, 622 Msps, FCM signal. The plots include the post subtraction after being received but do not include the receiver transfer function. **a)**, **b)** and **c)** are channels 1, 2 and 3 for 1/2 bit overlap and **d)**, **e)** and **f)** are channels 1, 2 and 3 for 1/3 bit overlap.

The eye diagrams suggest that the fractional bit overlap of 1/2 offers superior performance when the response of the MZ harmonic decoder is ideal. When the measured response of the free-space MZ decoder is used to calculate eye diagrams for the same input, the effects of having splitting and combining ratios that are not 50% can be seen. This is investigated in the next section.

4.4.2 Free-Space MZ Response to the FCM Signal.

The free-space beam splitter based MZ that was presented in Section 4.2 has a convenient choice of the product of ω_{DC} and $\tau_{\Delta L}$ that is given by the following equation,

$$\int_{t-\tau_{\Delta L}}^{t} \omega(t')dt' = \Delta\phi_{\tau}(t) + 2n_{MZ}\pi - \frac{\phi_{trtr}}{2} - \frac{\phi_{ttrr}}{2}. \qquad (94)$$

Equations (80) and (82) from Section 4.2 become the following equations,

$$\begin{aligned} P_{out1} &= T_{65}T_{25}(A_0(t))^2 + R_{65}R_{25}(A_0(t-\tau_{\Delta L}))^2 + \\ &\quad 2|t_{65}||t_{25}||r_{65}||r_{25}|A_0(t)A_0(t-\tau_{\Delta L})\sin\left(\Delta\phi_{\tau}(t) - \frac{\phi_{trtr} - \phi_{ttrr} - \pi}{2}\right) \end{aligned} \qquad (95)$$

and

$$\begin{aligned} P_{out2} &= R_{65}T_{25}(A_0(t))^2 + T_{65}R_{25}(A_0(t-\tau_{\Delta L}))^2 - \\ &\quad 2|t_{65}||t_{25}||r_{65}||r_{25}|A_0(t)A_0(t-\tau_{\Delta L})\sin\left(\Delta\phi_{\tau}(t) + \frac{\phi_{trtr} - \phi_{ttrr} - \pi}{2}\right). \end{aligned} \qquad (96)$$

The electrical signal is proportional to the difference of these optical powers, $P_{1\text{-}2}$, and will behave like the following equation,

$$\begin{aligned} P_{1-2} &= P_{out1} - P_{out2} \\ &= (T_{65}T_{25} - R_{65}T_{25})(A_0(t))^2 + \\ &\quad (R_{65}R_{25} - T_{65}R_{25})(A_0(t-\tau_{\Delta L}))^2 + \\ &\quad 2|t_{65}||t_{25}||r_{65}||r_{25}|A_0(t)A_0(t-\tau_{\Delta L})\sin(\Delta\phi_{\tau}(t))\cos\left(\frac{\phi_{trtr} - \phi_{ttrr} - \pi}{2}\right). \end{aligned} \qquad (97)$$

If the coefficients of the non-interference terms do not independently equal zero, some residual amplitude modulation will be present in the received electrical signal.

The response of the free-space MZ to the FCM signal is found by substituting the measured coefficient values, Equation (84 a) through Equation (86), into the response function, Equation (97), and using the Runge-Kutta laser simulations as the input optical signal. When Equation (86) is substituted into the signal response function, the phase argument of the cosine term is ~0.004 and the Taylor expansion approximation for the cosine term is 0.999992, to second order, which is close enough to 1 to neglect. Additionally, the optical powers should be balanced throughout the MZ such that the common mode terms of optical power at the outputs of the MZ are minimized. This requirement translates to a condition for the reflection and transmission coefficients that can be expressed by the following equation,

$$(T_{65}T_{25} - R_{65}T_{25}) + (R_{65}R_{25} - T_{65}R_{25}) \cong 0\,, \tag{98}$$

If this condition is not met, then the arm of the free-space MZ with the higher optical power can be attenuated using a neutral density filter (NDF) to balance the signal powers where the desired result of this attenuation maximizes the interference term of the MZ with respect to the common mode terms. When the optical power of the input signal is nearly the same for durations greater than the delay time of the MZ, the non-interfering terms will be minimized and the interference term will dominate the response. The eye diagrams in Figure 4-19 show the response of the free-space MZ to the same input waveforms as were used in Figure 4-18 a), b) and c) without (denoted Real in the figure) and with the NDF balancing the optical powers in the two arms, where the fractional bit overlap is 1/2.

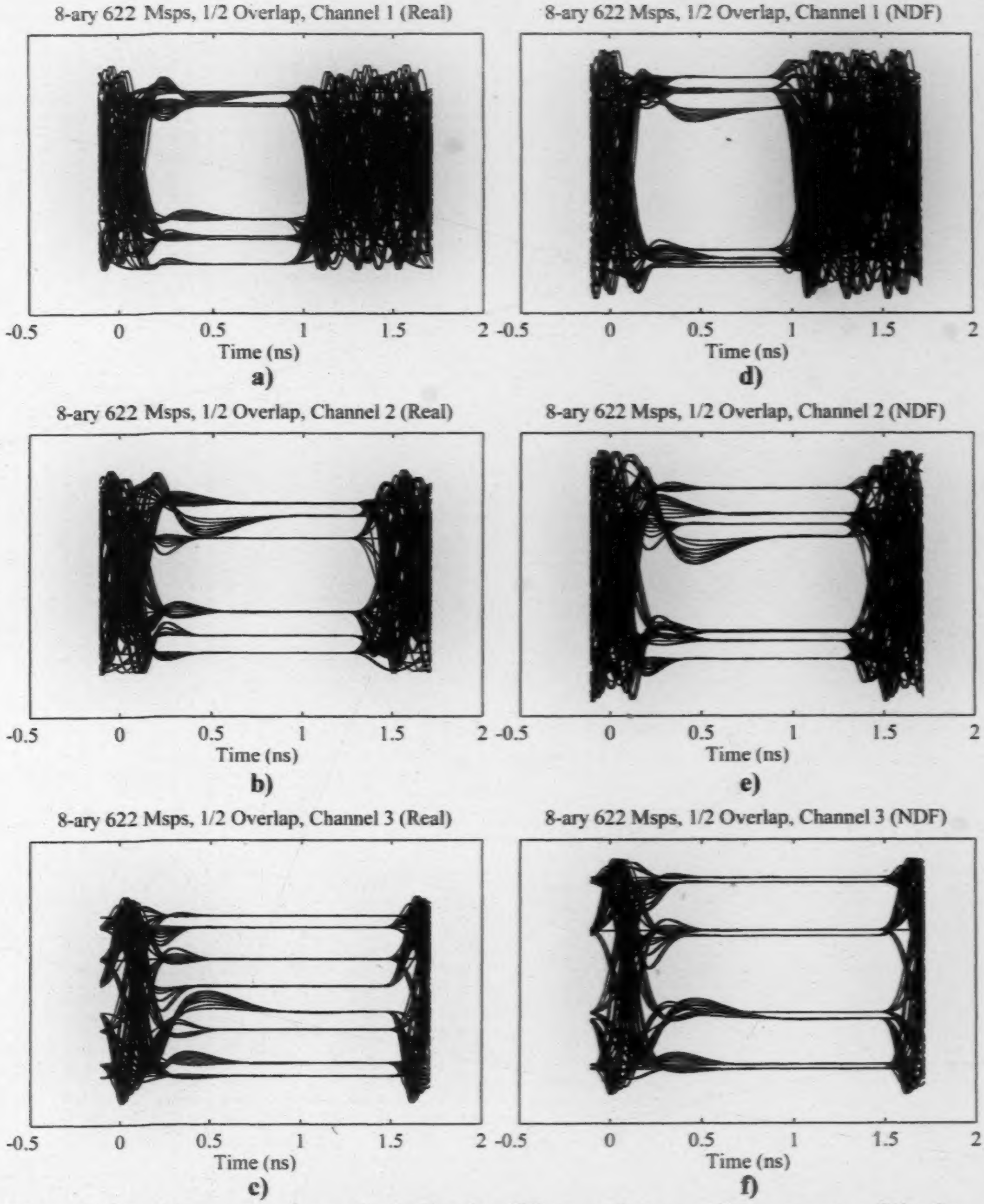

Figure 4-19: Six eye diagrams depicting the difference between the response of the free-space MZ without and with a neutral density filter (NDF) for all three channels of an 8-ary, 622 Msps, FCM signal. The plots include the post subtraction after being received but do not include the receiver transfer function. **a)**, **b)** and **c)** are channels 1, 2 and 3 without the NDF (denoted Real) and **d)**, **e)** and **f)** are channels 1, 2 and 3 with the NDF (denoted NDF).

The use of the free-space interferometer will cause significant eye closure for all three channels of the 8-ary FCM signal when the NDF is not in the optical path. Putting the NDF in the optical path improves the optical eye diagram dramatically, almost to the point of equalling the performance of the ideal MZ decoder. The downside of using the NDF is that it reduces the received optical power.

When the symbol rate is increased to Gigabit Ethernet, 1250 Msps, the number of channels that can be multiplexed is reduced to two for the transmitter design that was previously discussed. The chosen phase offsets and modulation indices for the injected optical signal are 0.950 radians and 0.76 for a fractional bit overlap of 1/2 to generate simulated input to this MZ decoder. The calculated responses of the MZ decoder to the FCM signal for this scenario are shown in Figure 4-20, for a free-space MZ without and with the NDF.

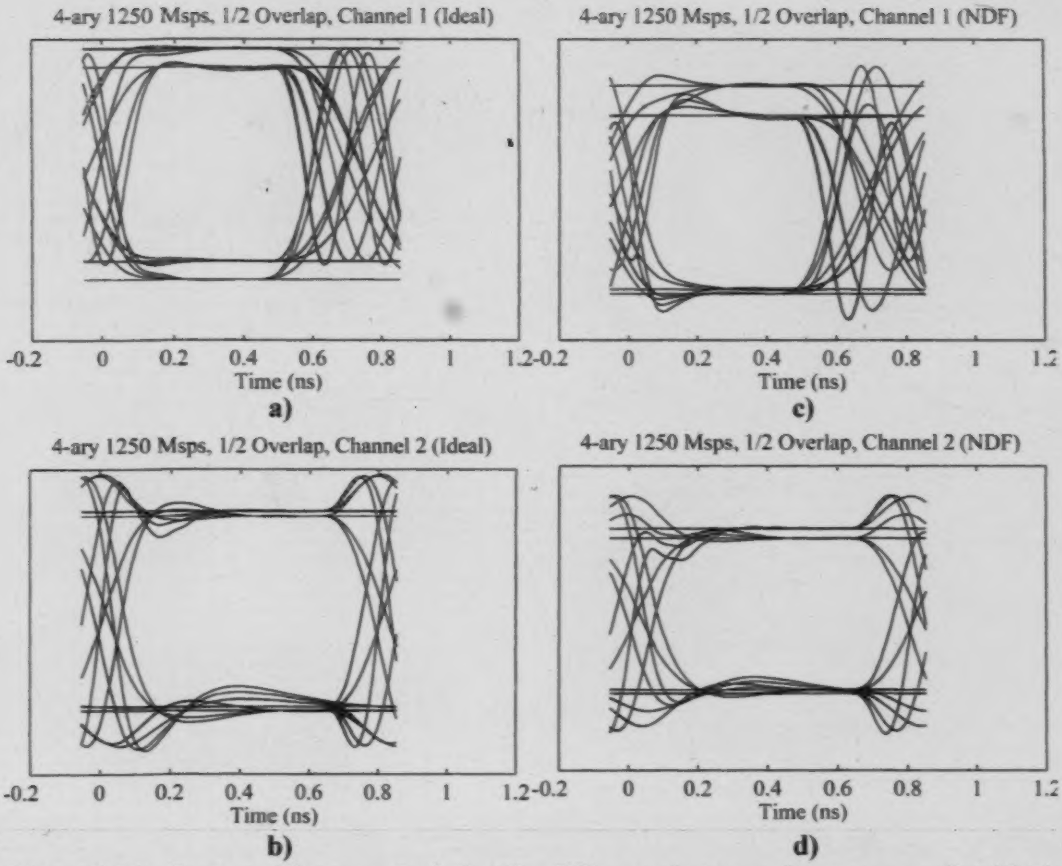

a) c)

b) d)

Figure 4-20: Four eye diagrams depicting the difference between the response of an ideal MZ to the free-space MZ with a neutral density filter (NDF) for both channels of a 4-ary, 1250 Msps, FCM signal. The plots include the post subtraction after being received but do not include the receiver transfer function. **a)** and **b)** are channels 1 and 2 for the ideal MZ and **c)** and **d)** are channels 1 and 2 with the NDF (denoted NDF).

The performance of the free-space MZ with the NDF is about the same as the performance of an ideal free-space MZ decoder.

The eye diagrams plotted in this section do not include noise. Receiver noise will be discussed in the following chapter but noise associated with the finite coherence of the optical signal will be introduced next. It will be demonstrated that this noise has a large impact on the FCM system performance.

4.5 Phase Noise Impact on Signal to Noise Ratio.

The phase noise of the lasing modes is driven by the spontaneous emission in the laser cavity that results in an unavoidable broadening of the laser line. This phase noise can be thought of a random walk of the phase where each spontaneous emission event is analogous to one step, which gives the phase noise a Gaussian probability density function (pdf) with zero mean. Observing the average rate of spontaneous emission events, R_S, over a known period of time will yield the width of the phase pdf. Alternatively, the linewidth of the laser is related to the average rate of spontaneous emission, as described in Section 2.10, and the time delay of interest is the bit overlap time, $\tau_{\Delta L}$, for the signal interference in the harmonic decoder. From [PETE1], the standard deviation, $\sigma_{\Delta\phi}$, of this Gaussian pdf, assuming white frequency noise from the spontaneous emission, is determined by the following relation,

$$\sigma_{\Delta\phi}{}^2 = 2\pi\tau_{\Delta L}\Delta\nu_{LW}, \qquad (99)$$

where $\Delta\nu_{LW}$ is the linewidth of the self-interfering light source. Other research has used this same expression to evaluate linewidth induced noise in coherent optical systems [HE3,JAC1].

In the context of the MZ decoder the output optical powers with a zero mean Gaussian additive phase noise can be rewritten as

$$P_{out1} = \left(\frac{A_0(t)}{2}\right)^2 + \left(\frac{A_0(t-\tau_{\Delta L})}{2}\right)^2 + \frac{A_0(t)A_0(t-\tau_{\Delta L})}{2}\sin(\Delta\phi_\tau(t) + \Delta\phi_N(t)) \qquad (100)$$

for output 1 of the MZ and

$$P_{out2} = \left(\frac{A_0(t)}{2}\right)^2 + \left(\frac{A_0(t-\tau_{\Delta L})}{2}\right)^2 - \frac{A_0(t)A_0(t-\tau_{\Delta L})}{2}\sin(\Delta\phi_\tau(t) + \Delta\phi_N(t)) \qquad (101)$$

for output 2, where $\Delta\phi_N(t)$ is the additive phase noise term with zero mean and standard deviation given by Equation (86).

By subtracting these two optical powers, which is done post detection, the received electrical signal will be proportional to the difference power, $P_{1\text{-}2}$,

$$P_{1-2} = P_{out1} - P_{out2} = (A_0(t)A_0(t-\tau_{\Delta L}))\sin(\Delta\phi_\tau(t) + \Delta\phi_N(t)) . \qquad (102)$$

This optical power is unphysical since it can be negative, but is a convenient expression to use to assess the influence of phase noise on the bit error ratio (BER) of the received signals. By using the deterministic part of the phase, $\Delta\phi_\tau(t)$, as the mean of the distribution (because it is the average phase of the interference term), the phase noise, which is given by the pdf [GART1]

$$p_{\Delta\phi}(\Delta\phi) = \frac{1}{\sqrt{2\pi}\sigma_{\Delta\phi}}\exp\left(-\frac{(\Delta\phi - \Delta\phi_\tau(t))^2}{2{\sigma_{\Delta\phi}}^2}\right), \qquad (103)$$

can be directly translated into a distribution of the total signal optical power. To demonstrate how this statement is physically manifested, consider the example phase distribution, optical power response function and optical power distribution as shown in Figure 4-21.

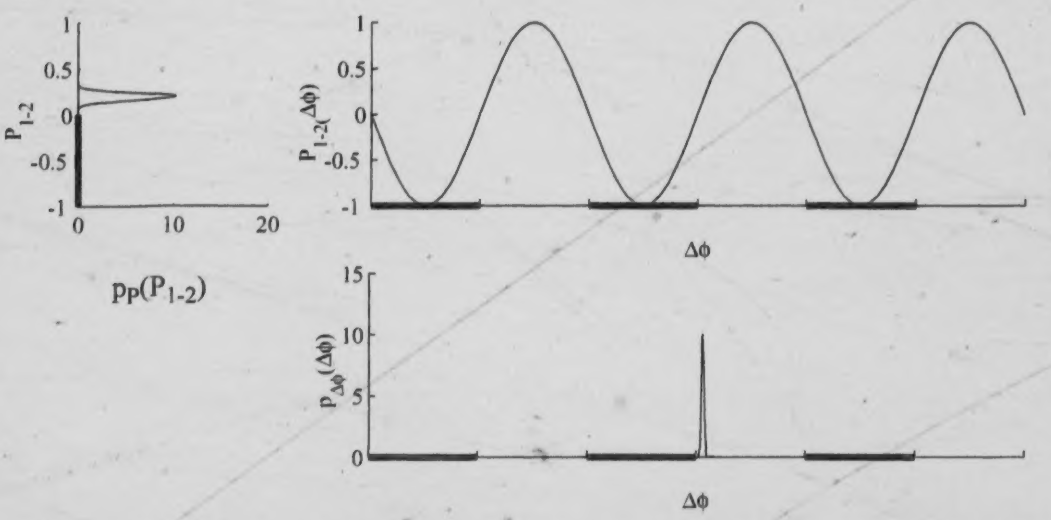

Figure 4-21: The response of the MZ decoder (post receiver subtraction) is shown at the top right. The bottom right plots the probability density function (pdf) for the phase of the incoming signal assuming an nominal linewidth. At the upper left is a plot of the probability density function for the optical power output from the MZ decoder. The dark lines indicate the ranges over which the pdfs must be integrated to obtain an equivalent cumulative error.

The phase distribution is for a 10 MHz linewidth laser where the optical frequency is calculated to be symbol 8 of a 16-ary signal being decoded for Channel 4 of a four channel

622 Msps FCM signal. The mean phase delay as viewed by the MZ decoder is $\pi/16$. For this transmitted symbol and subsequent decoding by the harmonic decoder a receiver error would occur if the differential optical power is less than zero. In Figure 4-21, the regions of the sinusoid that correspond to optical powers less than zero are marked with a heavy black line. These same regions are marked on the plot of the phase pdf shown, where integration of the phase pdf over these intervals would yield the probability of a receiver error. Conversely, integration of the (normalized) optical power pdf from -1 to 0 would give the same result.

The relative width of the phase pdf to the FSR of the demultiplexor is governed by the linewidth of the incident optical signal and the delay time, where the delay time is inversely proportional to the bit rate, through the standard deviation of the phase pdf.

A transformation of the phase pdf through the sinusoidal optical power response of the decoder results in the following function for a lossless decoder,

$$p_P(P) = \sum_n \frac{1}{\sqrt{2\pi}\sigma_{\Delta\phi}\left|\cos\left(\operatorname{asin}\left(\frac{P}{(A_0(t)A_0(t-\tau_{\Delta L}))}\right)\right)\right|} \times$$

$$\exp\left(-\frac{\left(\operatorname{asin}\left(\frac{P}{(A_0(t)A_0(t-\tau_{\Delta L}))}\right) - (-1)^n(\Delta\phi_\tau(t) - n\pi)\right)^2}{2{\sigma_{\Delta\phi}}^2}\right), \quad (104)$$

where the range of output optical power, $P_{1\text{-}2}$, is given by

$$-(A_0(t)A_0(t-\tau_{\Delta L})) \le P \le (A_0(t)A_0(t-\tau_{\Delta L})) \quad (105)$$

The summation is necessary to add all contributions to the total optical power from each degenerate phase value that yields the same optical power. The function is singular at the extreme values of optical power but, with careful numerical integration, the cumulative probability that the optical power is within a specific interval can be evaluated; the probability of receiver errors can be calculated from this formula. Equation (104) still contains $\Delta\phi_\tau(t)$ which can be replaced by the equivalent optical power expression if that becomes convenient.

If the mean phase, $\Delta\phi_\tau(t)$, is far enough away from the extreme values of the optical power response function and the standard deviation of the phase distribution is small enough, the power pdf can be linearly approximated directly from the Gaussian phase pdf and the result is,

$$p_P(P) = \frac{1}{\sqrt{2\pi}\sigma_{\Delta\phi}\left|\cos(\Delta\phi_\tau(t))\right|} \times \exp\left(-\frac{\left(\frac{(P + \cos(\Delta\phi_\tau(t))\Delta\phi_\tau(t) - \sin(\Delta\phi_\tau(t)))}{\cos(\Delta\phi_\tau(t))} - \Delta\phi_\tau(t)\right)^2}{2{\sigma_{\Delta\phi}}^2}\right), \qquad (106)$$

after normalizing the optical power to the absolute maximum optical power. It is this expression that can be used in simplified BER calculations that rely on the signal to noise ratio because a mean square noise power takes a simple form

$$\begin{aligned}\sigma_P &= \sigma_{\Delta\phi}\left|\cos(\Delta\phi_\tau(t))\right|(A_0(t)A_0(t-\tau_{\Delta L})) \\ &= \sqrt{2\pi\tau_{\Delta L}\Delta\nu_{LW}}\left|\cos(\Delta\phi_\tau(t))\right|(A_0(t)A_0(t-\tau_{\Delta L})), \qquad (107)\end{aligned}$$

which is now no longer normalized to the maximum optical power with the inclusion of the electric field amplitudes of the optical signal and the delayed optical signal. This also assumes a lossless and perfectly balanced MZ decoder.

The BER degradation caused by phase noise effects appears before the receiver as a direct reduction in optical power and, therefore, eye closure. And since the phase noise is correlated from port to port on the output of any of the MZ decoders, statistics cannot be used to reduce the overall impact of this type of noise. Also, the receiver errors that result from linewidth noise represent an error floor for the communication channel, meaning that the channel performance cannot be improved no matter how much optical power is received [GART1,ZH1]. The following section discusses the BER impact of phase noise errors on each of the multiplexed channels for all possible received signals for the 16-ary signal case assuming that the frequency levels of the signal are equally spaced.

4.5.1 Error Probabilities with Ideal Signal Levels.

An ideal signal consists of equally spaced frequency values that are spaced appropriately for the imbalance lengths of the MZ decoder to achieve the output optical power values depicted in Figure 1-13. As well, for the ideal signal, the optical power is a constant for the signal that enters the decoder. The decision threshold for this type of signal would be set to occur at the zero power point of the differential optical power signal. When these conditions are met, all levels with the same phase with respect to the harmonic decoder have the same error and the probability of a negative symbol to be above zero is the same as a symmetric positive symbol to be below zero. Only symbols that decode into the first quadrant have to be analyzed due to the symmetry. Table 4-5 provides error rates for the different symbols on their respective channels categorized by the harmonic decoder phase for a laser with a linewidth equal to 10 MHz. The $\pi/16$ symbols are on the channel with the shortest delay length (channel 4) and occur for symbols 0, 7, 8 and 15, and have the largest error rate. The $\pi/8$ symbols are on the channel with the second shortest delay length (Channel 3) and occur for symbols 0, 3, 4, 7, 8, 11, 12 and 15, and have appreciable error rates.

For a 16-ary ideally spaced signal it would be impossible to achieve a BER of 10^{-9} for Channel 4 at 622 Msps and a symbol frequency spacing of 622 MHz with a laser that has a linewidth of approximately 10 MHz. The situation becomes worse when the error rates for signals with non-ideal frequency level spacings are calculated, which will be done in the following section.

Table 4-5: Bit error ratios (BERs) are tabulated for the different phase values that comprise a 16-ary FCM signal. The decoder delay for the lowest FSR channel of the harmonic decoder is stated as a parameter. Any values of BER less than 10^{-21} are shown as 0.

Native Bitrate (Gsps)	Channel 1 Delay as a Fraction of the Bit Duration	Bit Error Ratio (BER) due to Linewidth Effects for all Values of Harmonic Decoder Phase for a Four Channel FCMA System (0 indicates < 10^{-21} probability of error)							
		Channel 1	Channel 2	Channel 3		Channel 4			
		π/2	π/4	π/8	3π/8	π/16	3π/16	5π/16	7π/16
0.622	1/4	0	1.385 x10^{-12}	3.874 x10^{-7}	0	2.381 x10^{-4}	0	0	0
	1/3	0	7.122 x10^{-10}	9.357 x10^{-6}	0	1.239 x10^{-3}	5.542 x10^{-20}	0	0
	1/2	0	3.864 x10^{-7}	2.375 x10^{-4}	0	6.740 x10^{-3}	6.201 x10^{-14}	0	0
1.25	1/4	0	0	1.240 x10^{-12}	0	3.681 x10^{-7}	0	0	0
	1/3	0	4.743 x10^{-18}	6.541 x10^{-10}	0	8.984 x10^{-6}	0	0	0
	1/2	0	1.228 x10^{-12}	3.644 x10^{-7}	0	2.307 x10^{-4}	0	0	0
2.488	1/4	0	0	0	0	1.451 x10^{-12}	0	0	0
	1/3	0	0	5.794 x10^{-18}	0	7.316 x10^{-10}	0	0	0
	1/2	0	0	1.398 x10^{-12}	0	3.912 x10^{-7}	0	0	0

4.5.2 Sensitivity of the BER to Linewidth and Signal Frequency Errors.

The end of Chapter 2 was devoted to the calculation of the linewidth and linearity of the FCM signal source from a simulation point of view. The linewidth calculations showed that for some reasonable assumptions about DFB lasers that could generate a frequency stable signal with about 9 GHz of frequency modulation depth would have linewidths of about 6-8 MHz. The overall linearity, from simulations, with assistance from the non-linear transfer function of an EO MZ modulator, could generate signals with symbol spacing errors of < 25% of the mean spacing. It is with these numbers in mind that the error rates of the multiplexed channels can be calculated for the proposed signal generation scheme. The reader must be reminded of the results presented in Table 2-2 already limit the design space for FCMA systems due to limitations on available frequency modulation depth. The results in this section can be used with the results of Chapter 2 only to further narrow the applications of the particular transmitter design, or, the data presented here can be used with any other conceivable FCMA transmitter design as they will be general enough to apply.

For the 16-ary FCM signal the worst case channel is the channel with the shortest delay time and worst case symbols on that channel are the ones that have the smallest differential signal at the output from the decoder. If 10 MHz linewidth will not be adequate, then what does the linewidth have to be in order to achieve a BER of 10^{-9}? Figure 4-22 plots the BER for these $\pi/16$ symbols as functions of linewidth with the fractional bit overlap as a parameter.The transmitter laser must have a linewidth of less than ~1.5 MHz to be considered for use in a 16-ary FCMA system, assuming perfect frequency level spacing and that the transmitter frequency range is large enough to accommodate 9.33 GHz of frequency levels (1/2 bit overlap). The other two bit overlap values (1/3 and 1/4) can be accommodated with transmitters whose linewidths are in the range of 2 to 3 MHz.

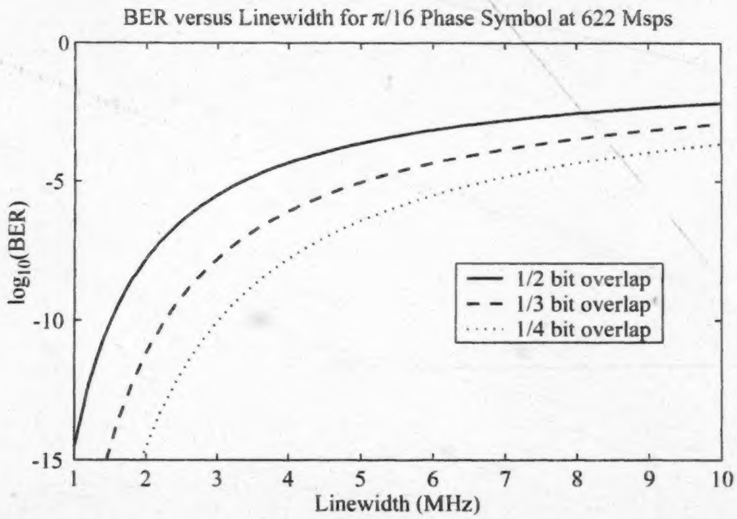

Figure 4-22: The BER of the π/16 symbol is shown for a symbol rate of 622 Msps as a function of signal laser linewidth, with the bit overlap as a parameter, when received on channel 4.

By including the transmitter frequency level spacing error, as defined in Chapter 2, the channels 3 and 4 of the 16-ary signal would be impossible to receive with a BER of 10^{-9} even if the transmitter could produce the necessary 9.33 GHz frequency range. For an 8-ary signal at 622 Msps with a linewidth of 10 MHz at the transmitter, channel 3 would suffer a large error rate when the channel spacing error is taken into account. The BER for a transmitter with 10 MHz linewidth is plotted against the level spacing error with bit overlap as a parameter in Figure 4-23. The error rate depends on whether the mean phase moves the received voltage to a lower absolute value (closer to the decision threshold) or higher absolute value (further from the decision threshold). A frequency level spacing error could be achieved within the 12-15% range with a symbol spacing in the neighbourhood of 622 MHz (see Figures 2.49 and 2.50). The direction of the spacing error cannot be read from either of these plots. Figure 2.45 plots the frequency level spacings for a quaternary system, and in the region of interest to the discussion it is evident that (combined with the results of Figure 2.44) the frequency error would move receiver voltage of this particular symbol away from the decision threshold and to better performance.

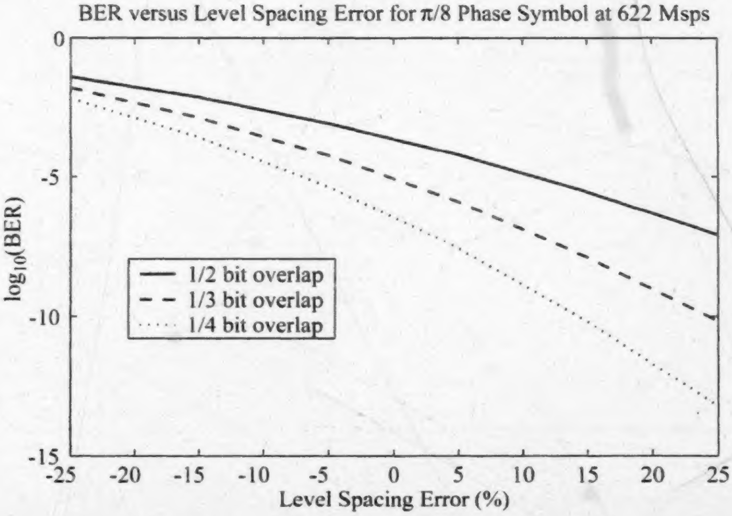

Figure 4-23: The BER is demonstrated to be a function of the frequency accuracy of the FCM symbols, specifically for the π/8 symbol of an eight or sixteen level signal received by channel 3. These calculations are for a laser linewidth of 10 MHz.

In order to calculate the exact impact of frequency level spacing in general cases, each value of frequency for all of the frequency levels has to be assessed independently, which will be left to Chapter 6.

The required transmitter linewidth that enables the reception of the multiplexed channels with acceptable BER (10^{-9}) can be found using the same optical power pdf and the results for symbols for channel 2 of a 622 Msps FCM system are presented in Figure 4-24. All of the symbols for channel 2 have the same absolute phase value of π/4 when referenced to the MZ decoder transfer function for this channel. The linewidth requirements are restrictive for symbol spacing errors that are negative for the bit overlaps of 1/3 and 1/4.

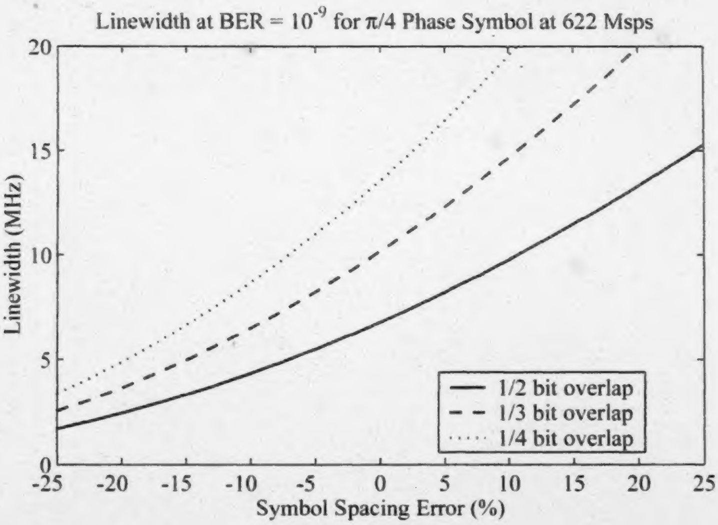

Figure 4-24: To achieve a BER of 10^{-9} or better at a symbol rate of 622 Msps with the π/4 symbols of the FCM signal, the linewidth of the signal laser line has to be less than the values shown for bit overlaps of 1/2 and 1/3.

When the bit overlap is 1/2 for channel 2 of the FCMA system at 622 Msps there is no possibility to achieve a BER of 10^{-9} with the linewidths calculated for the DFB laser in Chapter 2. Recalling the results for the 80% EO MZ modulation index as depicted in Figure 2.48, for 1/3 and 1/4 bit overlap FCMA designs the phase offset for the MZ in Chapter 2 is ~1.1 and ~1 respectively. These convert to ~7.5% and ~5% signal spacing errors which will give marginal performance for the 1/3 overlap system but acceptable for the 1/4 overlap system, where the full frequency extent of the signal is 2.8 GHz and 3.75 GHz respectively which is achievable in both cases. For an 8-ary system, the restrictions for linewidth imposed by channel 2 of the system become prohibitive with the range of around +/-20% level spacing error for 1/3 and 1/4 bit overlap.

Via similar analysis, the required transmitter linewidth that enables the reception of channel 2 of the 4-ary 1.25 Gsps FCM system with acceptable BER (10^{-9}) are found and the results are presented in Figure 4-25.

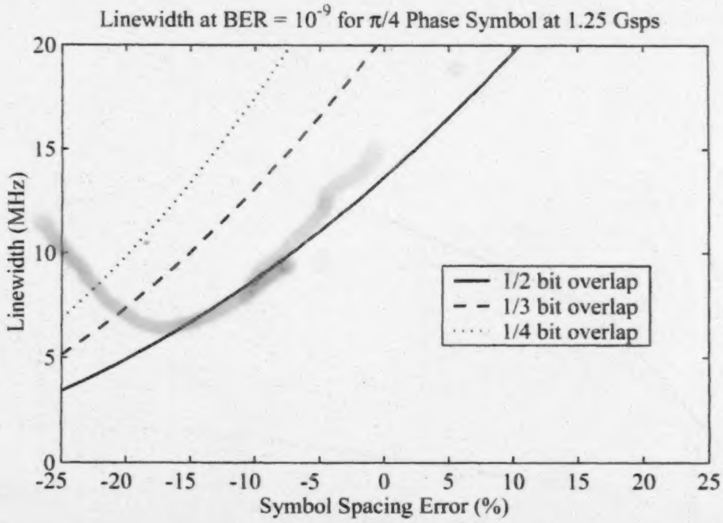

Figure 4-25: To achieve a BER of 10^{-9} or better at a symbol rate of 1.25 Gsps with the $\pi/4$ symbols of the FCM signal, the linewidth of the signal laser line has to be less than the values shown for bit overlaps of 1/2, 1/3 and 1/4.

If the transmitter linewidth could be reduced by a factor of two to 4 MHz, the system would have adequate performance with a reasonable total transmitter frequency range. The allowable symbol spacing error would extend down to -20% which would provide plenty of margin.

This analysis neglects all other noise sources at the receiver, the combined effect of phase noise errors and other noise sources will be re-addressed in Chapter 6. This concludes the design analysis of the MZ harmonic decoder, the next section summarizes the main results of this chapter.

4.6 Mach-Zehnder Harmonic Decoder Design Summary.

The design considerations of the Mach-Zehnder harmonic decoder based demultiplexor were investigated in this chapter. Some general results concerning the splitting and combining ratios of the Mach-Zehnder were presented and a specific example, the free-space MZ, was described in detail with examples of how non-ideal splitting and combining effects the decoding of the FCM signal. The phase properties of the interferometer combiner were included in the theoretical equations that describe the interference of MZ interferometers. These phase properties were neglected in the signal response analysis due to the small influence that they have in the examples that were presented. Examples of the response of ideal MZ interferometers were compared to the response of the real free-space MZ with and without optical power balancing provided by a neutral density filter in one arm of the MZ. It was found that the neutral density filter is necessary in some cases and does degrade the interferometer performance if it is not necessary.

The design of the free-space and integrated (planar) MZ harmonic decoders were described and the important design parameters were identified. Both designs could be improved, this will be discussed in Chapter 7.

The effects of the phase noise of the input signal were described in Section 4.5, where the conclusion is that the phase noise of the transmitted signal will limit the achievable bit error ratio of *M*-ary FCM signals regardless of the received optical power. This will be investigated in more detail in Chapter 6 when the overall system performance will be analyzed.

The results in this chapter were presented without regard to the receiver transfer function and receiver induced noise terms that must be included in the received BER analysis. The receiver design, including noise analysis, is the subject of the next chapter.

Chapter 5. Dual Differential Optical Receivers.

The function of optical receivers in a fiber communication link is to perform the conversion of a signal from the optical domain to the electrical domain. This conversion is performed by absorbing photons in an electrical device where the process of absorption leads to the promotion of electrons from a non-conductive state to a conductive state. Photodiodes are used to receive optical signals in communication systems. For high data rate communications the options for optical to electrical conversion are the positive-intrinsic-negative (PIN) photodiode and the avalanche photodiode (APD). An electric field bias is applied to the photodiode to generate a current from electrons that are promoted to the semiconductor conduction band. This current is then amplified to a reasonable signal level and, in a digital system such as FCMA, a decision circuit is used to determine the intended transmitted signal value.

For FCMA the transmitted signal is frequency shift keyed (FSK) with undesired, residual amplitude shifts that are produced via the modulation method. These amplitude shifts have to be decoupled from the frequency shifts while using the frequency shifts to generate electrical amplitude shifts. This can be accomplished by combining the optical harmonic decoders, discussed in Chapter 4, with a dual differential receiver. In a practical FCMA system using a dual differential receiver the residual optical amplitude shifts will not be completely eliminated, but it will be shown in this chapter that the FCMA system is quite tolerant of these amplitude shifts.

The design of the FCMA receiver section is a trade off between high bandwidth, in order to reduce signal distortion, and limiting the bandwidth to reduce noise. Ultimately, the bit error ratio (BER) will be calculated for the FCMA receiver design presented in this chapter to determine the receiver quality.

An introduction to the concept of dual differential receivers is presented in Section 5.1 with justifications for using a dual receiver arrangement for receiving differential coherent signals. Section 5.2 covers some basic design criteria for dual differential receivers and the use of transimpedance amplifiers in optical receivers. Some specific information on the PIN diodes and single chip transimpedance amplifiers will be presented in Section 5.3. Section 5.4 presents the receiver circuit schematics, simulation schematics and simulation results that were used in the design of the dual differential receivers. The physical layout of the RF substrate is shown in Section 5.5. Section 5.6 compares the simulated receiver response to the measured receiver response and discusses similarities and differences between them. Section 5.7 re-presents some of the eye diagrams presented in Chapter 4 where the receiver transfer function has been included and the effects inter-symbol interference (ISI) will be discussed. Section 5.8 presents a discussion of receiver noise calculations before presenting results for the simulated receiver design BER performance and Section 5.9 wraps up the chapter with a summary of the content.

5.1 Receiving Digital Data with Dual Differential Receivers.

Coherent optical transmission systems fall into two general categories; local oscillator systems and self interference systems. Local oscillator systems are those systems that rely on mixing an information bearing signal with another frequency, the local oscillator, to produce interference. The term "local oscillator" will be used here loosely regardless of whether or not the local oscillator is truly local (located at the receiver). The self interference systems mix the information bearing signal with a time delayed version of itself and therefore these systems only contain the transmitted signal.

Both types of coherent systems depend on interference to recover the transmitted information at the receiver. Interference based receivers typically use a 3 dB coupling system (for example a 50/50 beam splitter cube) where of all of the transmitted optical power can be recovered when both outputs of the 3 dB coupler are used to observe the interference. Using the full range of interference in a coherent binary transmission, that is from total destructive interference to total constructive interference, with one optical to electrical conversion device (i.e.; one PIN diode) only recovers half of the available transmitted signal power with the other half of available signal power being discarded. By employing another signal receiver to recover the "discarded" signal power, the total received power is doubled by using these two received signals. The received power (electrical) increases by 6 dB, and, since the noise amplitudes add as square roots (assuming white spectral noise), the increase in noise power is only 3 dB (electrical). Overall, an increase of 3 dB for the electrical signal to noise ratio (SNR) is realized. It is this fact that motivates designers of coherent binary communication systems to use dual differential receivers.

5.2 Dual Differential Receiver Design.

The receiver design implemented for this project uses two PIN photodiodes. Ideally, these photodiodes would be concatenated, with the anode of first PIN diode connected to the cathode of the other, as shown in Figure 5-1.

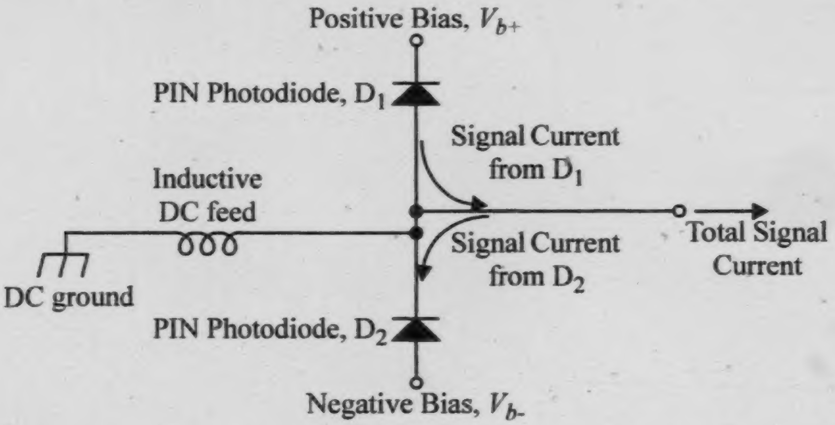
Positive Bias, V_{b+}
PIN Photodiode, D_1
Signal Current from D_1
Inductive DC feed
Total Signal Current
Signal Current from D_2
DC ground
PIN Photodiode, D_2
Negative Bias, V_{b-}

Figure 5-1: An example circuit schematic of the concatenation of PIN photodiodes in a dual differential receiver.

The circuit could be realized by integrating the two diodes on the same semiconductor chip with the connection shown, or two separate diode chips could be mounted on the same receiver substrate. Regardless of which circuit option is used, the total signal current at the output on the right of Figure 5-1 is the sum of the out of phase components of the currents from the two diodes. The in phase components of the diode signal currents interfere destructively and do not appear at the output. A differential receiver is designed to amplify a differential signal.

As an introductory design analysis consider Figure 5-2 which diagramatically depicts the reception of the differential optical signals, denoted b_{sig+} and b_{sig-}, and the subsequent addition of their electrical current counterparts, I_{sig+} and I_{sig-}. Enough of the relevant information for the calculations in this section is contained in Figure 5-2.

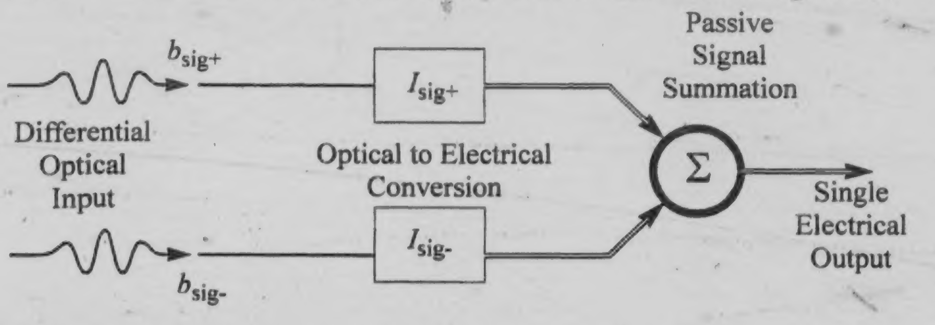
b_{sig+}
I_{sig+}
Passive Signal Summation
Differential Optical Input
Optical to Electrical Conversion
Σ
Single Electrical Output
I_{sig-}
b_{sig-}

Figure 5-2: Functional diagram depicting the operation of a differential optical receiver. Optical input signals, b_{sig+} and b_{sig-}, are converted to electrical signals and added to produce a single electrical output signal.

The input optical signals, b_{sig+} and b_{sig-}, can be written down as the sum and the difference of two other variables as in the following equations, Equations (108) and (109),

$$b_{sig+} = P_{cm} + P_{dm} , \tag{108}$$

and

$$b_{sig-} = P_{cm} - P_{dm} , \tag{109}$$

where P_{cm} is a common mode optical power term and P_{dm} is a differential mode optical power term from the interferometer harmonic decoder.

The optical to electrical conversion gives the following relations for the signal currents I_{sig+} and I_{sig-}, Equations (110) and (111),

$$I_{sig+} \propto (b_{sig+}) \tag{110}$$

and

$$I_{sig-} \propto -(b_{sig-}) \tag{111}$$

with identical constants of proportionality. Using Equations (108)-(111), the sum total signal current $I_{total} = I_{sig+} + I_{sig-}$ obeys the proportionality

$$I_{total} \propto 2P_{dm}\,. \tag{112}$$

The total signal current in this case is only proportional to the differential signal.

The optical power dependent noise terms, such as signal shot noise, $\langle i_s^2 \rangle$, are proportional to the sum of the total received optical power as in the following equation,

$$\langle i_s^2 \rangle \propto 2P_{cm}\,. \tag{113}$$

The signal dependent noise terms, such as shot noise, are proportional to the total received optical power. This fact leads to a reduction of the theoretical 3 dB gain in electrical SNR from using a dual receiver as opposed to a single receiver, this will be readdressed later in this chapter.

In Figure 5-1 the DC feed connection to DC ground is necessary to keep the bias of the two diodes balanced so that the voltage at the common connection between the diodes does not drift and contribute to the signal at the output of the circuit. The DC feed inductor presents an non-zero (usually high) impedance at high frequencies but is a short circuit for DC. All of the desired signal current flows to (and from) the output of the circuit.

High speed receivers almost always have a low noise amplifier and, in optical receivers, this amplifier is placed as close to the photodiodes as possible. The functions of the amplifier are to convert the signal current to signal voltage and to provide some signal gain. There are options for the circuit implementation of this amplifier, one of which is a transimpedance amplifier, see Figure 5-3.

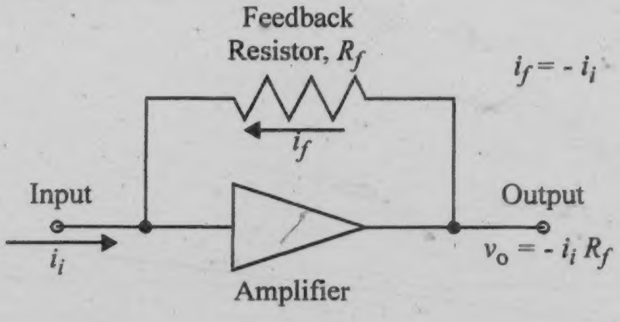

Figure 5-3: Circuit diagram of a transimpedance amplifier.

The output voltage, v_o, of a transimpedance amplifier is proportional to the product of incident current, i_i, and the feedback resistance, R_f, where the feedback current, i_f is the same magnitude as the incident current.

A commercial receiver design would include a signal limiter, a clock recovery circuit and a decision circuit (and possibly an equalizer). These functions are performed in the laboratory by using a Bit Error Ratio Test set (BERT) and this research assumes that any implementation of a fully functional receiver would incorporate these components.

The planned dual differential receiver design for this project was to include two PIN photodiodes on one substrate, connected as shown in Figure 5-1. This turned out to be infeasible due to the unavailability of diodes integrated on one chip with an anode connected to a cathode. The choice of putting two single diode chips on one RF substrate was also ruled out due to the difficulty involved with mounting two chips consistently together to providing adequate optical coupling to the active regions of both photodiodes. The solution was to package two diodes in separate enclosures with independent optical couplings. This simplified the mechanical design and electrical design of the receiver without adversely affecting performance.

The proposed functional arrangement of the dual differential receiver is depicted in Figure 5-4. Of the two pairs of receivers built, only two were successfully assembled and both were of the type labelled RECEIVER ENCLOSURE #2 in Figure 5-4. Fortunately, a receiver of type #2 can be substituted for a receiver of type #1 by inverting the output. An inverting amplifier with a gain of 10 dB was attached to the output of the receiver followed by a 10 dB attenuator. This arrangement degrades the signal to noise ratio but the function of the differential receiver is not altered.

The components that have the largest impact on the effectiveness of the differential receiver are the PIN photodiode and the transimpedance amplifier. The next section is dedicated to elaborating on some of the specific qualities of the photodiode and amplifier components that were chosen for the construction of the optical receiver.

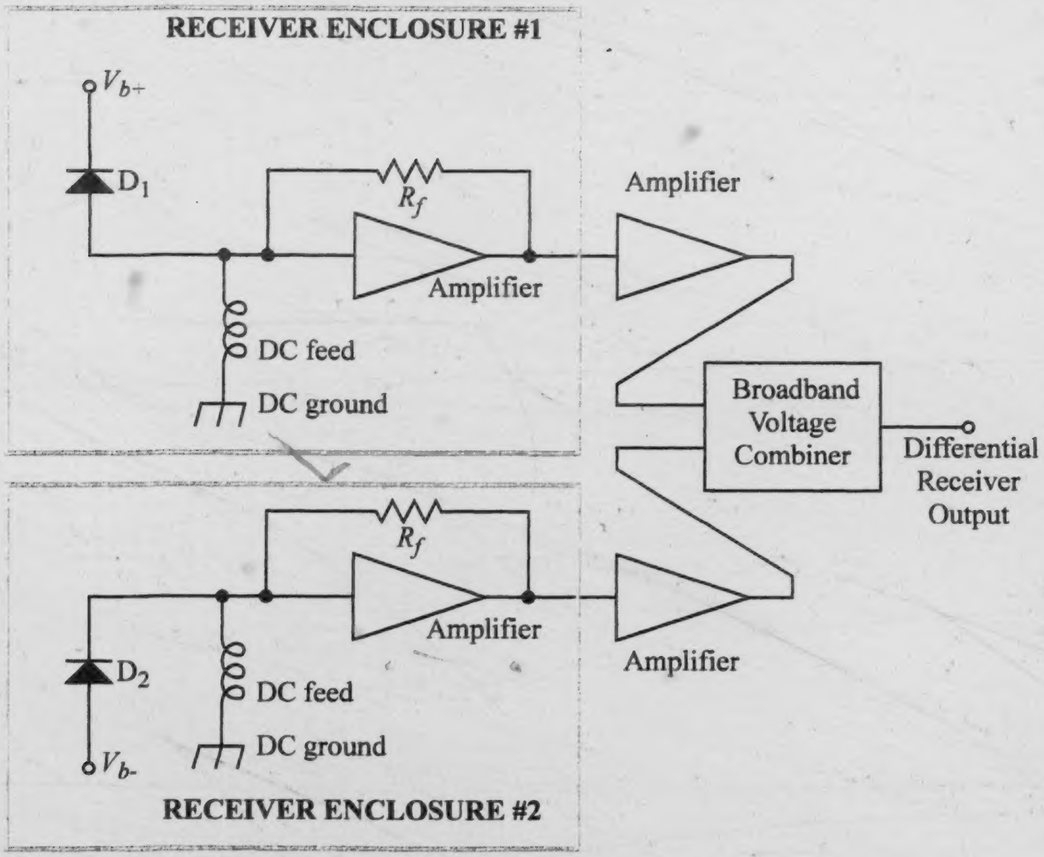
RECEIVER ENCLOSURE #1
V_{b+}
D_1
R_f
Amplifier
Amplifier
DC feed
DC ground
Broadband Voltage Combiner
Differential Receiver Output
R_f
Amplifier
Amplifier
D_2
DC feed
DC ground
V_{b-}
RECEIVER ENCLOSURE #2

Figure 5-4: Proposed functional arrangement of the dual differential receiver.

5.3 PIN Photodiodes and Transimpedance Amplifiers.

The PIN photodiodes were supplied courtesy of Nortel Networks Incorporated and have a bandwidth in excess of 10 GHz. The chips are 500 μm x 500 μm with a circular active region in the center of the chip with a diameter of 25 μm. The electrical connections are supplied by three pads on one edge, approximately 120 μm by 80 μm with the long dimension perpendicular to the edge and spaced approximately 140 μm apart. The center pad is the p contact and the outer pads are connected to a guard ring around the active region and supply the n contact. The substrate is semi-insulating n doped semiconductor. The material system of the diodes is InP with an external quantum efficiency of approximately 0.80 at 1550 nm [KAH1]. An external quantum efficiency of

0.75 was used in all of the following calculations to take into account the fiber pigtail reflection (~ 4% of the incident light) and an assumption that some of the light will not hit the active region of the detector.

The capacitances of the PIN diode (n doped region to ground, p doped region to ground and n doped region to p doped region) are all on the order of 100 fF with a guaranteed upper limit of 500 fF. The RC time constant of any of these capacitive contributions in a 50 Ω system is on the order of 25 ps which will be sufficiently low for the required bandwidth (~1.8 GHz) of the receiver that the time constants can be neglected.

The transimpedance amplifiers were a 50 Ω through impedance Silicon integrated circuit, part number INA-51063, supplied courtesy of Hewlett Packard. These devices supply 20 dB gain from DC to over 2 GHz with a noise factor of 3dB within the receiver bandwidth.

The PIN photodiode and the amplifier were chosen for these reasons. The receiver that was designed using these components is introduced in the following section.

5.4 Proposed Receiver Circuit.

The receiver labelled "RECEIVER ENCLOSURE #2" in Figure 5-4 is schematically drawn in Figure 5-5 with the addition of a T-filter between the PIN photodiode and the amplifier. The component values for the circuit in Figure 5-5 are listed in Table 5-1.

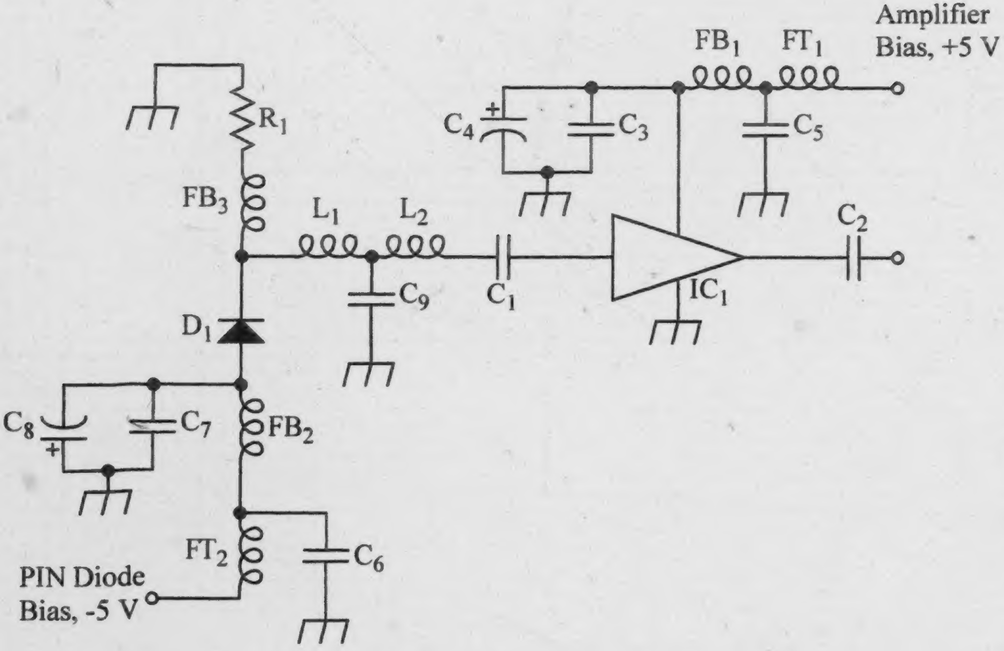
Amplifier
Bias, +5 V
FB1
FT1
R1
C4
C3
C5
FB3
L1
L2
C2
C9
C1
IC1
D1
C8
C7
FB2
FT2
C6
PIN Diode
Bias, -5 V

Figure 5-5: The optical receiver circuit schematic (component values are listed in Table 5-1).

Table 5-1: Component values for the circuit schematic in Figure 5-5.

Component	Function	Value and Unit
R_1	Ground Feed Resistor	50 Ω
C_1 & C_2	DC Blocking Capacitor	1 nF
C_3 & C_7	Power Supply Bypass Capacitor (High Frequency)	1 nF
C_4 & C_8	Power Supply Bypass Capacitor (Low Frequency)	1 μF
C_5 & C_6	Power Supply Bypass Capacitor	0.1 μF
C_9	T-filter Shunt Capacitor (ATC part number 111XAX1R6B100TT)	1.6 nF
L_1 & L_2	T-filter Series Inductors (μRata part number LQP21A2N2C14)	2.2 pH
FB_1, FB_2, and FB_3	Ferrite Beads	~ 50 Ω at passband frequencies
FT_1 & FT_2	DC Feed Throughs	N/A
IC_1	HP INA-51063 Transimpedance Amplifier MMIC	N/A
D_1	Nortel HS-PIN Diode	N/A

The signal received by the PIN diode is amplified by the INA-51063 monolithic transimpedance amplifier in this 50 Ω characteristic impedance circuit. The bias voltages present at the input and output of the amplifier are isolated from the rest of the circuit with the blocking capacitors C_1 and C_2. The amplifier has a broadband power gain of greater than 20 dB with a high frequency corner of approximately 2 GHz. The T-filter, represented by L_1, L_2, and C_9, reduces the 3 dB bandwidth to 1.630 GHz, which is appropriate for a OC-48 receiver [EL1,TO1]. Also, the T-filter compensates for a 1.5 dB rise in gain and distortion of the phase response of the receiver near 1.6 GHz. In order to model this receiver circuit with a microwave circuit simulation software, equivalent circuits for the components were used. The capacitors were modelled as a series RLC combination, the inductors were modelled as a series resistor and inductor with a parallel capacitance, and the PIN diode model was derived from measurements made with a network analyzer.

5.4.1 PIN Diode Equivalent Circuit.

The forward transfer characteristic of the PIN diode, current generated as a function of input optical power, was assumed to be flat across the bandwidth of the receiver with a linear phase response. The diode reflection characteristics, looking back into the diode as a one port device, were measured with a network analyzer due to the fact that the INA-51063 has a large value of S11 (> 0.2) above 2 GHz which could cause multiple reflections between the input of the amp and the PIN diode because of the potentially "large" impedance difference between the PIN diode and the transmission lines.

Appendix B discusses the method used to derive the PIN diode equivalent circuit model and the values that were assigned to the model components. The resulting circuit model is shown below in Figure 5-6.

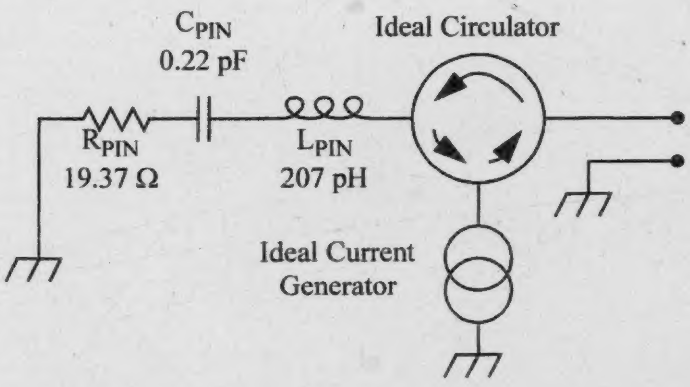

Figure 5-6: Equivalent circuit representation of a Nortel HS-PIN optical receiver diode.

This PIN diode equivalent circuit model was used in the receiver circuit model that is the subject of the following section.

5.4.2 Equivalent Circuit for Simulation.

The Hewlett Packard Microwave Design Simulator (MDS) software package was used to calculate the expected performance of the receiver circuit design. The PIN photodiode was modelled as per the circuit shown in Figure 5-6 and was used as the signal source in the simulations. The transimpedance (TZ) amplifier was modelled using the S-parameters that were supplied by the manufacturer. The passive components were modelled as per the data supplied by their respective manufacturers and the waveguides were modelled considering the properties of the RF substrate.

Figure 5-5 and Figure 5-6 along with the manufacturers data for the other passive components were used to arrive at the equivalent circuit model for the receiver design that is depicted in Figure 5-7.

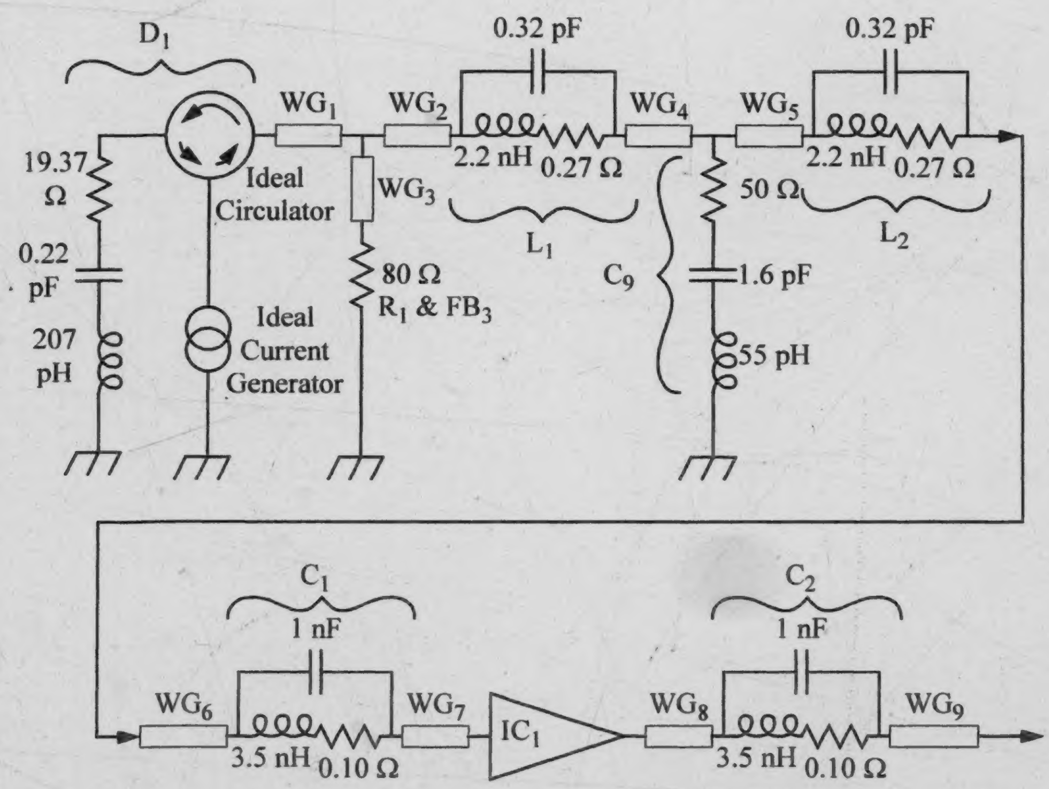
D_1
0.32 pF
0.32 pF
WG_1
WG_2
WG_4
WG_5
19.37 Ω
Ideal Circulator
WG_3
2.2 nH
0.27 Ω
2.2 nH
0.27 Ω
50 Ω
0.22 pF
L_1
L_2
80 Ω
R_1 & FB_3
C_9
1.6 pF
207 pH
Ideal Current Generator
55 pH
C_1
1 nF
C_2
1 nF
WG_6
WG_7
IC_1
WG_8
WG_9
3.5 nH
0.10 Ω
3.5 nH
0.10 Ω

Figure 5-7: Equivalent circuit for the optical receiver including parasitic contributions for passive components.

Manufacturers data sheets show the frequency response for passive RF components which give the designer a good idea of the resonant behaviour of a particular component due to parasitic resistance, inductance and capacitance. A series or parallel parasitic circuit model can then be used to represent the component in an RF circuit simulation that will behave in the simulator like the component will behave in a real circuit. The series inductors (L_1 and L_2) and the DC blocking capacitors (C_1 and C_2) were modelled as parallel resonant circuits and shunt capacitor of the T-filter (C_9) was modelled with a series resonant RLC combination.

The rectangles in Figure 5-7 represent electrical waveguides (hence the abbreviation WG next to each one). These waveguides were strip-line type waveguides where the widths of the tracks determine their characteristic impedances. The characteristic impedances and lengths of these waveguides are listed in Table 5-2.

Table 5-2: Waveguide impedances and lengths for the simulation circuit in Figure 5-7.

Microstrip Waveguide Label (see Figure 5-7)	Characteristic Impedance	Length (in units of 0.001 inches)
WG_1	50 Ω	110
WG_2	50 Ω	110
WG_3	110 Ω	100
WG_4	50 Ω	80
WG_5	50 Ω	80
WG_6	50 Ω	160
WG_7	50 Ω	140
WG_8	50 Ω	140
WG_9	50 Ω	120

The equivalent receiver circuit shown in Figure 5-7 neglects contributions to the receiver response due to the PIN diode bias circuitry and the power supply and ground circuits connected to the amplifier (IC_1). The difference between the design response and the actual response of the receiver circuitry will be discussed in a later section after the design response has been presented in the following section.

5.4.3 Optical Receiver Simulation Results.

The simulation of the optical receiver was performed using MDS in swept frequency mode assuming that the PIN diode generated the sinusoidal current waveform of a swept frequency generator. The simulation results could then be plotted in Bode plots to view the expected performance of the receiver. The receiver electrical power response is plotted below in Figure 5-8.

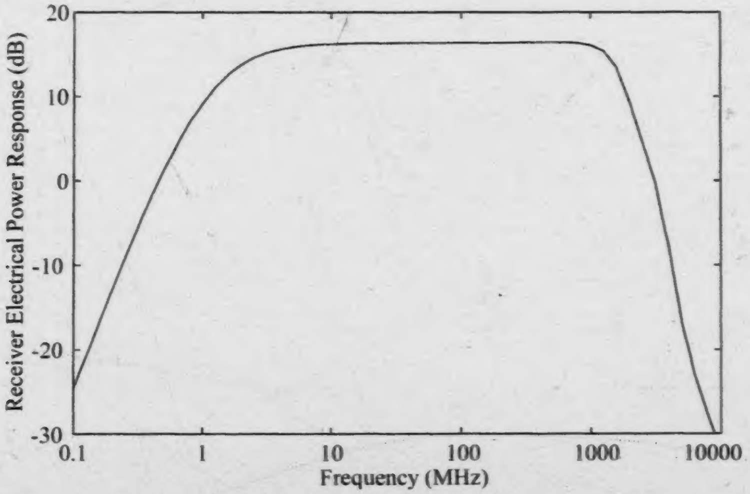

Figure 5-8: The electrical power response of the optical receiver as a function of frequency plotted as output electrical power referenced to electrical power generated by the PIN photodiode.

Figure 5-8 is the plot of the electrical circuit (Figure 5-7) output power referenced to the current generator output power. The response shows a flat power gain of approximately 16 dB from a few MHz to over 1 GHz, which is approximately 3 decades of frequency. The power response falls sharply on the high frequency side about 50 dB from the in-band gain in 1 decade of frequency. The high frequency 3 dB corner frequency of the response is at 1.630 GHz. The "rule of thumb", which is to have this corner frequency above 2/3 of the bitrate, is adequately met for an OC-48 SONET signal. The optical signal symbol width at the receiver for Gigabit Ethernet with a 1/2 bit duration overlap is about the same as binary SONET OC-48, so one would expect similar receiver performance for both transmission formats.

The simulated phase response of the receiver is plotted in Figure 5-9.

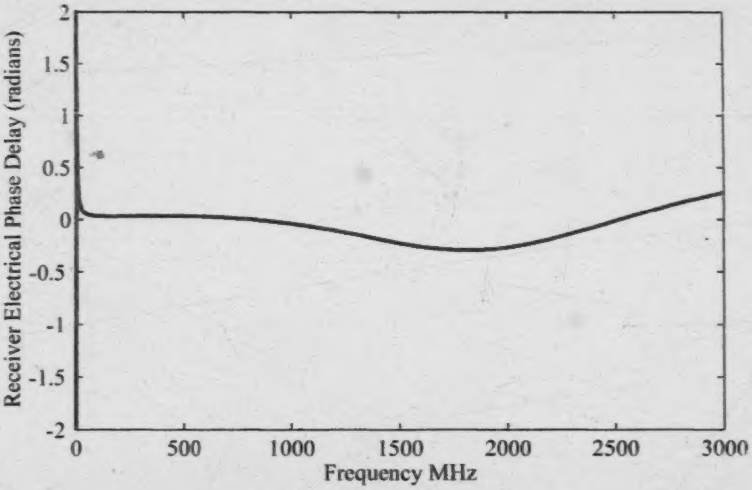

Figure 5-9: The electrical phase response of the optical receiver as a function of frequency plotted as output phase referenced to phase at the PIN photodiode with the linear phase contributions removed.

The simulated phase response of the receiver is reasonably flat out to the 3 dB corner frequency of the receiver. The phase response plotted in Figure 5-9 demonstrates an improvement in linearity of the phase response of the monolithic TZ amplifier as described in the manufacturer's data sheet which suggests that the T-filter corrects the phase, as well as limiting the bandwidth, of the amplifier. Having successfully simulated the receiver design, the next step is the RF substrate layout which is the subject of the following section.

5.5 Receiver RF Substrate Layout.

The RF substrate layout was done using the layout tool that comes with the HP MDS simulator. The layout software is based on orienting polygons, rectangles and circles to create the conductive features of the circuit as well as locating the via connections between the two sides of the substrate. The software generates standard files that can be used by the circuit board manufacturer to automate the circuit board lithography and via drilling manufacturing steps.

The top side of the substrate contained all of the passive and active electrical components as well as power supply connections and the PIN photodiode. All of the intercomponent electrical connections were made with microstrip waveguides where the impedance of the waveguides is determined by their width with respect to the properties of the substrate. The Rogers TMM-3 ceramic substrate was used because the width of a 50 Ω track is 0.050 inches which is the width of standard surface mount high speed 0805 passive circuit components. The layout of the top side of the circuit board is shown in Figure 5-10.

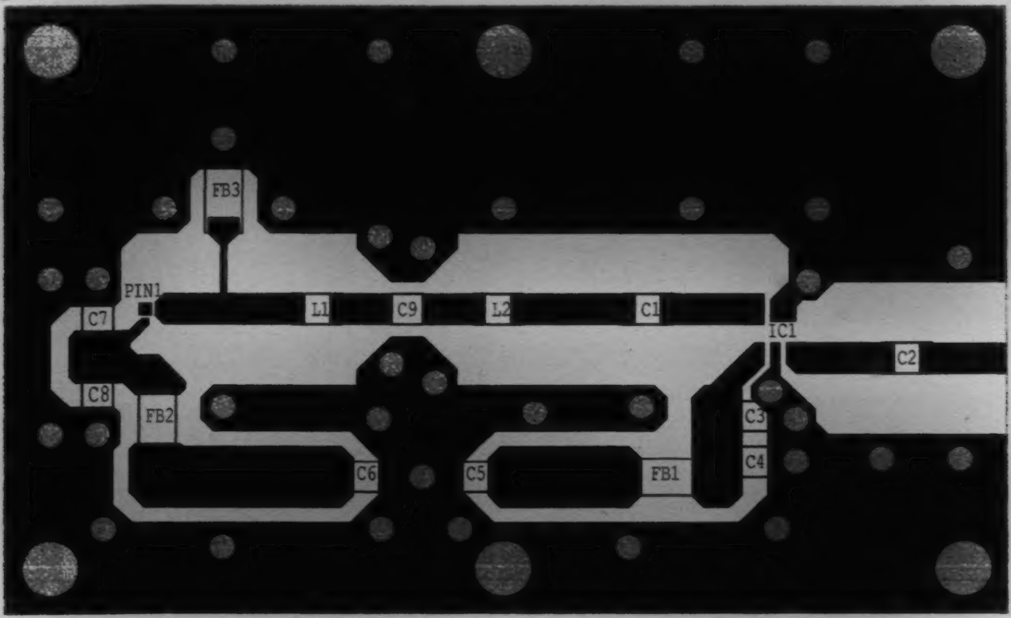

Figure 5-10: The top side (component side) of the receiver RF substrate. All of the circular features are via locations and all of the black areas are conductive. The circuit is not drawn to scale (see text).

The reverse side of the substrate provides the ground plane for the microstrip waveguides. Holes in the conductive surface of the reverse side of the substrate were intentionally put beneath inductive components. This is done so as not to increase the associated capacitance of those components which would lower their intrinsic parasitic resonance frequencies which are designed to be outside the signal band of the circuit.

This circuit layout was used to make RF circuit boards that were populated with components. The PIN diodes and the ATC capacitor (used for the T-filter) had to be wire-bonded into the circuit and the bias voltages were supplied to the circuits via feed throughs situated in the circuit board housings. A 3-axis positioner was used to locate a single mode fiber above the active region of the PIN photodiode to make the receiver ready for use. The receivers could then be tested which will be discussed in the following section.

5.6 Measured Response of the Optical Receiver.

Measuring the response of the optical receiver required the calibration of the measurement equipment which involved accurately measuring the modulation response of the Lucent MZ modulator that was used to produce the optical signal. As is explained in depth in Appendix C, the small signal transfer function from electrical domain to the optical domain can be characterized by knowing the V_π, the voltage required for a phase change of π, of the modulator as a function of frequency. The electrical systems, which are the modulation drive electronics and the receiver post-amplification electronics, can be measured back to back so they can be subtracted from later measurements. Measuring the entire system, from the modulation drive electronics through the modulator and receiver and finally the post-amplification electronics, and calibrating everything except the receiver contribution to the measurement is how the receiver transfer function was measured.

If the receiver had an infinite bandwidth and linear phase, the received electrical signal voltage would exactly mimic the optical power signal, meaning that electrical voltage signal is directly proportional to the incident optical power. In the measurement of the real optical receiver there is a linear transfer function between optical power and electrical voltage which is what is measured and what is displayed in the following plot, Figure 5-11.

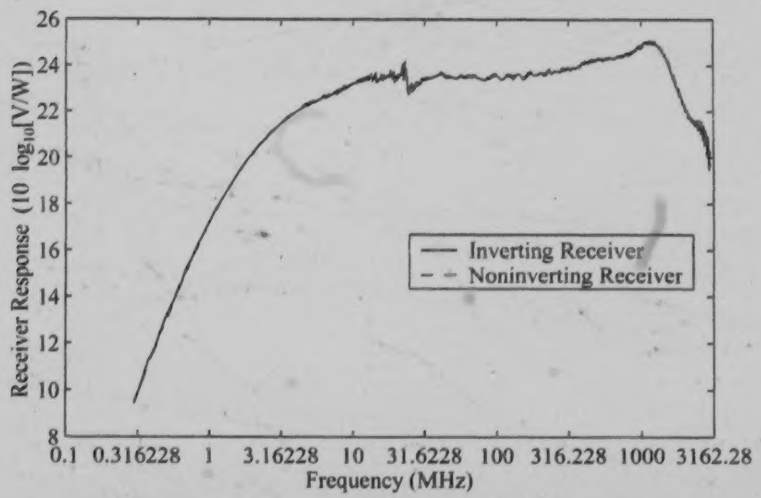

Figure 5-11: The optical power to electrical voltage response of two optical receivers. The inverting receiver and noninverting receiver are identical and inverting, an inverting gain stage is external to the noninverting receiver.

Taking the logarithm of a value with dimensional units is not mathematically correct, but in this case the plot of receiver output voltage versus incident optical power is more descriptive of the physical situation. To be mathematically correct one could simply provide a reference of 1 V/W gain and invent a unit similar to dBm. As an example consider the response of the receiver at ~500 MHz, which is approximately 24 dB, a 1 mW peak to peak sine wave of optical power at the input of the receiver would generate a 256 mV peak to peak sine wave at the output of the receiver.

To convert the response plot to a meaningful unit base, the input optical power is converted to PIN photodiode voltage by assuming an external quantum efficiency of 0.75 and knowing that the characteristic impedance of the circuit is 50 Ω. The following plot of the receiver transfer function, Figure 5-12, is the ratio of the output voltage to this calculated PIN photodiode voltage.

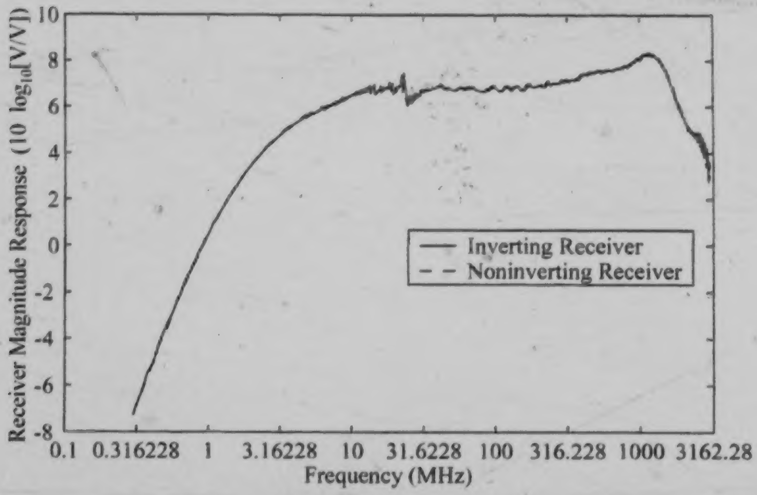

Figure 5-12: The PIN photodiode voltage (in 50 Ω) to output voltage response of two optical receivers. The inverting receiver and noninverting receiver are identical and inverting, an inverting gain stage is external to the noninverting receiver.

This plot uses a logarithm argument that is a ratio of voltages so, since the decibel unit is reserved for power ratios in a conventional engineering sense, the units are still not quite correct. The same response function plotted in true power per power decibels for the electrical power out from the receiver and the electrical power generated by the PIN diode is shown in Figure 5-13.

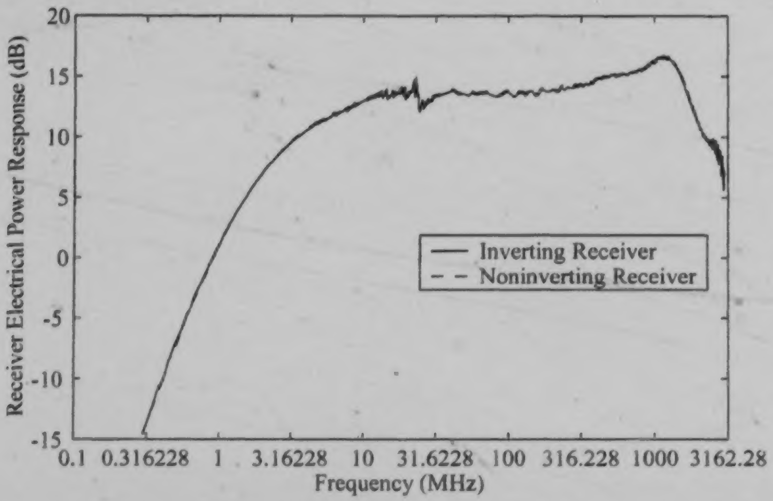

Figure 5-13: The PIN photodiode electrical power (in 50 Ω) to electrical output power response of two optical receivers. The inverting receiver and noninverting receiver are identical and inverting, an inverting gain stage is external to the noninverting receiver.

The magnitude and power responses of the two receivers that were measured are nearly identical, which suggests good repeatability in the performance from the design.

Before presenting the phase response of the receivers the reader is reminded that both receivers are inverting receivers. The receiver that has been called noninverting is identified in that way because it functions in the dual differential receiver as noninverting. An additional inverting unity-gain amplifier is used externally to make it non-inverting. The linear group delay was removed from the measurements so that the phase distortion would stand out. The measured phase responses of the two inverting receivers are presented in Figure 5-14.

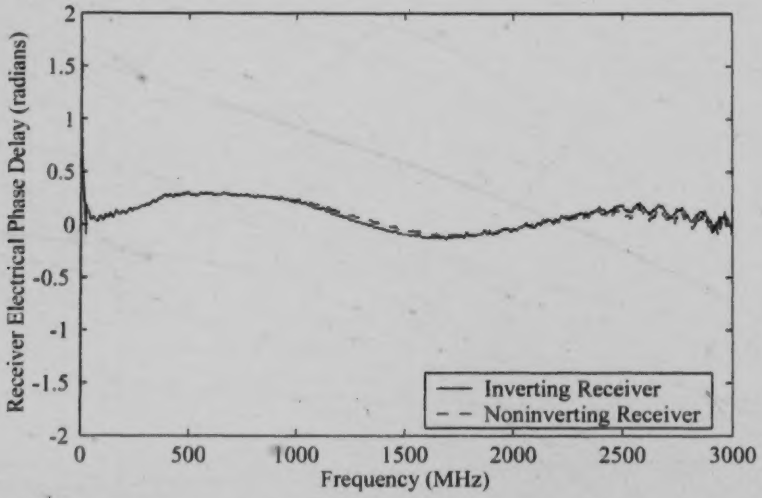

Figure 5-14: The phase response of two optical receivers. The inverting receiver and noninverting receiver are identical and inverting, an inverting gain stage is external to the noninverting receiver.

The phase response is plotted against linear frequency units with the same scale as the simulation results presented earlier in Figure 5-9. The phase response of the two receivers that were measured are nearly identical, which suggests good repeatability in the performance from the design. The following section is a comparison of the simulation and measurement results for the optical receiver for both magnitude and phase response.

5.6.1 Comparison of Receiver Simulations and Measurements.

The comparison of the simulation of the receiver response to the measurements performed on real receivers is done by visually comparing the previously presented data when both simulated and measured results are plotted on the same graph. Only one of the measured results for the receiver is presented to compare with the simulation since the two measurements are nearly indistinguishable. Figure 5-15 shows the electrical power response of the receiver for both measurements and simulations.

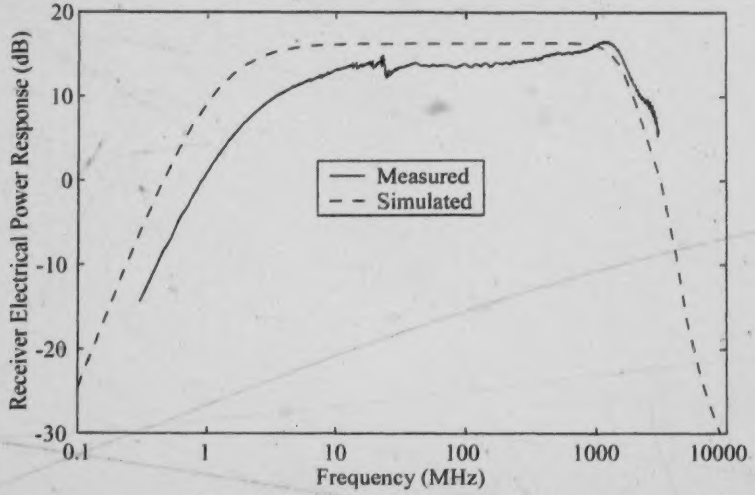

Figure 5-15: The measured and simulated electrical power response of the optical receiver assuming the quantum efficiency is 0.75 in a 50 Ω electrical circuit.

The measured result is about 2-3 dB lower in electrical power response than the simulation over most of the gain band and the low end corner frequency of the real receiver is quite a bit higher than it is in the simulated result. The primary reason for discrepancy in the power response is assumed to be due to signal power leaking through the PIN diode bias circuit which was not accounted for in the simulation. Another difference is the bump in the response above 1 GHz which is probably due to imperfections with the transimpedance amplifier bias circuitry, the natural response of the monolithic TZ amplifier has a slight bump in its response at those frequencies and the data sheet from the manufacturer implies that imperfect bias circuits will cause problems. Finally, the low end corner frequency being too high is probably due to poor performance in the series DC blocking capacitors that were used.

The phase response of the receiver has similar characteristics for the measured response and the simulated response as demonstrated by the figure below, Figure 5-16.

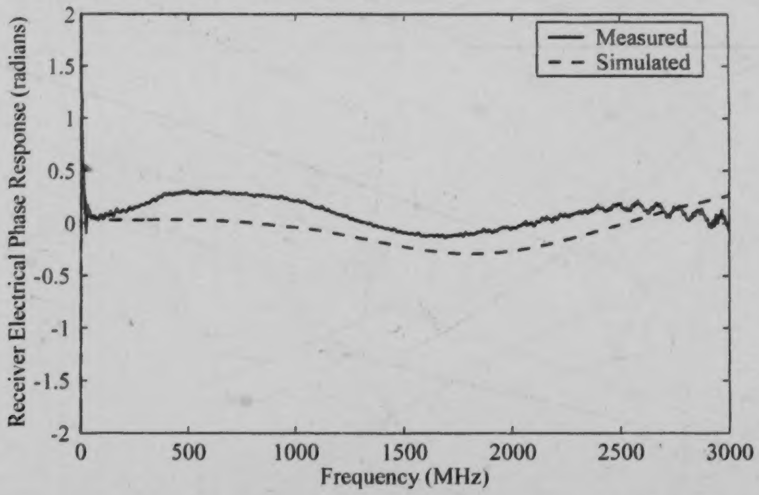

Figure 5-16: The measured and simulated phase response of the optical receiver in a 50 Ω electrical circuit.

The measured and simulated phase response of the optical receiver have similar shapes when plotted as function of modulation frequency. There is a dip in phase in both curves between 1.5 and 2 GHz and the phase, as shown in Figure 5-16, does not change much over the 3 GHz measurement band.

Based on the comparison of the measured and simulated responses of the optical receiver design, the design is considered to be a success. For the remainder of the presented results of this chapter the simulated response function of the receiver will be used. The section that follows this one presents received eye-diagrams, it is appropriate in this section to use the simulated receiver response function because all of the other contributions to calculating these eye diagrams are theoretical as well. The section that follows the eye diagram section deals with receiver noise and calculations of expected receiver performance and is also mostly about theoretical predictions, therefore the appropriate receiver function to use is the simulation response.

5.7 Received Signal Eye Diagrams for Back-to-Back FCMA Links.

The receiver limits the bandwidth of the optical signal that it receives. The effects of the theoretical receiver transfer function on the harmonically decoded FCM signal discussed in Chapters 2 through 4 are presented in this section for back-to-back transmission (a link that covers no distance). The effects of fiber dispersion are not taken into account in this situation and will be left for discussion is Chapter 6. In Section 4.4, theoretical eye-diagrams were presented for the laser simulation FCM signal results being passed through the MZ decoder and the mathematical results of the output signals from the two decoder outputs were subtracted and plotted. These eye-diagrams represent what would happen if the optical receivers in the FCMA system had infinite bandwidth with linear phase responses, which is not a physically realizable receiver system. When a real receiver transfer function is used to receive the optical signals, the effect on the received signal is that the best achievable performance is limited.

When the eye-diagrams were calculated in Chapter 4, the signal polarities were chosen such that the plotted signal was a result of subtracting the optical power from the decoder output labelled 2 from the decoder output labelled 1. To maintain the signal polarities of the decoded signals as presented in the signal state diagrams in Chapter 1, the channel with the shortest delay, $\tau_{\Delta L/(\log 2M)}$, is the only channel that has this subtraction polarity, $P_{1\text{-}2} \sim P_1 - P_2$. All of the other channels of the FCMA system must have a polarity consistent with the reverse of this channel, or $P_{2\text{-}1} \sim P_2 - P_1$. Eye diagrams presented throughout Chapter 4 have only the $P_1 - P_2$ optical power signal polarity shown. From this point forward, the signal polarities will correspond to the polarity matching the signal state diagrams of Chapter 1.

For an example case of Gigabit Ethernet, which is the symbol rate for this 4-level FCMA link, the frequency spacing of the symbols is chosen to be such that channel 1 of the decoder will have a delay equal to half of the bit period. This is the same example as was shown in Figure 4-20 of Section 4.4, where the time periods between successive bits for channel 1 contain some fast spikes in optical power which are incident on the receiver. The same laser-simulation generated FCM signal is passed through the decoder and modified by the receiver transfer function before subtracting the two output signals to produce the eye-diagrams presented in Figure 5-17.

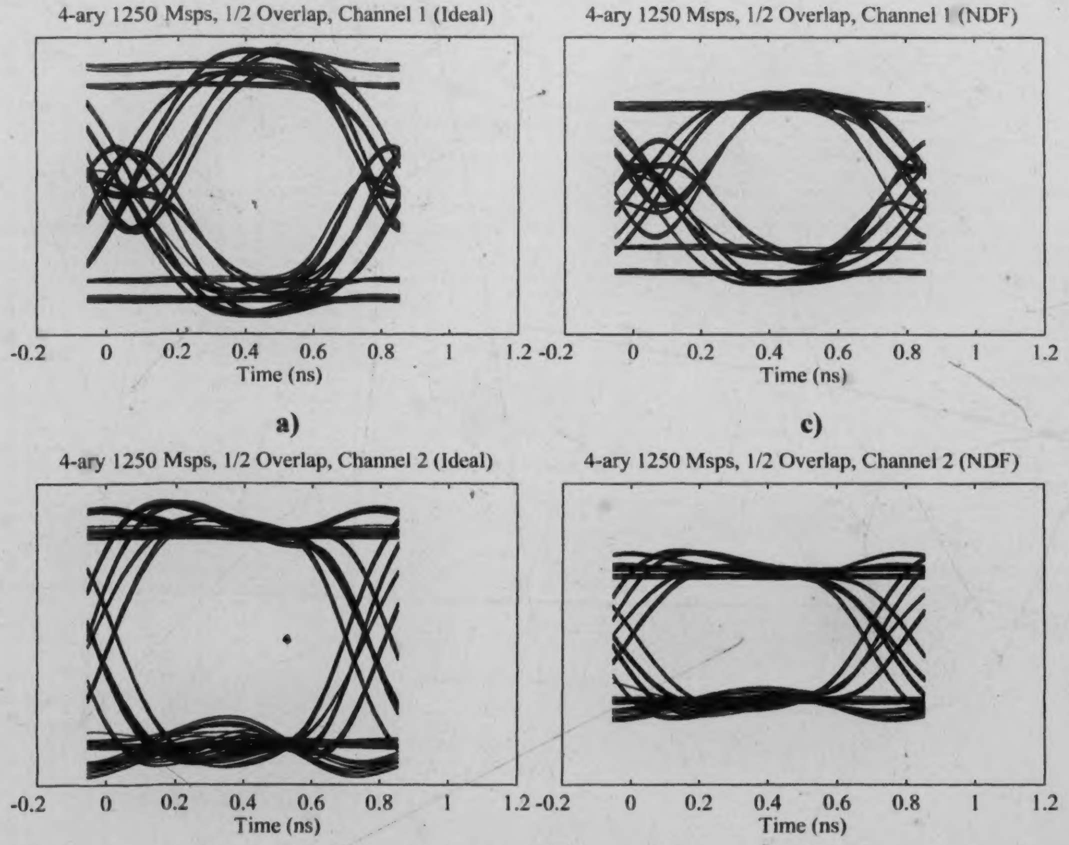

a) **c)**

b) **d)**

Figure 5-17: Four eye diagrams depicting the difference between the response of an ideal MZ to the free-space MZ with a neutral density filter (NDF) for both channels of a 4-ary, 1250 Msps, FCM signal. The plots include the post subtraction after being received and the receiver transfer function. **a)** and **b)** are channels 1 and 2 for the ideal MZ and **c)** and **d)** are channels 1 and 2 with the NDF (denoted NDF).

The calculated eye-diagrams in Figure 5-17 are for both channels 1 and 2 where the ideal decoder and the real decoder with the neutral density filter (NDF) are used to decode the channels. The receiver transfer function rounds off the edges of the signal and reduces the spiking behaviour of the signal (between successive bits) for channel 1. The eye-diagrams show that the receiver performance is more than adequate to receive the signal because it has been demonstrated that the eye remains open. Receiver induced ISI causes the thickening of the lines in these eye diagrams as can be evidenced by comparing them with Figure 4-20. Also, these eye diagrams can be compared to the similar binary FSK direct detection eye diagrams presented in [EL1].

The receiver performance, at least theoretically, was qualitatively shown to be adequate, but an analysis of the BER as a function of received optical power, the receiver sensitivity, should be done to provide a guarantee that the link will work. The following section discusses the theoretical analysis of the BER performance of the receiver and presents the results.

5.8 Theoretical BER Performance of Back-to-Back FCMA Links.

The BER performance of an FCMA system can be evaluated theoretically by calculating the electrical signal current in the receiver generated by the incident optical signal relative to the mean square noise current in the receiver electronics [PER1,PER2,SM1]. The theoretical details of the BER calculations are described in Appendix D and only the results of these calculations for a 4-level FCMA link are presented in this section. The BER performance of this FCMA link is evaluated for a back-to-back system only which effectively avoids introducing fiber dispersion into the discussion at this point. Also, these calculations do no include intersymbol interference (ISI) and laser source linewidth related terms. The ISI term is of minimal importance because it is a small, constant contribution to eye closure and the linewidth related impairment can be added into the calculation after the laser source has been chosen.

The symbol rate for this 4-level FCMA link is the native rate of Gigabit Ethernet and the frequency spacing of the symbols is chosen to be such that channel 1 of the decoder will have a delay equal to half of the bit period. The values of the signal current and the mean square noise terms are evaluated for both channel 1 and channel 2 and the BER is calculated for the three examples of harmonic decoder discussed in Chapter 4. The BER of channel 1 is plotted as a function of the optical power that is input to the channel 1 MZ decoder in Figure 5-18.

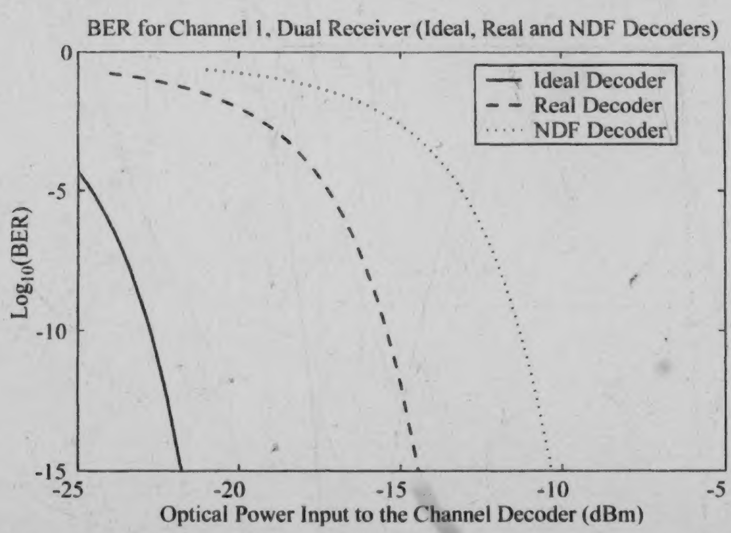

Figure 5-18: The BER for channel 1 of a 4 level FCM system evaluated for three different types harmonic decoder, ideal, real and NDF as defined in Chapter 4. The input optical power is referenced to the input of the delayed arm MZ decoder.

The ideal decoder is perfectly lossless and has 50% splitting and coupling ratios. The real decoder has the values of splitting and coupling ratios that were measured for the cube beam splitter based interferometer. The NDF based decoder has the neutral density filter inserted into one arm of the free-space MZ that can be used to improve the shape of the eye-diagram. The insertion of the NDF into the decoder causes quite a large loss in receiver sensitivity for no apparent gain due to better shaped signal pulses. The ideal decoder can be thought of as a theoretical best decoder performance with the combination of laser transmitter and receiver that were designed for this FCMA system.

The BER of channel 2 for the same transmitted signal and decoder types used in Figure 5-18 is plotted as a function of the optical power that is input to the channel 2 MZ decoder in Figure 5-19.

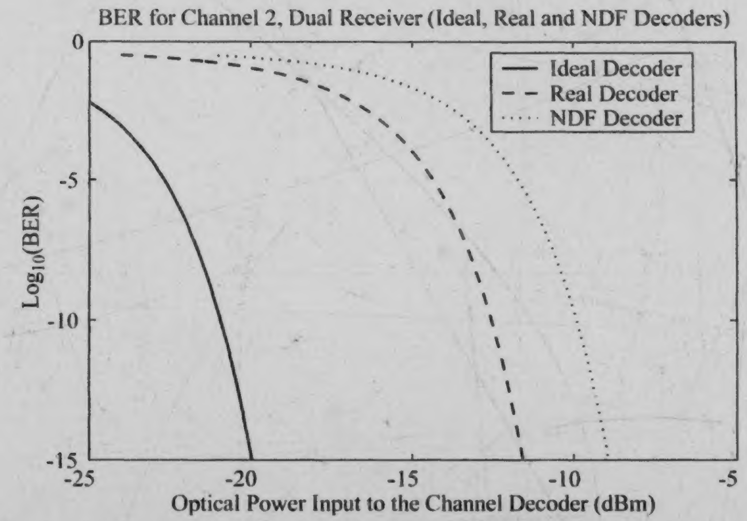

Figure 5-19: The BER for channel 2 of a 4 level FCM system evaluated for three different types harmonic decoder, ideal, real and NDF as defined in Chapter 4. The input optical power is referenced to the input of the delayed arm MZ decoder.

The real type of decoder outperforms the NDF decoder again for channel 2, but not by as much as with channel 1. The theoretical best performance presented as the ideal decoder type significantly outperforms the others.

The optical power loss of the real decoder relative to the ideal decoder is less than 5 dB, but the performance degradation is greater than 7 dB for both channels 1 and 2. This indicates that balanced splitting and coupling ratios in the MZ decoder play a significant role in determining the sensitivity performance of the decoder/receiver combination.

The same calculation of the BER can be performed using one MZ decoder output and calculating the noise for a single receiver. This will enable a meaningful comparison of the dual differential receiver to a single receiver. For the same conditions as the previous calculations in this section, the BER for the use of one receiver has been calculated using the ideal MZ decoder and plotted with the dual receiver result for channel 1 below in Figure 5-20.

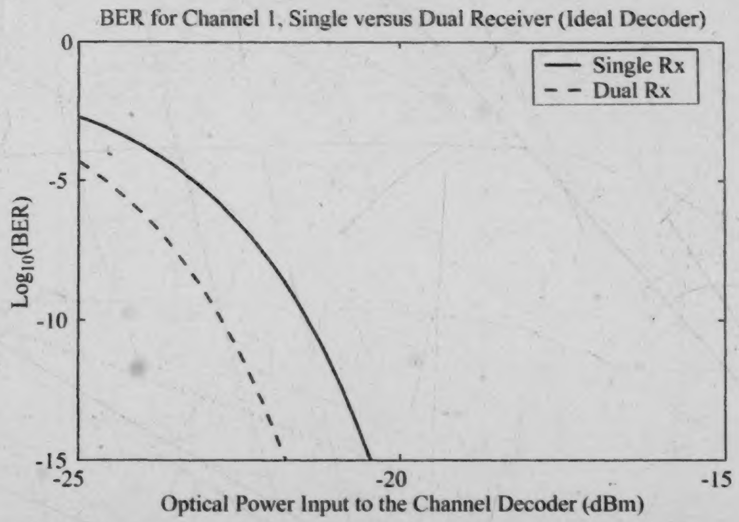

Figure 5-20: The BER for channel 1 of a 4 level FCM system evaluated for the ideal harmonic decoder, but operated either as a dual differential receiver or a single receiver. The input optical power is referenced to the input of the delayed arm MZ decoder.

The optical power sensitivity gain for operating in the dual differential mode is slightly less than 1.5 dB, which corresponds to slightly less than a 3 dB electrical power gain in sensitivity. The theoretical prediction of maximum electrical sensitivity gain from the dual differential receiver is 3 dB, the realization of something close to this gain is possible only for bit rates and receivers that are dominated by noise from the receiver electronics.

The same type of comparison can be made for channel 2 of the 4 level FCM signal and is shown on the graph in Figure 5-21. The sensitivity gain is nearly 1.5 dB in the optical power domain for channel 2 as well.

The results of this section suggest that the decoders presented in Chapter 4 combined with the receiver presented in this chapter would be able to receive the Gigabit Ethernet optical FCM signal with good performance, with BERs better than 10^{-9}, at realistic optical powers, in the neighbourhood of -10 dBm. The following section will summarize the content of this chapter.

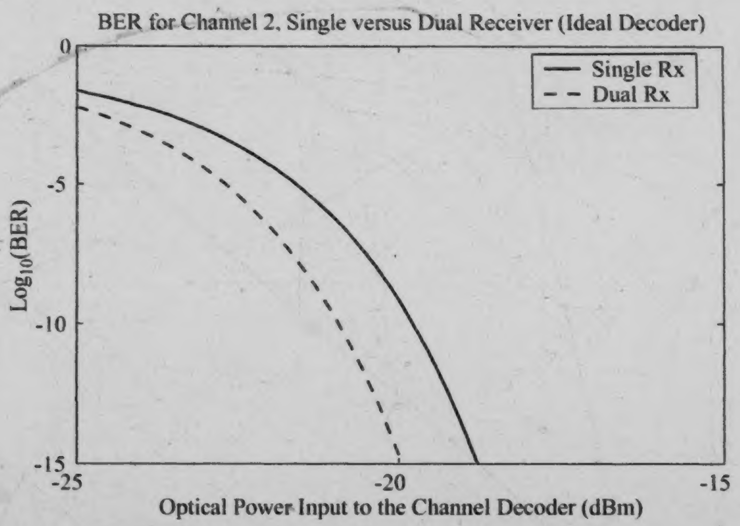

Figure 5-21: The BER for channel 2 of a 4 level FCM system evaluated for the ideal harmonic decoder, but operated either as a dual differential receiver or a single receiver. The input optical power is referenced to the input of the delayed arm MZ decoder.

5.9 Summary of Dual Differential Receiver.

The dual differential optical receiver is constructed using two receivers of the type that were presented in this chapter. The receiver is based on a PIN diode and transimpedance amplifier combination with a built in gain of approximately 15 dB (electrical power) with a high frequency corner of about 2 GHz. The receiver was successfully designed and built to meet the requirements of the FCM system, based on eye diagram performance. Theoretical BERs lower than 10^{-9} are achievable with less than -10 dBm of power at the input of the MZ decoders for 2 channels of Gigabit ethernet rate FCM transmissions. Also verified through error calculations was the sensitivity gain of 1.5 dB in optical power (3 dB in electrical power) for the dual differential receiver compared to a single optical receiver receiving the same data at the output of the MZ decoder.

The results presented for the receiver in this chapter can now be combined with the results for the transmitter design, Chapters 2 and 3, and the decoder design, Chapter 4, to evaluate the expected performance of FCMA optical communication links in Chapter 6.

Chapter 6. FCMA MAN Design - A Discussion and Review.

This chapter will re-address the optical system design aspects of a communication network link built using FCMA within the context of the specific material presented so far in this document. In Section 1.8 the design limitations of the FCMA system were discussed in terms of optical power limitations due to fiber losses and signal distortion due to chromatic dispersion in the transport fiber. By establishing a minimum required performance in terms of BER at the receiver, the required optical power at the end of the transmission fiber becomes a fixed parameter of the system design. The maximum transmission distance, with regard to optical power, becomes a function of the optical power loss per kilometer in the transmission fiber and the maximum optical power at the transmitter end of the communication link. Section 6.1 will present the results of this analysis in terms of the number of channels that are multiplexed and the design of the harmonic signal decoder based demultiplexor at the receiver.

When optical power proves not to be the system limiting parameter, the signal distortion from the chromatic dispersion of the transmission fiber may be significant. Section 6.2 will present a qualitative discussion of the negative effects of chromatic dispersion on FCM signals through a series of eye-diagrams of FCM transmissions passing through increasing amounts of transmission fiber.

When fiber dispersion proves not to be the system limiting parameter, and the system is "power starved" at the receiver, the optical power deficit can be remedied through optical amplification. There are technologies that can provide optical amplification for signals with wavelengths near 1550 nm; erbium doped fiber amplifiers (EDFAs), erbium doped waveguide amplifiers (EDWAs), semiconductor optical amplifiers (SOAs), and linear semiconductor optical amplifiers (LOAs). Debating which technology is best for optical amplification is not within the mandate of this thesis, therefore it will be assumed that EDFAs provide adequate performance for any optical amplification applications necessary to the discussion of FCMA system design. Section 6.3 provides a brief overview of the use of amplification with FCMA systems.

If optical amplifiers are used to overcome transmission fiber losses by being included in the design of FCMA systems, they can be used to overcome additional losses incurred by using WDM filters to multiplex several FCM signals on the same fiber. FCMA and WDMA can be combined in this way to reuse the transmission fiber infrastructure of a MAN to reduce the cost of the overall network. A generalized discussion of combining FCMA and WDMA with optical amplification is presented in Section 6.4.

Section 6.5 will be a review of Chapter 6 and will tie together the concepts presented in all of the preceding chapters within the context of Chapter 6. The section adds the inclusion of the linewidth of the transmission source will be included in plots of the BER versus the optical power input to the harmonic decoders MZs. The expected performance of the FCMA system will be reviewed in this final context.

6.1 FCMA Link Power Budget Revisited.

Quantifying the optical power budget of an FCMA link begins by assuming a specific level of performance, usually in terms of a minimum required BER. This minimum BER per FCMA channel determines the required optical power input to each dual differential receiver when the sensitivity of the receiver is considered. The minimum required optical power at each channel receiver determines the required input power to the MZ decoder particular to each channel and the required output power from the transmission fiber. The optical power required at the input to the channel specific MZ decoders is not the same for different channels, therefore the power split before the MZ decoders is not a symmetric power split. Section 6.1.1 will elaborate on this unequal power splitting.

All of the BER calculations in this chapter will be performed using the noise analysis of Chapter 5 and will use the calculated receiver transfer function. Also, since different MZ designs impact the BER substantially (as shown is Chapter 5), the ideal (lossless) harmonic decoders will be used for calculations. Chapters 4 and 5 provide the methods used to analyze the performance of an FCMA system that would be designed with different decoder and receiver components if such calculations became necessary.

Runge Kutta calculation results have been used up to this point to provide sample FCM signals for calculation of expected link performance and will continue to be used in Chapter 6. A "perfect" FCM signal, one that has constant optical power and assumes discrete values of optical frequency over the entire symbol period, will also be used in equivalent calculations to provide a benchmark comparison for the FCM signal that is produced by the numerical methods of Chapter 2.

The approach used in Section 6.1.1 to find the required optical signal power at the end of the fiber link is to see how much power is required at the respective channel receivers to achieve a BER of 10^{-9} for each channel. The following section explains how the required receiver power impacts the maximum transmission distance.

6.1.1 BER and the per Channel Optical Power Splitting of the Decoder.

The optical receivers of the FCMA system require the optical signal to be decoded by the passive harmonic decoder before the optical signal can be converted to more than one electrical bit sequence. The optical power required at the per channel dual differential receivers depends on the electrical signal amplitude of the decoded symbols with respect to the sum of the noise powers. The optical powers of each transmitted FCM signal symbol depend on the particular channel receiving that symbol, a fact that was explained with the signal state diagrams in Section 1.6. It is this symbol dependence of the received optical power that most strongly influences the differences in optical powers required by different channels for the FCMA receivers. The insertion loss of the optical splitter that precedes the individual channel MZ decoders can be optimized according to this optical power symbol dependence to achieve an equal performance for all the multiplexed channels while minimizing the overall optical input power required by the harmonic decoders. For a two channel FCMA system the harmonic decoders and power splitter is shown in Figure 6-1 which also indicates how the insertion loss of the power splitter is to be measured.

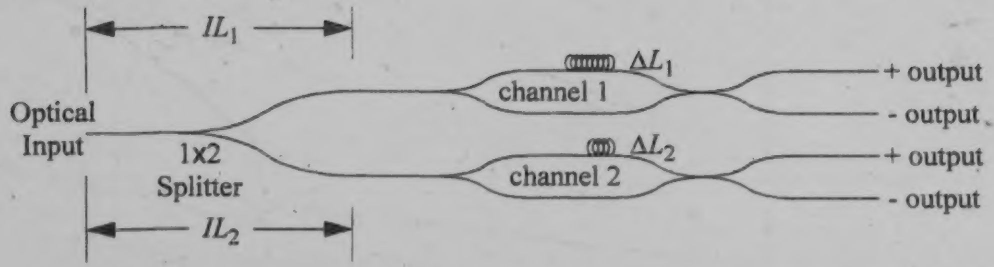

Figure 6-1: A schematic diagram of the harmonic decoders of a two channel FCMA system where the insertion losses of the 1x2 splitter, IL_1 and IL_2, are labelled at the point where they would be measured with respect to the optical input.

The calculation of the optimum splitting ratio was performed for three different types of FCM signal; 4 level (4-ary) Runge Kutta laser rate equation results, 4-ary constant power and square waveform frequency signal, and 16-ary constant power and square waveform frequency signal. The data rate was 1250 Msps (Gigabit Ethernet rate). Based on the receiver discussed in Chapter 5, including the noise calculations used to determine the BER, the received optical powers required on a per channel basis to achieve a BER of 10^{-9} are listed in Table 6-1.

Table 6-1: A comparison for three cases of the calculated optical power necessary to achieve a BER of 10^{-9} for each channel of multilevel FCMA transmissions.

FCMA Channel(s)	Received Optical Power (dBm) to Achieve BER = 10^{-9}		
	4 Level Runge Kutta Laser Signal	4 Level Constant Power, Square-Wave Frequency	16 Level Constant Power, Square-Wave Frequency
Channel 1	-23.0	-23.4	-23.4
Channel 2	-21.2	-21.1	-21.1
Channel 3	N/A	N/A	-18.2
Channel 4	N/A	N/A	-15.2
All Channels Combined	-19.0	-19.1	-12.4

The row of the table listed as All Channels Combined is the sum of the channel-wise required optical powers and is the total optical power that would be required at the input to the optical power splitter under the assumption that there are no extra losses associated with the power splitter or MZ decoders. The 4 level signals, Runge Kutta and the constant power signal, require about the same optical power input to the 1x2 splitter, approximately -19.0 dBm, even though the difference in the signal waveforms are substantial. The 16 level signal requires -12.4 dBm for 4 channels of Gigabit Ethernet. To guarantee the same performance as half the amount of data (2 channels) requires more than 4 times the optical power.

The Runge Kutta laser rate equation integration for the 4-ary (2 channel) Gigabit Ethernet FCM signal that was used for analysis from Chapter 2 forward has been used again to derive the splitting ratio for a 1x2 splitter that precedes the MZ decoders for those two channels. The splitting ratio has been calculated in terms of per channel insertion loss with respect to the input of the 1x2 splitter. The splitting ratio for the 2 channel (4-ary) and 4 channel (16-ary) FCM signals that have constant optical power and square frequency level waveform shapes have also been calculated in terms of per channel insertion loss with respect to the input of the channel splitter. The results are tabulated in Table 6-2.

Table 6-2: A comparison for three cases of the insertion loss for the distribution of the FCM optical signal to different MZ decoders to achieve a BER of 10^{-9} for each channel of multilevel FCMA transmissions.

FCMA Channel(s)	Channel Specific Insertion Loss for Lossless MZ Decoders with BER = 10^{-9}		
	4 Level Runge Kutta Laser Signal	4 Level Constant Power, Square-Wave Frequency	16 Level Constant Power, Square-Wave Frequency
Channel 1 (IL_1)	4.0	4.3	11.0
Channel 2 (IL_2)	2.2	2.0	8.7
Channel 3 (IL_3)	N/A	N/A	5.8
Channel 4 (IL_4)	N/A	N/A	2.8

The calculated splitting ratios for the 4 level signals, Runge Kutta integration and the constant power signal, are about 4 dB for channel 1 and about 2 dB for channel 2, within a few tenths of a dB. The difference in quality for these two signals (the Runge Kutta being inferior) does not make much difference for the calculated splitting ratios at the receiver. The 16 level signal requires 8.2 dB more power for channel 4 than for channel 1 in order to maintain the same level of performance.

These numbers are baseline required receiver powers for FCMA systems. To gauge whether or not these numbers are realistic, the potential reach in terms of possible transmission distances in single mode fiber have to be estimated which will be done in the following section.

6.1.2 Achievable FCMA Link Length.

The reach of an optical communication link, in the absence of optical amplifiers, is defined in terms of tolerable loss in the optical signal without compromising the performance beyond a minimum required BER. The minimum tolerable optical power at the end of the system is determined by the amount of optical power required by the receiver to maintain the minimum BER. Then the launched optical power into a transmission fiber of fixed loss per kilometer will determine the optical link length.

The typical output powers of modern signal quality DFB lasers are around 5 to 10 dBm and a good assumption for the design of fiber optic systems is to use approximately 0.2 dB/km optical loss for NDSF. With a launched optical power of 5 dBm and a required optical power at the end of the link of about -12.5 dBm, for 16 level signals, the maximum link length will be greater than 80 km. There may be extra losses introduced into the link and the launched optical power may be greater than 5 dBm, so 80 km is a reasonable minimum estimate for the 16 level FCM signal.

The 4 level signals exceed the range of the 16 level signals, based solely on optical power requirements and fiber losses, by greater than 30 km as calculated from the results of the previous section.

These expected transmission distances are based only on power requirements and a few assumptions about the power of signal lasers and losses of NDSF. At a transmission distance of 80 km the signal quality may be seriously degraded due to the signal distortion introduced by the chromatic dispersion effects of single mode fiber. The following section will qualitatively discuss the effects of chromatic dispersion on FCM signals.

6.2 Transmission Fiber Dispersion and FCM Signals.

The power budget analysis of the previous section suggests that the 16 level FCM signal could travel more than 80 km and the 4 level FCM signal could travel more than 110 km in standard NDSF at 0.2 dB/km loss. These distances were calculated from the BER performance at the receiver under the assumption that the signals were not distorted by being transmitted through the optical fiber. The fiber does distort the signal, mostly due to the chromatic dispersion [BR1,EL1]. The following two sections will present eye diagrams calculated from transmitting FCM signals through single mode fiber with the assumption that the fiber has a chromatic dispersion coefficient of 17 ps/nm/km, which is a good assumption for NDSF for light at approximately 1550 nm in wavelength.

6.2.1 Chromatic Dispersion and 16 Level FCM Signal Distortion.

The 16 level, 1250 Msps FCM signal can be used for fiber transmissions up to 80 km long in NDSF based on optical power loss only. The signal becomes distorted due to the dispersion properties of the transmission fiber. The effects on the signal quality can be qualitatively understood by calculating what happens to the signal when it would pass through a length of fiber with chromatic dispersion. The FCM signal in the time domain must be Fourier transformed and multiplied by a chromatic dispersion filter and inverse transformed to calculate this effect. The chromatic dispersion filter has a unity amplitude response across all frequencies but adds a quadratic phase delay to the signal, see [PETE1] for details.

The 16 level FCM signal that is used for these qualitative comparisons is a signal of constant optical power that assumes discrete values of optical frequency during the symbol periods to represent the symbol being transmitted. The effects of chromatic dispersion can be seen by comparing the eye diagrams later in this section to the following set of eye diagrams that depict what the signal would look like for a back to back experiment (0 km transmission distance), see Figure 6-2.

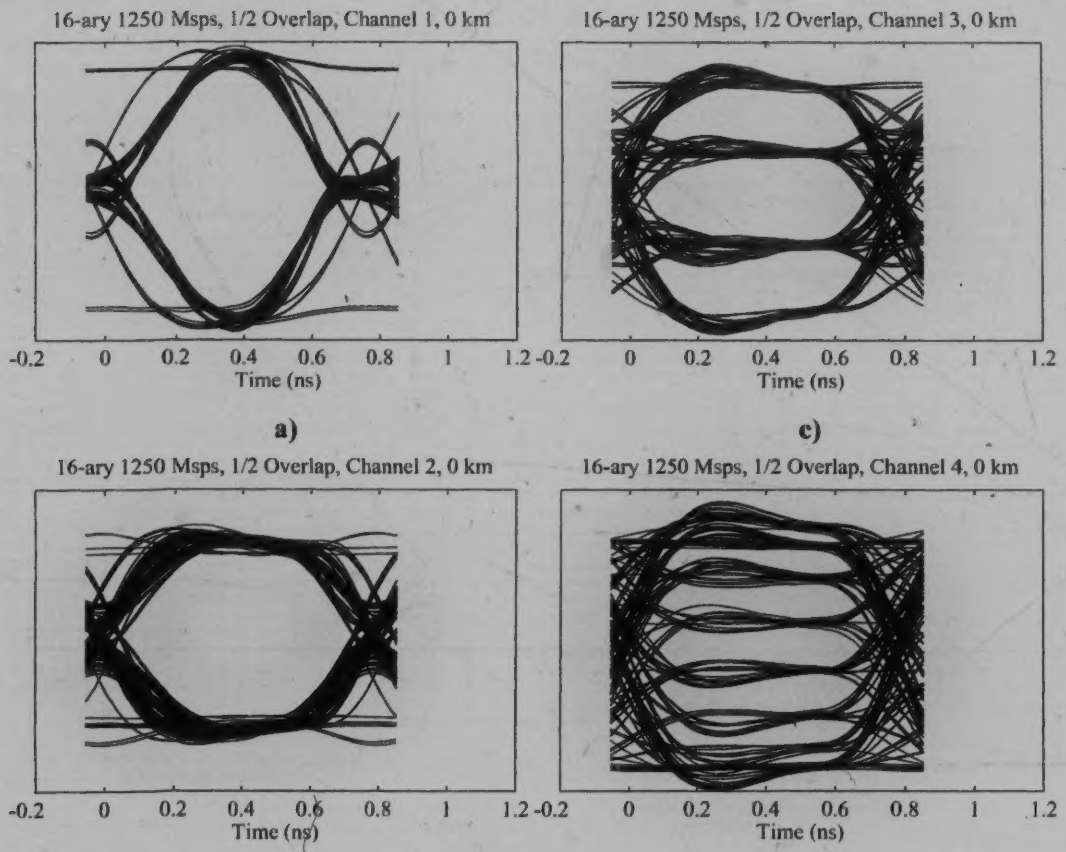

a) c)

b) d)

Figure 6-2: Four eye diagrams of the four channels of the 16 level FCM signal transmitted at 1250 Msps. The calculation is for a back to back experiment (0 km link length). Channels 1, 2, 3 and 4 are shown in subplots **a)**, **b)**, **c)** and **d)**, respectively.

Figure 6-2 shows that the eyes open predictably for all four channels of the FCM signal. The shapes of the eyes are influenced by the receiver transfer function where the slight overshoot or undershoot on the left side of the eye opening is due to the receiver transfer function. The overshoot and undershoot have the effect of introducing inter-symbol interference (ISI) into the signal waveform. The eye diagram would consist of thin lines above and below the eye opening in the absence of ISI, as in Figure 4-20 for example. The decision voltage for channels 1 and 2 is easily determined to be half way between the high and low voltages of the open eye. For channel 3, three openings are present in the eye diagram and the decision voltage must be placed in the vertical center of the middle opening. Also, the vertical center of the middle opening for the five openings of the channel 4 eye diagram is used to correctly receive the data for channel 4.

The eye diagrams in Figure 6-3 depict what the 16 level, 1250 Msps FCM signal would look like after being transmitted 40 km in NDSF with a chromatic dispersion coefficient of 17 ps/nm/km.

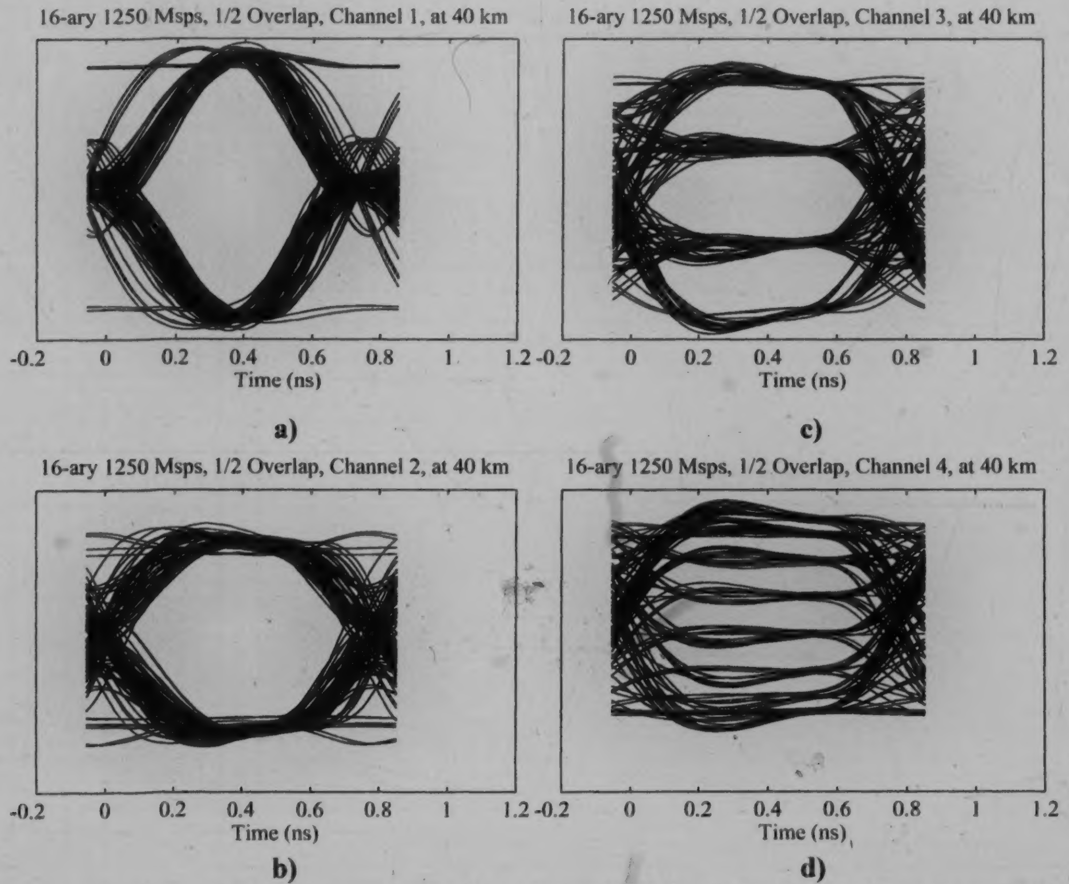

a) b) c) d)

Figure 6-3: Four eye diagrams of the four channels of the 16 level FCM signal transmitted at 1250 Msps. The calculation is for a 40 km link length. Channels 1, 2, 3 and 4 are shown in subplots **a)**, **b)**, **c)** and **d)**, respectively.

In Figure 6-3 the trajectory that is followed by the signal voltage is broadened, a wider range of signal voltages will be measured by the decision circuit, possibly contributing to a rise in the number of received errors. The greatest concern for signal degradation is displayed in the eye diagram for channel 1 in Figure 6-3, the receiver voltages for different symbols are moved temporally relative to each other which is causing a smearing and closing of the eye in the time dimension. The maximum and minimum voltages for the eye of channel 1 do not seem to be affected much at 40 km link length but, when considerations are made for including timing jitter in the response of a decision circuit, the error rate (performance) for this channel will definitely increase (decrease).

The eye diagrams in Figure 6-4 depict what the 16 level, 1250 Msps FCM signal would look like after being transmitted 80 km in NDSF with a chromatic dispersion coefficient of 17 ps/nm/km.

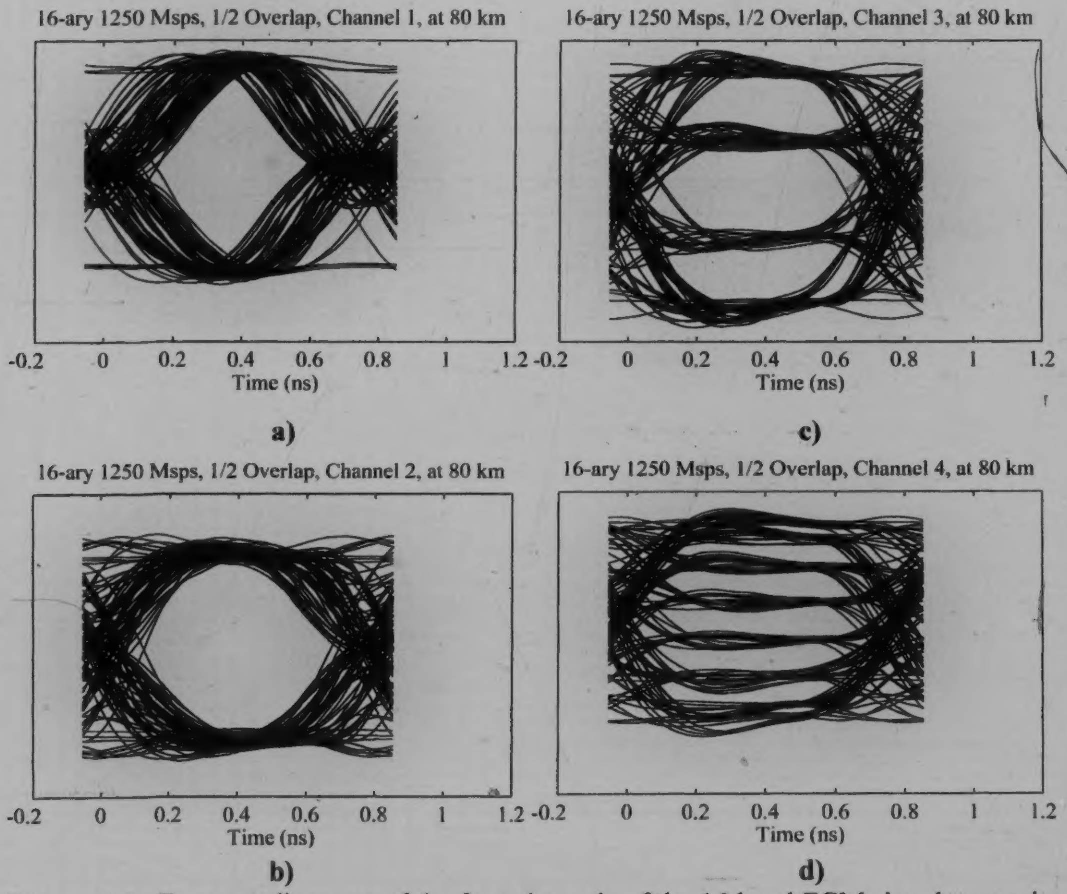
16-ary 1250 Msps, 1/2 Overlap, Channel 1, at 80 km

16-ary 1250 Msps, 1/2 Overlap, Channel 3, at 80 km

16-ary 1250 Msps, 1/2 Overlap, Channel 2, at 80 km

16-ary 1250 Msps, 1/2 Overlap, Channel 4, at 80 km

a)

c)

b)

d)

Figure 6-4: Four eye diagrams of the four channels of the 16 level FCM signal transmitted at 1250 Msps. The calculation is for an 80 km link length. Channels 1, 2, 3 and 4 are shown in subplots **a)**, **b)**, **c)** and **d)**, respectively.

In Figure 6-3 the trajectory that is followed by the signal voltage is even more broadened, and the maximum and minimum voltages for the eye of channel 1 are now affected at 80 km link length which will directly increase the error rate for this channel.

6.2.2 Chromatic Dispersion and 4 Level FCM Signal Distortion.

The 4 level FCM signal that is used in the first figures of this section is a signal of constant optical power that assumes discrete values of optical frequency during the symbol periods to represent the symbol being transmitted. This signal will be compared to the Runge Kutta integration for the same symbol rate, 1250 Msps, with 4 levels, which is the same signal that was used in Chapter 5 to demonstrate the BER calculation.

The baseline curves for these eye diagrams will be the plots in Chapter 5 (Figure 5-17) that show the back to back (0 km link length) eye diagrams for the Runge Kutta generated FCM signal. In the eye diagrams below, in Figure 6-5, the constant power 4 level FCM signal is depicted after 80 km of transmission in NDSF.

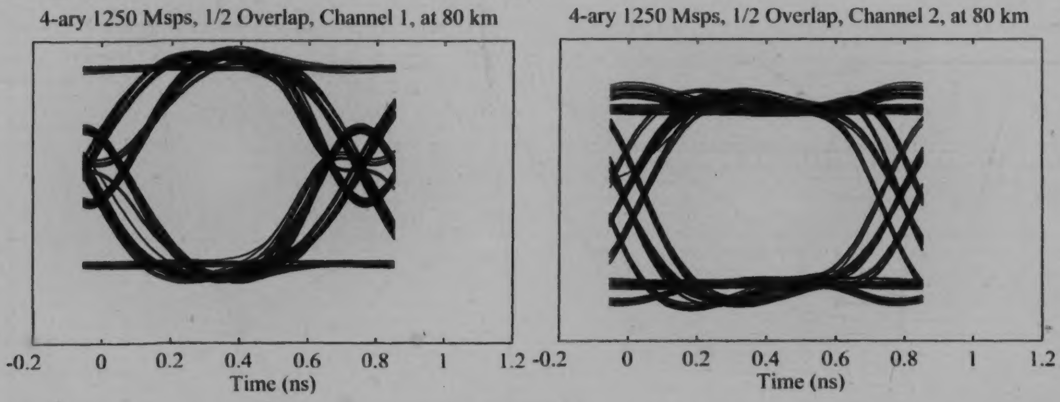

a) **b)**

Figure 6-5: Two eye diagrams of the two channels of the 4 level FCM signal transmitted at 1250 Msps. The calculation is for an 80 km link length and an FCM signal of constant optical power. Channels 1 and 2 are shown in subplots **a)** and **b)**, respectively.

The signal degradation is almost unnoticeable at 80 km, so the same signal is advanced to 320 km of transmission distance which is what is shown in Figure 6-6. These eye diagrams show a signal that has marginally passed the point where the receiver voltage is beginning to close in on the center of the eye and the BER is increasing.

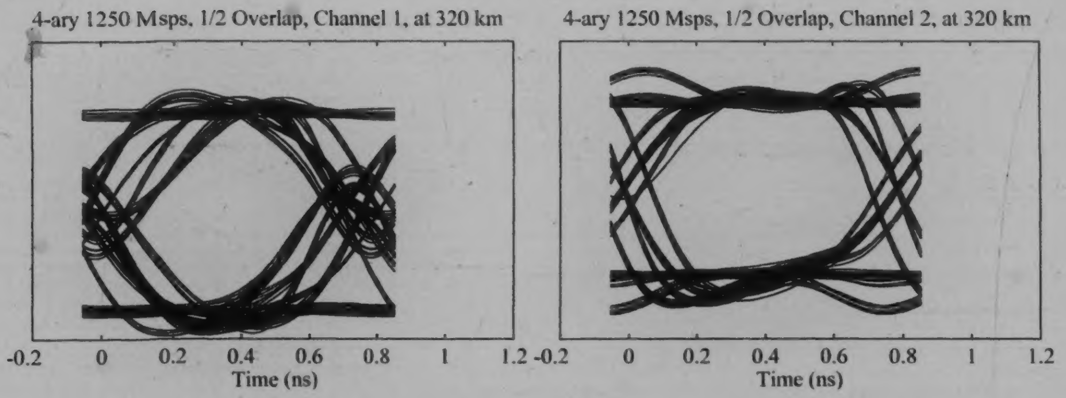

a) **b)**

Figure 6-6: Two eye diagrams of the two channels of the 4 level FCM signal transmitted at 1250 Msps. The calculation is for a 320 km link length and an FCM signal of constant optical power. Channels 1 and 2 are shown in subplots **a)** and **b)**, respectively.

In the eye diagrams below, in Figure 6-7, the Runge Kutta generated 4 level FCM signal is depicted after 80 km of transmission in NDSF.

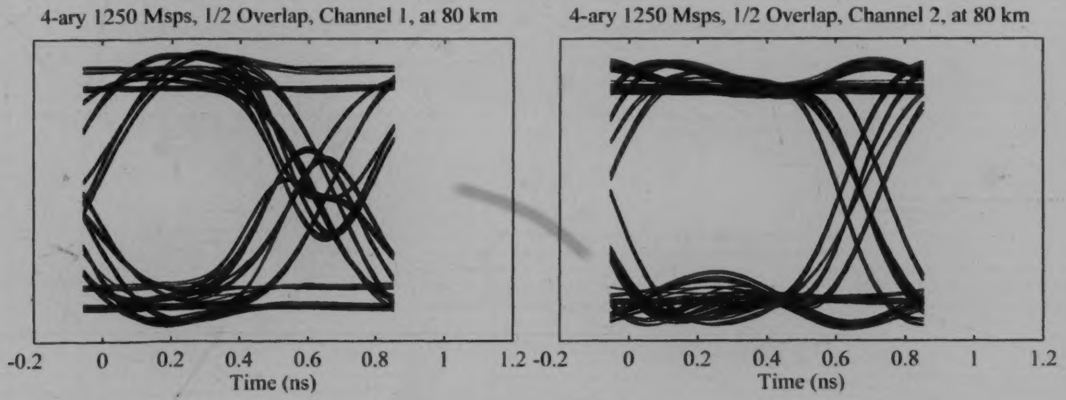

a) **b)**

Figure 6-7: Two eye diagrams of the two channels of the 4 level FCM signal transmitted at 1250 Msps. The calculation is for an 80 km link length and a Runge Kutta generated FCM signal. Channels 1 and 2 are shown in subplots **a)** and **b)**, respectively.

The signal degradation is noticeable in this signal at 80 km in channel 2, and channel 1 is not greatly affected. The Runge Kutta signal is also advanced to 320 km of transmission distance which is what is shown in Figure 6-8.

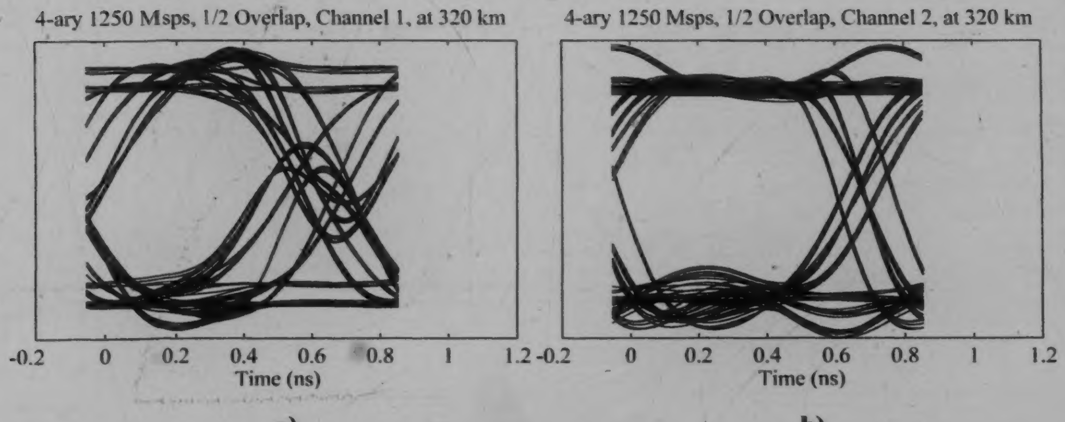

a) **b)**

Figure 6-8: Two eye diagrams of the two channels of the 4 level FCM signal transmitted at 1250 Msps. The calculation is for a 320 km link length and a Runge Kutta generated FCM signal. Channels 1 and 2 are shown in subplots **a)** and **b)**, respectively.

These eye diagrams show a signal that has definitely passed the point where the receiver voltage is beginning to close in on the center of the eye and the BER is increasing. When these eye diagrams are compared with what would be considered to be a perfect FCM signal, Figure 6-6, the effects of chromatic dispersion on a Runge Kutta generated FCM signal do not seem too prohibitive. A laboratory experiment should confirm that chromatic dispersion would not be a prohibitive factor for 4 level FCM signals at 1250 Msps and link lengths of up to ~300 km.

The optical power limitation determined through the analysis in Section 6.1.2 predicted a power limited link length of 110 km for this 4 level FCM signal. By qualitatively analyzing the effects of chromatic dispersion, this same signal could be used for transmission over much greater distances. Transmission of optical signals over 300 km is possible without signal regeneration, but would require optical amplification of some kind. The following section elaborates on the concepts associated with optically amplifying FCM signals to increase the maximum link length.

6.3 Optically Amplified FCMA System Concepts.

An optical communications link that is 320 km long corresponds to a 64 dB loss at 0.2 dB/km in NDSF. This optical power loss would render the signal irrecoverable considering that the typical launch power of modern DFB signal source lasers is ~5 dBm. To overcome this loss, optical amplifiers could be used. The detailed design of an FCM link with optical amplifiers in not going to be addressed here. The intent of the following paragraphs is to provide the reader with a sense of what would be involved in including optical amplifiers in a FCMA based system.

The most elementary design trade-off of optical amplifiers is the three-way competition between low minimum input power, high gain (highest possible output power) and low output noise. It is cost effective to have any two of these three amplifier attributes, but achieving all three with the same amplifier is expensive.

At the end of optical transmission systems that include amplifiers the receiver power can be increased to whatever is necessary to overcome the receiver noise and signal shot noise. The dominant noise source in the optically amplified system at high received optical powers is the optical amplifier related noise. More specifically, amplifier related signal-spontaneous beat noise is the most significant noise source if the optical noise is band limited (optically filtered). The band limiting in the optical domain is equivalent to using a WDM filter before the receiver to remove the spontaneous emission that is outside of the designated optical signal band. A more in depth investigation of the use of amplifiers is beyond the scope of this project. The reader is referred to [GI1] for more information on optical amplification in optical communication systems. The inclusion of optical amplifiers in the analysis of bit error ratios could be examined in terms of the maximum spontaneous emission noise spectral density allowed for a particular impact in the receiver sensitivity. In other words, without designing an amplifier or amplified link, the impact of the spontaneous emission noise could be estimated. Comments on required amplifier technologies could then be made.

The inclusion of optical filtering at the end of the link to remove spontaneous emission noise outside of the optical signal band opens up the discussion to using WDM on the FCMA based links. The following section will address this topic.

6.4 WDMA and Optically Amplified FCMA System Concepts.

With amplifiers in the optical transmission link to boost the signal, the requirement of prefiltering the signal in the optical domain is necessary. Instead of placing only one optical filter at the end of the transmission link to filter one optical channel it could be argued that placing more optical filters at the end of the link would not create unrealistic requirements for the optical power of additional channels and/or an optical amplifier at the end of the transmission link. This is the same argument for conventional WDMA so, with optical amplifiers in an FCMA based system that is 80 to 300 km long, why not also use WDMA with FCMA.

With the introduction of a wavelength division demultiplexor (deMUX) at the end of the link, an optical multiplexor (MUX) is required at the launch end of the system as well. The MUX may or may not be wavelength specific, it could be filtered or based on power combining through the use of fiber couplers. Irrespective of the particular design that is chosen for the WDM component of the system a representative diagram that illustrates the idea of combining WDMA with amplification in a optical system is given in Figure 6-9.

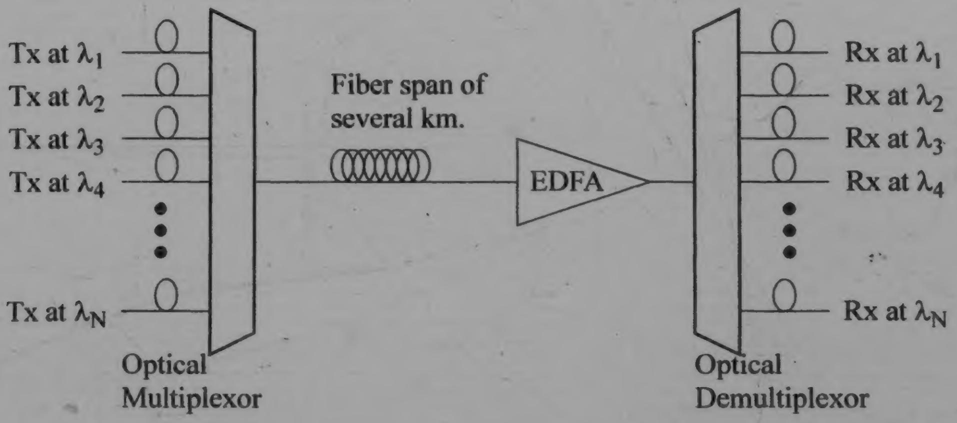
Tx at λ_1
Tx at λ_2
Tx at λ_3
Tx at λ_4
Tx at λ_N
Optical Multiplexor
Fiber span of several km.
EDFA
Rx at λ_1
Rx at λ_2
Rx at λ_3
Rx at λ_4
Rx at λ_N
Optical Demultiplexor

Figure 6-9: A diagram that illustrates the combination of a WDM multiplexor, WDM demultiplexor and an optical amplifier with multiple optical channels being transmitted over a fiber span of several km.

Figure 6-9 shows a number of optical channel transmitters, Txs, with specific wavelengths being combined at the input end of the WDM optical link by the optical multiplexor. The channels travel along the fiber for several kilometers and are amplified, with the amplifier shown as an EDFA. The output of the EDFA feeds directly to the optical demultiplexor which separates all of the WDM channels and directs them to the receivers, Rxs. The optical power at the receivers needs to be enough that the minimum optical performance requirements are met in terms of BER. This determines the maximum allowable loss per channel of the optical demultiplexor and the necessary output power of the EDFA per channel. Another way of looking at this is that the Tx power at any particular wavelength minus the fiber link loss, minus the losses of the optical multiplexor and demultiplexor, plus the gain of the amplifier must be above the minimum required received optical power to maintain the minimum level of performance.

Additional amplifiers can be added, as depicted in Figure 6-10, to extend the link length beyond the reach attainable with only one amplifier.

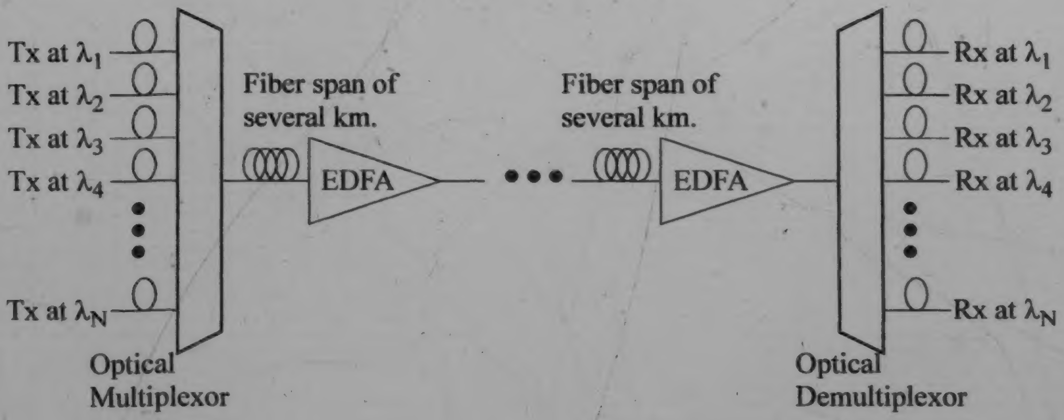
Tx at λ_1
Tx at λ_2
Tx at λ_3
Tx at λ_4
Tx at λ_N
Optical Multiplexor
Fiber span of several km.
EDFA
Fiber span of several km.
EDFA
Rx at λ_1
Rx at λ_2
Rx at λ_3
Rx at λ_4
Rx at λ_N
Optical Demultiplexor

Figure 6-10: A diagram that illustrates the combination of a WDM multiplexor, WDM demultiplexor and optical amplifiers with multiple optical channels being transmitted over several fiber spans of several km each.

The most important design consideration to be aware of in this instance is to ensure that the input optical power into the EDFAs for any channel does not go so low that the signal is overcome by ASE noise. These systems can be built using amplifiers until the accumulated distortions and noises are too high for the receivers to recover the signals.

The following section provides a review of the material introduced in this chapter and addresses the combined effects of signal shot noise, amplifier noise and linewidth related noise on the performance of FCMA systems.

6.5 FCMA - A Review.

The constraints on the performance and link length of FCMA based optical transmission systems are from three main limiting factors: The linewidth of the optical source used as a transmitter, the transmitted optical power and the chromatic dispersion induced distortion. Assuming that chromatic dispersion can be mitigated and a light source with sufficiently low linewidth could be employed, the ultimate limitation of the transmission system can be expressed in terms of the optical power quantum limit. The quantum limit is expressed in terms of either the signal to noise ratio or the minimum optical power, given a prescribed BER, when only the signal related shot noise is considered in the error calculation. A comparison of the best possible FCM system performance to the best possible ISK system performance at the quantum limit in terms of the Q of the system will provide another means of judging the utility of the FCMA system.

Elaborating on the noise calculations from Chapter 5 and Appendix D, the ISK system signal receiver current for a binary 1 can be written as

$$I_{sig,\,1} = \left(\frac{\eta q}{h\nu}\right) b_{ISK} \tag{114}$$

where b_{ISK} refers to the signal optical power during the timeslot of a transmitted 1. The shot noise generated by receiving a bit with optical power b_{ISK} is

$$\left.\sqrt{\langle i_s^{\,2}(0)\rangle}\right|_1 = \sqrt{2q\left(\frac{\eta q}{h\nu}\right) b_{ISK}(BW_{eq})} \tag{115}$$

where BW_{eq} is a normalizing factor that accounts for the bandwidth of the system. The signal and noise currents for a transmitted binary 0 are both zero. Using the standard binary definition for the Q of the optical system and inserting only the shot noise contribution to define a quantum limited system Q for ISK transmission, Q_{ISK} is equal to the following,

$$Q_{ISK} = \frac{I_{sig,\,1} - I_{sig,\,0}}{\sqrt{\langle i_s^{\,2}(0)\rangle}\Big|_1 + \sqrt{\langle i_s^{\,2}(0)\rangle}\Big|_0}$$

$$= \frac{\left(\frac{\eta q}{h\nu}\right)b_{ISK} - 0}{\sqrt{2q\left(\frac{\eta q}{h\nu}\right)b_{ISK}(BW_{eq})} + 0}$$

$$= \sqrt{\frac{\left(\frac{\eta q}{h\nu}\right)b_{ISK}}{2q(BW_{eq})}} \quad , \tag{116}$$

where the definitions of the parameters can be found in Appendix D.

For an FCMA system the shot noise term is defined as the sum of the individual mean square noises for the dual differential receivers,

$$\sqrt{\langle i_s^{\,2}(0)\rangle_{symbol,channel}} = \sqrt{2q\left(\frac{\eta q}{h\nu}\right)(b_{1,\,symbol,\,channel} + b_{2,\,symbol,\,channel})(BW_{eq})}\,, \tag{117}$$

defining the total optical power received for a particular symbol and channel as $b_{total,symbol,channel}$, the shot noise becomes,

$$\sqrt{\langle i_s^{\,2}(0)\rangle_{symbol,channel}} = \sqrt{2q\left(\frac{\eta q}{h\nu}\right)(b_{total,\,symbol,\,channel})(BW_{eq})}\,. \tag{118}$$

For the FCM signal of constant optical power (independent of the transmitted symbol), the shot noise becomes independent of the symbol and channel due to the constant total received optical power, b_{FCM}, as

$$\sqrt{\langle i_s^{\,2}(0)\rangle_{FCM}} = \sqrt{2q\left(\frac{\eta q}{h\nu}\right)(b_{FCM})(BW_{eq})} \quad . \tag{119}$$

The total received signal power and hence total mean signal current is given by the following equation as taken from Appendix D,

$$\overline{I_{symbol,channel}} = \left(\frac{\eta q}{h\nu}\right)(b_{2,symbol,channel} - b_{1,symbol,channel}) \tag{120}$$

An ideal MZ harmonic decoder modifies this equation such that the signal current is now proportional to the total received optical power and the sine of the phase difference between the MZ arms for the given symbol as per the channel delay length of the MZ,

$$\overline{I_{symbol,channel}(\Delta\phi_\tau)} = \left(\frac{\eta q}{h\nu}\right)(b_{total,symbol,channel})\sin(\Delta\phi_\tau(t)). \tag{121}$$

The total optical power can be replaced by b_{FCM} as above in the shot noise if the transmitted optical power is assumed to be independent of the transmitted symbol,

$$\overline{I_{FCM}(\Delta\phi_\tau)} = \left(\frac{\eta q}{h\nu}\right)(b_{FCM})\sin(\Delta\phi_\tau). \tag{122}$$

$Q_{FCM,\Delta\phi}$ of the FCM system for a particular symbol pair with delay of +/-$\Delta\phi_\tau$ is given by the following equation,

$$\begin{aligned} Q_{FCM,\Delta\phi} &= \frac{\overline{I_{FCM}(\Delta\phi_\tau)} - \overline{I_{FCM}(-\Delta\phi_\tau)}}{2\sqrt{\langle i_s^2(0)\rangle}} \\ &= \frac{2\left(\frac{\eta q}{h\nu}\right)(b_{FCM})\sin(\Delta\phi_\tau)}{2\sqrt{2q\left(\frac{\eta q}{h\nu}\right)(b_{FCM})(BW_{eq})}} \\ &= \sqrt{\frac{\left(\frac{\eta q}{h\nu}\right)(b_{FCM})}{2q(BW_{eq})}}\sin(\Delta\phi_\tau) \end{aligned} \tag{123}$$

$Q_{FCM,\Delta\phi}$ is calculated for pairs of FCM symbols with the same phase magnitude but opposite phase polarity. For example, symbol 7 and symbol 8 would constitute such a pair for any of the FCM channels.

Comparison of the quantum limit for ISK and FCM signals is done by comparing the optical powers required to achieve equal Q for both systems with $\Delta\phi_\tau$ as a parameter of the FCM system,

$$\begin{aligned} Q_{ISK} &= Q_{FCM,\Delta\phi} \\ \sqrt{\frac{\left(\frac{\eta q}{h\nu}\right) b_{ISK}}{2q(BW_{eq})}} &= \sqrt{\frac{\left(\frac{\eta q}{h\nu}\right) b_{FCM}}{2q(BW_{eq})}}\sin(\Delta\phi_\tau) \\ \sqrt{b_{ISK}} &= \sqrt{b_{FCM}}\sin(\Delta\phi_\tau) \end{aligned} \tag{124}$$

The ratio of the required peak optical power for the same Q is characterized by the following equation and is only dependent on the phase delay from the MZ for the symbols with the same absolute phase and opposite polarity,

$$\frac{b_{FCM}}{b_{ISK}} = \frac{1}{sin^2(\Delta\phi_\tau)} \tag{125}$$

If knowledge of the ratio of the mean optical powers is required then the given ratio is increased by a factor of 2. For the different channels and symbols of a 16 level FCMA system, the peak power and average power ratios to achieve equal Q are given in Table 6-3.

Table 6-3: The ratio of optical power at the receiver for equal system Q for FCM versus ISK transmission for FCM channels of a 16 level signal calculated for FCM symbol pairs with the same phase difference but opposite polarity. Calculated for equal peak powers and equal average powers for FCM versus ISK.

	Optical Power Ratio (dB) to Achieve an Equivalent Q for FCMA Relative to ISK Based on the Respective Quantum Limits. Calculated for all Differential Symbol Pairs for a 16 level FCM Signal.							
	Channel 1	Channel 2	Channel 3		Channel 4			
	π/2	π/4	π/8	3π/8	π/16	3π/16	5π/16	7π/16
Equal Peak Optical Powers	0	0.169	0.688	1.603	3.010	5.105	8.343	14.20
Equal Mean Optical Powers	3.010	3.179	3.698	4.613	6.021	8.116	11.35	17.21

The quantum limit ratios are independent of bitrate, assuming that the bandwidth of the

ISK and FCM systems are the same.

To include the effects of linewidth noise in the bit error ratio calculation Equation (107) from Chapter 4 is the expression for σ_P evaluated using a linear approximation and converted to an equivalent noise current, σ_{ILW}, by multiplying by the responsivity of the photodiode,

$$\sigma_{ILW} = \sigma_P \frac{\eta e}{h\upsilon}, \tag{126}$$

where the explicit expression for the mean square noise current is given by the following equation,

$$\sigma_{ILW}^2 = 2\pi\tau_{\Delta L}\Delta\nu_{LW}\left(\frac{\eta e}{h\upsilon}\right)^2 \left|\cos(\Delta\phi_\tau(t))\right|^2 \left|A_0(t)\right|^2 \left|A_0(t-\tau_{\Delta L})\right|^2. \tag{127}$$

The squared cosine term modulates the phase noise contribution from minimum to maximum depending on the relative phase of the electric fields at the output of the MZ interferometer and $|A_0(t)|^2$ is the optical power of the optical signal at the input to the MZ and $|A_0(t - \tau_{\Delta L})|^2$ is the same optical power function delayed by a time given by $\tau_{\Delta L}$. This linewidth related mean square noise term is equal to zero for $\Delta\phi_\tau = +/- \pi/2$, which is a problem for Gaussian pdf which becomes a delta function in the limit of $\Delta\phi_\tau$ going to zero. But, when it is added to the other noise terms from the amplifier and signal shot noise, the total mean square noise is non-zero and the problem does not appear for the total noise.

Adding these linewidth related noise contributions to the results for the BER calculations presented in Section 5.8 on the BER performance of FCMA links can be done by adding the mean square linewidth noise to the total mean square noise as calculated in Appendix D. The results for the 4 level Runge Kutta integration at 1.25 Gsps FCM signal with the properties discussed in Section 5.8 are presented for the case of an "ideal" decoder in Figure 6-11.

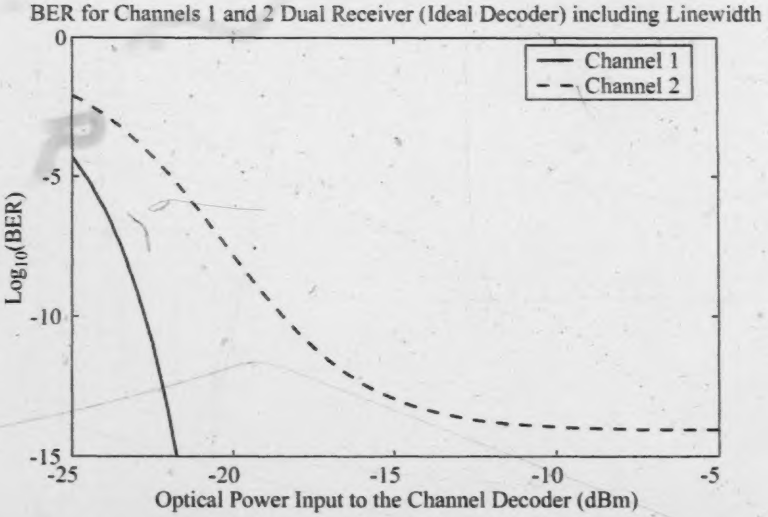

Figure 6-11: The received BER versus the optical power input to the MZ harmonic decoder, assuming ideal decoders, for channels 1 and 2 of a four level FCM transmission based on the Runge Kutta simulations of Chapter 2. The calculation includes the contribution of linewidth related noise.

The BER of channel 1 is not affected by the addition of the linewidth noise effects to the total noise at the dual differential receiver. Channel 2, however, is quite substantially affected since the sensitivity at BER = 10^{-9} increased from -21.2 dBm to -19.2 dBm (or an approximate increase in power of 60%). Channel 2 also has a BER floor of 10^{-14} regardless of how high much optical power received. The receiver sensitivity and the 1x2 splitter asymmetry are summarized below in Table 6-4. The received optical power to achieve a BER of 10^{-9} for channel 1 does not change from the calculation that does not include the linewidth related noise. The optical power for channel 2 increases by 2 dB to achieve the BER of 10^{-9} when the linewidth is included in the calculation and the total power for all channels combined is increased by 1.3 dB.

Table 6-4: The calculated optical power necessary to achieve a BER of 10^{-9} for both channels of a 4 level FCMA 1.25 Gsps transmission and the optimized power splitter insertion losses for the 4 level Runge Kutta generated FCM signal.

FCMA Channel(s)	Received Optical Power (dBm) to Achieve BER = 10^{-9}	Channel Specific Insertion Loss (dB) for Lossless MZ Decoders with BER = 10^{-9}	
	4 Level Runge Kutta Laser Signal		
Channel 1	-23.0	(IL_1)	5.3
Channel 2	-19.2	(IL_2)	1.5
All Channels Combined	-17.7		N/A

The application space limitations considering the optical frequency modulation depth as calculated in Table 2-2 and from the linewidth of the signal source as calculated in Table 4-5 for a BER of 10^{-9} is visualized in Table 6-5.

Table 6-5: A visual summary of the calculated results of Table 2-2 and Table 4-5 which limit the application space of the FCMA systems. The white cells in this table represent acceptable performance, grey cells are borderline performance and black cells are unacceptable performance.

Native Bitrate (Gsps)	Channel 1 Delay as a Fraction of the Bit Duration	Transmitted Symbols Represented by the Phase Delay Between Paths for the Channel MZ Harmonic Decoder							
		Channel 1	Channel 2	Channel 3		Channel 4			
		$\pi/2$	$\pi/4$	$\pi/8$	$3\pi/8$	$\pi/16$	$3\pi/16$	$5\pi/16$	$7\pi/16$
0.622 OC-12	1/4	□	□	■	▨	■	■	■	■
	1/3	□	□	■	▨	■	■	■	■
	1/2	□	■	■	▨	■	▨	▨	▨
1.25 Gigabit Ethernet	1/4	□	□	■	■	■	■	■	■
	1/3	□	□	■	■	■	■	■	■
	1/2	□	□	■	▨	■	■	■	■
2.488 OC-48	1/4	□	■	■	■	■	■	■	■
	1/3	□	■	■	■	■	■	■	■
	1/2	□	□	■	■	■	■	■	■

It is possible to build a four level FCMA system with these considerations at any of the proposed bitrates, OC-12, Gigabit Ethernet, and OC-48, considering the modulation depth and the linewidth limited performance. The quantum limit of received optical power is not unreasonable for these two channels: no increase in peak power compared to ISK for channel 1 and only a 3 dB increase in peak power compared to ISK for channel 2 where the total increase in optical power is 4.8 dB over the ISK quantum limit.

If the performance meets the expectations of the calculations FCMA would be adequate for transmission over links in a typical metropolitan area which is tens of kilometers in physical size. Chapter 7 will present conclusions and future work.

Chapter 7. Conclusions and Future Work.

This chapter is organized into a chapter by chapter summary of conclusions and future work for Chapter 2 through 6 first. A summary of FCMA and future work that applies to Chapter 1, and FCMA in general, will be provided in a final section.

7.1 Chapter 2 Conclusions and Future Work.

Chapter 2 introduced rate equation analysis of semiconductor lasers as a means to identify the properties of semiconductor lasers that would enable the use of such a laser in the transmitter of an optical fiber communication link that is based on baseband FSK, such as an FCMA system. The results of Chapter 2 demonstrate that optical injection modulation of semiconductor lasers produces the most stable and robust optical waveforms that most closely approximate the desired optical FCMA waveform as it is described in Section 1.4.1.

Through analysis based on the rate equations for semiconductor lasers and the knowledge of the relative intensities of the sidemodes for Fabry-Perot (FP) and distributed feedback (DFB) semiconductor lasers, optical injection was investigated theoretically and a few general conclusions can be drawn from the results:

- DFB lasers must be used for the slave laser due to the large natural sidemode suppression ratio and the fact that this enables narrow linewidth operation of the free-running emission mode of the laser.
- Optical injection with optical power modulated injected light results in modulation of the slave laser output up to modulation rates that are on the order of the relaxation oscillation frequency of the semiconductor laser (several GHz).
- The required injection power for the modulation of the slave laser in order to create FCM signals at or above OC-12 line rates is in excess of 1 mW of

optical power (incident on the external face of the laser facet).

- The efficiency of the injected optical power to free-running slave laser adiabatic frequency shift conversion is linearly related to the linewidth enhancement factor, α, and the gain compression coefficient, κ_s, of the semiconductor laser.
- The linewidth of the DFB laser that has the parameters as they are defined and listed in Chapter 2 is expected to have a dynamic linewidth of the free-running laser line which is less than 10 MHz.
- The stability of the slave laser under optical injection depends on the relative frequency difference of the injected light to the natural resonance of the slave laser mode. Generally, the injection is stable when the optical frequency of the injected light is close to the natural resonance of the slave laser mode.
- Equal frequency spacings of the successive levels of the optical FCM signal relies on the injection by an optical power modulation signal that does not have equal successive optical power levels. The sensitivity of this linearity has been explored in terms of the transfer function of voltage signals being applied to a Mach-Zehnder (optical) modulator through to the output frequency level spacing. The spacing of the frequency levels of the FCM signal is greatly improved by the use of the MZ modulator and choosing the correct bias point for the modulator.
- The optical injection modulation of semiconductor lasers produces amplitude modulation in the free-running slave laser mode in addition to the desired optical frequency modulations.

Future work on the theoretical laser rate equation analysis of optical injection would involve extending the semiconductor laser models to include spectral variations of parameters to more accurately approximate actual laser performance. The parameters that are spectrally dependent are the linewidth enhancement factor, α, the semiconductor gain derivative as a function of mode number, g_m, and the laser threshold (for different modes) which can be varied by assuming different values of the spontaneous inversion factor, n_{sp}, for different optical frequencies. Two other laser parameters that can be easily modified and have major effects on the frequency modulation characteristics of semiconductor lasers are the laser facet loss, α_m, and the laser length, L. There are a number of papers that describe the effects of modifying the laser rate equations to accommodate these spectrally dependent parameters and the changes in facet loss and laser length: for α, see [OS1]; for α_m, see [OL1,OS1]; for L, see [GAL1,OL1]; for different gains (g_n), see [CARE2,LU1]; for different mode thresholds, see [CARE2]. Particular attention needs to be paid to the reduction of the laser length which would increase the range of stability for optical injection based on the results of the above quoted papers.

Variations in these parameters would result in changes to the optical output waveforms generated by Runge Kutta integration of the rate equations. These different waveforms could be analysed by methods similar to those presented in the chapters following Chapter 2 to predict the sensitivity of the FCMA system performance to the variations in optical parameters of semiconductor lasers used as optical signal transmission sources.

7.2 Chapter 3 Conclusions and Future Work.

Chapter 3 built upon the results of Chapter 2 and demonstrated several attempts to construct a FCMA transmitter with actual laboratory hardware. Master and slave lasers were arranged with an optical modulator and several optical filters, optical amplifiers, interface electronics, optical monitors and other electrical and optical experimental gear to create a system capable of producing an FCM signal (baseband *M*-ary FSK). The following list draws specific attention to conclusions that can be drawn from Chapter 3:

- Experimental verification showed that the shift of the laser frequency is a function of the injected optical power for both DFB and FP lasers.
- FP lasers with ASE injection have large linewidth of oscillation mode due to noise injection.
- DFB laser exhibits good predictable behaviour as the optical injection power

is increased.

- Figure 3-28 demonstrates that spectral width of the free running DFB laser mode does not increase with the optical injection within the 100 MHz spectral resolution of the FFP that was used to perform the measurements.

The Runge Kutta calculations of Chapter 2 predict good dynamic behaviour for DFB semiconductor lasers with optical injection. It would be an extension of the material that was presented in Chapter 3 to show experimental evidence that the dynamic response (optical power and frequency) of the DFB laser to optical injection is so well behaved.

Another prediction of the material in Chapter 2 that would be preferable to measure experimentally is the linewidth of the DFB laser with DC optical injection and with AC optical injection. The linewidth during modulation should approximate the convolution of the steady state linewidth with the modulation waveform as in [TO1]. A possible experiment that would yield results for AC optical injection could involve the injection of a sinusoidally modulated optical waveform (generated with the use of the MZ modulator) and the sidebands of the free-running slave laser mode could be analyzed via the usual linewidth measurement technique of delayed interference viewed on an electrical spectrum analyzer [BA1]. This method would provide an out-of-band measurement as well as enabling the measurement to be taken on the dynamic linewidth of the slave laser.

7.3 Chapter 4 Conclusions and Future Work.

Chapter 4 presented an extensive amount of material dealing with Mach-Zehnder based optical interferometers (filters). The theoretical background and design information provided apply specifically to MZ filters either based on PLC or free-space optics. Each of the PLC and free-space optics approaches to the construction of MZ harmonic decoders was discussed also in terms of construction or fabrication of practical devices. The following list summarizes conclusions from Chapter 4 on the MZ harmonic decoders:

- Theoretically, the output waveforms from the harmonic decoders, when the Runge Kutta results of Chapter 2 are used as input waveforms, produce acceptable differential binary waveforms at the optical outputs of the MZs.

- The output waveforms from the harmonic decoders is dependent upon the splitting ratio at the input to the MZ, the combining ratio at the output of the MZ, and any loss imbalance that is incurred between the arms of the interferometer.
- The output waveforms from the harmonic decoders can be influenced by the relative phases of the different light paths in the MZ that are imposed on the light by the physical properties of the splitting and combining structures (e.g. mirrors).
- The measured properties of the free-space MZ decoder that was built for testing the FCMA system were shown to be acceptable for a prototype FCMA system via the calculated results.
- A specific derivation of the theoretical transfer function of the MZ harmonic decoder was presented and a description on its application to the FCM signal was given.
- The required linewidth of the laser source was investigated with respect to the predicted values of linewidth and FCM signal frequency level spacing from Chapter 2. The engineering space based on these results was presented in a table that demonstrates that systems built at line rates of 0.622 Gsps, 1.25 Gsps and 2.488 Gsps are feasible considering the results of Chapter 2 combined with realistic performances of MZ based harmonic decoders.

Work that remains to be done involves experimental verification of the error rates predicted with respect to the linewidth related error which is expected to be independent of received optical power as long as the linewidth noise is the dominant contributor.

Fabrication of the PLC devices would need to be redone and experiments need to be performed to verify of all of the predicted values of the physical parameters: coupling losses, bending losses, absorption and scattering losses as well as numerical aperture. Also required for completeness would be the testing of the proposed thermal control system which relies on the bulk heating of the glass near the corners of the device substrates.

Finally, testing the response of the MZ to a real FCM signal or even a DFB laser that is directly modulated at a known high frequency ASK modulation would verify the actual dynamic response of the MZ filters.

7.4 Chapter 5 Conclusions and Future Work.

Chapter 5 was focused on the construction and testing of the dual differential optical receiver. The receiver that was designed was based on a PIN photodiode and a monolithic transimpedance amplifier. There was a T-filter placed between the PIN diode and the amplifier in the receiver design to modify the combined transfer function in order to limit the bandwidth of the receiver. The receiver transfer function was measured and the design was considered to be successful although it was never tested using an FCM signal. The receiver was tested using binary intensity shift keyed optical signals and was deemed to operate adequately. The following list summarizes conclusions from Chapter 5 on the dual differential receivers:

- The receiver design is adequate based on the simulated response, compared to the measured response, and the calculated effects of the simulated transfer function on the simulated FCM input waveforms.
- The receiver noise, which is mostly due to the amplifier, is adequately low to receive the optical signals with reasonable optical intensities, at or less than ~ -10 dBm.
- The receiver response does generate some ISI but not enough to be a major impairment to the use of the receiver.
- The receiver introduces enough distortion to be noticeable but not enough to preclude its use.
- The sensitivity gain of 3 dB in electrical power from using the dual differential receiver has been shown theoretically.

One of the reasons that this receiver was designed in this particular way was to get a steep roll off in the high frequency end to get rid of the sharp spikes in the signal that appear in the optical signal between the decoded symbols. The receiver was optimized for transfer function shape and not for noise. A future improvement would be designing a receiver that has similar transfer function with greatly reduced noise. This could be accomplished by placing a single stage transistor based (low noise) transimpedance amplifier immediately adjacent to the PIN diode and adding an equalizer external to the receiver to limit the bandwidth of the receiver after the first stage of amplification has taken place.

Also worth exploring would be the option of integrating two PIN diodes onto one substrate with an electrical waveguide feed off the chip for connection to a low noise amplifier. This would enable the packaging of both receivers in one RF receiver housing, with a common amplifier for both parts of the differential electrical signal.

7.5 Chapter 6 Conclusions and Future Work.

Chapter 6 combined the results of the previous chapters in an attempt to demonstrate that the FCMA based optical network links could be constructed using the transmitter, decoder and receiver designs presented in the previous chapters. The particular subjects of Chapter 6 included the optimization of the signal splitting ratio prior to the channelized harmonic decoders, the simulated effects of fiber dispersion on the received FCMA signal for reasonable link distances, the power limited transmission distances achievable with the discussed receiver design, and the combined effects of all of the noise components at the receiver that were previously discussed. The following list summarizes conclusions from Chapter 6 on the design of FCMA based optical links:

- Link lengths that are achievable using the FCMA based optical links for a four level signal at 1.25 Gsps would be optical power limited at roughly 80 km (with 0 dBm launch power) and dispersion limited at roughly 320 km.
- Link lengths that are achievable using the FCMA based optical links for a sixteen level signal at 1.25 Gsps would be optical power limited at roughly 80 km (at 5 dBm launch power) and dispersion limited at roughly 80 km.

- The link capacity of an FCMA based link could be expanded using WDMA at the above stated optical power link limits with the addition of one low noise optical amplifier (probably an EDFA).
- The link capacity of the FCMA based network could be expanded further (assuming WDMA) to the dispersion limited transmission limit (320 km for 4 levels at 1.25 Gsps) using low noise optical amplifiers.
- 4 level FCMA is possible at symbol rates equal to OC-12, Gigabit Ethernet, and OC-48 with the DFB laser simulated in Chapter 2 and considering the linewidth noise, frequency modulation depth, output power and dispersion distortion of the transmitted symbols.

The noise effects of optical amplifiers [GI1] would have to be added to the analysis to verify the performance for longer link lengths, but results should not be any more prohibitive than current commercial WDM and dense WDM (DWDM) communication products. Also, the optimum channel spacing (100 GHz, 200 GHz, 400 GHz, 800 GHz, etc.) for the WDM combination of FCM signals remains to be determined.

7.6 General Conclusions and Future Work.

Section 1.9 outlined the implementation options for the FCMA hardware that were available to achieve the design goals stated in Section 1.10. This section reviews these general options and goals with respect to the results of the work presented previously in this thesis. The section ends with some specific ideas for future work and some ideas that are more speculative.

From Section 1.9.1 on the choices of transmitter option, optical injection was chosen in favor of direct modulation of a laser diode and external modulation of a laser diode. This option most closely fulfils the requirements outlined in Section 1.9.1. The laser properties for the simulated device in Chapter 2 are good targets for the desired laser properties for the FCM signal source.

Harmonic decoder options as outlined in Section 1.9.2 shows good potential for the PLC type of implementation if the problems of coupling losses could be mitigated.

Another problem that would require additional work is the polarization dependent loss of the PLC devices especially when considering the waveguide bends. When using free-space optics, in the manner described in Chapter 4 or otherwise, the optics would have to be designed particularly to optimize the splitting and combining ratios as well as the additional phase offsets incurred at the splitting and combining mirrors. The power splitting to optimize the received optical power on a per channel basis can be accomplished as was described in Chapter 6. These concerns can be achieved with either of the presented options, free-space or PLC MZ, or by an all fiber solution as can be achieved through thermal control of a fiber MZ which is expected to soon be the state of the art.

Section 1.9.3 proposes two options for high speed receivers; the PIN diode or the APD. The PIN diode is still the optimum choice of technology for receiving these high speed optical signals. The APD could improve the receiver sensitivity for the receiver that was designed for this research since it adds amplification directly to the received signal and would be lower noise than the amplifier that was chosen for the receiver design described in Chapter 5. This point is moot as per the arguments that are presented in Section 7.4 of this chapter. Additionally the 3 dB gain in receiver sensitivity as discussed in Section 1.9.2 is achieved as per the arguments of the conclusions drawn in Section 7.4.

The goals of the prototype FCMA system as stated in Section 1.10 are restated here and elaborated with explanations as to the degree of which they were achieved.

1) Construction of the FCMA transmitter using only fiber compatible components.

This was confirmed as per the discussions in Chapter 3 which described the construction of this transmitter but the test of whether or not the performance of this transmitter will behave as predicted by the results of Chapter 2 remains as future work.

2) Demonstration of frequency modulation by optical injection in distributed feedback (DFB) and Fabry-Perot (FP) semiconductor laser diodes.

This was achieved in Chapter 3 with DC optical injection where the rate of change of this optical injection and it subsequent resulting frequency modulation was not shown at high modulation rates but was predicted to be possible through the results of Chapter 2.

3) Demonstration of the generation of a binary frequency shift keyed signal of known modulation depth corresponding to odd multiples of the multilevel

signal separation $\Delta\nu$.

This was not achieved but is believed to be possible by the results of Chapter 2 and other research [CHRY1,DUR1,MI1].

4) Studying the effectiveness of frequency decoding by Mach-Zehnder interferometers and identify relevant limitations.

As a study this is considered successful through the theoretical evidence that was presented throughout Chapters 4, 5 and 6, particularly the relationship between the linewidth of the transmitter source and the floor in the achievable error rate (BER).

5) The design, construction and testing of a set of four harmonically-related integrated Mach-Zehnder interferometer filters.

The design is considered successful via the evidence presented in Chapter 4. The construction and testing would require additional attempts but, judging by the success of other research, is deemed to be possible [BON1,WOR1].

6) The design and construction of a dual differential receiver.

Also considered a success, even though this was not tested on the FCM signal, this was tested on intensity shift keyed signals with excellent performance.

7) Characterization of the performance of a link using binary frequency shift keying.

8) Demonstration of symbol rates equal to OC-12 (622 Mbps), OC-48 (2.488 Gbps) and Gigabit Ethernet (1.25 Gbps).

The receiver and harmonic decoder were shown to work as expected, the transmitter was never tested beyond DC changes in optical frequency so it seems that everything will work the only question is up to what bit rate.

Future work can include investigating the benefits of forward error correction (FEC) schemes applied to FCMA transmissions. A particular benefit is expected to be the mitigations of linewidth related noise effects because phase noise in the laser diode is the right kind of random noise (due to Markovian nature of the phase statistics) to be compensated for using FEC.

The extension of the harmonic decoders to one optical interferometer with *M* outputs and receiver diodes that relies on electrical manipulation of the output signals to decode the input frequency coded symbol. This achieves an effective optical gain by eliminating the excess loss of the optical splitter, as well as having equal average optical powers for all of the receiver diodes. A harmonic decoder such as this can be constructed using a 90° optical MMI hybrid, as described in [PENS1], or a higher order MMI hybrid for phase or frequency symbols spaced at 45° or 22.5° as in 8 and 16 level FCM signals. Such hybrids have two input waveguides and *M* output waveguides and would require *M* receiver diodes.

Another means of producing the FCM signal is an additional area for future investigation. A special laser source, like those described in [AK1],[CHRY1], and [YAM1], may prove to be better suited to producing the FCM signal or another modulation scheme may be easier to implement than optical injection at high rates.

A single channel of FCM transmission would encounter fiber chromatic dispersion (CD), polarization dependent loss (PDL), polarization mode dispersion (PMD) and self phase modulation (SPM). The penalties associated with these phenomena and the methods of compensating for them have been discussed for other types of transmission and the same types of fiber systems analysis could be applied to FCMA (for CD see [EL1,SU1], PMD see [MAJ5,GARA1], SPM see [MAJ4,SU1,TA1]).

If FCMA were to be combined with WDMA then the design of the filters needs to be accounted for in the performance of the system. Filters add bandwidth narrowing, PDL and PMD, and have group delay ripples. The fact that the FCM signal bandwidth is significant (on the order of 10 GHz) makes the investigation of phase properties of the filter necessary [PENX1].

The introduction of multiple channels to one fiber adds concern for additional nonlinearities and the need to account for them in the link performance calculations. The additional nonlinearities include cross phase modulation (XPM), four wave mixing (FWM) and stimulated raman scattering (SRS). The penalties associated with these phenomena and the methods of compensating for them have been discussed for other types of transmission and the same types of fiber systems analysis could be applied to FCMA (for XPM see [BE1,CARO1,CHIG1,NO1], FWM see [EI1,FO1,ZE1], SRS see [CHRS1])

As was suggested in Section 1.2.2, a clear accounting of the network efficiency must be performed on the FCMA based network to determine the effects of the unique network features of FCMA compared to established network architectures.

FCMA may or may not be more expensive than traditional methods of optical information transport. A detailed economic analysis would be required to accurately compare FCMA to other solutions. The traditional system cost estimates must include not only the cost of the optical transmission equipment, but also the TDMA muxing and demuxing of higher rate signals as well as the cost of some of the switching gear associated with traditional optical networks. This would be necessary due to the fact that FCMA incorporates some stages of electrical muxing and demuxing and some switching functions into its optical layer. Additionally, the network architectures possible with FCMA allow for network reconfiguration without the necessity of optical switching or manual network reconfiguration at the optical network level which could also bring cost savings.

The technical feasibility of FCMA based optical networks for deployment in the metropolitan area network optical communications application space has been demonstrated.

List of References

[AC1] Anthony S. Acampora, *An Introduction to Broadband Networks*, New York, New York, Plenum Press, 1994.

[AG1] Govind P. Agrawal, "Generalized rate equations and modulation characteristics of external-cavity semiconductor lasers," *J. Applied Physics*, vol. 56, no. 7, pp. 3110-3115, 1984.

[AG2] Govind P. Agrawal, Charles H. Henry, "Modulation Performance of a Semiconductor Laser Coupled to an External High-*Q* Resonator," *IEEE J. Quantum Electronics*, vol. 24, no. 2, pp. 134-142, 1988.

[AK1] Yuliya A. Akulova, Gregory A. Fish, Ping-Chiek Koh, Clint L. Schow, Peter Kozodoy, Anders P. Dahl, Shigeru Nakagawa, Michael C. Larson, Michael P. Mack, Timothy A. Strand, Christopher W. Coldren, Eric Hegblom, Steven K. Penniman, Torsten Wipiejewski, Larry A. Coldren, "Widely Tunable Electroabsorption-Modulated Sampled-Grating DBR Laser Transmitter," *IEEE J. Selected Topics in Quantum Electronics*, vol. 8, no. 6, pp. 1349-1357, 2002.

[BA1] Douglas M. Baney, Wayne V. Sorin, "Linewidth and Power Spectral Measurements of Single-Frequency Lasers," *Hewlett-Packard Journal*, pp. 92-96, February 1990.

[BE1] S. Betti, M. Giaconi, "Effect of the Cross-Phase Modulation on WDM Optical Systems: Analysis of Fiber Propagation," *IEEE Photonics Technology Letters*, vol. 13, no. 4, pp. 305-307, 2001.

[BON1] G. L. Bona, R. Germann, F. Horst, B. J. Offrein, H. W. M. Salemink, "Versatile Silicon-Oxynitride Planar Lightwave Circuits for Interconnect Applications," (preprint), 1999.

[BORI1] A. C. Bordonalli, C. Watson, Alwyn J. Seeds, "High-Performance Phase Locking of Wide Linewidth Semiconductor Lasers by Combined Use of Optical Injection Locking and Optical Phase-Lock Loop," *J. Lightwave Technology*, vol. 17, no. 2, pp. 328-342, 1999.

[BORN1] Max Born, Emil Wolf, *Principles of optics*, (Seventh Edition), Cambridge, Cambridge University Press, 1999.

[BOY1] Joseph T. Boyd, "Photonic Integrated Circuits," *Photonic Devices and Systems*, ed Robert G. Hunsperger, New York, Marcel Dekker Inc., 1994.

[BR1] Chris Bradford, "Managing chromatic dispersion increases bandwidth," *WDM Solutions*, February 2001, pp. 71, 2001.

[CARE1] J. C. Cartledge, G. S. Burley, "The Effect of Laser Chirping on Lightwave System Performance," *J. Lightwave Technology*, vol. 7, no. 3, pp. 568-573, 1989.

[CARE2] John C. Cartledge, Aly F. Elrefaie, "Threshold Gain Difference Requirements for Nearly Single-Longitudinal-Mode Lasers," *J. Lightwave Technology*, vol. 8, no. 5, pp. 704-715, 1990.

[CARE3] John C. Cartledge, "Theoretical Performance of Multigigabit-Per-Second Lightwave Systems Using Injection-Locked Semiconductor Lasers," *J. Lightwave Technology*, vol. 8, no. 7, pp. 1017-1022, 1990.

[CARE4] John C. Cartledge, "Optimizing the Bias and Modulation Voltages of MQW Mach-Zehnder Modulators for 10 Gb/s Transmission on Nondispersion Shifted Fiber," *J. Lightwave Technology*, vol. 17, no. 7, pp. 1142-1151, 1999.

[CARO1] Adalfo V. T. Cartaxo, "Cross-Phase Modulation in Intensity Modulation - Direct Detection WDM Systems with Multiple Optical Amplifiers and Dispersion Compensators," *J. Lightwave Technology*, vol. 17, no. 2, pp. 178-190, 1999.

[CHIN1] M. K. Chin, "On the Figures of Merit for Electroabsorption Waveguide Modulators," *IEEE Photonics Technology Letters*, vol. 4, no. 7, pp. 726-728, 1992.

[CHIN2] Mee K. Chin, William S. C. Chang, "Theoretical Design Optimization of Multiple-Quantum-Well Electroabsorption Waveguide Modulators," *IEEE J. Quantum Electronics*, vol. 29, no. 9, pp. 2476-2488, 1993.

[CHIG1] Ting-Kuang Chiang, Nobuyuki Kagi, Thomas K. Fong, Michel E. Marhic, Leonid G. Kazovsky, "Cross-Phase Modulation in Dispersive Fibers: Theoretical and Experimental Investigation of the Impact of Modulation Frequency," *IEEE Photonics Technology Letters*, vol. 6, no. 6, pp. 733-736, 1994.

[CHRS1] D. N. Christodoulides, R. B. Jander, "Evolution of Stimulated Raman Crosstalk in Wavelength Division Multiplexed Systems," *IEEE Photonics Technology Letters*, vol. 8, no. 12, pp. 1722-1724, 1996.

[CHRY1] A. R. Chraplyvy, R. W. Tkach, A. H. Gnauck, B. L. Kasper, R. M. Derosier, "8 Gbit/s FSK modulation of DFB lasers with optical demodulation," Electronics Letters, vol. 25, no. 5, pp. 319-321, 1989.

[CON1] Marco Conti, Enrico Gregori and Luciano Lenzini, *Metropolitan Area Networks*, London, England, Springer-Verlag, 1997.

[COR1] P. J. Corvini, T. L. Koch, "Computer Simulation of High-Bit-Rate Optical Fiber Transmission Using Single-Frequency Lasers," *J. Lightwave Technology*, vol. LT-5, no. 11, pp. 1591-1595, 1987.

[DUD1] Thomas Dudley, "Components and cost considerations for 10 Gbits/sec in the enterprise backbone," *Lightwave*, vol. 16, no. 3, pp. 76-79, 1999.

[DUR1] T. Durhuus, R. J. S. Pedersen, B. Mikkelsen, K. E. Stubkjaer, M. Öberg, S. Nilsson, "Optical Wavelength Conversion Over 18 nm at 2.5 Gb/s by DBR-Laser," *IEEE Photonics Technology Letters*, vol. 5, no. 1, pp. 86-88, 1993.

[EI1] Michael Eiselt, "Limits on WDM Systems Due to Four-Wave Mixing: A Statistical Approach," *J. Lightwave Technology*, vol. 17, no. 11, pp. 2261-2267, 1999.

[EL1] A. F. Elrefaie, R. E. Wagner, D. A. Atlas, D. G. Daut, "Chromatic Dispersion Limitations in Coherent Lightwave Transmission Systems," *J. Lightwave Technology*, vol. 6, no. 5, pp. 704-709, 1988.

[EM1] K. Emura, M. Shikada, S. Fujita, I. Mito, H. Honmou, K. Minemura, "Novel optical FSK heterodyne single filter detection system using a directly modulated DFB-laser diode," *Electronics Letters*, vol. 20, no. 24, pp. 1022-1023, 1984.

[FO1] Fabrizio Forghieri, R. W. Tkach, A. R. Chraplyvy, "WDM Systems with Unequally Spaced Channels," *J. Lightwave Technology*, vol. 13, no. 5. pp. 889-897, 1995.

[GAL1] P. Gallion, G. DeBarge, "Influence of amplitude-phase coupling on the injection locking bandwidth of a semiconductor laser," *Electronics Letters*, vol. 21, no. 7, pp. 264-266, 1985.

[GARA1] J. Sánchez García, "Polarization Mode Dispersion Power Penalty; Influence of Rise/Fall Times, Receiver *Q* and Amplifier Noise," *IEEE Photonics Technology Letters*, vol. 8, no. 12, pp. 1719-1721, 1996.

[GART1] Ian Garrett, Gunnar Jacobsen, "Theoretical Analysis of Heterodyne Optical Receivers for Transmission Systems Using (Semiconductor) Lasers with Nonneglegible Linewidth," *J. Lightwave Technology*, vol. LT-4, no. 3, pp. 323-334, 1986.

[GI1] C. R. Giles, Emmanuel Desurvire, "Propagation of Signal and Noise in Concatenated Erbium-Doped Fiber Optical Amplifiers," *J. Lightwave Technology*, vol. 9, no. 2, pp. 147-154, 1991.

[GO1] L. Goldberg, H. F. Taylor, J. F. Weller, "Time-dependent thermal effects in current-modulated semiconductor lasers," *Electronics Letters*, vol. 17, no. 14, pp. 497-499, 1981.

[GO2] L. Goldberg, H. F. Taylor, J. F. Weller, "Intermodal injection locking of semiconductor lasers," *Electronics Letters*, vol. 20, no. 20, pp. 809-811, 1984.

[HE1] Charles H. Henry, "Theory of the Phase Noise and Power Spectrum of a Single Mode Injection Laser," *IEEE J. Quantum Electronics*, vol. QE-19, no. 9, pp. 1391-1397, 1983.

[HE2] Charles H. Henry, Paul S. Henry, Melvin Lax, "Partition Fluctuations in Nearly Single-Longitudinal Mode Lasers," *J. Lightwave Technology*, vol. LT-2, no. 3, pp. 209-216, 1984.

[HE3] Charles H. Henry, "Phase Noise in Semiconductor Lasers," *J. Lightwave Technology*, vol. LT-4, no. 3, pp. 298-311, 1986.

[HN1] Alan Hnatiw, *A Silica Based Integrated Optic Microwave Power Sensor*, Masters Dissertation, University of Alberta, 1996.

[HO1] Jürgen Hörer, Erwin Patzak, "Large-Signal Analysis of All-Optical Wavelength Conversion Using Two-Mode Injection-Locking in Semiconductor Lasers," *J. Quantum Electronics*, vol. 33, no. 4, pp. 596-608, 1997.

[HU1] Rongqing Hui, "Optical PSK Modulation Using Injection-Locked DFB Semiconductor Lasers," *IEEE Photonics Technology Letters*, vol. 2, no. 10, pp. 743-746, 1990.

[IW1] Katsushi Iwashita, Kiyoshi Nakagawa, "Suppression of Mode Partition Noise by Laser Diode Light Injection," *IEEE J. Quantum Electronics*, vol. QE-18, no. 10, pp. 1669-1674, 1982.

[JAC1] G. Jacobsen, I. Garrett, "Error-rate floor in optical ASK heterodyne systems caused by nonzero (semiconductor) laser linewidth," *Electronics Letters*, vol. 21, no. 7, pp. 268-270, 1985.

[JAI1] Raj Jain, *FDDI Handbook*, Reading, Massachusetts, Addison-Wesley Publishing Company, 1994.

[JO1] R. J. Jones, P. S. Spencer, K. A. Shore, "Detuned side-mode injection for enhancing oscillation frequency of a semiconductor laser," *IEE Proceedings—Optoelectronics*, vol. 148, no. 1, pp. 35-39, 2001.

[KAH1] J. M. Kahn, A. H. Gnauck, J. J. Veselka, S. K. Korotky, B. L. Kasper, "4-Gb/s PSK Homodyne Transmission System Using Phase-Locked Semiconductor Lasers," *IEEE Photonics Technology Letters*, vol. 2, no. 4, pp. 285-287, 1990.

[KAZ1] Rudolf F. Kazarinov, Charles H. Henry, "The Relation of Line Narrowing and Chirp Reduction Resulting from the Coupling of a Semiconductor Laser to a Passive Resonator," *IEEE J. Quantum Electronics*, vol. QE-23, no. 9, pp. 1401-1409, 1987.

[KE1] Gary C. Kessler and David A. Train, *Metropolitan Area Networks*, New York, New York, McGraw-Hill, Inc., 1991.

[KIMO1] Hoon Kim, Alan H. Gnauck, "Experimental Investigation of the Performance Limitation of DPSK Systems Due to Nonlinear Phase Noise," *IEEE Photonics Technology Letters*, vol. 15, no. 2, pp. 320-322, 2003.

[KIMY1] Hyun Deok Kim, Seung-Goo Kang, Chang-Hee Lee, "A Low-Cost WDM Source with an ASE Injected Fabry-Perot Semiconductor Laser," *IEEE Photonics Technology Letters*, vol. 12, no. 8, pp. 1067-1069, 2000.

[KOB1] Soichi Kobayashi, Yoshihisa Yamamoto, Minoru Ito, Tatsuya Kimura, "Direct Frequency Modulation in AlGaAs Semiconductor Lasers," *IEEE J. Quantum Electronics*, vol. QE-18, no. 4, pp. 582-595, 1982.

[KOC1] T. L. Koch, R. A. Linke, "Effect of nonlinear gain reduction on semiconductor laser wavelength chirping," *Applied Physics Letters*, vol. 48, no. 10, pp. 613-615, 1986.

[KOY1] Fumio Koyama, Kenichi Iga, "Frequency Chirping in External Modulators," *J. Lightwave Technology*, vol. 6, no. 1, pp. 87-93, 1988.

[LA1] Roy Lang, "Injection Locking Properties of a Semiconductor Laser," *IEEE J. Quantum Electronics*, vol. QE-18, no. 6, pp. 976-983, 1982.

[LI1] J. M. Liu, H. F. Chen, X. J. Meng, T. B. Simpson, "Modulation Bandwidth, Noise, and Stability of a Semiconductor Laser Subject to Strong Injection Locking," *IEEE Photonics Technology Letters*, vol. 9, no. 10, pp. 1325-1327, 1997.

[LU1] Jhy-Ming Luo, Marek Osinski, John G. McInerney, "Side-mode injection locking of semiconductor lasers," *IEE Proceedings*, vol. 136, pt. J, no. 1, pp. 33-37, 1989.

[MAC1] Private communication with Ian MacDonald, 1996.

[MAJ1] S. P. Majumder, R. Gangopadhyay, "Simulation of optical heterodyne single-filter FSK system with line coding," *Electronics Letters*, vol. 27, no. 7, pp. 563-565, 1991.

[MAJ2] S. P. Majumder, R. Gangopadhyay, M. S. Alam, G. Prati, "Performance of Linecoded Optical Heterodyne FSK Systems with Nonuniform Laser FM Response," *J. Lightwave Technology*, vol. 13, no. 4, pp. 628-638, 1995.

[MAJ3] Satya P. Majumder, Mohammad S. Alam, "Performance analysis and simulation of optical direct detection FSK and DPSK systems," pp. 686-693, 1996.

[MAJ4] S. P. Majumder, F. M. Abbou, B. C. Sarker, "Analytical evaluation of the effect of self-phase-modulation on coherent optical CPFSK system," pp. 897-901, 2000.

[MAJ5] S. P. Majumder, M. Z. Yusoff, A. F. Muhammad, H. T. Chuah, "Effect of Polarization Mode Dispersion on Optical Heterodyne CPFSK System," pp. 1233-1236, 2000.

[MAL1] D. J. Malyon, W. A. Stallard, "565 Mbit/s FSK direct detection system operating with four cascaded photonic amplifiers," *Electronics Letters*, vol. 25, no. 8, pp. 495-497, 1989.

[MARE1] Dietrich Marcuse, Tien-Pei Lee, "On Approximate Analytical Solutions of Rate Equations for Studying Transient Spectra of Injection Lasers," *IEEE J Quantum Electronics*, vol. QE-19, no. 9, pp. 1397-1406, 1983.

[MARE2] Dietrich Marcuse, "Classical Derivation of the Laser Rate Equation," *IEEE J Quantum Electronics*, vol. QE-19, no. 8, pp. 1228-1231, 1983.

[MART1] Near Margalit, "Intelligent DWDM takes Gigabit Ethernet to the MAN," *Lightwave*, vol. 16, no. 7, pp. 101, 1999.

[MEC1] Antonio Mecozzi, A. Sapia, Paolo Spano, Govind P. Agrawal, "Transient Multimode Dynamics in Nearly Single-Mode Lasers," *IEEE J. Quantum Electronics*, vol. 27, no 3, pp. 332-343, 1991.

[MEN1] Xue Jun Meng, Tai Chau, Ming C. Wu, "Experimental demonstration of modulation bandwidth enhancement in distributed feedback lasers with external light injection," *Electronics Letters*, vol. 34, no. 21, pp. 2031-2032, 1998.

[MI1] B. Mikkelsen, R. J. S. Pedersen, T. Durhuus, C. Braagaard, C. Joergensen, K. E. Stubkjaer, "Wavelength conversion of high speed data signals," *Electronics Letters*, vol. 29, no. 19, pp. 1716-1718, 1993.

[MOG1] F. Mogensen, H. Olesen, G. Jacobsen, "FM noise suppression and linewidth reduction in an injection-locked semiconductor laser," *Electronics Letters*, vol. 21, no. 16, pp. 696-697, 1985.

[MOG2] Finn Mogensen, Henning Olesen, Gunnar Jacobsen, "Locking Conditions and Stability Properties for a Semiconductor Laser with External Light Injection," *IEEE J. Quantum Electronics*, vol. QE-21, no. 7, pp. 784-793, 1985.

[MOH1] Stefan Mohrdiek, Herbert Burkhard, Herbert Walter, "Chirp Reduction of Directly Modulated Semiconductor Lasers at 10 Gb/s by Strong CW Light Injection," *J. Lightwave Technology*, vol. 12, no. 3, pp. 418-424, 1994.

[NO1] Seiji Norimatsu, Katsushi Iwashita, "The Influence of Cross-Phase Modulation on Optical FDM PSK Homodyne Transmission Systems," *J. Lightwave Technology*, vol. 11, no. 5/6, pp. 795-804, 1993.

[OL1] N. A. Olsson, H. Temkin, Ralph A. Logan, L. F. Johnson, G. J. Dolan, Jan P. Van Der Ziel, J. C. Campbell, "Chirp-Free Transmission Over 82.5 km of Single Mode Fibers at 2 Gbit/s with Injection Locked DFB Semiconductor Lasers," *J. Lightwave Technology*, vol. LT-3, no. 1, pp. 63-67, 1985.

[OS1] Marek Osinski, Jens Buus, "Linewidth Broadening Factor in Semiconductor Lasers—An Overview," *IEEE J. Quantum Electronics*, vol. QE-23, no. 1, pp. 9-29, 1987.

[PENS1] E. C. M. Pennings, R. J. Deri, R. Bhat, T. R. Hayes, N. C. Andreadakis, "Ultracompact, All-Passive Optical 90°–Hybrid on InP Using Self-Imaging," *IEEE Photonics Technology Letters*, vol. 5, no. 6, pp. 701-703, 1993.

[PENX1] Denis Penninckx, Sabry Khalfallah, Philippe Brosson, "System impact of phase ripples in optical components," 2000.

[PER1] S. D. Personick, "Receiver Design for Digital Fiber Optic Communication Systems, I," *Bell Systems Technical J.*, vol. 52, no. 6, pp. 843-874, 1973.

[PER2] S. D. Personick, "Receiver Design for Digital Fiber Optic Communication Systems, II," *Bell Systems Technical J.*, vol. 52, no. 6, pp. 875-886, 1973.

[PETE1] Klaus Petermann, *Laser Diode Modulation and Noise*, Dordrecht, Holland, Kluwer Academic Publishers, 1998.

[PETE2] Klaus Peterman, Günther Arnold, "Noise and Distortion Characteristics of Semiconductor Lasers in Optical Fiber Communication Systems," *IEEE J. Quantum Electronics*, vol. QE-18, no. 4, pp. 543-555, 1982.

[PETI1] I Petitbon, P. Gallion, G. DeBarge, C. Chabran, "Locking bandwidth and relaxation oscillations of an injection-locked semiconductor laser," *Electronics Letters*, vol. 22, no. 17, pp. 889-890, 1986.

[PETI2] Isabelle Petitbon, Philippe Gallion, Guy DeBarge, Claude Chabran, "Locking Bandwidth and Relaxation Oscillations of an Injection-Locked Semiconductor Laser," *IEEE J. Quantum Electronics*, vol. 24, no. 2, pp. 148-154, 1988.

[PRE1] William H. Press, Saul A. Teukolsky, William T. Vetterling, Brian P. Flannery, *Numerical Recipes in FORTRAN*, (Second Edition), New York, Cambridge University Press, 1992.

[PRO1] John G. Proakis, *Digital Communications*, (Third Edition), Boston, Massachusetts, McGraw-Hill, Inc., 1995.

[SA1] Bahaa E. A. Saleh, Malvin Carl Teich, *Fundamentals of Photonics*, New York, John Wiley & Sons, Inc., 1991.

[SE1] Young-Kwang Seo, Woo-Young Choi, "Analysis of Transmission Performance Enhancement with Injection-Locked Semiconductor Lasers," CLEO/Pacific Rim ′99, P2.43, pp. 916-917, 1999.

[SHA1] Hamutal Shalom, Avi Zadok, Moshe Tur, Peter J. Legg, W. D. Cornwell, Ivan Andonovic, "On the Various Time Constants of Wavelength Changes of a DFB Laser Under Direct Modulation," *IEEE J. Quantum Electronics*, vol. 35, no. 10, pp. 1816-1822, 1998.

[SHI1] M. Shirasaki, H. Nishimoto, T. Okiyama, T. Touge, "Fibre transmission properties of optical pulses produced through direct phase modulation of DFB laser diode," *Electronics Letters*, vol. 24, no. 8, pp. 486-488, 1988.

[SHU1] Nikolaus Schunk, Klaus Petermann, "Noise Analysis of Injection-Locked Semiconductor Injection Lasers," *IEEE J. Quantum Electronics*, vol. QE-22, no. 5, pp. 642-650, 1986.

[SI1] T. B. Simpson, J. M. Liu, "Enhanced Modulation Bandwidth in Injection-Locked Semiconductor Lasers," *IEEE Photonics Technology Letters*, vol. 9, no. 10, pp. 1322-1324, 1997.

[SM1] R. G. Smith, S. D. Personick, "Receiver Design for Optical Fiber Communication Systems," *Semiconductor Devices for Optical Communication*, ed H. Kressel, New York, Springer-Verlag, 1982.

[SO1] Lucas B. Soldano, Erik C. M. Pennings, "Optical Multi-Mode Interference Devices Based on Self-Imaging: Principles and Applications," *J. Lightwave Technology*, vol. 13, no. 4, pp. 615-627, 1995.

[ST1] William Stallings, *Local and Metropolitan Area Networks*, (Fourth Edition), New York, New York, MacMillan Publishing Company, 1993.

[SU1] Nobuo Suzuki, Takeshi Ozeki, "Simultaneous Compensation of Laser Chirp, Kerr Effect, and Dispersion in 10-Gb/s Long-Haul Transmission Systems," *J. Lightwave Technology*, vol. 11, no. 9, pp. 1486-1494, 1993.

[TA1] Noboru Takachio, Seiji Norimatsu, Katsushi Iwashita, Kazushige Yonenaga, "Transmission Limitations Due to Self-Phase Modulation in Optical PSK Heterodyne Detection Systems Employing Chromatic Dispersion Equalization," *J. Lightwave Technology*, vol. 12, no. 2, pp. 247-253, 1994.

[TO1] Hiromu Toba, Kazuhiro Oda, Kiyoshi Nosu, "Design and Performance of FSK-Direct Detection Scheme for Optical FDM Systems," *J. Lightwave*

Technology, vol. 9, no. 10, pp. 1335-1343, 1991.

[TR1] Bjarne Tromborg, Henning Olesen, Xing Pan, Shigeru Saito, "Transmission Line Description of Optical Feedback and Injection Locking for Fabry-Perot and DFB Lasers," *IEEE J. Quantum Electronics*, vol. QE-23, no. 11, pp. 1875-1889, 1987.

[VA1] Kerry Vahala, Amnon Yariv, "Semiclassical Theory of Noise in Semiconductor Lasers—Part II," *IEEE J. Quantum Electronics*, vol. QE-19, no. 6, pp. 1102-1109, 1983.

[VO1] R. S. Vodhanel, "5 Gbit/s Direct Optical DPSK Modulation of a 1530-nm DFB Laser," *IEEE Photonics Technology Letters*, vol. 1, no. 8, pp. 218-220, 1989.

[VO2] Richard S. Vodhanel, Aly F. Elrefaie, M. Z. Iqbal, Richard E. Wagner, James L. Gimlett, Shinji Tsuji, "Performance of Directly Modulated DFB Lasers in 10-Gb/s ASK, FSK, and DPSK Lightwave Systems," *J. Lightwave Technology*, vol. 8, no. 9, pp. 1379-1386, 1990.

[WH1] John K. White, J. V. Moloney, A. Gavrielides, V. Kovanis, A. Hohl, R. Kalmus, "Multilongitudinal-Mode Dynamics in a Semiconductor Laser Subject to Optical Injection," *IEEE J. Quantum Electronics*, vol. 34, no. 8, pp. 1469-1473, 1998,

[WI1] Sebastian Wieczorek, Daan Lenstra, Bernd Krauskopf, "Bifurcations of chaotic attractors in a semiconductor laser subject to optical injection," pp. 64-65, 2000.

[WOO1] S. L. Woodward, G. E. Bodeep, "Uncooled Fabry-Perot Lasers for QPSK Transmission," *IEEE Photonics Technology Letters*, vol. 7, no. 5, pp. 558-560, 1995.

[WOR1] Kerstin Wörhoff, Paul V. Lambeck, Alfred Driessen, "Design, Tolerance Analysis, and Fabrication of Silicon Oxynitride Based Planar Optical Waveguides for Communication Devices," *J. Lightwave Technology*, vol. 17, no. 8, pp. 1401-1407, 1999.

[YAM1] S. Yamazaki, K. Emura, M. Shikada, M. Yamaguchi, I. Mito, "Realisation of flat FM response by directly modulating a phase tunable DFB laser diode," *Electronics Letters*, vol. 21, no. 7, pp. 283-285, 1985.

[YAS1] Hiroshi Yasaka, Kiyoto Takahata, Kazuo Kasaya, Kunishige Oe, "Frequency Response of a Unidirectional-Output Optical Frequency Conversion Device with an Asymmetrical-κ DBR Laser Structure," *IEEE Photonics Technology Letters*, vol. 5, no. 11, pp. 1306-1310, 1993.

[ZE1] Wolfgang Zeiler, Fabrizio Di Pasquale, Polina Bayvel, John E. Midwinter, "Modeling of Four-Wave Mixing and Gain Peaking in Amplified WDM Optical Communication Systems and Networks," *J. Lightwave Technology*, vol. 14, no. 9, pp. 1933-1942, 1996.

[ZH1] Xiupu Zhang, Peixuan Jiang, "Limiter-Discriminator Detection of a Coherent Optical Heterodyne *M*-ary CPFSK Receiver," *J. Lightwave Technology*, vol. 10, no. 8, pp. 1127-1131, 1992.

Appendix A. Mach-Zehnder Delay Lengths.

The determination of exact MZ delay lengths for the harmonic decoding of the FCM signal can be related directly to the steady state response functions for the optical output of MZ interferometers as expressed in Equations (1) and (2). After converting the optical signals exiting from the interferometer to electrical signals, the difference of these signals is taken in the electrical domain and hence Equation (3). The fourth channel of a 16 level FCM signal would generate a voltage signal as described in the following equation,

$$V_{MZ4}(\nu) \propto P_{MZ4+}(\nu) - P_{MZ4-}(\nu) = P_{MZmax}\cos\left(\frac{2\pi\mu_{eMZ}\Delta L_4}{c}\nu\right), \qquad (128)$$

where the subscript 4 is used to denote the fourth channel.

The received signal can be represented in the optical frequency domain with respect to the optical frequency of the signal when a 0 symbol is transmitted for symbols with values m from 0 to M-1,

$$P_{MZ}(m) = P_{MZmax}\cos\left(\frac{2\pi\mu_{eMZ}\Delta L}{c}(\nu_0 + m\Delta\nu)\right) . \qquad (129)$$

When the signal is transposed in frequency with respect to a center symmetric optical frequency reference, Equation (129) can be rewritten to become,

$$P_{MZ}(m) = P_{MZmax}\cos\left(\frac{2\pi\mu_{eMZ}\Delta L}{c}\left(\nu_0' + m\Delta\nu - \frac{M-1}{2}\Delta\nu\right)\right) . \qquad (130)$$

All of the delay lengths for all the MZ based decoders must meet the following mathematical conditions for the correct decoding of the FCM signal into individual channels,

$$\frac{2\pi\mu_{eMZ}\Delta L_1}{c}\nu_0{}' = 2n'_{MZ1}\pi + \frac{\pi}{2}, \tag{131}$$

$$\frac{2\pi\mu_{eMZ}\Delta L_2}{c}\nu_0{}' = 2n'_{MZ2}\pi + \frac{\pi}{2}, \tag{132}$$

$$\frac{2\pi\mu_{eMZ}\Delta L_3}{c}\nu_0{}' = 2n'_{MZ3}\pi + \frac{\pi}{2} \tag{133}$$

and

$$\frac{2\pi\mu_{eMZ}\Delta L_4}{c}\nu_0{}' = 2n'_{MZ4}\pi - \frac{\pi}{2}, \tag{134}$$

where the n'_{MZ} variables are the MZ filter orders with respect to the center symmetric optical frequency. The phase condition between adjacent transmitted symbols is only approximately required to meet these conditions;

$$\frac{2\pi\mu_{eMZ}\Delta L_1}{c}\Delta\nu \approx \pi, \tag{135}$$

$$\frac{2\pi\mu_{eMZ}\Delta L_2}{c}\Delta\nu \approx \frac{\pi}{2}, \tag{136}$$

$$\frac{2\pi\mu_{eMZ}\Delta L_3}{c}\Delta\nu \approx \frac{\pi}{4} \tag{137}$$

and

$$\frac{2\pi\mu_{eMZ}\Delta L_4}{c}\Delta\nu \approx \frac{\pi}{8}. \tag{138}$$

When the longest delay, ΔL_1, is equivalent to 1/3 of the symbol period, then the frequency level spacing is 150% of the symbol rate, writing Equation (137) in these terms it becomes

$$\Delta L_4 \approx \frac{c}{24\mu_{eMZ}B} \tag{139}$$

The substitution of this equation into Equation (134) to find ΔL_4 for a given ν'_0 with the requirement that n'_{MZ4} is an integer precisely determines the filter order in terms of the center symmetric optical frequency reference and the bitrate. The filter orders for all four channels of a 16 level FCM signal are given by the following equations;

$$n'_{MZ4} = round\left(\frac{\nu_0'}{24B} + \frac{1}{4}\right) \tag{140}$$

$$n'_{MZ3} = round\left(\frac{\nu_0'}{12B} - \frac{1}{4}\right) \tag{141}$$

$$n'_{MZ2} = round\left(\frac{\nu_0'}{6B} - \frac{1}{4}\right) \tag{142}$$

and

$$n'_{MZ1} = round\left(\frac{\nu_0'}{3B} - \frac{1}{4}\right) \tag{143}$$

The filter order and the center symmetric optical frequency of the transmitted signal determine the exact values of the delay lengths that are required through Equations (131) to (134). The relationships between the delay lengths of the successive decoder MZs are not exactly harmonic, but are actually required not to be so. The lack of exact harmonic relationships is not a concern due to the large filter order of the interference and the fact that a small change in filter order does not force a large change in the amplitude of the received signal for any of the channels. The decoder will still be referred to as harmonic because it remains approximately harmonic.

Appendix B. PIN Diode Characterization and Simulation.

Characterization of the PIN diodes used in the design and implementation of the differential receiver required measurement of the reflection scattering parameter, S_{11}, response at normalized impedance of 50 Ω at the bonding electrodes on the chip substrate, schematically depicted in Figure B-1.

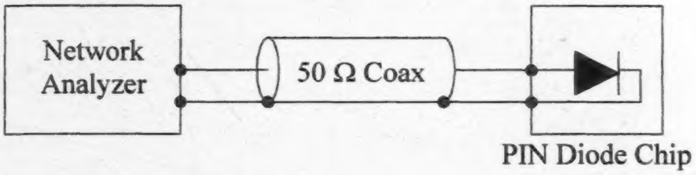
Network Analyzer
50 Ω Coax
PIN Diode Chip

Figure B-1: Functional electrical test schematic for measuring the (reflection) impedance of the PIN photo-diode chips.

The purpose of performing this measurement was to obtain an equivalent circuit model for the PIN diodes that consisted of separate active and passive electrical equivalent circuits. An analytic model was found that accurately represented the reflection data and replaced the diode reflection with a lumped equivalent as depicted in Figure B-2.

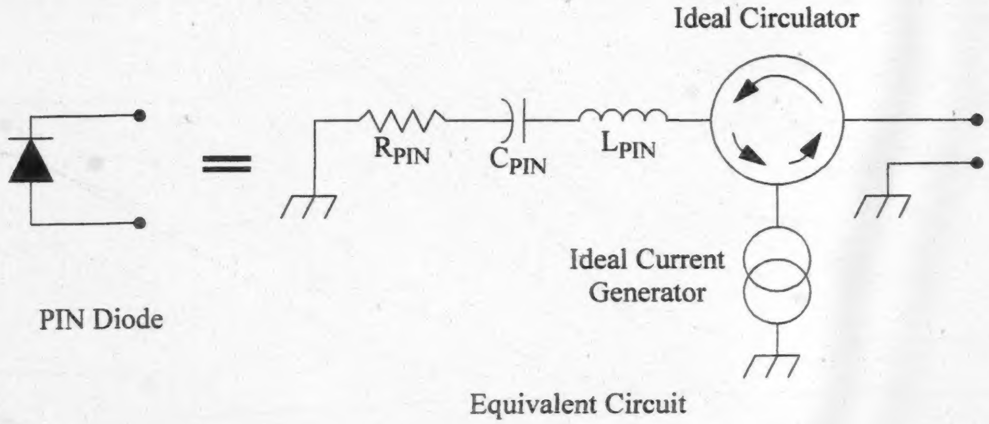
Ideal Circulator
R_{PIN}
C_{PIN}
L_{PIN}
Ideal Current Generator
PIN Diode
Equivalent Circuit

Figure B-2: Circuit schematic of the equivalent circuit for the PIN diode detector.

The electrical circuit model in Figure B-2 was used in Hewlett Packard (HP) Microwave Design System (MDS) to simulate the reflection of the PIN diode. This will be discussed in detail after the method of obtaining the model and "component" values has been discussed.

B.1 Network Analyser Measurement of PIN Diode S_{11}.

An HP Network Analyser, 8510B, was used to measure the S_{11} response of a Nortel PIN Diode optical receiver chip. A radio frequency (RF) ground-signal probe, with ground and signal contacts space at 140 μm, was lowered onto the bond pads of the PIN Diode after being calibrated for 50 Ω. The S_{11} response of the diode was measured from 50 MHz to 20 GHz for reverse bias voltages from 0V to 8V at 1V intervals. The measured S_{11} data was then plotted in terms of reflection coefficient versus frequency on Smith charts. Typical diode responses are shown in Figure B-3, with the 50 MHz end of the frequency sweep at the far right of each plot. The S_{11} response of the PIN diodes is almost circular on the Smith chart and was easy to characterize. The phase varies linearly with angle about the center of the Smith chart and the approximately circular response follows a line of constant impedance.

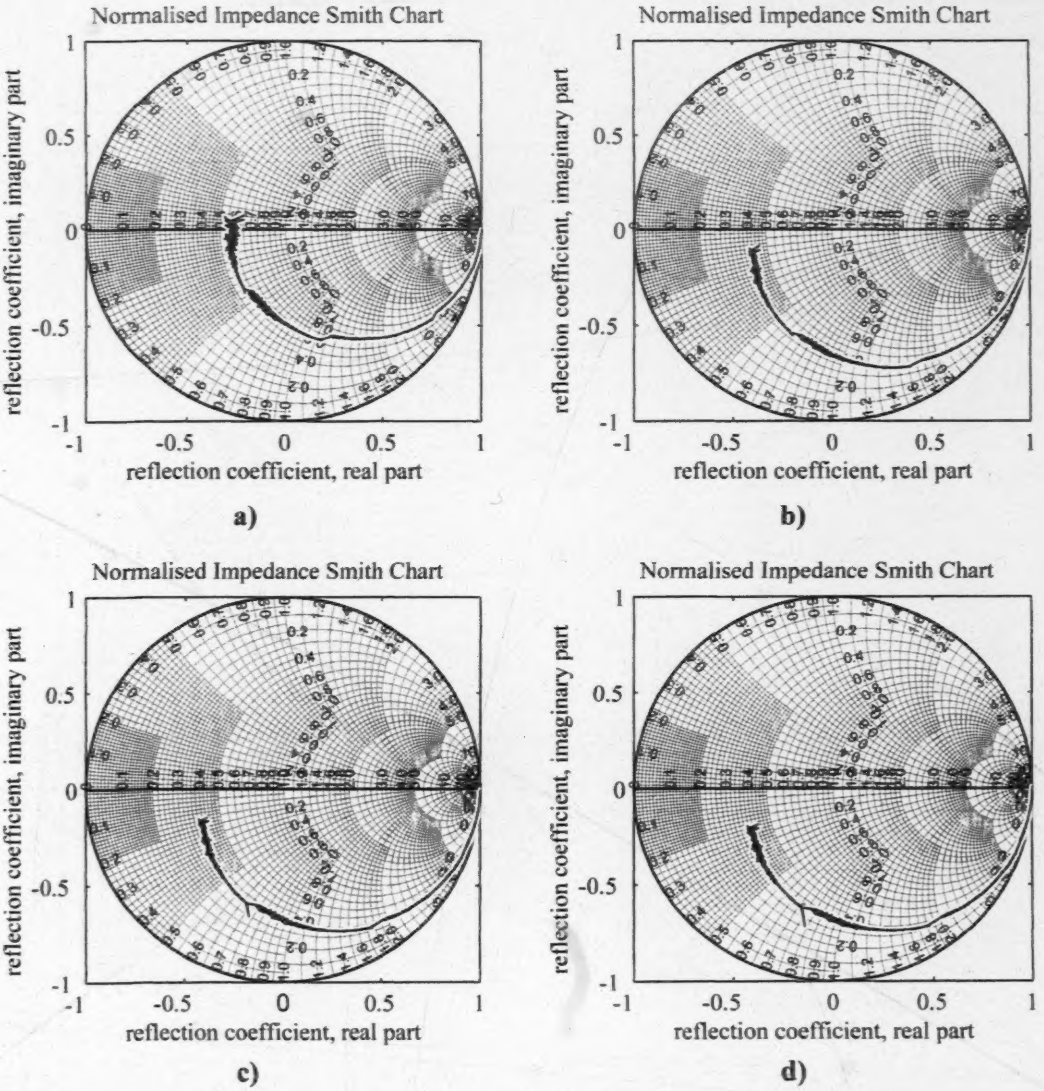

Figure B-3: Smith chart plots for S_{11} reflection data from PIN diode measurements at **a)** 0 V reverse bias, **b)** 3 V reverse bias, **c)** 5 V reverse bias and **d)** 8 V reverse bias.

B.2 From Measured Data to Equivalent Circuit Model.

The equivalent reflection impedance of these PIN diodes is derived from measured data that roughly traces out a circle on the normalized impedance Smith chart. This circle is assumed to be centered on the horizontal axis of the Smith chart (on the locus of real impedances) which worked quite well for fitting a curve to the data and generates a very simple equivalent circuit model. It was necessary to find the offset from the center of the Smith chart to the center of the S_{11} response circle.

The center and radius of this offset circle, and therefore the equivalent impedance, are found by first choosing points along the real impedance axis (horizontal line, vertically centered) to use as the center of the circle. The next step is minimizing the mean square error between the measured data and a circle starting with the DC response at the open circuit point of the Smith chart and proceeding clockwise with increasing frequency.

Since the reverse bias of the PIN diode for the receiver design was chosen to be 5 V, the remainder of the analysis in this appendix will be for 5 V reverse bias only.

The equivalent impedance magnitude was found to be 19.37 Ω. The phase of the S_{11} (reflection) response was modelled to be linear around 50 Ω resistance point at the center of the Smith chart with respect to frequency. The result of a mean square error minimization fit to the raw data was performed and the slope of the phase as a function of frequency was found to be -0.1337 radians/GHz.

The combination of reflection magnitude and reflection phase were used to derive equivalent circuit component values for a series RLC circuit model. The model values for the components depicted in Figure B-2 are: R_{PIN} = 19.37 Ω, C_{PIN} = 0.22 pF, and L_{PIN} = 207 pH.

B.3 Discussion of the PIN Diode Model.

The equivalent circuit schematic of the PIN diode is repeated here, Figure B-4, for clarity.

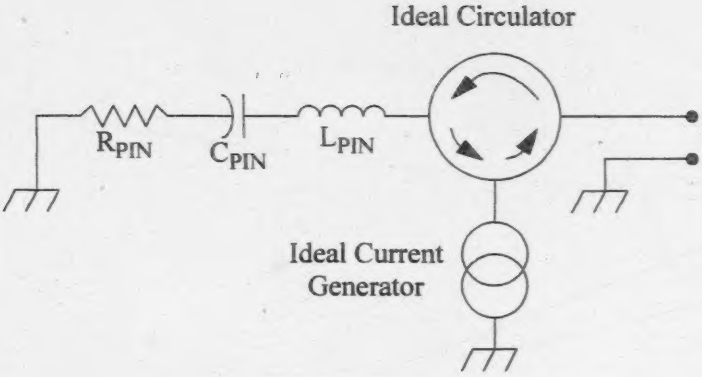

Figure B-4: Equivalent circuit model for the PIN diode.

The ideal current generator acts as an AC signal source and is assumed to have a flat magnitude response and linear phase response at all frequencies of interest, 50 kHz to 4 GHz for the receiver design. Ideal current generators also have infinite port impedances, a fact that is important to the model.

Any signal incident on this equivalent circuit from the port at the right in Figure B-4 goes counter-clockwise through the ideal circulator and is modified correctly (in magnitude and phase) by the equivalent passive components. The reflected signal from these components goes counter-clockwise through the circulator and is reflected from the ideal current generator. This reflection is 100% in magnitude and does not modify the phase which was verified in the MDS simulation tool. The signal is then fed back into the circulator and appears at the PIN diode port to be retransmitted to the receiver circuitry.

As for the signal that is generated by the PIN diode (through optical to electronic conversion of photons), it passes counter-clockwise through the ideal circulator and does not see the equivalent reflection impedance of the PIN diode. This model accurately describes the function of the PIN diode in the receiver circuit.

Appendix C. Receiver Transfer Function Measurement.

An optical receiver transfer function, $H_{REC}(f)$, is defined as the ratio of the output voltage of the receiver and the input optical power as,

$$H_{REC}(f) = \frac{V_{REC}(f)}{P_{opt}(f)}, \tag{144}$$

where V_{REC} is the output voltage of the optical receiver and P_{opt} is the input optical signal power at the receiver. A network analyzer is used to perform the measurement of H_{REC}.

Network analyzers, like the HP 8753A used for this measurement, measure ratios of voltages in the form of scattering parameters (otherwise known as S-parameters) where S_{21} is the forward transfer characteristic (the ratio of the output voltage and the input voltage). The ratio of output voltage to input optical power, as is required by Equation (144), and cannot be measured directly using a network analyzer. The electrical signal of the network analyzer must first be converted to an optical signal. A convenient means of performing the transfer function measurement is to use a Mach-Zehnder modulator for electrical to optical conversion. Any measurement of the combined Mach-Zehnder modulator and optical receiver system includes the transfer function of the electrical to optical conversion as well as the optical to electrical transfer function of the optical receiver,

$$H_{REC}(f) = \frac{V_{REC}(f)}{V_{RF}(f)H_{LMZ}(f)}, \tag{145}$$

where V_{RF} is the input voltage to the modulator and H_{LMZ} is the electrical to optical conversion transfer function of the modulator.

The receiver transfer function must be separated from the overall measured transfer function by measuring the transfer characteristic of the optical modulator. The following section explains how the Mach-Zehnder transfer characteristic is measured and the concluding section of this appendix explains how the receiver response is separated from the measurement of the Mach-Zehnder and receiver combination.

C.1 Measurement of the Lucent Mach-Zehnder Modulator Transfer Function.

The Lucent Mach-Zehnder optical modulator is a Lithium-Niobate two arm integrated interferometer with electro-optic drive electrodes on both optical paths. DC electrical bias can be supplied to one of the two (or both) electrodes to change the operating point of the modulator to any point on its voltage to optical power conversion curve.

The experiment conducted to determine the conversion characteristic of the modulator used a single arm of the Mach-Zehnder for bias and RF drive. The electrode for the other arm was shorted out with a co-axial shorting cap and the modulator was biased at its optical 3dB point. The voltage to optical power characteristic for this configuration is,

$$P_{opt} = \frac{1 + \sin\left(\frac{\pi V_{RF}}{V_\pi}\right)}{2} P_{in}, \tag{146}$$

where P_{opt} is the output optical power of the modulator (modulated at RF frequencies), V_{RF} is the input RF voltage signal, V_π is the Mach-Zehnder switching voltage, and P_{in} is the input optical power.

Measuring V_π as a function of modulation frequency completely specifies the transfer function of a Mach-Zehnder, Equation (146). With an AC drive voltage, Equation (146) becomes

$$P_{opt} = \frac{1 + \sin\left(\frac{\pi V_{RF0-p}\sin(2\pi f_{mod} t)}{V_\pi}\right)}{2} P_{in}, \tag{147}$$

where $V_{RF0\text{-}p}$ is the modulation amplitude, f_{mod} is the modulation frequency, and t is time. Oscilloscope traces are captured for values of $V_{RF0\text{-}p}$, which is varied from a small fraction of V_π to greater than $V_\pi/2$, and the received output voltage is measured at points where the drive voltage is at an extremum. The difference in received voltage when the drive voltage is maximum and when the drive voltage is minimum varies sinusoidally with peak input drive voltage, $V_{RF0\text{-}p}$. Plotting this difference between output voltage at maximum and minimum drive versus $2V_{RF0\text{-}p}$ yields V_π as the twice the drive voltage (the value of $2V_{RF0\text{-}p}$) corresponding the peak of this graph.

The HP 8753A network analyzer was used as an RF source and the HP 54120B oscilloscope was used to make the voltage measurements. Figure C-1 depicts the optical and electrical circuit used to perform these measurements.

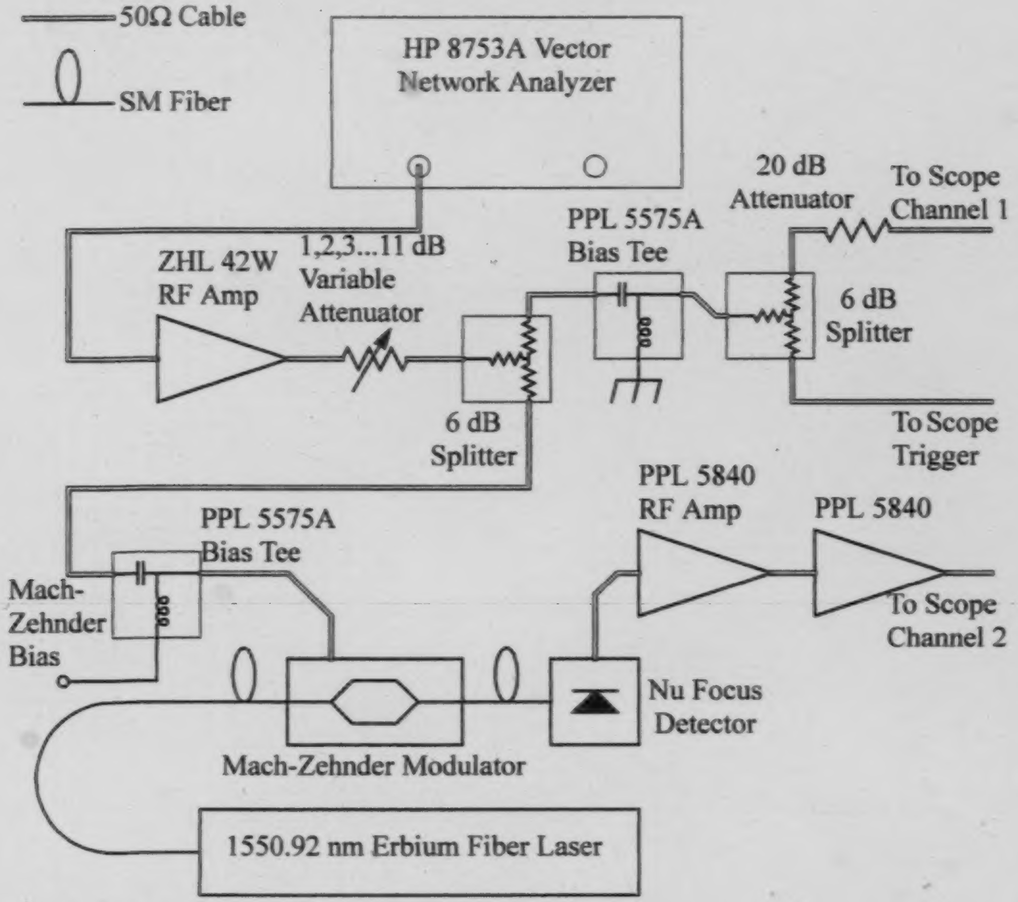
50Ω Cable
SM Fiber
HP 8753A Vector Network Analyzer
ZHL 42W RF Amp
1,2,3...11 dB Variable Attenuator
6 dB Splitter
PPL 5575A Bias Tee
20 dB Attenuator
To Scope Channel 1
6 dB Splitter
To Scope Trigger
PPL 5575A Bias Tee
Mach-Zehnder Bias
PPL 5840 RF Amp
PPL 5840
To Scope Channel 2
Nu Focus Detector
Mach-Zehnder Modulator
1550.92 nm Erbium Fiber Laser

Figure C-1: Electrical and optical circuits for the measurement of the Lucent Mach-Zehnder switching voltage, V_π. (ZHL 42W is the part number of a Mini-Circuits amplifier and PPL stands for Picosecond Pulse Labs.)

The output voltage of the network analyzer is set at a particular value and the variable attenuator is used to vary the drive voltage to the Mach-Zehnder in 1 dB increments. The first 6 dB splitter is used to send the drive voltage to the Mach-Zehnder and to the oscilloscope for drive voltage measurement. Broadband bias tees are present in both electrical paths, by necessity for supplying bias voltage to the Mach-Zehnder and as a means of including the bias tee response in the drive voltage measurement. Another 6 dB splitter is used in the calibration path to provide triggering for the HP oscilloscope. V_π was measured at 11 frequencies and is plotted as a function of frequency in Figure C-2.

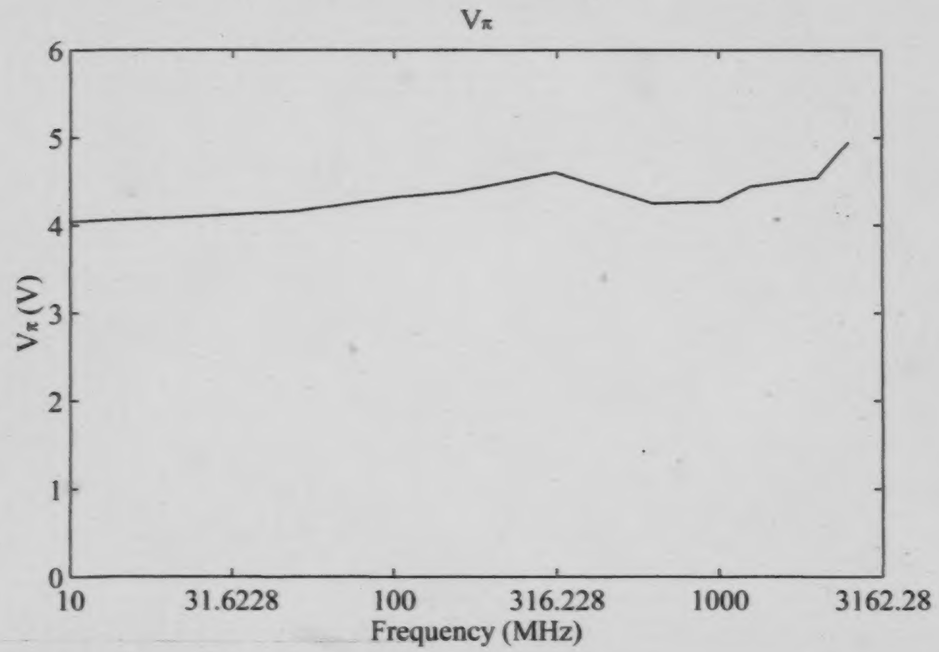

Figure C-2: Measured values of V_π for the Lucent Mach-Zehnder modulator as a function of frequency.

C.2 Separation of the Mach-Zehnder and Receiver Responses.

Using a small signal modulation input to the modulator simplifies the Mach-Zehnder transfer function by use of the sine small angle approximation, Equation (146) becomes Equation (148),

$$P_{opt} = \frac{\pi V_{RF}}{2V_\pi} P_{in}. \quad (148)$$

Using Equation (144), isolating the ratio of P_{opt} to V_{RF}, with Equations (145) and (148) yields the transfer function of the receiver,

$$H_{REC}(f) = \frac{2V_\pi}{\pi P_{in}} \frac{V_{REC}(f)}{V_{RF}(f)}. \qquad (149)$$

Once V_π is known as a function of frequency, the network analyzer can be used to measure the receiver transfer function for a known input optical power.

C.2.1 Measured Optical Receiver Transfer Function.

The erbium fiber laser (1550.92 nm wavelength) was set at - 4.16 dBm and connected to the Lucent Mach-Zehnder modulator. The modulator electrical drive was used in a one electrode configuration an biased at the 3 dB point. An HP 3753A vector network analyzer was connected to the input of the modulator and the output of the optical receiver. The forward transfer function of the system was measured with the network analyzer set at 0 dBm electrical power (50 Ω impedance) with an actual output power of less than -12 dBm. This test circuit is shown schematically in Figure C-3.

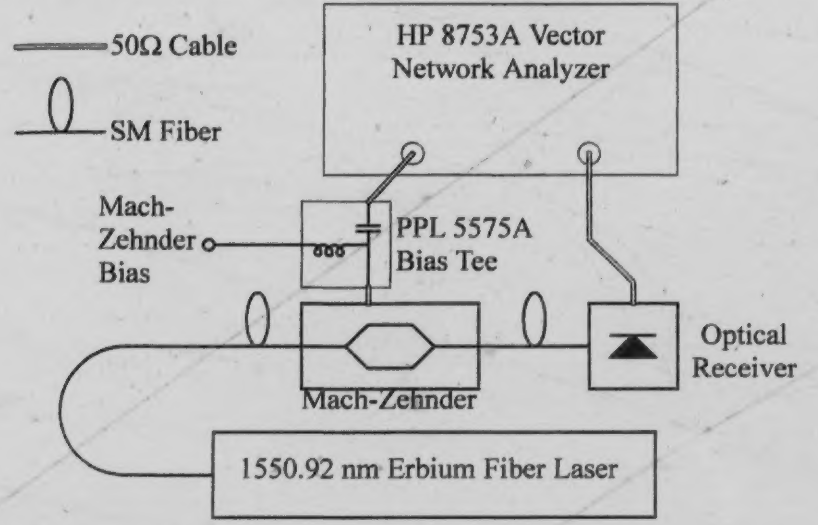
50Ω Cable
SM Fiber
HP 8753A Vector Network Analyzer
Mach-Zehnder Bias
PPL 5575A Bias Tee
Optical Receiver
Mach-Zehnder
1550.92 nm Erbium Fiber Laser

Figure C-3: Circuit Schematic for the measurement of the optical receiver transfer function. (PPL stands for Picosecond Pulse Labs.)

The transfer function measurements for two optical receivers were made for two frequency ranges, 300 kHz - 30 MHz and 30 MHz to 3 GHz (the full bandwidth of the network analyzer). The magnitude response of $H_{REC}(f)$ are plotted in Chapter 5.

Appendix D. Receiver Sensitivity from Noise Calculations.

Receiver sensitivity is defined as the signal power at the receiver to achieve a desired Signal to Noise Ratio (SNR) for analogue signals or Bit Error Ratio (BER) for digital signals. The data format for which these receivers are designed is digital, therefore, the BER is calculated.

The BER is defined as the mean number of incorrectly received data bits divided by the total number of bits received and is a measure of the quality of the receiver and the communication link. The BER can be measured experimentally but, during the design process, before the receiver has been built the BER as a function of received signal power can only be estimated by calculating the expected signal power and the expected noise power. The details of these calculations are a standard subject included in most optical communications text books and will not be explained here. The particular method used in this appendix follows closely from Smith and Personick's method described in "Semiconductor Devices for Optical Communication" [SM1]. Modifications were made to the calculation method and are described in later sections of this appendix.

Smith and Personick used a normalized frequency method that relies on calculating integrals of the noise terms over the bandwidth of the receiver using the receiver transfer function. In [SM1], assumed pulse shapes at the input and output of the receiver are used to specify the transfer function as the ratio of the Fourier transform of the output pulse to the Fourier transform of the input pulse. By specifying the pulse widths for both the input and the output any arbitrary receiver transfer function can be synthesized for any bit-rate and the integrals become independent of the absolute received power and the magnitudes of individual noise terms because the Personick's integrals are only functions of the pulse widths and assumed pulse shapes. If the transfer function is predetermined, as it is in the case of the receiver designed for the FCMA system, an input pulse shape is assumed and the integral formulae have to be modified.

D.1 Calculation of Personicks Integrals for a Known Transfer Function.

In the form found in [SM1], Personicks integrals are evaluated for known input and output waveforms. The equations used here are for an assumed input waveform and a known transfer function and are a derived equivalent to those found in the reference.

Using Smith and Personick's notation, the definition of the input pulse shape is $h_p(t)$ and the normalization condition for this pulse is (Equation 4.22 in [SM1])

$$\frac{1}{T}\int_{-\infty}^{\infty} h_p(t)dt = 1 , \tag{150}$$

where T is the bit period in seconds. The output pulse is defined as $h_{out}(t)$ where the output normalization condition is (Equation 4.27 in [SM1])

$$h_{out}(0) = 1 , \tag{151}$$

where the argument of the function is time and suitable offset in time such that the maximum of the pulse occurs at $t = 0$.

Smith and Personick define the transfer function, $H_T(\omega)$ from these equations as (Equation 4.30 in [SM1])

$$H_T(\omega) = \frac{H_{out}(\omega)}{H_p(\omega)} , \tag{152}$$

where $H_p(\omega)$ is the Fourier transform of $h_p(t)$ using the definition

$$H_p(\omega) = \int_{-\infty}^{\infty} h_p(t)e^{-i\omega t}dt , \tag{153}$$

and $H_{out}(\omega)$ is the Fourier transform of $h_{out}(t)$. The definitions of Personick's integrals use these definitions and equations.

When the transfer function is predetermined and an input pulse shape is assumed, the output pulse shape must be determined and the transfer function must be normalised such that the conditions in Equations (151) and (152) are obeyed. Equation (152) can be rewritten in the form

$$H_{out}(\omega) = H_p(\omega)H_T(\omega) \quad , \qquad (154)$$

and by performing and inverse Fourier transform of $H_{out}(\omega)$, $H_T(\omega)$ can be normalised so that $h_{out}(t)$ satisfies Equation (150).

D.2 Justification of Relevant Noise Terms.

The components that comprise the receiver are the PIN detector, low pass T-filter, a silicon transimpedance amplifier, and the bias circuits.

The bias circuits and T-filter do not contain resistive components, and therefore do not contribute resistive thermal noise to the noise spectrum and are not included in the noise calculation.

The PIN diode leakage current is neglected and only the dominating contribution of signal shot noise is considered for noise associated with the diode. Evaluation of the noise contributions from signal pulses in other time slots will also be neglected.

The amplifier, being a complex monolithic device, does not have specifications for shunt current and series voltage noise terms. The noise specification for the amplifier is given in the form of a noise figure. The noise associated with the amplifier is assumed to be white current noise over the entire bandwidth and will be treated as a shunt noise source, i.e. evaluated considering only Personick's second integral.

Only the evaluation of Personick's first and second integral are necessary for this noise estimation.

D.3 Evaluation of Personick's Integrals.

Personick's first and second integrals, I_1 and I_2 respectively, can be evaluated at any bit rate relative to the scaling of $H_T(\omega)$. The definitions of I_1 and I_2 (not normalized) are

$$I_1 = \frac{T}{(2\pi)^2} Re\left\{ \int_0^{\infty} H_p(\omega)[H_T(\omega) * H_T(\omega)]d\omega \right\}, \tag{155}$$

where Re{} denotes taking the real part and * denotes convolution, and

$$I_2 = \frac{T}{2\pi} \int_0^{\infty} |H_T(\omega)|^2 d\omega \,. \tag{156}$$

The input pulse shape is assumed to be a square pulse occupying the entire bit period as

$$h_p(t) = \begin{Bmatrix} 1 & |t| \le T/2 \\ 0 & |t| > T/2 \end{Bmatrix}, \tag{157}$$

and $H_T(\omega)$ is unitless and normalized with respect to the input and output pulse conditions based on the transfer function discussed in Chapter 5. The calculated values of Personick's integrals for the receivers are presented in Table D-1.

Table D-1: Evaluated values of Personick's first and second integral for various data rates for standard transmissions and of an FCM channel 1 signal.

		Data Bit Period, T (nsec)	Equivalent Data Rate (Gbps)	Personick's Integral Value	
				I_1	I_2
OC-12	native	1.608	0.622	2.327	2.333
	1/3 overlap	1.072	0.933	1.558	1.563
	1/2 overlap	0.804	1.244	1.164	1.175
GigE	native	0.8	1.25	1.158	1.170
	1/3 overlap	0.6	1.333	0.7767	0.7881
	1/2 overlap	0.4	2.50	0.6131	0.6268
OC-48	native	0.402	2.488	0.6149	0.6284
	1/3 overlap	0.268	3.732	0.5381	0.5880
	1/2 overlap	0.201	4.976	0.5275	0.6498

The values for Personick's integrals in Table D-1 are for channel 1 of the FCM transmission only. For the other channels (2, 3 or 4) the data bit period would be longer than those shown in the table column which would change the integral values. General trends can be seen for both I_1 and I_2, as a function of increasing equivalent data rate the integral values decrease. At the highest equivalent data rate I_2 begins to increase again, which is due to the fact that the receiver is limiting the magnitude of the signal at that data rate. Because the Personick's integrals account for the receiver transfer function, when the total noise power is calculated it is also referenced to the maximum signal that is allowed through the receiver.

D.4 Signal and Noise Amplitudes as Functions of the Received Power.

The calculations from this point forward in this appendix will reference all receiver signal and noise amplitudes to the equivalent electrical current that would be present at the input to the receiver (at the input to the first amplifier stage). The following equations for signal current, Equation (158), and mean-square noise currents, Equations (159) and (160), come from Smith and Personick [SM1] and are identical restatements of Equations (4.46) and (4.47) (with the APD multiplication factor set equal to 1) and slightly modified versions of Equations (4.52) and (4.56). The definition of signal current, I_{sig}, is,

$$I_{sig} = \left(\frac{\eta q}{h\nu}\right) b, \tag{158}$$

where η is the external quantum efficiency of the detector, q is the electron charge, h is Planck's constant, ν is the optical frequency of the signal photons and b is the signal power at the decision time. The term in parenthesis is called the responsivity of the detector and is usually algebraically represented as R, this will not be used here to avoid confusion with all of the other Rs used in this document. The definition of the mean square signal shot noise, $\langle i_s^2(0)\rangle$ is,

$$\langle i_s^2(0)\rangle = 2q\left(\frac{\eta q}{h\nu}\right) bBI_1 . \tag{159}$$

The definition of the mean square amplifier noise, $\langle i_a^2\rangle$, is,

$$\langle i_a^2\rangle = \frac{4k_B T_K}{R_{amp}} BI_2 , \tag{160}$$

where k_B is Boltzman's constant, T_K is the detector temperature in Kelvin, and R_{amp} is the receiver amplifier noise resistance (for a 50 Ω system) and is calculated from

$$\frac{1}{R_{eq}} = \frac{10^{(NF)/10}}{50\Omega} = \frac{50\Omega + R_{amp}}{(50\Omega)(R_{amp})}, \tag{161}$$

where NF is the amplifier noise figure and R_{eq} is the equivalent parallel resistance of the receiver noise resistance and a 50 Ω resistor. And the total mean square noise current for a single optical receiver, $\langle i^2(0)\rangle_{total}$, is given by Equation (162),

$$\langle i^2(0)\rangle_{total} = \langle i_s^2(0)\rangle + \langle i_a^2\rangle \quad . \tag{162}$$

The signal current, I_{sig}, is the mean received signal at the decision time and the total mean square noise current, $\langle i^2(0)\rangle_{total}$, are the arguments of the Gaussian distribution which can now be used to evaluate the rate of errors once a decision threshold is chosen. This information is used in the next section to calculate the BER for two receiver units used as a differential receiver.

D.5 Bit Error Ratios for a Differential Receiver.

Calculation of the BER for the differential receiver requires the redefinition of the signal current and the mean square noise currents at the decision time to account for the fact that two receivers are being used. For the $\log_2 M$ channel of the M-level FCM system the mean signal current follows the following equation,

$$I_{sig,\, symbol,\, channel} = \left(\frac{\eta q}{h\nu}\right)(b_{1,\, symbol,\, channel} - b_{2,\, symbol,\, channel}), \tag{163}$$

where all of the other channels (channel 1 included) follow the equation below,

$$I_{sig,\, symbol,\, channel} = \left(\frac{\eta q}{h\nu}\right)(b_{2,\, symbol,\, channel} - b_{1,\, symbol,\, channel}), \tag{164}$$

where $I_{sig,symbol,channel}$ refers to the total signal current for the dual differential receiver for a particular symbol and channel at the decision time, and $b_{1,symbol,channel}$ and $b_{2,symbol,channel}$ are the received optical powers at the two outputs of the MZ decoder for a particular channel and symbol. The new subscripts, symbol and channel, are for keeping track of the fact that each symbol on each channel may have a unique signal amplitude and the 1 and 2 subscripts for the signal optical power at the decision time refer to the MZ decoder output, P_{out1} and P_{out2}. This mean optical power is redefined to a new variable for convenient expression in future equations as,

$$\overline{I_{symbol,channel}} = I_{sig,\, symbol,\, channel} \tag{165}$$

For the total mean square noise current, $\sigma^2_{symbol,channel}$, the following equation will be used,

$$\sigma^2_{symbol,channel} = \langle i_s^2(0) \rangle_{symbol,channel} + 2\langle i_a^2 \rangle \tag{166}$$

where the amplifier noise term is doubled due to the presence of two amplifiers and the shot noise is defined as,

$$\langle i_s^2(0) \rangle_{symbol,channel} = 2q\left(\frac{\eta q}{h\nu}\right)(b_{1,symbol,channel} + b_{2,symbol,channel})BI_1 \tag{167}$$

where the subscripts have the same meanings as they did for the signal current. The amplifier noise term obeys Equation (160) where the amplifier noise resistance is taken to be 50 Ω because a good approximation of the amplifier noise figure is 3 dB within the receiver bandwidth.

For a particular symbol whose intended received value is 0 for a particular channel, the probability that a 1 will be received in error, $P_{symbol,channel}(e|0)$, is evaluated using the following equation,

$$P_{symbol,channel}(e|0) = \int_{I_{dt}}^{\infty} \frac{1}{\sqrt{2\pi}\sigma_{symbol,channel}} \exp\left(\frac{(I - \overline{I_{symbol,channel}})^2}{2\sigma^2_{symbol,channel}}\right) dI. \tag{168}$$

The integral of the Gaussian probability density function runs over all values of current greater than the decision threshold, I_{dt}. The probability that any intended zero is received in error over all transmitted 0 symbols for a particular channel, $P_{channel}(e|0)$, is given by

$$P_{channel}(e|0) = \frac{\sum\limits_{0symbols} P_{symbol,channel}(e|0)}{M/2}, \tag{169}$$

where it is assumed that all symbols are transmitted with equal probability.

The probability of receiving a 0 instead of an intended 1 for each transmitted 1 symbol on a particular channel, $P_{symbol,channel}(e|1)$, is given by the following equation,

$$P_{symbol,channel}(e|1) = \int_{-\infty}^{I_{dt}} \frac{1}{\sqrt{2\pi}\sigma_{symbol,channel}} \exp\left(\frac{(I - \overline{I_{symbol,channel}})^2}{2\sigma^2_{symbol,channel}}\right) dI, \tag{170}$$

where the integral now runs over all values of current below the decision threshold. When all of the errors are summed over all intended 1 symbols for a particular channel the result, $P_{channel}(e|1)$, is given by the equation,

$$P_{channel}(e|1) = \frac{\sum_{1symbols} P_{symbol,channel}(e|1)}{M/2}, \tag{171}$$

where again it is assumed that all symbols are transmitted with equal probability.

The total probability of receiving errors on a particular FCM channel, $P_{channel}(e)$, when all symbols are transmitted with equal probabilities is given by this final equation,

$$BER = P_{channel}(e) = \frac{P_{channel}(e|0) + P_{channel}(e|1)}{2}., \tag{172}$$

which is also the value of the BER of that channel.

The decision threshold will be chosen to be the condition that optimizes the decision threshold for binary ISK systems, which is given by the following equation,

$$\sum_{0symbols} \frac{1}{\sqrt{2\pi}\sigma_{symbol,channel}} \exp\left(\frac{(I - \overline{I_{symbol,channel}})^2}{2\sigma^2_{symbol,channel}}\right) =$$

$$\sum_{1symbols} \frac{1}{\sqrt{2\pi}\sigma_{symbol,channel}} \exp\left(\frac{(I - \overline{I_{symbol,channel}})^2}{2\sigma^2_{symbol,channel}}\right). \tag{173}$$